

**The Seismic Conversion Log and its
Application to Vertical Seismic Profiling at the
German Continental Deep Drilling Site (KTB)**

Dissertation
zur Erlangung des Doktorgrades
der Mathematisch-Naturwissenschaftlichen Fakultät
der Christian-Albrechts-Universität
zu Kiel

vorgelegt von
Thies Carl Helmut Beilecke

Kiel 2003

Bibliographic information published by Die Deutsche Bibliothek
Die Deutsche Bibliothek lists this publication in the Deutsche Nationalbibliographie;
detailed bibliographic data are available in the Internet at <http://dnb.ddb.de>.

Beilecke, Thies Carl Helmut:

The Seismic Conversion Log and its Application to Vertical Seismic Profiling
at the German Continental Deep Drilling Site (KTB) / vorgelegt von Thies
Carl Helmut Beilecke. - 1. Aufl. - Kiel : Selbstverlag Thies Beilecke, 2003

Zugl.: Kiel, Univ., Diss., 2003

ISBN: 3-00-012281-8

ISBN: 3-00-012281-8

© 2003 by Selbstverlag Thies Beilecke, Kiel

1. Auflage, 2003

Satz: Thies Beilecke - pdfL^AT_EX mit hyperref package

Alle Rechte vorbehalten. Das Werk ist urheberrechtlich geschützt. Jede Verwertung
außerhalb der gesetzlich geregelten Fälle muß vom Verlag schriftlich genehmigt
werden.

Referent:

Korreferent:

Tag der mündlichen Prüfung:

Zum Druck genehmigt:

Prof. Dr. Wolfgang Rabbel

Prof. Dr. Rolf Meißner

Kiel, den 11. Juni 2003

Kiel, den 16. Oktober 2003

Der Dekan

Abstract

The Continental Deep Drilling Site (KTB) in southern Germany has been the location of many different, detailed research projects that have come up with a wealth of geoscientific results. A large number of parameters are therefore available for comparative studies. The KTB site is one of a few places in the world where boreholes were drilled deep into the crystalline part of the Earth's crust. It is believed that the results obtained within the KTB wells are also representative for many basement rocks, inaccessible for direct observation in many sedimentary environments.

In April and September of 1999 a deep vertical seismic profile (VSP) was acquired in the depth range from 3.0-8.5 km in the main hole of the KTB site (maximum depth 9101 m). The experiment yielded high quality seismic data in terms of signal bandwidth, signal-to-noise ratio, amplitude reference, and stability of the source signal. This was confirmed by a stationary reference geophone in the pilot hole of the KTB site (maximum depth 4000 m). Surface reference geophones were systematically not capable of providing an equivalent quality control. The explosive source provided highly repeatable signals.

The seismic data show varying compressional to shear wave conversion along the borehole. The objective was to use this conversion information to determine the influence of cracks and fissures on the seismic wave pattern in the crust. The newly developed seismic conversion log processing method can quantify this conversion. Through the compound analysis of wave conversion and compressional wave attenuation with borehole information from the KTB database important facts were obtained:

The source signal proved to be simple. The multi-phase seismic signature at depth is a result of multi-pathing within the crust, i.e., the fractioning of the wavefront in crustal structures with different elastic properties oriented parallel to the ray trajectory. The determination of attenuation values in a complicated crustal environment is hampered by the structural features. In the presence of steeply dipping structures the conversion is basically independent from the angle between the incident seismic wave and the impedance contrast surface. In a scattering environment the wave conversion log method is not only capable of determining the conversion amplitude originating from the direct vicinity of the borehole but also from distant conversion points. The conversion in the field data as well as in the model data is frequency dependent in an unusual manner; intermediate frequency signals (30-60 Hz) convert less than low (15-30 Hz) and high frequency signals (60-240 Hz). In the crust at the KTB site only about 10%-50% of the conversion originates from the variation of the mineral composition of the rocks. Wave conversion depends on the fracture density, i.e., the influence of cracks and fissures on the elastic parameters. However, the wave conversion is also highly dependent on chlorite content, that seems to 'heal' the influence of cracks and fissures. This is important for crustal surface seismic experiments aiming at reflections from fault zones.

Zusammenfassung

Die Kontinentale Tiefbohrung der Bundesrepublik Deutschland (KTB) ist Lokation vieler verschiedener Untersuchungen gewesen, die eine große Zahl geowissenschaftlicher Ergebnisse erbracht haben. Eine Vielzahl von Parametern stehen deswegen für vergleichende Analysen zur Verfügung. Die KTB ist einer der wenigen Orte auf der Erde, an denen Bohrungen tief in die kristalline Kruste reichen. Es wird angenommen, dass Erkenntnisse aus den KTB Bohrungen repräsentativ für viele Basementstrukturen sind, die in sedimentären Gebieten unerreichbar für die direkte Beobachtung sind.

Im April und September 1999 wurde ein vertikalseismisches Profil (VSP) im Teufenbereich 3 bis 8,5 km in der KTB Hauptbohrung (Endteufe 9101 m) vermessen. Die Messung erbrachte einen Datensatz mit hoher Qualität in Bezug auf Signalbandbreite, Signal zu Noise Verhältnis, Amplitudenreferenz und Stabilität des Quellsignals. Das konnte mit Hilfe eines stationären Geophons in der KTB Vorbohrung (Endteufe 4000 m) referenziert werden. Die Oberflächenreferenzgeophone waren systematisch nicht in der Lage die Qualitätskontrolle zu gewährleisten. Das Explosionsquellsignal war hochgradig reproduzierbar.

Die seismischen Daten zeigen eine variierende Kompressions- zu Scherwellen Konversion entlang der Bohrung. Das Ziel der Untersuchung war, den Einfluß von Rißstrukturen auf den Charakter der seismischen Wellen in der Kruste zu bestimmen. Dazu wurde das Konversions-Log, eine neue seismische Datenbearbeitungsmethode, entwickelt, die in der Lage ist, die Konversion seismischer Wellen zu quantifizieren. Die kombinierte Analyse der Konversion und der Kompressionswellendämpfung mit Bohrlochinformationen aus der KTB Datenbank erbrachte wichtige Erkenntnisse:

Das Quellsignal ist sehr einfach. Die mehrphasige Signatur der seismischen Spuren im Bohrloch beruht allein auf der komplizierten Krustenstruktur. Sie ruft Multipathing hervor, also die Zerfaserung der Wellenfront in parallel zur Ausbreitungsrichtung verlaufenden Strukturen mit unterschiedlichen elastischen Eigenschaften. Die Bestimmung von Dämpfungswerten wird durch komplexe Krustenstrukturen behindert. Beim Vorliegen steil einfallender Krustenstrukturen ist die Konversionsamplitude weitestgehend unabhängig vom Winkel zwischen einfallender Welle und Impedanzkontrastgrenzfläche. In einem streuenden Medium ist die Konversions-Log Methode nicht nur in der Lage die Konversionsamplitude, aus der direkten Umgebung des Bohrlochs zu quantifizieren, sondern auch von weiter entfernt liegenden Konversionspunkten. Die Konversion sowohl in den Felddaten als auch in den Modelldaten zeigt eine ungewöhnliche Frequenzabhängigkeit; Signale mittlerer Frequenzen (30-60 Hz) konvertieren schwächer, als Signale tiefer (15-30 Hz) oder hoher Frequenzen (60-240 Hz). In der Kruste an der KTB werden nur 10%-50% der Konversion von den Unterschieden der Mineralzusammensetzung bestimmt. Die Konversion ist in hohem Maße von der Rißdichte abhängig, d.h. von dem Einfluß der Rißstrukturen auf die elastischen Parameter. Aber die Konversion ist genauso abhängig vom Chloritgehalt in der Kruste, was bedeutet, daß Chlorit Klüfte oder Risse 'heilt'. Dieses ist von enormer Bedeutung für krustenseismische Experimente, mit dem Ziel Störungssysteme zu untersuchen.

Contents

1	Preface	1
1.1	Motivation	1
1.2	Overview	3
2	Geoscientific Frame	5
2.1	Tectonic Setting	5
2.2	Lithology	7
2.3	Petrophysics at the KTB site	9
2.4	Seismics at the KTB site	10
2.5	Summary	14
3	Theoretical Background	15
3.1	Seismic Waves	15
3.2	Attenuation	16
3.3	Quality Factor Q	18
3.4	Wave Phenomena and Approximations	22
3.4.1	Conversion, Reflection	22
3.4.2	Scattering, Diffraction	22
3.4.3	Random Media	23
3.4.4	Finite-Difference Modeling	23
4	Seismic Field Data	25
4.1	Deep VSP at the KTB site	25
4.2	Geometry	26
4.3	Data Quality	27
4.4	Seismic Sections	31
4.4.1	Vertical Component	32
4.4.2	Horizontal Components	32
4.5	Amplitude Decay with Depth, Q	37
4.5.1	Pilot Hole Reference Amplitude Values	37
4.5.2	Full Spectrum Analysis	38
4.5.3	Octave Analysis	40
4.6	Summary	44

5	Conversion Log Processing	47
5.1	Basic Data Processing	48
5.1.1	Shot Statics	48
5.1.2	Trace Rotation	48
5.1.3	Amplitude Considerations	49
5.2	P-to-S converted Waves in Transmission	51
5.2.1	Frequency-Wavenumber (f-k) Filtering	51
5.2.2	Velocity Reduction	52
5.2.3	Residual Statics	55
5.2.4	Stack	60
5.2.5	Time to Depth Conversion	64
5.2.6	Geophone Inclination	64
5.3	Other Conversions	66
5.4	Summary	67
6	Conversion Log Analysis	69
6.1	Phase Preserving Stack	69
6.1.1	Full Spectrum Analysis	69
6.1.2	Octave Analysis	74
6.2	Envelope Stack	80
6.2.1	Full Spectrum Analysis	80
6.2.2	Octave Analysis	83
6.3	Summary	83
7	Analytical Calculations	87
7.1	Wave Conversion	89
7.1.1	Simulated Isotropic Rock Matrix Velocities	89
7.1.2	Measured Velocities	95
7.2	Summary	100
8	Finite-Difference Modeling	101
8.1	Spatial Resolution	103
8.2	Simulated Isotropic Rock Matrix	110
8.2.1	60° Foliation Dip Model	111
8.2.2	Complex Model	128
8.3	Summary	145
9	Discussion	147
9.1	Quality Factor Q	148
9.2	Wave Conversion in Transmission	148
9.2.1	Conversion Log Capability	148
9.2.2	Field Data Conversion	150
9.3	Frequency Considerations	160

10 Conclusions and Future Work	163
10.1 Conclusions	163
10.1.1 Wave Pattern	163
10.1.2 Q	164
10.1.3 P-to-S Conversion	164
10.1.4 Crustal Properties	164
10.2 Future Work	166
Bibliography	167

Chapter 1

Preface

1.1 Motivation

Converted seismic waves have traditionally been analyzed in global seismology. They carry detailed information about the internal structuring of planets. However, the conversion of waves attenuates the energy of the nursing wave. Traditionally, in prospection seismology, compressional waves were considered as more important for the detection of crustal or reservoir structures than shear waves. Hence, they have been enhanced by field geometry or processing means suppressing the shear waves, to yield a higher compressional wave signal to noise ratio.

Only recently converted waves have also been focused on for prospection purposes in the oil and gas industry and in mineral exploration, despite the practical problems that have to be overcome in each case. This new perspective is partly due to the fact that the strongest conversion takes place from compressional (P) waves to shear (S) waves. S-waves carry additional information about reservoir parameters that enable the analyst to quantify reservoir characteristics more precisely. In consolidated regimes S-waves also provide the interpreter with a higher spatial resolution because of their lower velocities. Sometimes the recording and processing of shear waves or even the exclusive work with shear waves answers otherwise remaining open questions.

The vertical seismic profile (VSP) study of the lower part of the continental deep drilling “Kontinentale Tiefbohrung der Bundesrepublik Deutschland” (KTB) that was carried out in 1999 yielded superb seismic data. These data show very strong conversion of seismic energy. Shear wave analysis in VSP geometry is easier than with data recorded at the surface because weathering effects do not disturb the particle motion. It was therefore only natural to quantitatively analyze the phenomenon of seismic wave conversion with respect to other parameters obtained over the years at the KTB site.

The main objective of this study was the determination of the reason for the apparently strong conversion and its amount. The answer was not only expected to be important for prospection purposes, but also for the interpretation of the many crustal seismic data sets existing from many parts of the world. Another objective was the

attempt to correct the signal decay along the borehole for the amount of conversion, in order to derive quality factor values (Q) that represent the intrinsic order of magnitude more realistic than a traditional field data Q analysis.

Owing to the detailed geoscientific information available for this location a detailed comparative analysis could be carried out with respect to the large scale crustal structure, but also with respect to individual small scale parameters. Seismic finite-difference calculations proved to be crucial for the interpretation of the field data. The modeling was the pivot between analytic calculations and seismic field data. This work demonstrates the importance of the often neglected effort to model seismic data.

The aim of this thesis is not to prove or disapprove certain attenuation or scattering theories. It is rather supposed to provide some hints and additional field data values to constrain speculation on attenuation mechanisms. Special about these values are the well defined multi-scale reference information.

History

In 1977 the geoscientific community in Germany had first discussions about the investigation of the continental crust by means of a super-deep borehole. One major objective was an accuracy analysis of geoscientific measuring methods applied on the earth's surface for the prediction of its internal structuring. Another was the *in situ* measurement of different properties in the crystalline crust, down to the middle crust.

For the development of adequate drilling and probing techniques a test hole, the so called pilot hole (Vorbohrung, VB), was drilled from 1987 until 1989 to a depth of 4000 m. The main hole (Hauptbohrung, HB) was drilled from 1990 until 1994 to a final depth of 9101 m. Drilling was repeatably interrupted for borehole measurements, in the open hole where necessary, or else from within the later installed casing.

The whole KTB project proved to be very successful, because many of the predictions made before drilling started were wrong. Geological and geophysical methods and models could be refined owing to this project.

VSP Experiments

Frequent seismic measurements were conducted before the site selection, throughout the whole drilling process, until the Deep VSP measurements in 1999, and a combined offset VSP – $2^{1/2}$ d surface seismic experiment in 2000. The VSP measurements carried out in the boreholes comprise a few data sets recorded to roughly 3600 m depth in the pilot hole in 1989, a VSP from 3000 m to 6000 m recorded in the main hole in 1992, and a VSP recorded in the main hole in 1999 from 3000 m to 8500 m depth with a reference geophone in the pilot hole. The reference geophone in the pilot hole proved to be crucial for the overall success of the 1999 VSP experiment. Because of this valuable reference it was decided to only rely on the 1999 VSP data for the wave conversion analysis presented in this thesis.

1.2 Overview

The result of the processing method presented here is a *conversion log*. It quantifies the amount of energy being converted with respect to depth. This method was compared with detailed analytic and modeling work to determine its spatial and amplitude resolution capacity; it was also compared with logging information and petrophysical parameters to determine its practical use. The following chapter sequence was chosen for this thesis:

- **Chapter 2** gives an overview of the regional tectonic and geologic setting around and in the KTB boreholes
- **Chapter 3** explains the theoretical foundation of the phenomena to be analyzed in the course of this thesis
- **Chapter 4** describes the field data basis for the analysis
- **Chapter 5** serves as seismic data processing guide. The result of the processing sequence is the conversion log
- **Chapter 6** presents the analysis of the acquired conversion logs
- **Chapter 7** deals with analytic calculations of the possible amount of conversions for different models as a guideline to the limits of the measured data and modeling processes
- **Chapter 8** focuses on seismic finite-difference computations of some crustal models. Conversion logs for these models are being discussed
- **Chapter 9** compares theory, field data results, analytic calculations, and modeling results with other information available from the boreholes to decide on the feasibility of the presented data processing routine
- **Chapter 10** concludes and provides an outlook for possible processing optimization and future work.

Chapter 2

Geoscientific Frame

The geographical region Oberpfalz is situated in the northeastern corner of Bavaria, Germany, at the western margin of the Bohemian Massif. Its complicated geological evolution is described in detail in a variety of papers. A summary can be found in [Emmermann & Lauterjung \(1997\)](#).

2.1 Tectonic Setting

Tectonically, this region comprises parts of the Variscan fold belt, parts of the Saxothuringian terrane in the north, some of the Moldanubian terrane in the south and parts of the Tepla-Barrandian in the east. This basement block is separated in the southwest at the Franconian Lineament from Permo-Mesozoic sediments which have a thickness of up to 3000 m (Figure 2.1). The KTB site is situated about 4 km northeast of the Franconian Lineament and about the same distance south of the border between the Saxothuringian and the Moldanubian terranes ([Kossmat, 1927](#)). The drillholes lie within a small, isolated tecto-metamorphic unit, the so-called Zone of Erbendorf-Vohenstrauß (ZEV).

North of the KTB site remnants of large faults of the Variscan collision front trending southwest-northeast were detected through the interpretation of crustal surface seismic profiles. Within the boreholes these faults are not prominent; they only appear in terms of minor faults in the lowest part of the main hole and can possibly be related to a greenschist zone at the surface a couple of kilometers north of the KTB site, close to the postulated suture zone (Figures 2.2 and 2.4) ([Hirschmann, 1996](#)). The vague appearance of the Variscan collision is probably due to the fact that Variscan faulting took place in a semi-ductile to ductile environment ([Emmermann & Lauterjung, 1997](#)). Therefore, it is rather the metamorphic details of the rocks and their protoliths within the KTB main hole that can serve as the basis for the unraveling of the Variscan history.

The Franconian Lineament is located perpendicular to the Variscan collision front. It is a northwest-southeast striking deep reverse fault zone of regional size with a *total*

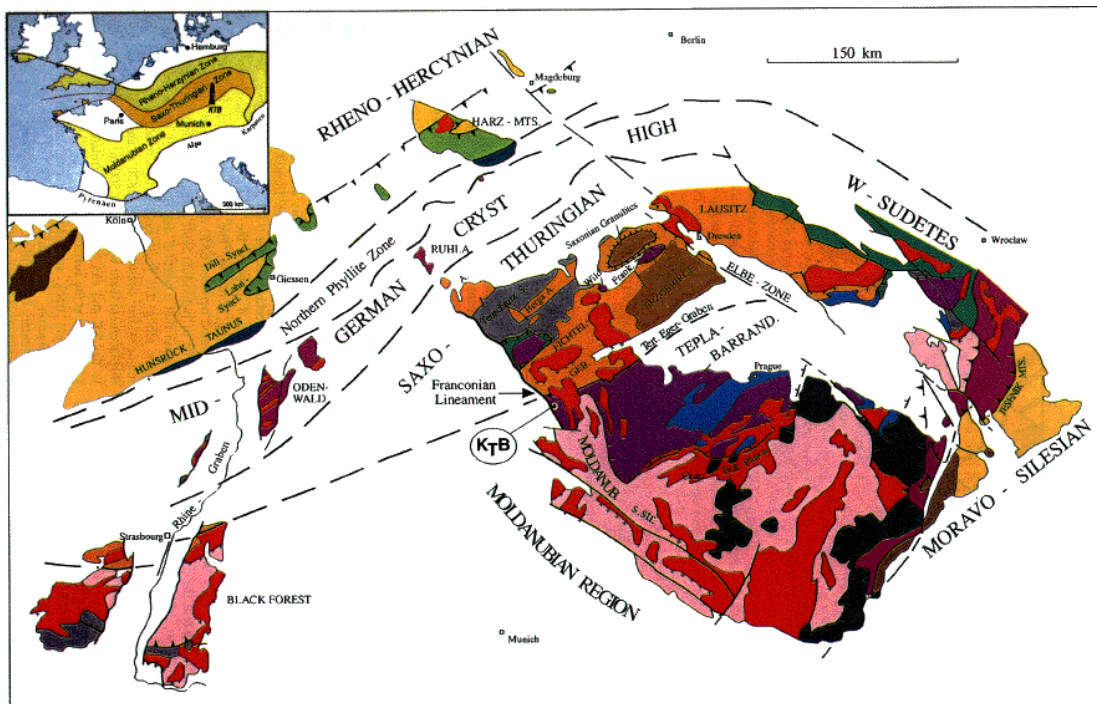


Fig. 2.1: Image of selected geological units of the Variscan region. The KTB site is located in a small, isolated unit (Zone von Erbdorf-Vohenstrauß, ZEV) at the border of the Moldanubian and Saxothuringian regions (from *Emmermann & Lauterjung, 1997*).

displacement of about 5-6 km (*Hirschmann, 1996*) as a result of intense, polyphase, mostly reverse faulting in late Variscan and Cretaceous (*Duyster et al., 1994, 1995a*). Because the post-Variscan history of the ZEV is characterized by sudden and strong, multi-phase, brittle deformations (*Wagner et al., 1997*) the most important large scale tectonic elements in both drillholes are the graphite bearing reverse faults of this lineament. They can preferably be traced in paragneisses and in alternating layer sequences. In seismic studies their main branches were identified as the so called SE1- and SE2-reflector. The two reflectors cross the drillholes in about 7.0 and 3.5 km depth (e.g., *Dürbaum et al., 1992; Hirschmann, 1996; Harjes et al., 1997; Buske, 1999*).

Right before the intense faulting of the Franconian Lineament granitic intrusions migrated in two 'pulses' into the crust east and northeast of the ZEV. These intrusions also crosscut the metamorphic rocks within the ZEV in decimeter to meter scale (*Rohrmüller, personal communication, 2001*) to a depth of 7800 m (*Emmermann & Lauterjung, 1997*).

The youngest structural elements in the vicinity of the KTB site are probably related to the formation of the Eger-Rift (Eger-Graben) during late Oligocene and Miocene (*Emmermann & Lauterjung, 1997*).

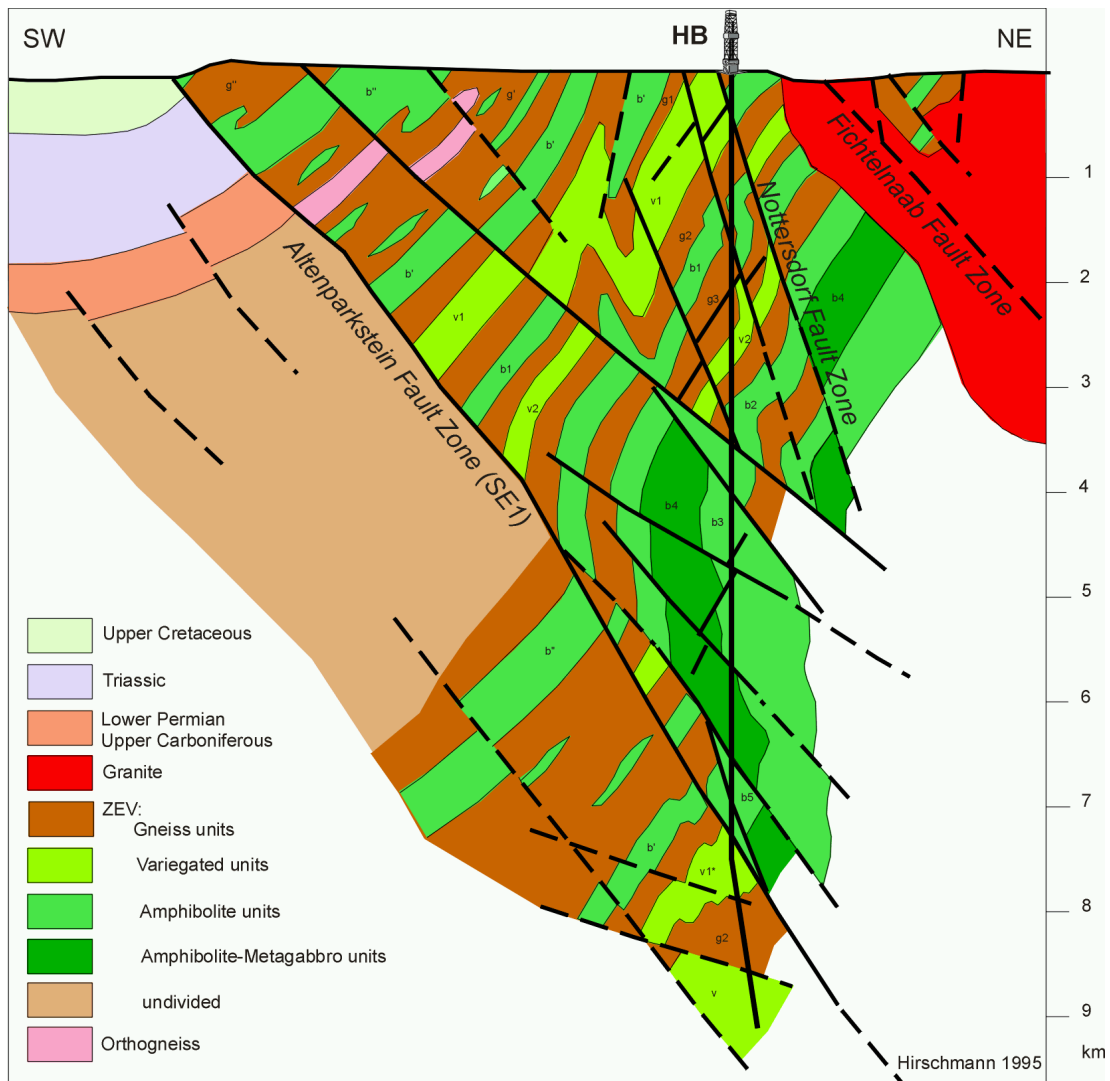


Fig. 2.3: Geological cross-section of the drilling location comprising prominent structures. Surface geology and drilling results as well as seismic interpretation have been combined in this image (from Hirschmann, 1996)¹.

into three groups: paragneiss, metabasic rocks and alternating layers of gneiss and amphibolite (Figure 2.3). Most of the rocks show a steep dip between 50°-80° to the southwest or northeast and are strongly folded, with the main fault zone axis trending from northwest to southeast, parallel to the Franconian Lineament.

The paragneisses have a uniform composition of plagioclase, quartz, biotite, muscovite, granate, sillimanite and/or kyanite, often incorporating graphite-flakes. The

¹redrawn by GFZ-Potsdam; Internet address on September 2nd 2002:
<http://icdp.gfz-potsdam.de/html/ktb/Schnitt.gif>

protoliths of the paragneisses were rather immature and represent a turbidite sequence of graywackes inter-layered at centimeter scale with pelitic graywackes probably from a former active continental margin. The metabasites consist of fine and coarse amphibolites (plagioclase, hornblende, granate and illimanite), massive metagabbros with residual ophitic texture and thin layers (up to 6 m thick) of mafic and ultramafic rocks. Most of the rocks have the chemical composition of enriched or usual *Middle Ocean Ridge Basalts* (MORB) and hence, represent former ocean floor deposited in a back arc environment or Red Sea type oceanic basin. The alternating or variegated series comprise massive granate-amphibolite, fine grained, textured amphibolite with layers of limestone-silicate, marble, hornblende-biotite-gneisses and paragneisses (Emmermann & Lauterjung, 1997).

The metamorphism affecting the lithological units of the ZEV can be divided into cycles. Since these cycles occurred during different evolution stages of the ZEV not all of the units are affected by each cycle. The metabasic units show signs of early eclogite facies conditions, followed by a garnet granulite facies overprint (O'Brien *et al.*, 1997) related to an active continental margin. Basically all three lithological units suffered a common continuous Barrovian-type metamorphism at upper amphibolite-facies conditions (600-800 MPa, 720°C peak conditions in the paragneisses) in combination with an intense ductile deformation resulting in a penetrative foliation. The first common evolution step of ZEV, Moldanubian, and Saxothuringian was the intrusion of the Falkenberg granite and the Leuchtenberg granite in late Carboniferous only affecting marginal and deeper parts of the ZEV by high-temperature and low pressure (Emmermann & Lauterjung, 1997).

The isotopic patterns of the protoliths seem to have been preserved in the rocks found at the KTB site today, despite the multi-phase metamorphism implying nearly closed system conditions without massive fluid flow (Möller *et al.*, 1997).

2.3 Petrophysics at the KTB site

In the framework of the KTB project a large number of petrophysical parameters were recorded, with a variety of different methods within the boreholes, as well as on cores and cuttings. Because of the large depth of the KTB main hole the difference between *in situ* and *laboratory* measuring environments is very special. The validity of surface measuring techniques could be tested because parameters are differently dependent on pressure and temperature (Berckhemer *et al.*, 1997). This fundamental comparison was one of the goals of the KTB project. Subsequently, a lot of different data are available for comparative analysis.

During drilling, fluids, solids, and gases were routinely analyzed in the KTB field laboratory. Among the determined parameters were density, radioactive elements, radioactively induced temperature, *ultra-sonic* P- and S-wave velocity, thermal conductivity, electrical resistance, natural magnetization, magnetic susceptibility, porosity, and permeability (Emmermann *et al.*, 1995). The same properties were also analyzed

under varied p-T-conditions in participating universities. A detailed list, explanations about the specific conditions, and the experiment locations can be found in [Berckhemer et al. \(1997\)](#). Information is also available on the mineralogical composition, orientation of the rock foliation as well as the orientation of cracks and their spatial frequency ([Hirschmann & Lapp, 1994](#)).

2.4 Seismics at the KTB site

The Oberpfalz region is one of the best surveyed regions in Germany. From the pre-site survey until today a large number of seismic experiments have been carried out addressing various topics. [Harjes et al. \(1997\)](#) provide an overview of the seismic data from the vicinity of the KTB site analyzed until 1996 (Figure 2.4)

- Near vertical vibroseis reflection seismics of crustal scale in 2D (DEKORP4, KTB8501 - KTB8506) were supplemented by wide angle explosives reflection seismics in 2D on profile DEKORP4 to enhance steeply dipping crustal structures in the resulting seismograms and to gather velocity information.
- Around the borehole near vertical vibroseis and wide angle explosives 3D experiments were carried out within the frame of the ISO89 project (*Integrated Seismics Oberpfalz 1989*) to understand the complicated 3D structure of the location.
- Borehole experiments in the pilot hole comprised multiple source type VSP, vibroseis walkaway VSP (MSP), and a vibroseis multi-azimuth downhole experiment (MAZE), also within ISO89.
- A special explosives seismic reflection experiment was aimed at the Franconian Lineament fault zone (INSTRUCT).
- Borehole experiments in the main hole comprised a vibroseis VSP experiment from 3000 m to 6000 m depth (VSP6000), an explosives VSP from 3000 m depth to 8500 m (DEEP VSP 1999), and a vibroseis MSP survey.
- A surface/borehole wide angle experiment was conducted in 2000 with three depth positions within the boreholes in combination with inline and crossline surface spreads.

The main results of the experiments will be explained in the following sections. Within the frame of the deep crustal reflection seismic program *DEKORP* (*DEutsches KOntinentales Reflexionsseismisches Programm*) the DEKORP4-Line was recorded in 1985 as one of the presite survey experiments. The profile reached from southwest of the Bohemian Massif within the Moldanubian region (Hoher Bogen) in the southeast into

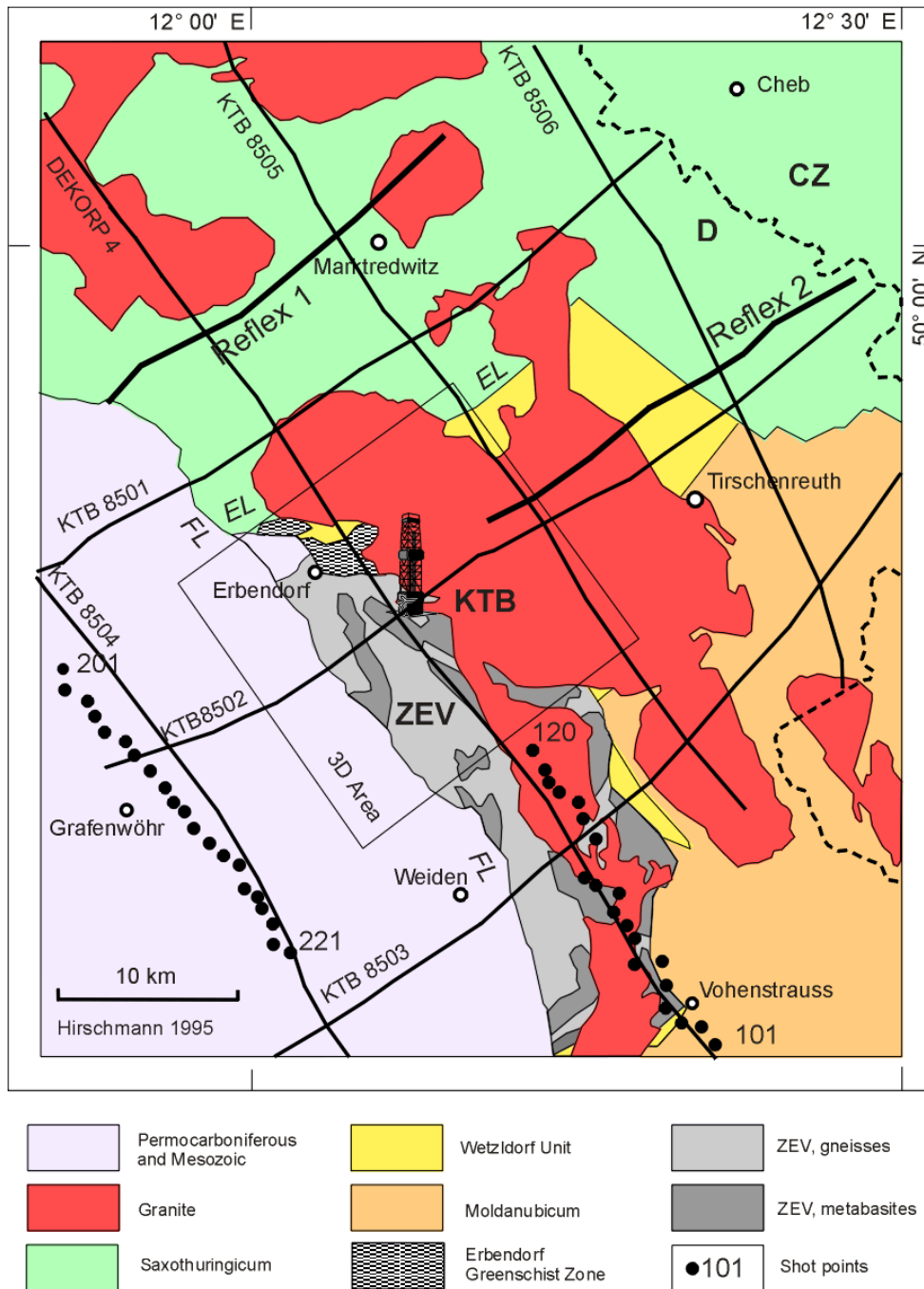


Fig. 2.4: Tectono-metamorphic units west of the Bohemian Massif (FL - Franconian Lineament, EL - Erbendorf Line, Variscan collision zone) and seismic profiles: The square with the drill rig in the center represents the CDP plane of wide angle (Reflex 1 and 2) and zero offset 3D survey from 1989. The 2D profiles DEKORP4 and KTB8501-8506 are also indicated (from Harjes et al., 1997)¹.

¹redrawn by GFZ-Potsdam; Internet address on September 2nd 2002:
<http://icdp.gfz-potsdam.de/html/ktb/Karte.gif>

the Saxothuringian region in the northwest (Frankenwald). Also a network of six 2D lines (KTB8501-8506) shot by the DEKORP consortium in the vicinity of the drilling location was surveyed to get a first 3D impression of the region. It became obvious that the crustal region along the profile DEKORP4 is very complex (Schmoll *et al.*, 1989). Since these profiles did not unravel the postulated suture zone between the terranes of the Saxothuringian and the Moldanubian and to gather crustal velocity information a special wide angle reflection experiment was carried out on the DEKORP4 profile which was very successful (e.g., Gebrande *et al.*, 1989; Simon, 1993). It demonstrated that the results of seismic experiments especially in crystalline regimes very much depend on the spread; some crustal features are simply not visible without the proper experiment layout. But also the necessity of migrating steep events became obvious. One important prerequisite for the true-amplitude processing was the use of envelopes instead of amplitudes, because true-phase processing in crustal scale generally suffers from destructive interference.

The dip and azimuth of the seismic reflections was regarded as being very un-uniform. Therefore, a 3D survey was carried out, both in near vertical and wide angle configuration, with the goal to gather detailed information about the crustal structure of the KTB site. This 3D survey covered a CDP area of 19x19 km and was carried out in the framework of ISO89 in 1989. The steep reflective fault zone of the Franconian Lineament had not been detected before drilling started. Especially this 3D experiment was able to exhibit this important structure in a detailed manner and led to a successful re-processing of line KTB8502 (Harjes *et al.*, 1997).

A special experiment called INSTRUCT, was aimed at the Franconian Lineament, seismically called SE1 (Steep Event 1), to estimate the reflectivity of this structure. It was helpful to carry out this experiment, because single explosive shots yield a more distinct signal signature with a higher signal to noise ratio, as opposed to the single vibroseis shots recorded in the KTB85 or ISO89 experiments. The main modeling result is that the petrophysical parameters of the rocks present within the fault zone cannot explain the strong reflections (Harjes & Janik, 1994). The presence of water filled cracks or fissures might explain this phenomenon in spite of the depth, since fluid filled holes of cm scale have been found within the borehole.

The pilot hole offered the first opportunity to measure a VSP at the KTB location to 3000 m depth. This was carried out in cooperation with the 3D survey of ISO89. Different seismic sources were tested, among which were vibroseis (vertical, horizontal linearly polarized, horizontal circularly polarized), explosives, and a large scale shear wave hammer, truck mounted. In the main hole a vibroseis VSP was recorded between 3000 and 6000 m depth in 1992 (Söllner *et al.*, 1992). The DEEP VSP from 3000 to 8500 m depth was measured in 1999 using dynamite sources. It is the data set this work is being based upon.

Three causes of reflectivity were tested with the data available until 1992 (Harjes *et al.*, 1997): (1) lithological changes with depth, forming first-order discontinuities; (2) changes of fabric and/or of the orientation of fabric causing anisotropy; (3) zones of mechanical weakness associated with low seismic velocities, such as fluid-filled

cracks and cataclastic fracture zones. [Lüschen *et al.* \(1991, 1996\)](#) and [Rabbel \(1994\)](#) proved the existence of split shear waves with an observed velocity difference of up to 10%, locally even as high as 14% (Rabbel, personal communication, 2002). Laboratory measurements on rock samples had predicted a considerable amount of anisotropy before ([Stroh *et al.*, 1990](#); [Kern *et al.*, 1991](#); [Siegesmund *et al.*, 1993](#)). Differences between observed azimuthal velocity values and a least squares fitting curve for a hexagonal symmetry system can be explained by locally varying fracture densities ([Rabbel, 1994](#)). Adjacent granites show a maximum amount of anisotropy of only 3%. Generally, the orientation of the anisotropy system varies with depth, basically being related to the foliation or crack orientation.

[Lüschen *et al.* \(1991, 1996\)](#) observed P-to-S converted waves with considerable amplitude. [Lüschen *et al.* \(1996\)](#) come to the conclusion that this can only be explained by the presence of steeply dipping heterogeneities of low elastic constants, such as fluid filled fractures. These were found in drill cores but also through interpretation of gamma ray, caliper log, and full wave sonic log data ([Bram *et al.*, 2001](#)), as well as hydraulic experiments by [Kessels & Kück \(1995\)](#). In some cases it was not possible though, to distinguish gneiss-amphibolite contrasts from coinciding fluid-filled fracture zones ([Harjes *et al.*, 1997](#)). Unfortunately, lithologic contrasts are often accompanied by fracture zones. Here, the V_p/V_s ratio drops. This is due to the considerably stronger lowering of the compressional wave velocity (V_p) as compared to the shear wave velocity (V_s) within zones of higher fracture density (e.g., [O'Connell & Budansky, 1974](#); [Kuster & Toksöz, 1974](#); [Lüschen *et al.*, 1996](#)). A first order approach to discriminate the two effects is the comparison of impedance values derived from borehole logs with artificial values derived from the mineral composition ([Spangenberg & Umsonst, 1993](#)).

The upward traveling wavefield shows a scattered appearance of reflections. This favors the interpretation of a limited extent of the lithological contacts or structures responsible for the reflections ([Lüschen *et al.*, 1991](#)).

In some of the VSP's the attenuation of the P-waves was studied with different concepts to derive the quality factor Q . [Li \(1995\)](#) analyzed the dynamite VSP from 85 to 3623 m depth recorded in the pilot hole and the vibroseis VSP6000 data recorded in the main hole from 3000 to 6013 m depth. [Pujol *et al.* \(1998\)](#) only used on the vibroseis VSP6000 data. Additional studies were carried out by [Jia & Harjes \(1997\)](#) and [Li & Richwalski \(1996\)](#). One surprise all investigations have in common are the low Q -values which are well below 40. [Jia & Harjes \(1997\)](#) and [Li \(1995\)](#) found an increasing Q with respect to frequency. However, [Li & Richwalski \(1996\)](#) found the opposite. [Pujol *et al.* \(1998\)](#) state the possible influence of the processing on the frequency dependency of their Q -value determination.

Laboratory measurements of Q on core samples are provided by [Prasad *et al.* \(1994\)](#) and [Kern & Popp \(1995\)](#). For air-dry gneiss samples and a frequency of 1 MHz [Prasad *et al.* \(1994\)](#) report Q -values depending on the foliation orientation between 10 and 40 for small confining pressure and about 90 to 300 for a confining pressure corresponding to a depth of about 7.1 km. [Kern & Popp \(1995\)](#) report smaller, but

also orientation dependent values for a dry gneiss sample, with a signal frequency of 2 MHz. They report no orientation dependency for a wet sample; however, the values are close to the highest values in the dry sample.

2.5 Summary

The Oberpfalz region in the vicinity of the two KTB drillholes shows a very complicated geological structure. The foliation of the local lithology is steeply inclined with water bearing fractures and fault zones all the way to the bottom of the main hole. Traditional and specialized seismic experiments were used to unravel the basic crustal structure at the KTB site. A detailed image was acquired by drilling; however, restricted to the direct vicinity of the borehole. The model of the crustal structures used today was derived from a combination of seismic investigations and drilling results.

Various petrophysical in situ and laboratory data were collected and have been published. In some cases different analyzing methods produced somewhat different results being a possible indicator of the variability of values that can be encountered in crustal environments. The results of the various experiments confirm the paradigm of reflection seismology that the most recent tectonic events determine the upper crustal reflectivity pattern (Meissner & the DEKORP Research Group, 1991).

Chapter 3

Theoretical Background

This thesis is not intended to analyze the theoretical concepts of seismic wave attenuation in detail. Rather, it is focused on the practical application of an existing concept. Therefore, this chapter only provides a basic glance at underlying theories and methods for the determination of the *quality factor* Q . The concept of a possible improvement of the measured Q -values by accounting for the amount of energy conversion from P- to S-waves is presented.

The most basic quality information of a medium is normally called *intrinsic* Q . A term also found in the literature is *specific* Q (Meissner, 1986). It is a synonym for the energy ‘absorption’ potential of a medium. Compensating for absorption is important to improve the resolution of seismic images by inverse Q -filtering (Yilmaz, 2001) and for the inversion for material properties (Zhang & Ulrych, 2002). A possible compensation is also of special importance in AVO/AVA analysis (Samec & Blangy, 1992). A collection of articles on seismic wave attenuation and the quality factor Q can be found in Toksöz & Johnston (1981).

3.1 Seismic Waves

The theoretical description of the propagation of seismic waves is complicated. Generally, the propagation depends on the elastic properties of the transmitting medium. Elasticity is the relation between forcing stress and resulting changes in size and shape of the rocks; the latter being the concept of strain. The tensor relating stress and strain contains 81 constants in the general case, but only up to 21 are independent; the exact number depends on the type of anisotropy of the medium. In the transversely isotropic case, i.e., a sequence of horizontal, isotropic layers with different elastic properties, the number is reduced to five independent constants. In the isotropic case only two remain. Detailed deductions of the wave equations in elastic but also anelastic media can be found in Aki & Richards (1980). In the anelastic case the absorption of energy is also taken into consideration. Small forces and linearization are important prerequisites for the whole theoretical concept.

A lot of different terms exist to describe the apparent loss of energy of a seismic wave. It is often hard to distinguish one term from the other, because authors tend to use them differently. This is probably a representation of the fact that in most cases there is more than one factor involved in the energy dissipation. This common superposition of several factors in seismic field data is the main reason why there has been debate for a long time whether it is possible to derive this dissipation in an exact manner for it to be used as an additional parameter describing the *quality* of the medium. This problem and the bad spatial resolution of seismic waves is the reason why laboratory data on Q is normally needed for prospection purposes. The following terms are often used discussing the apparent loss of signal amplitude:

“Attenuation” is used more universal or supreme than any other. The definition of attenuation as given by [Sheriff \(1991\)](#) is the “reduction in amplitude or energy caused by the physical characteristics of the transmitting media or system” usually incorporating geometric effects such as the decrease in amplitude with respect to distance. Thus, the attenuation of seismic waves is the superimposed concept for a variety of energy dissipating phenomena.

“Damping” seems to be just a subcategory. According to [Sheriff \(1991\)](#) it is “a slowing down or opposition to oscillation due to dissipation of the oscillating energy” often in combination with resonant effects. The focus seems to be on (local) structural and/or intrinsic effects. Geometrical spreading of a seismic wave is not considered to be part of damping.

The term “absorption” is used as a synonym for intrinsic or specific Q . It is used because this part of the energy apparently disappears with time in a seismogram. The reason for this ‘loss’ of energy is the energy conversion into energy forms not detectable with seismic sensors, like e.g., heat or fluid flow. [Sheriff \(1991\)](#) uses an even stronger definition for absorption being “a process whereby energy is converted into heat while passing through a medium.”

Another definition provided by [Sheriff \(1991\)](#) is the one of “elasticity” being “the ability [of the elastic body] to return to original shape after removal of a distorting stress. The return of shape is complete and essentially instantaneous rather than gradual.” The opposite is “anelasticity”. “Viscoelastic” is often used as a synonym for anelastic. In this case a rock model is assumed that combines the *viscose* behavior of a fluid with the *elastic* behavior of a spring ([Bohlen, 1998](#)), taking into consideration that, for example, frictional dissipation is small compared to the effects of pore fluid flow for all but the lowest effective confining stresses ([Worthington et al., 2001](#)). An anelastic or viscoelastic medium *absorbes* energy.

3.2 Attenuation

Attenuation is the general term used to describe the reduction of amplitudes apparent in field data. An illustration of the various factors involved in wave attenuation was given by [Sheriff \(1975\)](#) (Figure 3.1). A theoretical concept adapted here, was provided

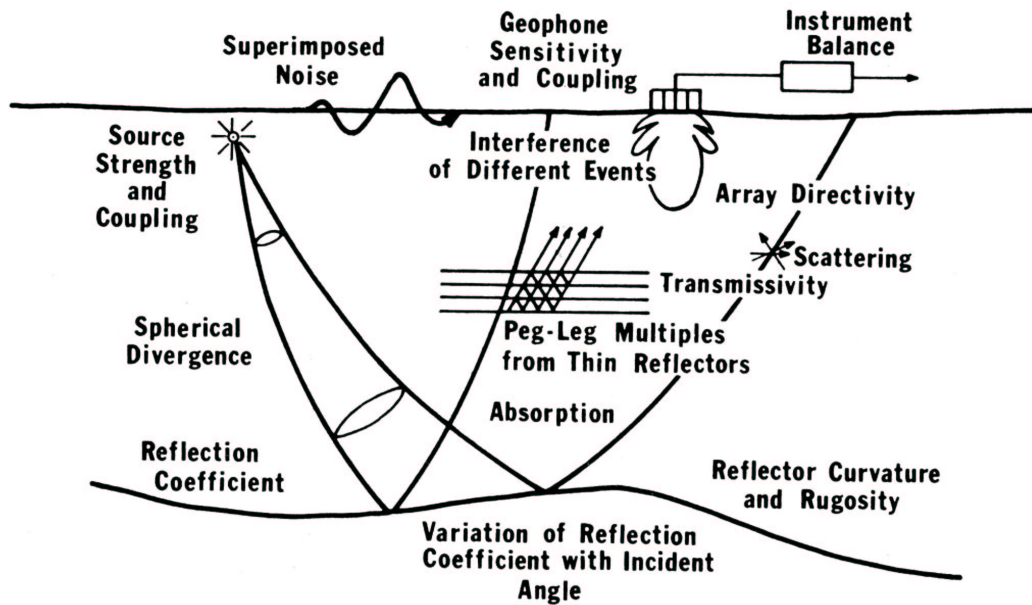


Fig. 3.1: Factors influencing the amplitude of a seismic wave (Sheriff, 1975).

by Bath (1974) and Tonn (1988) regarding the influence of the different factors on the amplitude spectrum:

$$X(\omega, r) = S(\omega) B(\theta) G(r) P(\omega, r) I(\omega) L(\omega, r) A(\omega, r) + N(\omega) \quad (3.1)$$

where

$X(\omega, r)$:	receiver spectrum at distance r
$S(\omega)$:	source spectrum
$B(\theta)$:	source space function, where θ stands for direction from source
$G(r)$:	geometrical spreading
$P(\omega, r)$:	path effect on spectrum
$I(\omega)$:	instrumental response and mechanical coupling
$L(\omega, r)$:	influence of primary and secondary waves which are generated in the immediate vicinity of the geophone
$A(\omega, r)$:	anelastic damping
$N(\omega)$:	Noise.

Normally, the aim of an attenuation analysis is the determination of $A(\omega, r)$. $P(\omega, r)$ and $L(\omega, r)$ can be related to scattering, which can be regarded as stratigraphic filtering or a 'loss' of energy due to reflection or conversion. It is basically a function of the heterogeneity of the medium. The three factors combine to the loss of coherent elastic energy of the primary seismic arrival.

Including absorption into the elastic wave equation results in a complex description of wave propagation. One of the implications is the resulting frequency dependency of the phase velocity, leading to dispersion and a frequency dependent absorption. [Tonn \(1988\)](#) discusses this frequency dependency and comes to the conclusion that for seismic frequencies Q can be regarded as frequency-independent, though. This seems to be in agreement with the present practice known as *constant-Q* ([Yilmaz, 2001](#)), originally introduced by [Kjartansson \(1979\)](#).

For a very high frequency bandwidth however, there seems to be a frequency dependency, resulting in a surprising similarity between absorption values obtained in ultrasonic and surface seismic frequency ranges, as opposed to frequencies typical for cross-hole and sonic-log data ([Sams et al., 1997](#)). The authors assume the local viscous flow to be responsible for this, also known by the term squirt flow, a term introduced by [Jones \(1986\)](#). If this model was valid not only for sedimentary rocks this would imply a well defined comparability of core data with in situ VSP data.

3.3 Quality Factor Q

The original definition of the quality factor Q was given by [Knopoff & McDonald \(1958\)](#) for a sine signal:

$$Q = 2\pi \frac{E_0}{\Delta E} \quad (3.2)$$

where E_0 represents the maximum strain energy that is stored in the specific volume and ΔE the loss of energy per period because of inelasticity.

Normally, it is not possible to determine the influence of each share in equation [3.1](#) separately, to end up with the absorption $A(\omega, r)$ or *intrinsic Q* (Q_i), respectively. Instead, only the total Q , the so called *effective Q* (Q_{eff}) can be determined from the data. It can be written according to equation [3.2](#)

$$\frac{1}{Q_{eff}} = \frac{1}{2\pi} \frac{\Delta E}{E_0} \quad (3.3)$$

Q_{eff} can be related to Q_i and *apparent Q* (Q_a) ([Spencer et al., 1982](#)) in the following way, also taking equation [3.2](#) into account:

$$1/Q_{eff} = 1/Q_i + 1/Q_a = \frac{1}{2\pi} \frac{\Delta E_i + \Delta E_a}{E_0} \quad (3.4)$$

where ΔE_i represents the absorption (intrinsic) energy loss per period. [Richards & Menke \(1983\)](#) proposed Q_a to be the result of scattering. ΔE_a hence, represents the scattering (apparent) energy loss per period.

Scattering can be regarded as the energy loss due to conversion in transmission (forward) as well as in reflection (backward), and reflection of the P-wave energy. Therefore,

$$\Delta E_a = \Delta E_{PS}^f + \Delta E_{PS}^b + \Delta E_{PP}^b \quad (3.5)$$

or

$$1/Q_a = 1/Q_{PS}^f + 1/Q_{PS}^b + 1/Q_{PP}^b \quad (3.6)$$

with, for example,

$$\frac{1}{Q_{PS}^f} = \frac{1}{2\pi} \frac{\Delta E_{PS}^f}{E_0} \quad (3.7)$$

The question is, how to determine the portion of each share in equation 3.1. In the case of the KTB Deep VSP'99 data some of the factors are either known or are neglectable, because they are small or do not differ from trace to trace. The following two factors are under control with the reference geophone data from the pilot hole:

- the source spectrum is basically known and does not differ much from shot to shot; the amplitude is under control
- the spreading characteristics of the source with θ is also basically the same for all traces

In the main hole VSP data:

- the spreading characteristics of the source with a slightly different θ as compared to the pilot hole is also basically the same for all traces (note the velocity gradient in the crust depicted in Figure 4.1 on page 27 and the similarity of the traces in the pilot hole in Figure 4.2)
- the signal to noise level is basically very high, except for a few very short noise burst events. These do not spoil the first break amplitudes, though, because they do not appear within the first break
- in a first order approach $G(r)$ can be approximated with $1/z$ (z being distance or depth) because in a homogeneous medium the *amplitude* decays proportionally to $1/r$ where r is the radius of the wavefront

Taking this into account, equation 3.4 is valid and can be rewritten as

$$1/Q_i = 1/Q_{eff} - 1/Q_{PS}^f - 1/Q_{PS}^b - 1/Q_{PP}^b \quad (3.8)$$

However, the original definition of Q in equation 3.2 has no practical value. Futtermann (1962) derived Q for seismic waves (s), not being restricted to a single frequency but restricted to $Q \gg 1$:

$$\frac{1}{Q_{eff}^s} = \frac{1}{2\pi} \frac{\Delta e}{e_0} \quad (3.9)$$

where e_0 is the amplitude of the kinetic energy density and Δe represents the decrease of the kinetic energy density within a wavelength. In the case of a linear stress-strain relation (Tonn, 1988)

$$\frac{1}{Q_{eff}^s} = \frac{1}{2\pi} \frac{\Delta a^2}{a^2} \quad (3.10)$$

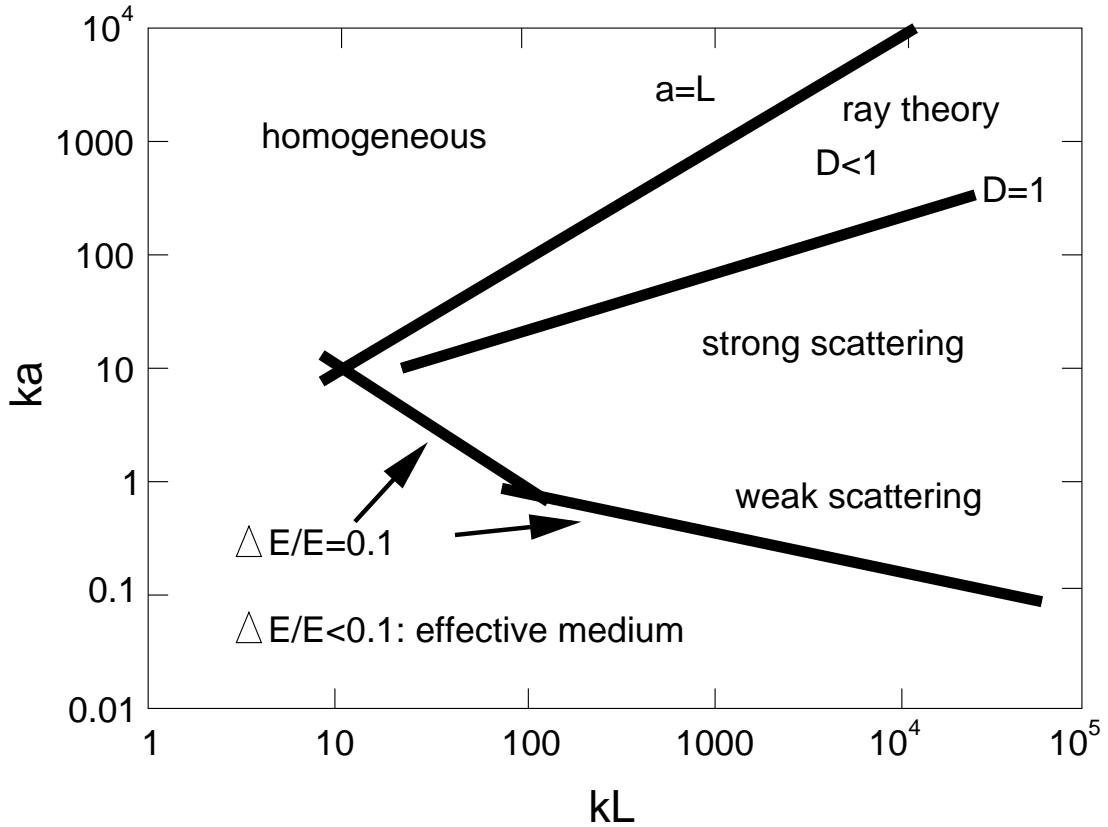


Fig. 3.2: Scattering regimes: ka is the so called normalized frequency, where a is the maximum size of the inclusion, k is the wavenumber. L is the travel distance of a wave and D is the ratio of the first Fresnel zone to the scale length of the heterogeneity (after [Aki & Richards, 1980](#)).

where a represents the amplitude of a seismic wave. This final derivation leads to a possible application of the Q concept. Although an energy relation is taken for the basic definition of Q , the signal amplitude relation can be used for the practical determination of Q .

Common methods exist to quantify Q_{eff} in seismic data. One approach is established for *effective media* with intrinsic absorption and scattering structures $\gg \lambda$ (Figure 3.2). In the case that the absorption coefficient $\alpha = \pm const.$ in a quasi-homogeneous medium with continuing energy flux (e.g., [Futtermann, 1962](#)):

$$a(x) = a_0 e^{-\alpha x} e^{i(\omega t - kx)} \quad (3.11)$$

where $a(x)$ is the amplitude at distance x and a_0 the amplitude at the source, ω the angular frequency, and k the wavenumber. The prerequisite of $\alpha = \pm const.$ is a strong limitation. However, it is common practice to take equation 3.11 as a starting point. The relation between the *quality factor* Q and α has been approximated also for $Q \gg 1$:

$$1/Q = \alpha V / \pi \nu = \alpha \lambda / \pi \quad (3.12)$$

where V , ν , and λ , are velocity, frequency, and wavelength, respectively (Sheriff, 1991).

One method for the determination of Q_{eff} is known by the name *amplitude decay method* (Tonn, 1988, 1991):

$$\frac{a(x_2)}{a(x_1)} = \exp\left(\frac{\omega}{2cQ}(x_2 - x_1)\right) \quad (3.13)$$

or

$$Q = \frac{\omega \Delta x}{2c} \left(\ln\left(\frac{a(x_1)}{a(x_2)}\right) \right)^{-1} \quad (3.14)$$

where $a(x_1)$ and $a(x_2)$ the amplitudes at x_1 and x_2 , c being the interval velocity, ω the angular frequency, and Q the quality factor. These equations can be derived starting with equation 3.11 but improved by accounting for the spherical divergence $G(\omega, t)$ from equation 3.1 approximated with $1/z$, as indicated above. The imaginary part of equation 3.11 is dropped:

$$a(z) = a(z_0) \frac{z_0}{z} e^{-\alpha(z-z_0)} \quad (3.15)$$

where z and z_0 define the spread along the depth axis. It can be rewritten as

$$\alpha = - \frac{1}{z - z_0} \ln\left(\frac{zA(z)}{z_0A(z_0)}\right) \quad (3.16)$$

Q can be described in terms of α taking equation 3.12

$$Q = \pi f(t - t_0) \left(\ln\left(\frac{z_0A(z_0)}{zA(z)}\right) \right)^{-1} \quad (3.17)$$

This represents Q_{eff} in equation 3.8. To basically match equation 3.14 it can be written as

$$Q = \frac{\omega \Delta z}{2c} \left(\ln\left(\frac{z_0A(z_0)}{zA(z)}\right) \right)^{-1} \quad (3.18)$$

where $f = \omega/2\pi$, c the internal velocity ($\Delta z/\Delta t$), and $\Delta z = z - z_0$. This equation is equal to equation 3.14 except for the integrated spherical divergence. The frequency f normally used in the calculations is the main or center frequency. Equation 3.17 is used for the determination of Q_{eff} in the field data in Chapter 4 and the model data in Chapter 8. This Q -value can subsequently be corrected for conversion.

Once the amplitudes of the converted S-waves in transmission are known with depth in relation to the incident P-wave, the resulting *transmission conversion* Q (Q_{PS}^f) can be determined with equation 3.10, whereby Δa represents the S-wave amplitude in relation to the incident P-wave amplitude a . Q_{PS}^f can be included in equation 3.8 and results in *effective* Q -values corrected for P-to-S conversion in transmission. How to determine the order of the P-to-S conversion in transmission and its values in the KTB field data and corresponding model data are going to be discussed in the following chapters.

3.4 Wave Phenomena and Approximations

Different aspects of wave behavior can be simulated or calculated analytically. This is normally restricted to simple models. However, these calculations can serve as a reference for more sophisticated wave modeling methods. The following sections summarize typical wave phenomena and simulation methods, some of which were used to simulate VSP data of different crustal models that will be compared with the field data in the following chapters.

3.4.1 Conversion, Reflection

The term conversion describes the fact that at interfaces of different elastic properties and in the case of oblique incidence acoustic and body waves partly convert into one or the other form. This conversion reduces the energy of the incident P- or S-wave. Reflections can also take place in the case of normal incidence. The amount of *conversion* and *reflection* strongly depends on the incident angle and can be determined analytically within a simple crustal model.

A means to calculate the angles of incidence and emitted rays is provided by Snell's law, the corresponding conversion and reflection coefficients can be calculated with the Zoeppritz equations (Zoeppritz, 1919). The equations are only valid for *plane* incident and emitted waves generated at a first order interface of *large* extent. The condition of a plane wave is almost fulfilled in the case of the KTB Deep VSP'99, because the profile starts at 3000 m depth. The second condition is of course not completely realistic. Compared to sedimentary structures a crystalline crustal segment shows a lot of small scale and often almost random structure perturbations. However, there is a certain layering of geological units present at the KTB site (Figure 2.3) that are superposed by these small scale perturbations. The presumption of large scale interfaces to be able to use the Zoeppritz equations for the determination of the converted energy can therefore be considered as valid only as a first order approach.

Another draw-back is the validity only for high frequencies. Lower frequency signals need to be convolved with the interface properties which produces additional problems in the case of thin layers, i.e., with a layer thickness basically smaller than the signal wavelength.

An algorithm designed by Rabbel (1987) based on the ray method described by Červený *et al.* (1977) is used in practice to derive values for the reflection and transmission coefficients. Because of the explained limitations the conversion values derived, can only serve as first order reference.

3.4.2 Scattering, Diffraction

For many crustal models the limitations of the Zoeppritz equations result in reflection and conversion coefficient errors too large to be neglected. This happens, for example, at edges of interfaces resulting in diffractions or edge waves. Another problem are

inclusions of limited extent, resulting in a scattered wavefield. The term scattering is used in the case of large signal wavelengths with respect to the subsurface heterogeneity. A typical sign of scattering is the existence of incoherent traveltimes perturbations (Sheriff & Geldart, 1995).

To be able to calculate the response of such perturbations, scattering and diffraction theories have been developed. A plot describing the different terms and their limits is depicted in Figure 3.2. The main draw-back with these methods is the restriction to single bodies. Although responses can be calculated for shapes which can be described as closed functions, a complicated crustal block, perhaps with gradients cannot be simulated.

In some of their experiments Neep *et al.* (1996) found negative Q-values due to focusing, they consider as scattering Q. For crosshole data and horizontal layers they propose the calculation of synthetic seismograms based on the in situ velocities and density with no intrinsic Q to determine the scattering Q. This can then be used to subtract it from the total Q.

3.4.3 Random Media

One disadvantage of many crustal segments is the lack of detailed structural knowledge. The possible variety of structural shapes subsequently results in possible reflection and conversion coefficients of many orders of magnitude. It would not be evident, whether the values result from the shapes, the size of the inclusions, or the elastic property perturbations. This problem is basically not restricted to the KTB site. It is a problem that is commonly encountered in more complicated environments and has led to random media theories with a statistical approach. A typical scenario for the random media method is the estimation of a signal amplitude below a section of thin layers.

Because within a real subsurface volume the size of elastic property perturbations is variable, i.e., comparably large in the case of large rock units, scattering theories are not always valid. The random media theories have been derived with the aim to get the signal response with respect to the different perturbation scales. However, the method cannot determine attenuation values for individual locations.

3.4.4 Finite-Difference Modeling

For complicated media, the only way to derive realistic amplitudes is the calculation of finite-difference (FD) models. Whereas first implementations could only simulate acoustic waves (Alford *et al.*, 1974), the development of the staggered grid technique enabled the calculation of elastic waves (e.g., Virieux, 1986), as well as viscoelastic effects (e.g., Robertsson *et al.*, 1994; Bohlen, 2002). Recently, the limitations to the modeling of low impedance contrasts could be solved by the use of the rotated staggered grid technique (Gold *et al.*, 1997; Saenger *et al.*, 2000).

However, the impedance contrasts that were calculated in the course of this thesis did not make the use of the rotated staggered grid technique necessary. Therefore, the parallel viscoelastic code of [Bohlen \(2002\)](#) was used for the calculation of some models described in Chapter 8.

Chapter 4

Seismic Field Data

In 1999 a Vertical Seismic Profile (VSP) experiment was carried out in the deeper part of the KTB main hole, between 3.0 and 8.5 km depth (Deep VSP 1999). The experiment was only possible, because a new 3-component geophone tool (BG-250) had been designed and built by CREATECH, France, especially for this experiment. It is able to withstand extreme high pressure ($P_{max.}$: 136 MPa) and temperatures ($T_{max.}$: 250°C). The survey was carried out in April and September 1999. The aim was to extend the existing VSP data from 1989 and 1992 as deep as possible. The deepest part of the main hole between 8.5 and 9.1 km depth was not accessible for the geophone tool because of its housing diameter.

4.1 Deep VSP at the KTB site

The measurements in 1999 had been scheduled for April '99, but limited resources and technical problems in April made it necessary to carry out additional VSP measurements in September '99, to get as many equally spaced traces as possible for the data analysis. One of the specialties of this VSP experiment was the existence of the pilot hole, a drill hole that had been drilled until 1989 to a final depth of 4000 m to get important geological and technical informations about the drilling location, prior to the drilling of the main hole. The pilot hole played an important role in the overall success of the VSP experiment of 1999. The geophone sonde deployed there (BS-125, also manufactured by CREATECH, France) was used as a reference geophone to confirm the strong repeatability and the high bandwidth of the shots used as sources for the Deep VSP '99. Also, its data provide the amplitude reference for the real amplitude processing of the main hole data. As it turned out, the reference geophones at the surface did not succeed in this respect.

The natural frequency of the geophones installed in the BG-250 sonde is 10 Hz. The one of the geophones in the BS-125 used in the pilot hole is also 10 Hz but is electronically expanded to 1 Hz. The signals from the BG-250 sonde were amplified with amplifiers integrated in the sonde electronics. These amplifiers were the main reason

for the limited working time of the sonde during operation because they are mounted within a dewar housing for heat protection. The housing protects the inside from being overheated by the outside environment but prevents internal amplifier heat to escape to the outside as well. The engineers operating the sonde suspected that about 90% of the heating within the housing is produced by the electronics of the sonde itself and only 10% merge in from the outside (C. Carnein & M. Hönig, personal communication, 1999). Switching off the amplifiers any spare time, measurably prolonged the sonde working time. Hence, despite the fact that the geophone sonde BG-250 has a dewar housing for the protection of the downhole electronics, high temperatures ($\sim 250^\circ\text{C}$ at 8.5 km depth) limited the measuring time each day. It took a total of 14 days (net time of 9 days) to carry out the whole experiment.

The amplification of the signal was 60 dB most of the time. For the uppermost part of the VSP (3000-3500 m) it was set to 40 dB during the April '99 survey. The recording units in April and September '99 were two different GEOMETRICS Strataview. The amplification within these recording units was 36 dB and the data sampling interval 0.5 ms.

4.2 Geometry

The scheme of the field geometry of the Deep VSP 1999 is depicted in Figure 4.1. The zero offset shot point had an offset of about 250 m from the well head to suppress tube waves. The 8 km offset shot point served as a reference shot point to be able to rotate the 3-component geophone coordinate system into the geographical coordinate system. A geophone tool mounted compass would not have worked within the steel casing of the main hole. This offset shot point was not available during the measurements in September 1999.

Whereas the reference geophone in the pilot hole was kept in its position during the course of the experiment (3728 m depth) the main hole geophone sonde was moved from 8.5 to 3.0 km. At every depth position the two source point shots were successively recorded. In the lower part of the borehole, these depth positions were chosen in such a manner that the same overall depth interval (with a distance between individual depth points of 25 m) was probed on consecutive days, with a shift of 12.5 m. On the one hand this was done to be able to end up with a successful experiment, even in the case of a major instrument failure, on the other hand to be able to possibly detect differences in the nature of the shot signal, by comparing two sets of data of the same depth interval. This precaution turned out to be unnecessary, though. The experiment ended up with a trace spacing of 12.5 m in the depth interval between ~ 5.2 km and 8.5 km. In the depth interval between 3.0 and ~ 5.2 km a trace spacing of only 25 m was acquired, because of limited resources.

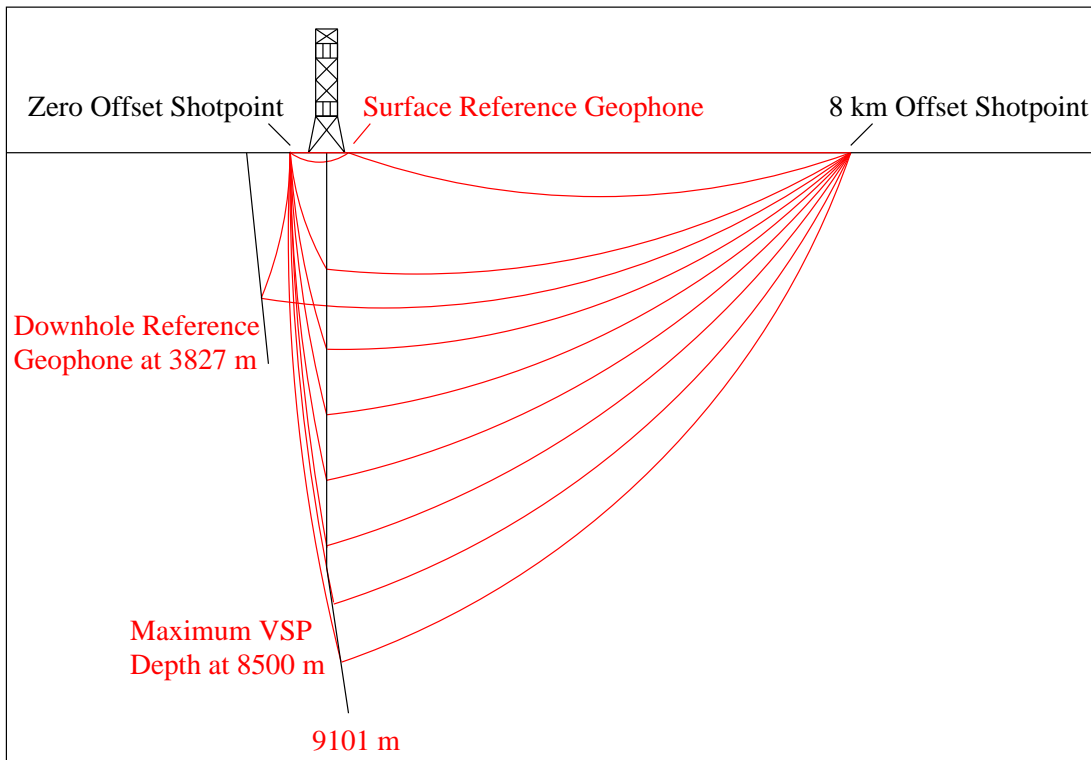


Fig. 4.1: Schematic field geometry of the VSP experiment at the KTB site in 1999. The reference geophone in the pilot hole on the left was kept in place during the experiment. Note the curved ray paths due to the velocity gradient in the crust. Therefore, the zero offset ray paths towards the reference geophone and the different geophone positions in the main hole are closer together than they would be in the case of a homogeneous velocity half space with resulting straight rays. The offset shot point rays indicate that the offset shot point P-wave first break can be used to determine the geophone tool orientation

4.3 Data Quality

The quality of the data set is very unique. The pilot hole played the central role in the possibility to quantify this quality. As can be seen in Figure 4.1, the ray-paths from the zero offset shot point towards the reference geophone do not differ much from the ones that point towards the main hole in the uppermost part of the crust; they are curved, the reason for this being the positive velocity gradient in the crust. The rays stay closer together for a longer range than they would, in the case of straight rays. That way the waves towards the pilot hole and the main hole penetrate the same rock units for a large segment of either travel path. This increases the wealth of the reference geophone information.

The nature of the zero offset shot field (sp101) apparently permitted a high repeatability of shots, as indicated by seismic sections and frequency analysis of the reference geophone data from the pilot hole (Figures 4.2, 4.3, and 4.4). The sequence of onsets

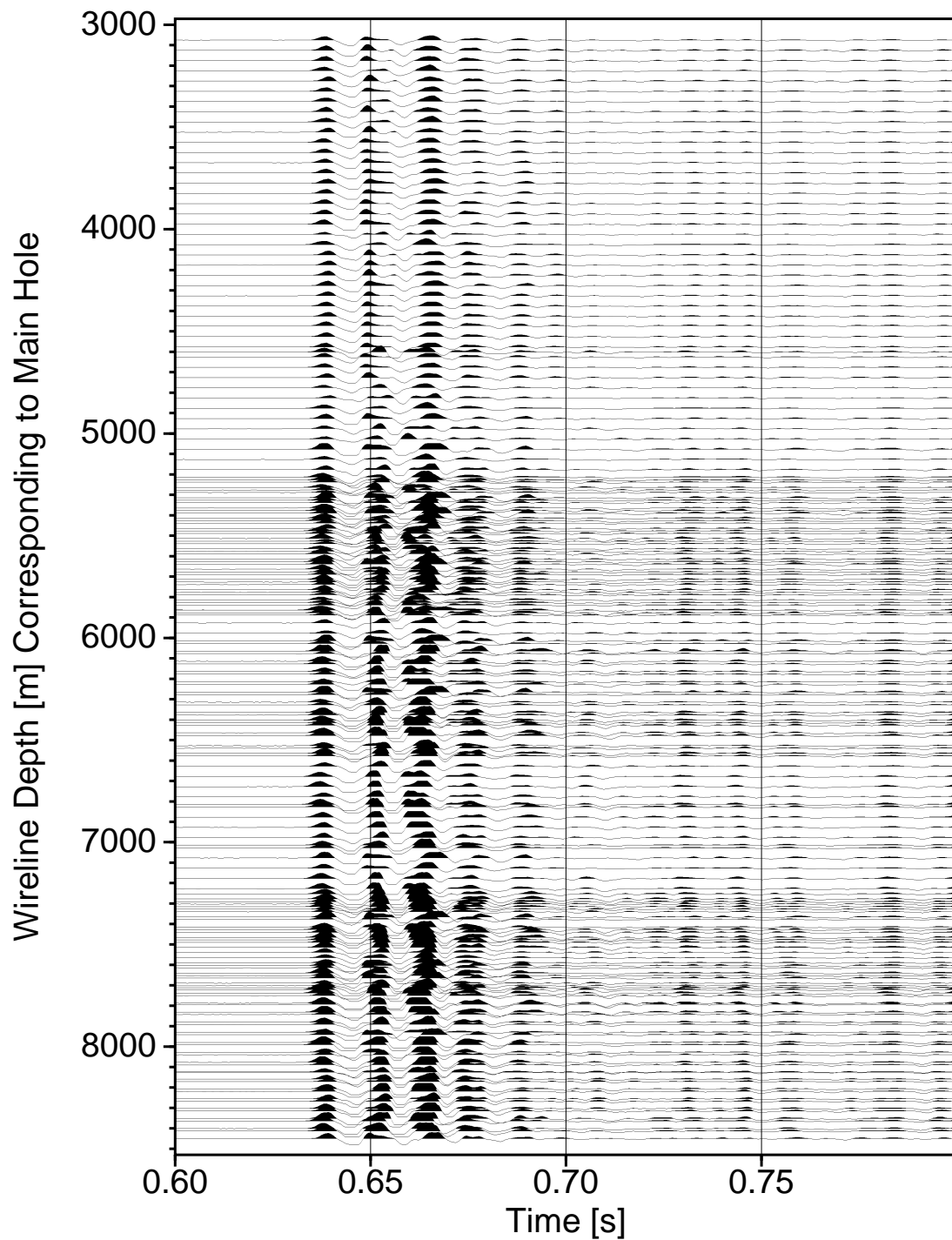


Fig. 4.2: Traces of the vertical component first break, recorded with the reference geophone in the KTB pilot hole during the VSP experiment in September 1999, trace-normalized. Although the wireline depth was kept at 3827 m the traces are plotted according to the corresponding depth position of the main hole geophone sonde for shot control. No vertical component data is available of the April '99 experiment.

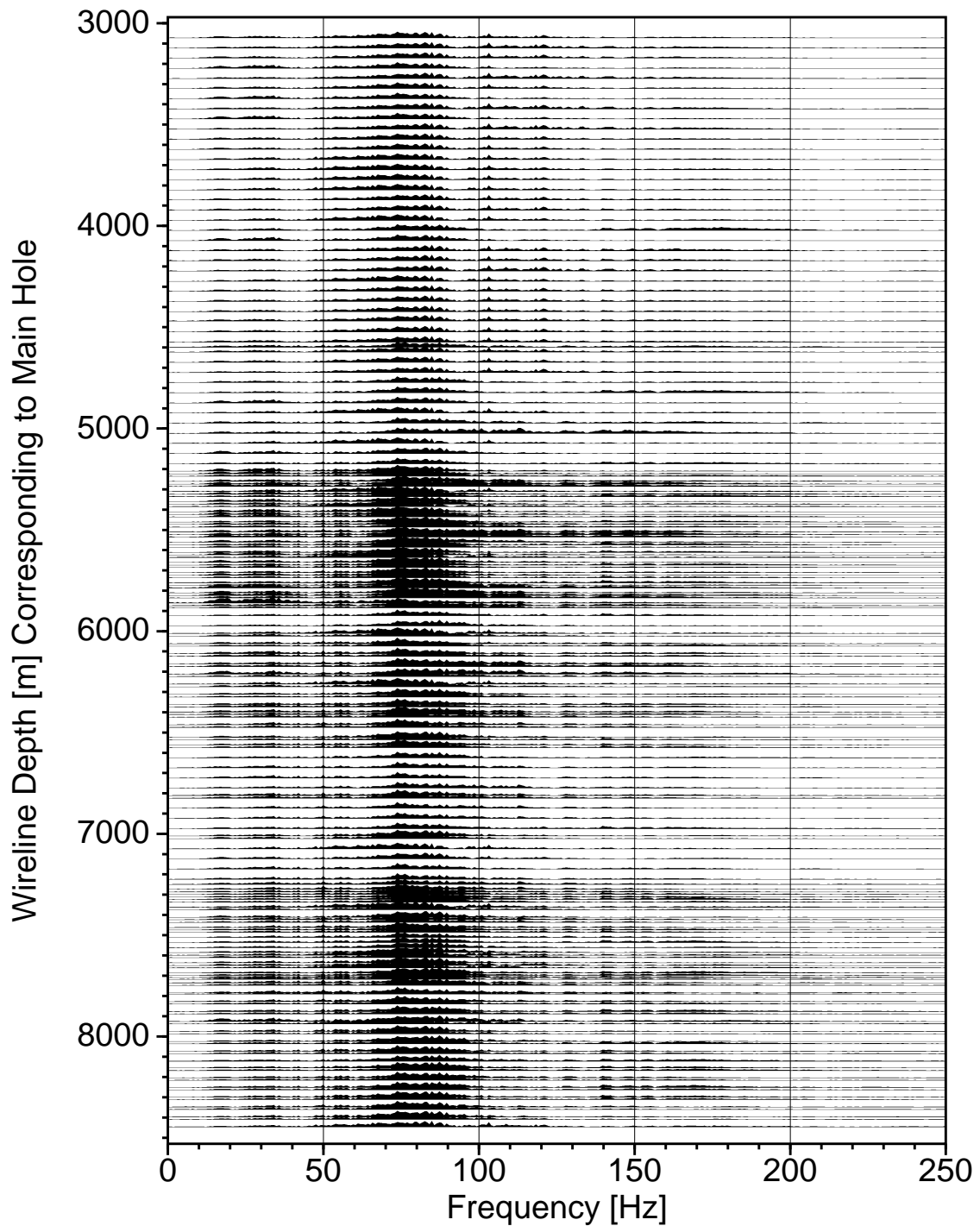


Fig. 4.3: Spectrum of the vertical component data, recorded with the reference geophone in the KTB pilot hole during the VSP experiment in September 1999, trace-normalized. Although the wireline depth was kept at 3827 m the traces are plotted according to the corresponding depth position of the main hole geophone sonde for shot control. No vertical component data is available of the April '99 experiment.

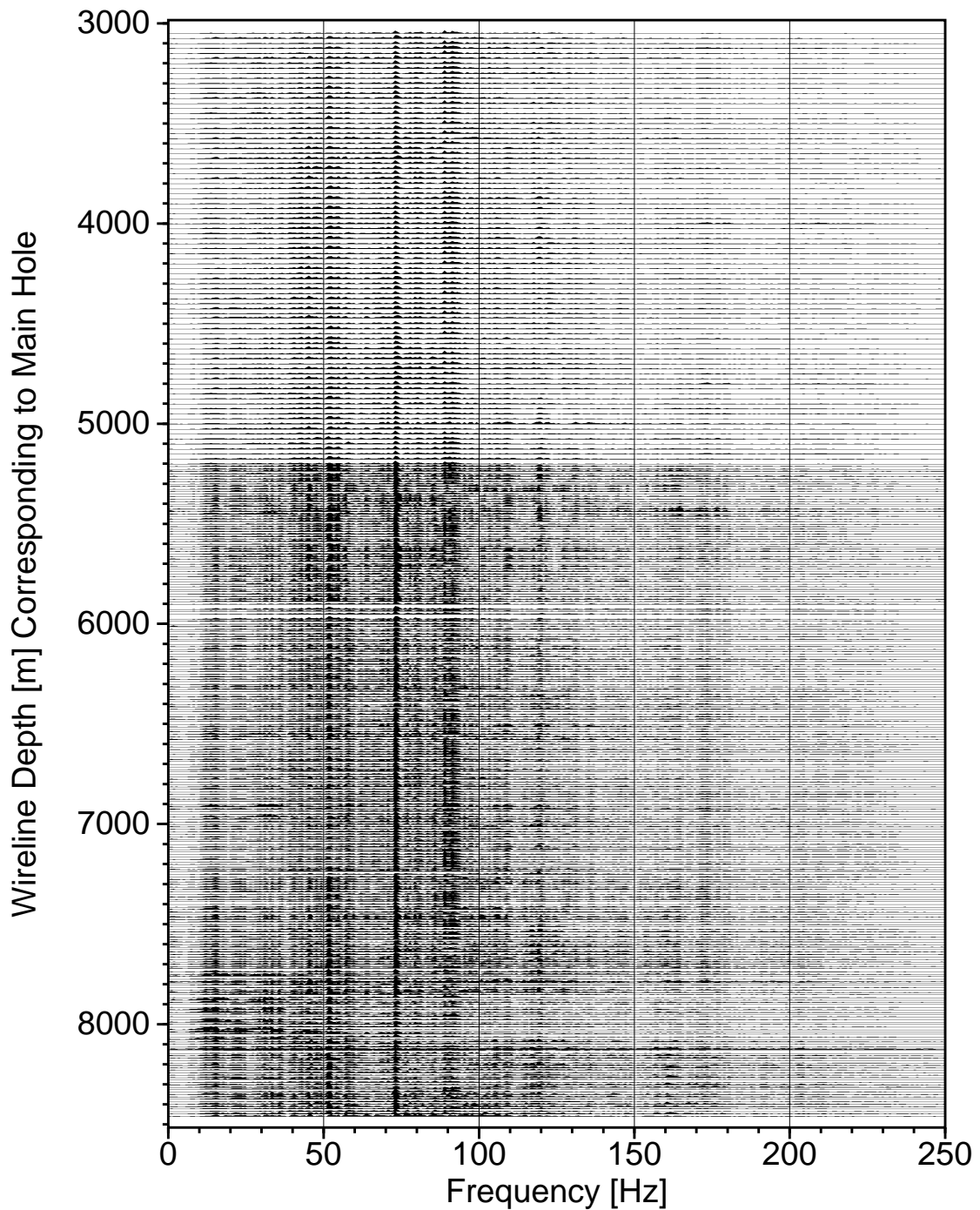


Fig. 4.4: Spectrum of the second horizontal component recorded with the reference geophone in the KTB pilot hole during the VSP experiment in April and September 1999, trace-normalized. Although the wireline depth was kept at 3827 m the traces are plotted according to the corresponding depth position of the main hole geophone sonde for shot control. This component is the only one working during both, the spring and fall survey periods.

and the frequency content of the traces do not vary much, neither within each survey period, nor from spring to fall 1999. This repeatability is even more a surprise since due to the high shot repetition rate the shot holes were only partly water filled.

The wider the frequency content of the source the better the imaging potential and the better the chance to study frequency dependent phenomena like dispersion or attenuation. The frequency analysis of the signals recorded in the pilot hole (Figures 4.3 and 4.4), exhibits the bandwidth of the signals. The center frequency of the signals recorded with the vertical component geophone and hence mainly the compressional waves is ~ 80 Hz, the major bandwidth reaches from ~ 15 Hz to ~ 150 Hz. Some of the energy has an even higher frequency.

The vertical component spectrum of the reference geophone is only available for the data recorded in September '99, because the vertical component did not work in April. For the analysis of the spectral consistency of the signals for both, April and September, only the horizontal component spectrum can serve as a basis (Figure 4.4). Here, the highest amplitudes are observed at about 90 Hz, a peak seems to exist close to 72 Hz, and a secondary maximum appears at about 50 Hz. The latter seems to be part of the natural shot signal or the result of interference patterns and does not seem to be dominated by electrical mains. Basically, the same bandwidth as in the compressional wave data is observable. The signal bandwidth thus results in wavelengths from ~ 15 m for the highest frequencies and slow S-waves to ~ 400 m for the lowest frequencies and fast P-waves.

4.4 Seismic Sections

The offset shot point (sp819) data permitted the azimuthal reorientation of the geophone sonde in the main hole (see Section 5.1.2 for details). Due to the positive velocity gradient in the upper crust and due to the geometry, the wavefront of the P-wave first break from the offset shot point is stronger on the horizontal components than on the vertical component for most of the main hole (Figure 4.1). By azimuthally maximizing the P-wave first break oscillation ellipsoid on one of the two horizontal components in the offset shot point data and by correcting the zero offset data with these angles, it was possible to rotate the horizontal components into the geographical coordinate system. This was only possible for the April '99 data because in September '99 the offset shot point holes were not available anymore.

Another rotation, independent from the geographical rotation, was carried out to separate the two split shear waves that can be detected (Figure 5.1, with the azimuth of the seismic traces color-coded). The two S-waves are polarized perpendicular to each other, due to seismic anisotropy of varying strength being present in this crustal section. The amount of anisotropy had been quantified in the pilot hole to be as high as 14% in places (W. Rabbel, personal communication, 2002). This rotation had to be carried out with a frequency low pass applied before (Fischer, 2000) to enhance the phase consistency of the S-wave signals.

The VSP sections analyzed in this thesis, are depicted in Figures 4.5, 4.6, and 4.7. A notch filter of 50 and 150 Hz and a trace normalization have been applied. The trace spacing is 25 m from 3000 to ~ 5200 m and 12.5 m below.

VSP data, especially in crystalline crust, not necessarily show P-waves on the vertical component and S-waves on the horizontal ones. The challenge is to identify the onsets in the seismic sections with respect to these wave modes. This is even more complicated in regions with steeply dipping structural elements. Here, conversion of seismic waves and reflections appearing with unusual apparent velocities are more likely to be present and hamper the identification process.

4.4.1 Vertical Component

The most striking feature in the vertical component (Figure 4.5) is the multi-phase first break of the P-wave. Deconvolution tests and finite-difference modeling (see Chapter 8) but also a frequency analysis of the first break by J. Pujol (personal communication, 2001) indicate that this can be related to the complicated crustal structure, and is not the representation of the source signal signature. In fact, it seems that the source signal is simple.

Another important feature in the data is an onset with almost infinite apparent velocity at ~ 1.3 s one way traveltime. PP-migration of one horizontal component and PS-migration of the vertical component resulted in matching images of this feature (Frank, 2002). Therefore, in the vertical component seismogram it can be regarded as a PS-conversion in reflection on a steeply dipping structure, namely the SE1 reflector or Franconian Lineament fault zone, respectively. Special velocity filtering before the migration process worked well to strongly enhance this reflection element. Frank (2002) found exceptionally high reflection amplitudes.

With this exception however, the reflected wavefield of the brittle upper crust generally seems to be weak in this seismogram. There are two main reasons. On the one hand, reflectors in crystalline environments usually do not show large extent. On the other hand, reflections are not always reflected upwards due to the often complicated steeply dipping tectonic geometry. Reflections therefore cannot be detected by simply searching in the upward traveling wavefield.

4.4.2 Horizontal Components

The horizontal component data in Figures 4.6 and 4.7 have been rotated into the system of anisotropy. They show far more complex images. After the split shear wave separating rotation the S1 component contains the first and hence mostly faster S-wave. It is more or less northwest-southeast oriented, parallel to the strike of foliation and perpendicular to the S2 component at each depth position, as explained in Figure 4.8.

The main observable features are waves traveling with apparent shear wave velocity. Because of the high bandwidth of the signals the S-waves that originate from the

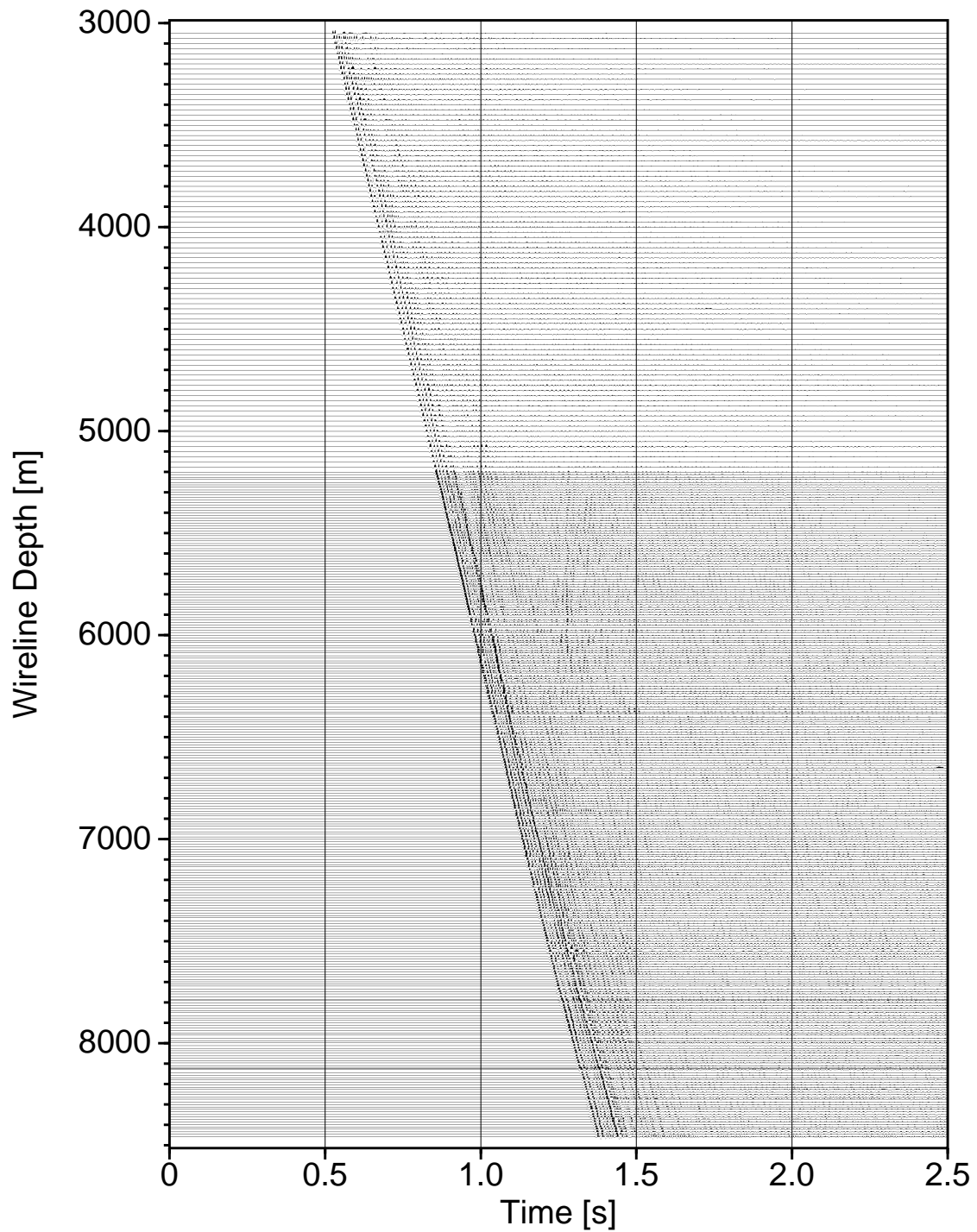


Fig. 4.5: Seismic section of the zero offset VSP vertical component in the KTB main hole, notch filtered at 50 and 150 Hz and trace-normalized. The trace spacing is 25 m above ~ 5200 m depth and 12.5 m below.

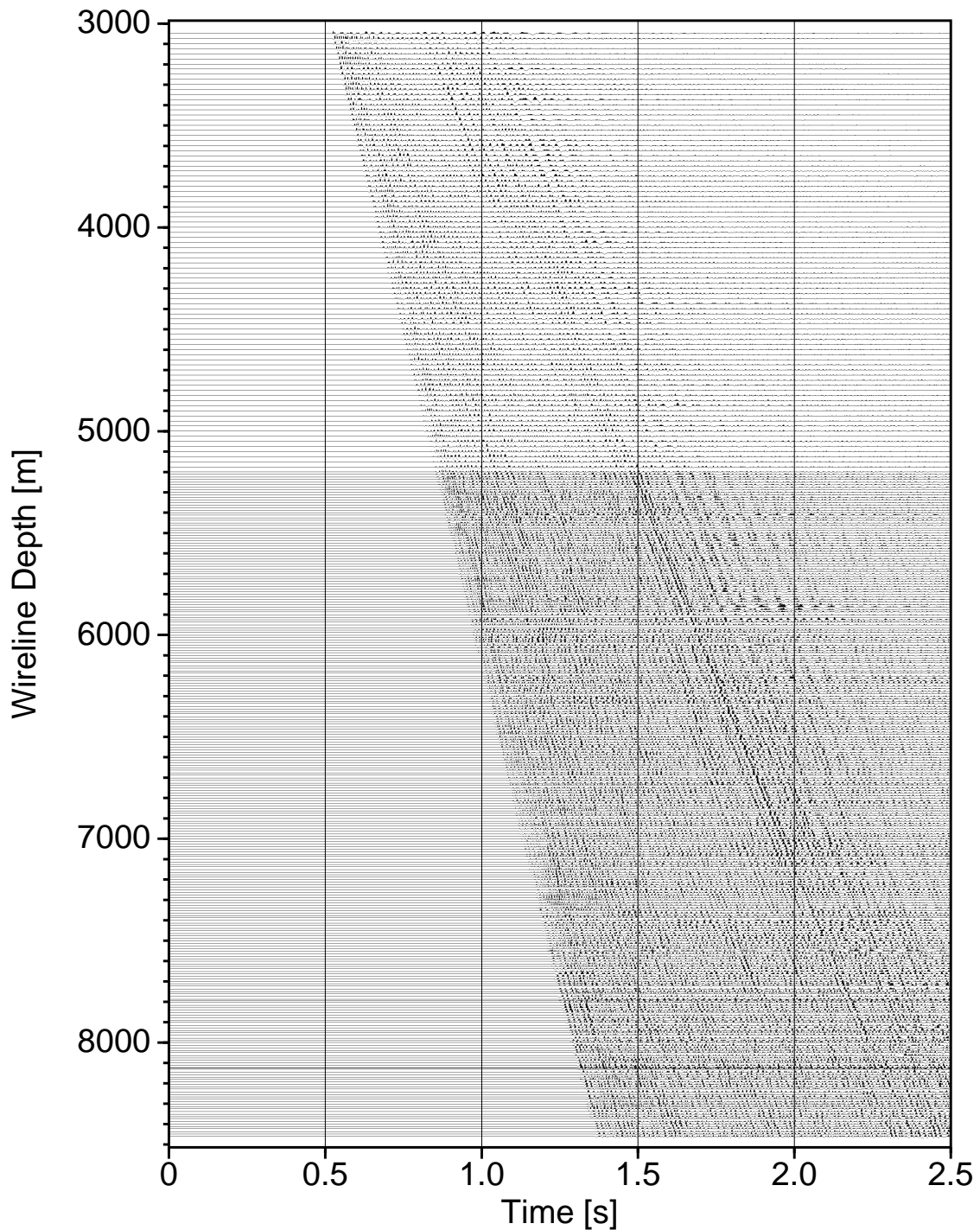


Fig. 4.6: Seismic section of the zero offset VSP horizontal component $S1$ (including the first direct S -wave) in the KTB main hole after shear wave splitting optimized azimuthal rotation, notch filtered at 50 and 150 Hz, trace-normalized. The oscillation plane is basically northwest-southeast. The trace spacing is 25 m above ~ 5200 m depth and 12.5 m below.

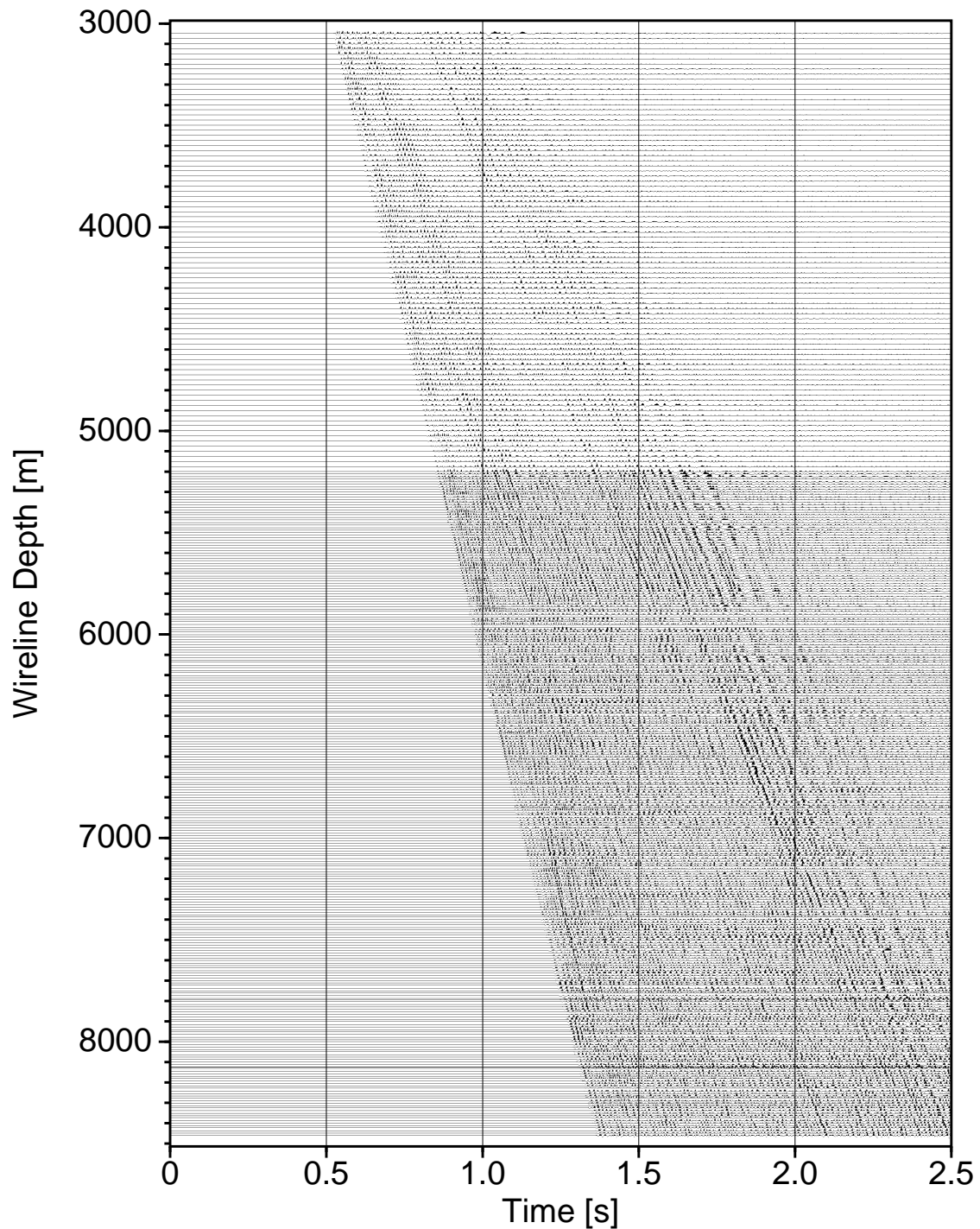


Fig. 4.7: Seismic section of the zero offset VSP horizontal component S2 (including the second direct S-wave) in the KTB main hole after shear wave splitting optimized azimuthal rotation, notch filtered at 50 and 150 Hz, trace-normalized. The oscillation plane is basically southwest-northeast. The trace spacing is 25 m above ~5200 m depth and 12.5 m below.

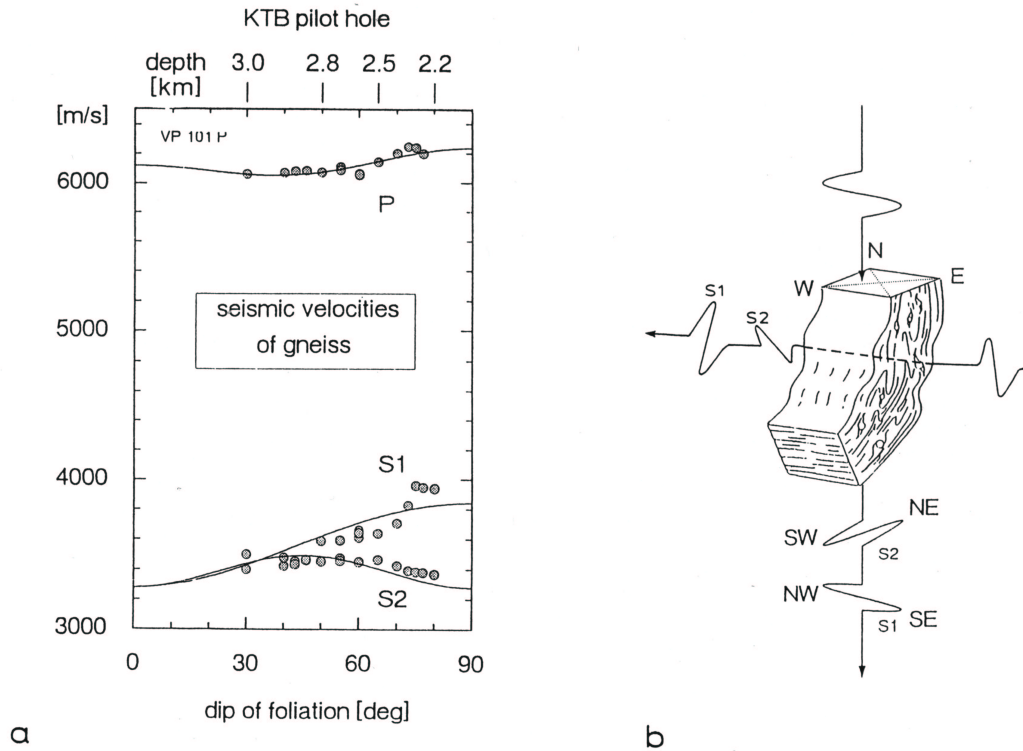


Fig. 4.8: a) Seismic anisotropy of a gneiss layer between 2.2 and 3.3 km depth in the pilot hole for vertical ray paths (dots) and the corresponding least squares fit of velocity versus dip of foliation for hexagonal anisotropy. b) Behavior of shear waves encountering the same foliated crustal structure originating from different source points with respect to dip and azimuth of the foliation (from [Harjes et al., 1997](#)).

surface are not as clear as they are in a low pass filtered version used for the determination of the shear wave velocities and the rotation angles by [Fischer \(2000\)](#). Some of the waves clearly emerge from the P-wave first break, a feature also present in older VSP data (e.g., [Lüschen et al., 1991](#)). These waves convert from P to S in transmission at certain depth positions within the borehole. There seem to be differences in the conversion strength with respect to depth, as there are points at the P-wave first break from where distinct and strong S-waves originate and there are others where no conversion takes place. Differences between the two horizontal components in this respect are not clear.

Since reflected waves in the vertical component are hard to detect it was decided to take these P-to-S conversions in transmission as a possible indicator for impedance contrasts but also to quantify the amount of energy converting from P to S to be able to correct the amplitude decay of the P-wave for this effect. The remaining amplitude decay should represent the amplitude decay partly corrected for the scattering Q . The determination of the P-to-S amplitudes is crucial for this correction though. This

is carried out with a slant stack approach described in Chapter 5. The amplitude of the converted waves is a function of P-wave and S-wave velocities as well as density and the dip of these parameters along the borehole. The precision of the slant stack approach is being determined in Chapters 8 and 9.

A hyperbola-shaped onset is basically only visible on component S2 at about 1.2 s and 5.2 km depth to about 1.4 s and 7.9 km depth. This is probably the PP-reflection from the Franconian Line because this seismogram comprises the traces with the oscillation azimuths more or less in the plain of Figure 2.3 and is therefore sensitive to this dipping structure. The S1 component only shows remnants of this reflection in some places. This reflection does not show a strong branch reaching into the borehole, but seems to vanish within the later wavefield. The same is true for the P-to-S converted wave, reflected on the same structural feature, described in the vertical component seismogram. This is well in agreement with the obscure nature of the Franconian Lineament in the direct vicinity of the borehole, observed in older seismic images (Harjes *et al.*, 1997), but also in new prestack migration images of the 3D data recorded in 1989 (Buske, 1999). As in the vertical component seismogram upward traveling waves are not detectable.

4.5 Amplitude Decay with Depth, Q

The analysis of the amplitude decay with depth or the *quality factor* Q , respectively, is one of the aims of this work (see Chapter 3). The analysis was carried out with the full spectrum and within four of its octaves. This seems reasonable, because the amplitudes are well known due to the pilot hole reference geophone recordings, the spectrum of the source signal shows a wide range, it is consistent during the whole experiment, and the geophone tool in the main hole was able to pick the signals with a high signal to noise ratio. The technique used for the determination of Q is very basic, though. The intention was to get starting values to be corrected by subsequent subtraction of the energy dissipated into converted waves.

4.5.1 Pilot Hole Reference Amplitude Values

The amplitude of the recorded main hole signals were corrected for the maximum shot amplitude picked in the pilot hole. This correction value was picked in the (P-wave) first break of horizontal component H2, for it is the only one with reliable values for both survey periods - April and September of 1999. Tests with the April '99 data of the pilot hole with both working horizontal components show that the relation between their maximum amplitudes is $\sim 1.1 \pm 12\%$. In this respect the amplitude of one horizontal component is a representation of the other and can be used as an input signal amplitude reference - for both survey periods.

To make sure this representation is also valid for the vertical component amplitude, a comparison was carried out between reliable vertical component data and cor-

responding data from component H2. This was only possible for the data recorded in fall of '99 because of a vertical geophone failure in the pilot hole in April of '99. Not all of the vertical component data of this survey were reliable though, because some of the signals had reached the saturation capacity of the recording unit. For the remaining data the resulting maximum vertical component to horizontal component amplitude relation is $\sim 3.2 \pm 19\%$. Although this error value is higher than in the relation between the two horizontal components it is still obvious that the H2-component data of the pilot hole reference geophone can basically be used for an amplitude correction of all components of the main hole data.

4.5.2 Full Spectrum Analysis

Amplitudes

The full spectrum amplitude decay with depth is depicted in Figure 4.9, separately for the April and September 1999 survey period. This is done basically for three reasons: (1) During the April survey the amplifiers integrated in the main hole geophone tool were switched from 60 to 40 dB above 3.5 km depth. (2) The September shot charge was reduced from 1 to 0.5 kg above 4.9 km depth and (3) an additional amplifier had been installed between the cable winch and the recording unit with an expected amplification of 6 dB. By plotting separate functions these possible sources of amplitude uncertainty are kept unmixed. Reason (2) should not have any influence, because its impact should have been removed in the shot amplitude corrections with the pilot hole recordings.

Eye striking are the high values in the upper part of the April '99 data. All of the amplitude anomalies above 3.5 km depth can be related to the reduction of the amplification within the geophone tool and subsequent correction. The nominal 20 dB reduction does not seem to reflect the real amplification difference. An explanation could be a possible but unknown temperature sensitivity of the amplifiers within the geophone tool. Unfortunately, the amplitude values in the September '99 survey for the same depth range have reached the saturation capacity of the recording unit. Therefore, amplitude values above 3500 m depth within the main hole are not reliable.

Q

The analysis of Q was only carried out for the compressional wave. The direct S-waves are hard to detect in the later wavefield and shear wave amplitude values would therefore hardly be reliable.

The compressional wave amplitude values drop by a factor of about 2.8 from 3500 m depth to 8.5 km in the main hole or an average 1.79 dB/km, respectively. For the center frequency of the source of 80 Hz, as determined by the reference geophone in the pilot hole and a wavelength of about 80 m, this results in an amplitude drop of 0.14

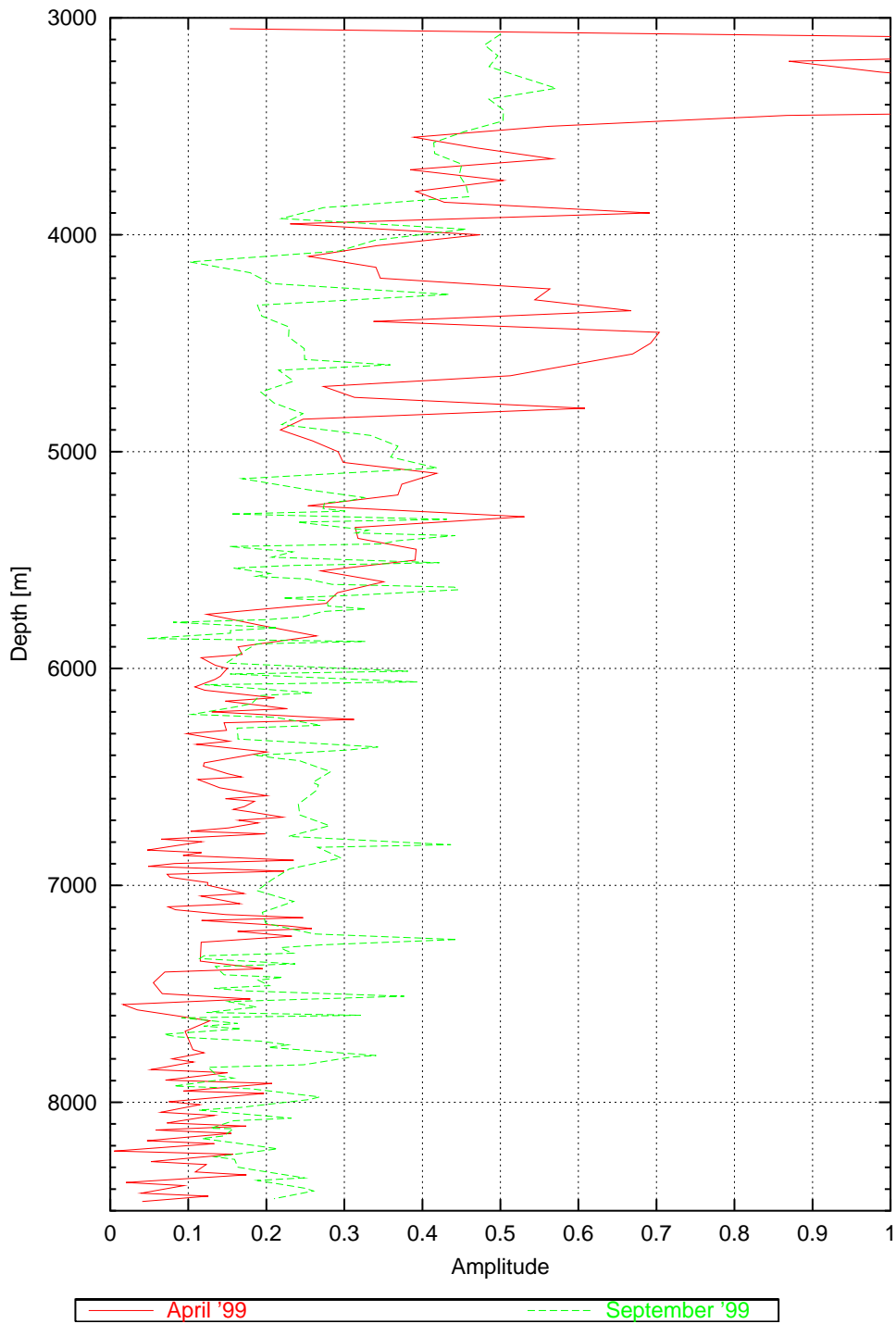


Fig. 4.9: Full frequency spectrum amplitude decay of the downward traveling P-wave with respect to the survey period (April, red and September 1999, green). The values above 3500 m are not reliable.

dB/wavelength. Using equation 3.17, these values result in an *average* Q_p of about 1400 with respect to a length of 5 km.

From the VSP6000 vibroseis VSP experiment carried out in the main hole of the KTB in 1992, Pujol *et al.* (1998) estimated frequency dependent Q_p -values between 14 and 30 for the depth interval between 3576-4538 m in the KTB main hole. They chose that depth range to avoid uncertainties of source signal variations and lithological effects.

In the following, the amplitude decay method was used for the determination of depth dependent Q -values, corrected for spherical divergence (equation 3.17). The full spectrum range was limited from 15 to 240 Hz with f being the main frequency of 80 Hz. Before the calculation of Q , a median filter with a moving window of 1000 m length and 25 m increment was applied. The result is somewhat surprising. Q -values basically oscillate between positive and negative values (Figure 4.10). However, the oscillation effect has been reported before (e.g., Frenje & Juhlin, 2000). For readability reasons $1/Q$ is plotted with depth instead of Q . $1/Q$ -values around 0 represent Q -values close to infinity, the ones of about 0.02 or larger represent Q -values of 50 or less which is the range determined by many authors. These small Q -values are the minority within the depth range analyzed, though. Positive values represent attenuation whereas negative values represent amplification. It is obvious that any apparent signal amplification within the crust can only be an effect of wave interference.

It is remarkable that large positive and negative values normally are in direct succession. But since the absolute positive and negative values are almost equal, it seems reasonable to suspect that most of the amplitude behavior is interference induced, partly probably due to multi-pathing; hence, a structural phenomenon. These values can therefore not be interpreted as intrinsic Q -values.

In some cases, the April and September values show the opposite behavior, in other cases they match surprisingly well. This seems reliable though, since the two amplitude graphs depicted in Figure 4.9 show basically the same pattern.

4.5.3 Octave Analysis

Amplitudes

Because of the wide frequency spectrum of the data all the way to the bottom of the main hole, it was decided to study the frequency dependency of the P-wave amplitudes with depth. The analysis of the main hole data was carried out in four octaves calculated through trapezoid zero-phase bandpass-filtering, the design of which is displayed in Figure 4.11. Within the second octave a notch filter of 50 Hz needed to be integrated because electrical mains had contaminated the recorded seismic signals. This alters the results only slightly, though. The same octave separation technique was used in the P-to-S conversion analysis processing described in Chapter 5. An optional notch filter working in the time domain (Buttler & Russell, 1993; Adam & Langlois, 1995) was also tested, but did not show any advantage with respect to the amplitude values.

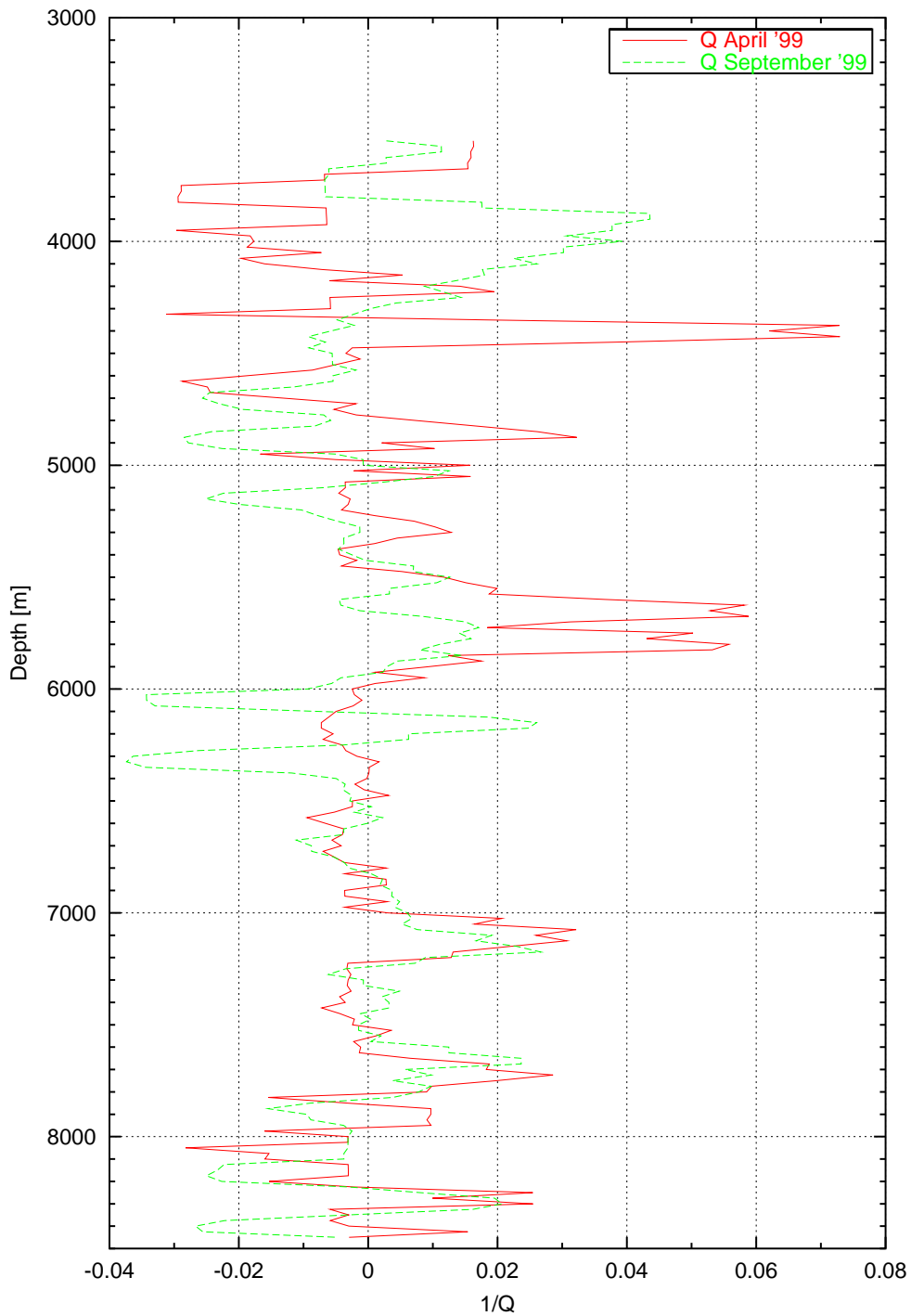


Fig. 4.10: $1/Q_p$ -values determined with equation 3.17. A moving window along the depth axis was used for the determination of Q_p . The amplitudes were smoothed prior to the determination with a moving median filter window length of 1000 m and 25 m increment. Values above 3500 m were dropped.

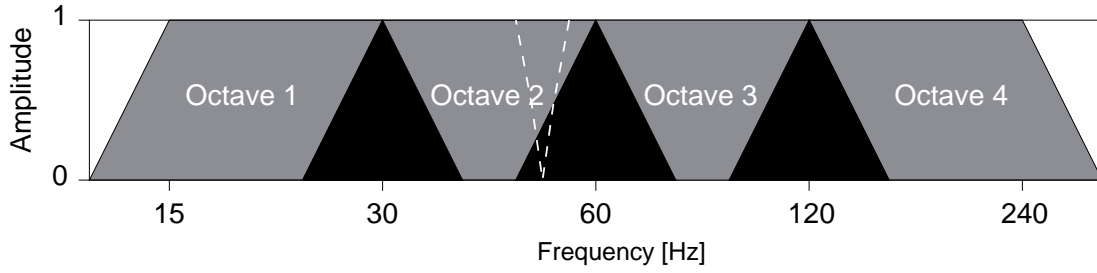


Fig. 4.11: Zero-phase bandpass design for the separation of the 4 octaves of the seismic data collected during the deep VSP 1999 at the KTB site. The dotted line indicates the position of the 50 Hz notch filter.

Before the analysis of the P-wave first break spectrum, the full spectrum signal was normalized, at each depth position. That way, the amplitudes are corrected for any signal decay with depth. After the application of each octave bandpass the maximum amplitude within the P-wave first break was picked again at every depth position (Figure 4.12). The result is the amplitude share of each octave within the downward traveling P-wave at every depth position in the form

$$A(n, z) = \frac{A(\omega_n, z)}{A(\omega_1, z) + A(\omega_2, z) + A(\omega_3, z) + A(\omega_4, z)} \quad (4.1)$$

where n denotes the octave number 1,2,3, or 4, ω the frequency octave, and z the depth position. Because the raw data is difficult to interpret, a median filter was applied with an analysis window length of 350 m and 25 m increment.

In general, one would expect the low frequency share of the source signal to grow, and the high frequency shares to decrease with depth. It is not as simple here. In a first order trend interpretation of Figure 4.12 the lowermost octave values basically stick around 0.1. The second and third octave shares increase with depth. The highest frequency share is the only one that shows an expected behavior. Its share decreases. It seems, the frequencies between 30 and 60 Hz basically increase the most, with respect to the others.

However, in a higher order analysis the situation is more complicated. The frequency shares oscillate with respect to depth. In this context, the octave 60-120 Hz shows the most interesting behavior. It often shows an opposite trend compared to the other octaves. Its shares show positive anomalies in many positions where the other shares show negative ones and vice versa. This seems like a parasitive effect probably resulting from interference phenomena related to geological structures. A similar behavior can be found in model data shown in Chapter 8. It can be expected that there are other influences affecting the amplitude spectrum as well, the crustal structure seems to be dominant, however.

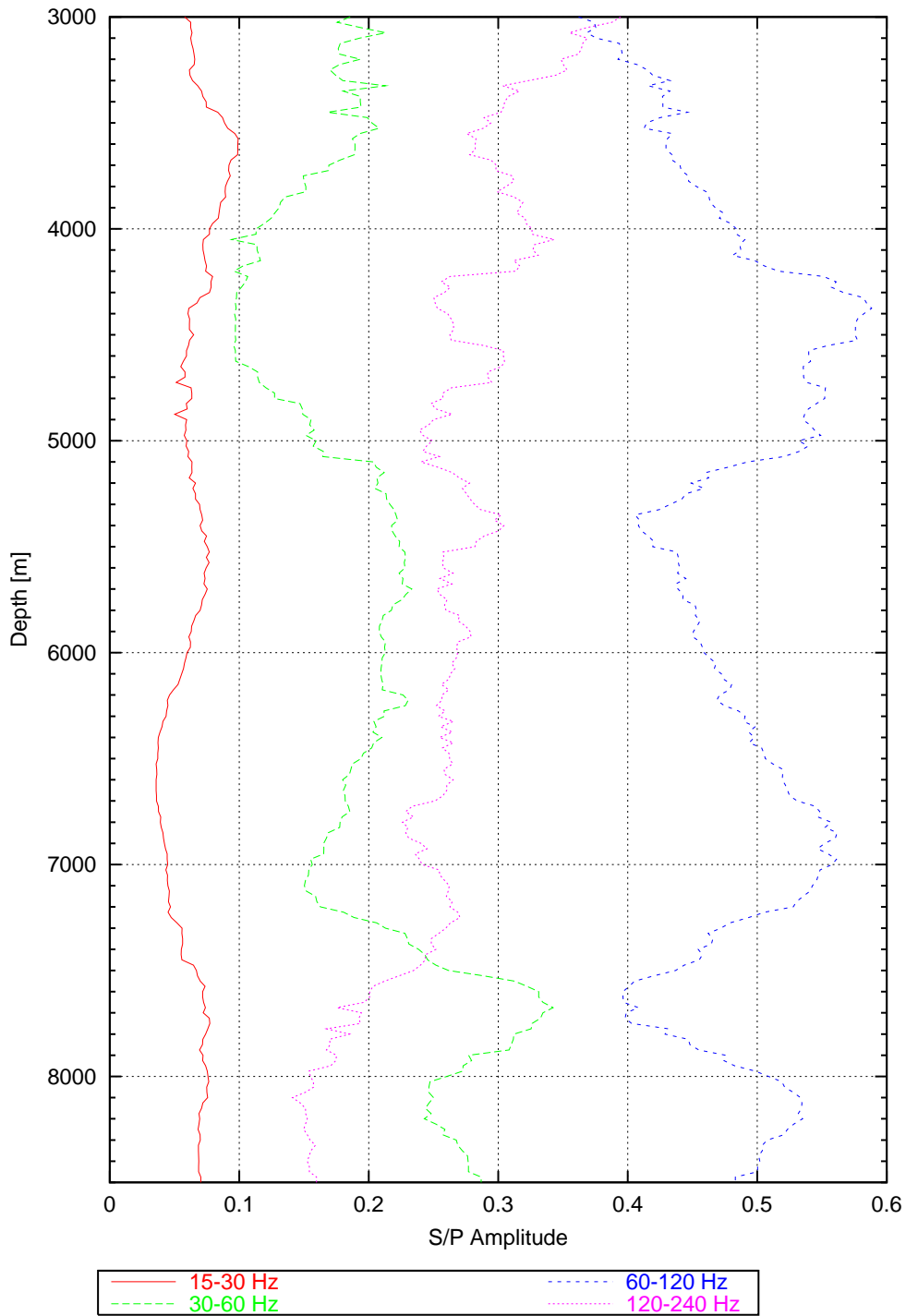


Fig. 4.12: Amplitude share of each of the four main octaves making up the signal of the downward traveling P-wave first break with respect to depth. To be able to discriminate the curves, a moving median filter is applied with a window length of 350 m and an increment of 25 m.

Q

The determination of an octave dependent Q was carried out with the same method as in the full spectrum analysis, and with the same median filter. This time, the frequency f in equation 3.17 was set to the center frequency within each octave. The resulting inverse Q-values are only shown for the September data (Figure 4.13). The basic observation is a frequency dependency of Q with the low frequencies showing smaller Q-values (higher $1/Q$ -values) than the high frequencies. A positive-negative oscillation with depth can be observed as in the full spectrum analysis. However, there seems to be only little correlation with the September full spectrum Q plot (green in Figure 4.10). This apparent contradiction disappears though, if the plot of the amplitude shares of the four octaves is also taken into account (Figure 4.12). The dominant frequency range is 60-120 Hz (blue) whereas the low frequency octave amplitudes (red) basically make up only about 10% of the whole signal. Not as prominent as in the amplitude octave share plot (Figure 4.12) the 60-120 Hz octave shows an opposing behavior compared to the other octaves. That this effect is less obvious in the Q-values is probably the result of the smoothing of the amplitudes before the determination of Q.

Basically, the determination of Q-values is not simple. Variations in amplitude values have stronger impacts on Q-values than variations in first arrival times. It depends on how the parameters taken into account are smoothed. The impact of different median filter window lengths has not been thoroughly studied. It can be expected that windows of a certain length have a stronger impact on higher frequency Q-values than on values in the lower frequency range. Furthermore, it is known that the time window length within which the amplitudes are picked has an impact, (e.g., [Frenje & Juhlin, 2000](#)).

4.6 Summary

In 1999 the technology to measure seismic signals in high pressure and high temperature environments encountered within the main hole of the KTB deep drilling site was finally available. A vertical seismic profile with a zero offset shot point and an 8 km offset shot point was conducted in the depth range from 3000 to 8500 m. This geometry setting permitted the reliable reorientation of the geophone tool within the geographical coordinate system. The high quality of the data set was refined by information from the reference geophone in the pilot hole in 3827 m depth which provided the necessary data for an individual static correction for P- and S-waves and for the amplitude correction of shot amplitudes. The high repeatability of the shots in terms of seismic signature and frequency spectrum was a surprise and could only be recognized in the pilot hole reference geophone. This repeatability made any signal deconvolution or spectral shaping unnecessary.

The high reflection amplitudes found in the later wavefield can be interpreted as the

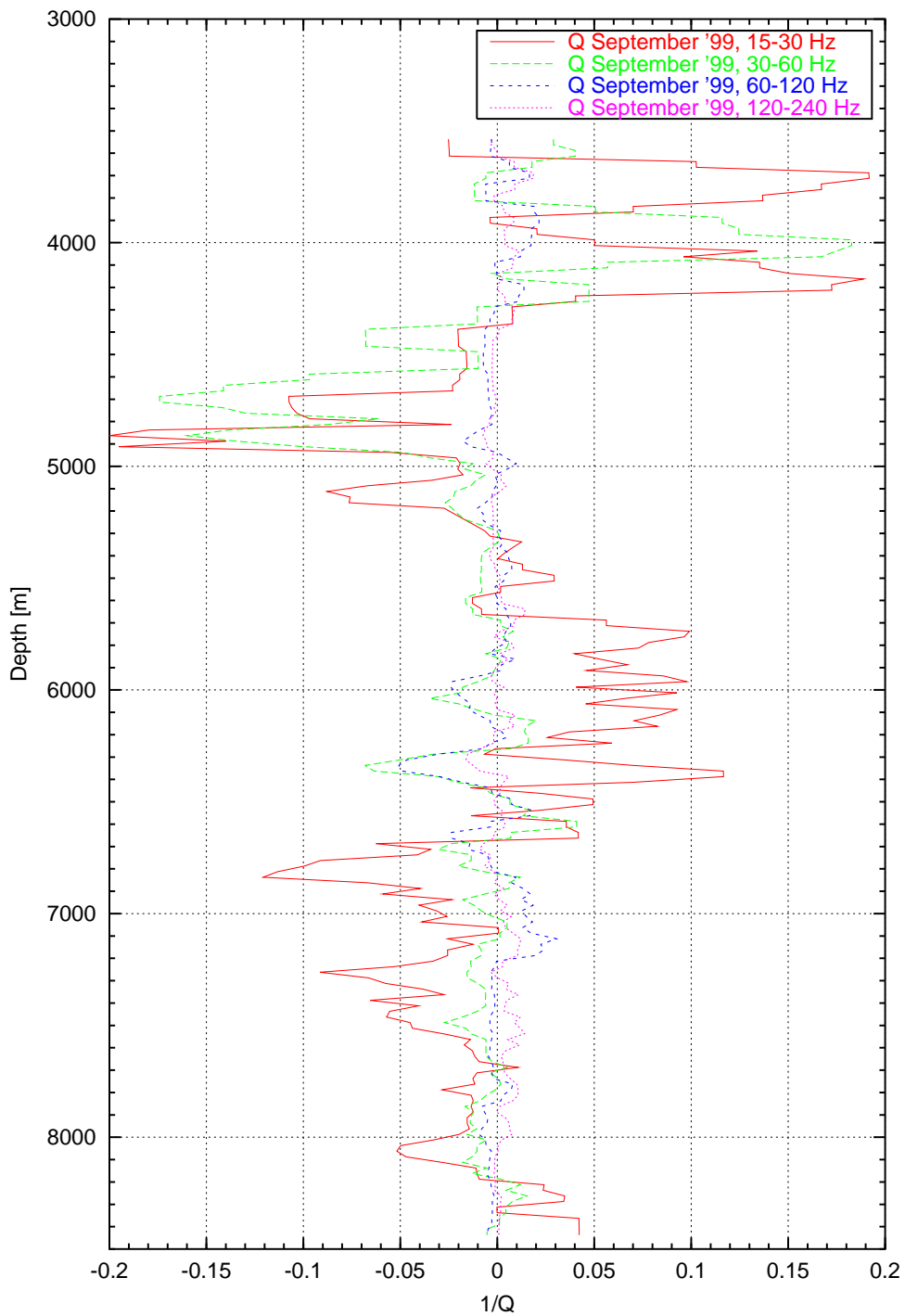


Fig. 4.13: Median filtered quality factor Q of each of the four main octaves making up the signal of the downward traveling P -wave with respect to depth. The moving median filter window length is 1000 m with an increment of 25 m.

result of open fissures or cataclastic zones within the crust. Open fissures had already been encountered during drilling operations. One of the questions resulting from this is, whether they also produce high P-to-S conversion in transmission amplitudes to be picked in the horizontal component geophone data, or whether these converted waves rather represent lithology related parameters, encountered in the borehole. The quantification of the P to S conversion compared with corresponding results from models described in later chapters, will be taken as such an indicator.

A surprise is the high spectral variability of the downward traveling P-wave first break along the main hole, as opposed to the stationary pilot hole reference geophone readings. It is analyzed in the course of this work whether this behavior is related to the lithology, open cracks or fissures, or the complicated tectonic structure of the crust.

Q-values of the KTB rocks in the literature derived from seismic data reveal surprisingly low values, basically between about 5 and 40 in the upper part of the depth range analyzed here. Laboratory measurements for high confining pressure show values between 90 and 300. The amplitude decay method used here for the determination of *Q* yields values that apparently oscillate between negative and positive. Values of 50 and less have been found, but only in few places. Normally, the absolute values are much higher, suggesting structural influence and hence scattering attenuation camouflaging the *intrinsic Q-values*.

The P-to-S converted waves should explain parts of the amplitude decay of the P-wave with depth. The correction of this decay with the amplitudes of the converted waves should at least partly correct for the scattering *Q*.

Chapter 5

Conversion Log Processing

Basically, vertical seismic profiling provides the crucial link between surface seismics and downhole “truth”. Its application has been widely established (Hardage, 1985). Yet, the data handling described here is somewhat unusual. The aim of the presented processing sequence is to quantify the wave conversion with respect to depth. The result is a log that could be called “conversion log” which can be integrated into further analysis like any other borehole log.

The disadvantage of a scattering environment like at the KTB site is the strong amplitude variation along individual seismic onsets. Because of the uncertainties in the determination of the exact amplitudes of the converted waves by individual amplitude picking a slant stack process is used to gain a certain average conversion amplitude. Subsequently, *scatter Q* can be approximated at least for the amplitude “loss” resulting from conversion, in order to obtain more realistic *intrinsic Q*-values.

The advantage of a scattering environment is that it is possible to record signals in the borehole from offset conversion points. This can help in the interpretation of a greater subsurface volume generally inaccessible for most borehole measurement techniques.

The whole processing sequence consists of a preprocessing part and the individual conversion type processing. The preprocessing sequence incorporates basic steps like trace rotation, amplitude correction, and shot static correction. The individual treatment of the different conversion types to be quantified needs to be carried out in an individual, specialized processing sequence. In this case, the specialized processing sequence is focused only on the P-to-S converted waves in transmission. Other conversion types are hard to detect in the VSP data and show small amplitudes. Basically, a higher order of effort would be needed to quantify them.

The seismic data processing was carried out with Seismic Unix (e.g., Cohen & Stockwell, 2001) and FOCUS/DISCO (© CogniSeis Development, Inc.), depending on the processing step. The possibility to use either program in batch mode enables the setup of processing flows integrating both software packages in the same flow.

5.1 Basic Data Processing

5.1.1 Shot Statics

The zero offset shot point was in fact a shot field of about 50x50 m with 46 shot holes of 35 m depth maximum and charge depths between 5 and 34 m. The charges were only partly water covered. The varying depths of the individual charges resulted in depth dependent first break times in the main hole data, but also at the reference geophone in the pilot hole. In the pilot hole recordings these first break time variations were picked separately for P- and S-waves and subtracted from the main hole VSP data, to correct for the charge depth time differences. This correction was carried out depending on which of the two wave types was to be analyzed in subsequent processing steps.

The necessity of applying individual anisotropic S-wave statics was also tested for (Fischer, 2000). Surprisingly, a single S-wave static correction for both horizontal components yielded the best result. The most probable explanation for this observation is that the time difference originates from within the weathering layer where the velocity is controlled rather by the (isotropic) weathering intensity than by any foliation anisotropy.

In the case of PS-conversion though, neither the application of P-wave static corrections nor S-wave static corrections, nor a combination of both yielded a satisfying result. For different reasons (see Section 5.2.2 and Chapter 8 for details) residual statics had to be calculated and applied additionally before the quantifying analysis of the conversion. Therefore, the shot static correction is only one step in the static shift sequence.

5.1.2 Trace Rotation

The geophone sonde in the main hole of the KTB was moved to a new depth position each time one shot in the zero offset and in the 8 km offset shot points had been triggered (Figure 4.1). Since the borehole cable naturally rotates once with every revolution of the cable winch the exact rotation azimuth varies from depth position to depth position. In reality it is not possible to predict the rotation angle from the number of winch wheel revolutions. Hence, to correct for this the offset shot point P-wave first break oscillation ellipsoid on the horizontal components was azimuthally maximized on one of the two components as already hinted in Section 4.2 on page 26. The rotation angle necessary for this optimization was then applied to the zero offset data individually for every depth position available. This rotation makes up for the orientation of the geophones (traces) within the geographical coordinate system.

For the September '99 data, for which no offset shot point first break information exists, this would be possible by visual interpolation between two already corrected (April '99) traces in the zero offset data because the April and September 1999 data cover the same depth range with only a shift of 12.5 m maximum. Because of this small depth difference the interpolation error between two known ellipsoid orientations is not

large. Since the geographical reorientation is of no importance for the data analysis in this thesis, no additional effort was put into a possible interpolative reorientation. However, the April '99 azimuth information permits the determination of the absolute strike direction of the anisotropy.

To optimize the azimuthal orientation of traces within the system of anisotropy, to be able to analyze each of the two split shear waves separately, a different and more important rotation was applied. This rotation can be carried out without the geographical reorientation in the first place if the geographical azimuth information is of no importance. The shear wave oscillation orientation analysis was calculated within the S-wave first break. A key role in this processing step was a trapezoid bandpass filter of (8, 10, 30, 35) Hz applied prior to the rotation analysis, to yield phase consistent S-wave onsets (Fischer, 2000). After low pass filtering two distinct differently polarized shear waves were detected and enabled the picking of the anisotropy rotation angles. The rotation angles picked in the low frequency range were applied to the data with the whole frequency range resulting in images already shown in Chapter 4 (Figures 4.6 and 4.7). This can be visualized in a more intuitive way in a seismogram showing the wiggles color-coded with respect to the azimuth (Figure 5.1), also confirming that no tube waves are present.

After this processing step distinct phases of certain onsets are now consistent over a long depth range. The traces in the horizontal geophone seismograms are not oriented into a certain geographical azimuth any more but their azimuth varies with depth, more or less according to the strike direction of the rock foliation. This needs to be kept in mind regarding the following processing steps.

5.1.3 Amplitude Considerations

The amplitudes of the traces recorded in the main hole varied because of differences in shot amplitude and variations in the coupling of the geophone sonde to the casing and the casing to the rock with respect to depth. Finite-difference modeling also suggests that some of the amplitude variations encountered in the main hole data are related to the velocity perturbations, introduced by the complicated structure of the crust, varying the spherical divergence locally with subsequent amplitude variations.

The correction for the shot amplitudes was successful because the shots did not vary much, neither in seismic signature (Figure 4.2) nor in frequency content (Figures 4.3 and 4.4) and because the reference geophone in the pilot hole was able to pick these signals excellently during the experiments. As analyzed in detail in Section 4.5 this correction for the amplitude can be regarded as reliable and is important for the analysis of the amplitude decay of the P-wave with depth.

For an analysis of the amplitude relation of P- and S-waves over the whole depth range, not regarding the amplitude decay with depth, it is feasible to use an approach for which the shot amplitude correction is of no importance. A simple normalization of the vertical and horizontal components with the P-wave first break amplitude at each depth position fits this need. That way, the amplitude relations between the different

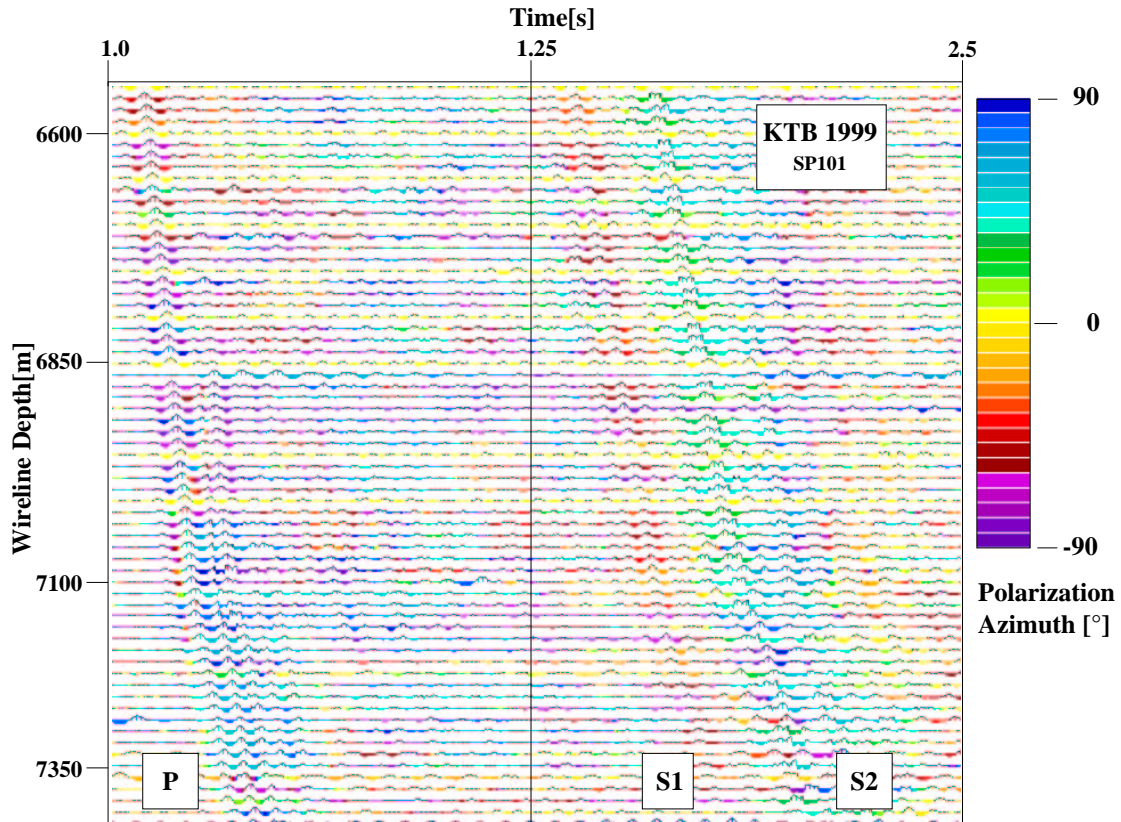


Fig. 5.1: Seismogram of a subset of the zero offset VSP data with the azimuthal orientation color-coded. The first shear wave (S1) is depicted mainly in reddish colors, the second S-wave (S2) mainly in bluish colors - a difference of 90° in the color table (after Rabbel et al., 1999).

components and wave modes are preserved; yet, the amplitude decay with depth is balanced. This is important because for further analysis a stack of traces across certain depth ranges is performed.

The best method for picking the reference amplitude of the downward traveling P-wave is to pick the maximum amplitude within the first onsets. This is especially true for the octave analysis later described in this chapter. The mean amplitude is not as precise. Three explanations are possible for this observation: (1) In case a bandpass filter was used, noise produced by this filter is also taken into account in the amplitude estimation, if the analyzing window is too long, (2) reflected onsets coming in from the side partly obscure the calculation, (3) “multi-pathing” of the shot signal spoils the analysis in the immediate vicinity of the first break. The term multi-pathing is used to describe the fact that a wavefront is split into segments or fractions in crustal structures with different elastic properties oriented parallel to the wave propagation direction. The result is multiple onsets for any wavefront having been multi-pathed. Argument (3) is supported by modeling (see Chapter 8 for details) and a frequency analysis of the first onsets in the downward traveling P-wave by J. Pujol (personal communication, 2001).

Probably a combination of all three arguments is responsible for the bad performance of a mean amplitude approach.

Another question is whether to take the maximum amplitude, the minimum amplitude or the maximum absolute amplitude as reference. For the phase preserving analysis it seems reasonable to take either the maximum or minimum amplitude because the phase of the incoming P-wave signal needs to be related to the maximum corresponding true phase amplitude of the converted wave. For the envelope analysis the maximum envelope amplitude is used as the reference.

5.2 P-to-S converted Waves in Transmission

P-to-S conversions in transmission are the most prominent features present in the seismograms of the horizontal components besides the direct shear waves. The basis of the following steps were the two S-wave components rotated for optimum shear wave separation and normalized with the individual P-wave first break at each depth position. The aim of the further processing was the quantification of this P-to-S conversion with respect to depth.

This special processing sequence for the P-to-S converted waves in transmission consists of suppressing events that propagate with velocities different from shear wave velocities by (5.2.1) frequency-wavenumber (f-k) filtering, (5.2.2) velocity reduction with the shear wave first break times, (5.2.3) residual statics corrections for the converted events, (5.2.4) phase preserving stack or optional envelope stack of a certain number of traces right after the first break. Basically, this sequence can be regarded as a refined slant stack procedure.

5.2.1 Frequency-Wavenumber (f-k) Filtering

One of the most crucial processing steps with many potential pitfalls is the velocity- or f-k filtering. This filter was useful to enhance events with more or less shear wave velocities in the seismograms to be able to quantify the P to S conversion of energy more precisely.

The f-k filter technique makes use of the Fourier transform in two dimensions. Along the time axis a frequency axis is calculated and along the depth axis a wavenumber axis is computed. Within the resulting frequency-wavenumber domain the filtering is performed. Finally the inverse Fourier transform is applied onto each axis to regain seismograms in x-t domain. By applying a certain filter mask within the frequency-wavenumber domain, certain apparent velocities being present in the seismic data, can either be suppressed or passed. In our case velocities were suppressed that did not fit the needs of the following processing steps. Filtering this way does not enhance the amplitudes of the passed phases but suppresses the unwanted ones. Therefore, this filter process is amplitude preserving in this respect.

Since the filtering is carried out in the frequency-wavenumber domain this filter is a multi-trace filter. Large amplitude differences between traces result in a certain crosstalk which appears as unnatural seismic events in the filtered sections. The normalization with the P-wave first break described above, did not leave such large amplitude differences. Nevertheless, a trace normalization applied before the f-k filter process and removed afterwards was used to reduced possible crosstalk and improve the filter process (Frank, 2002). Because this normalization was removed afterwards, the processing step can basically be regarded as amplitude preserving in this respect as well.

The fast Fourier transform used in software packages presumes evenly spaced samples along either seismogram axis and hence also defines the need for evenly spaced traces. This necessity was met basically by splitting the data set into two parts, one with 25 m and one with 12.5 m spacing.

Another phenomenon related to the sample and trace spacing is aliasing. An upper limit in sampling frequency results in a limit in the representation of high frequencies, an upper limit in trace spacing results in a limit of high wave-numbers resolvable and hence a limit to resolve low apparent velocities. The sampling interval in the time domain was high enough to collect all of the relevant bandwidth. A possible trick to circumnavigate the problem in the wavenumber domain is the velocity reduction of the seismograms before the f-k filter process and inverse velocity reduction afterwards (Yilmaz, 1987).

A perfidious problem is related to the Gibb's phenomenon. The selection of sharp filter limits or small filter tapers, respectively, results in an unnatural exaggeration of certain events related to velocities close to these filter limits. One rule of thumb to grade the success of the filtering reads that there should only exist such onsets in the resulting seismogram that were already present in the unfiltered seismogram. The filter limits used successfully for the definition of the velocity filter mask (including the tapers) for the PS conversion in transmission onsets were 2.0, 2.8, 4.1, 5.6 km/s. This filter mask is narrow enough to suppress wave modes different from shear waves but also large enough let pass unusual shear wave velocities.

Figures 5.2 and 5.3 show the two horizontal components after the application of the f-k filter. The converted waves have become even more prominent without appearing artificial, yet, the amplitudes have basically not been modified.

5.2.2 Velocity Reduction

The aim of the velocity reduction was to plot the converted phases horizontally for stacking purposes. A first guess of the velocity present in the converted waves was the velocity of the direct shear waves, since the P-to-S converted waves are in fact shear waves. Therefore, a velocity reduction with the picked S-wave first break times picked by Fischer (2000) was applied. Although these times had been picked in low pass filtered seismograms this had also worked well for the direct S-waves in the seismograms with the full frequency range.

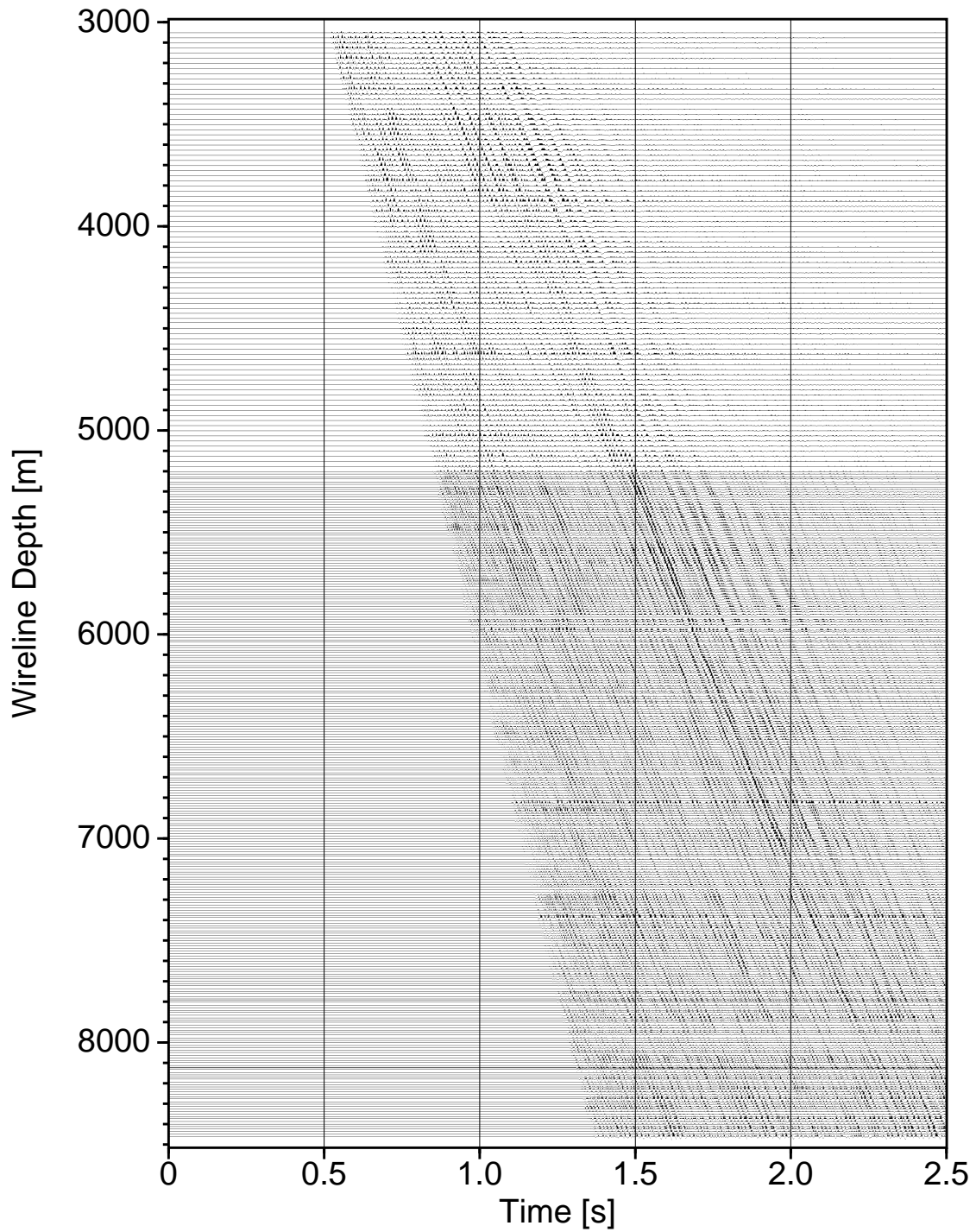


Fig. 5.2: The horizontal component $S1$ (Figure 4.6) after the application of the shot statics for P-waves, rotated into the system of anisotropy, normalized according to the P-wave first break amplitude at each depth position, and f - k filtered to suppress velocities different from shear wave velocities.

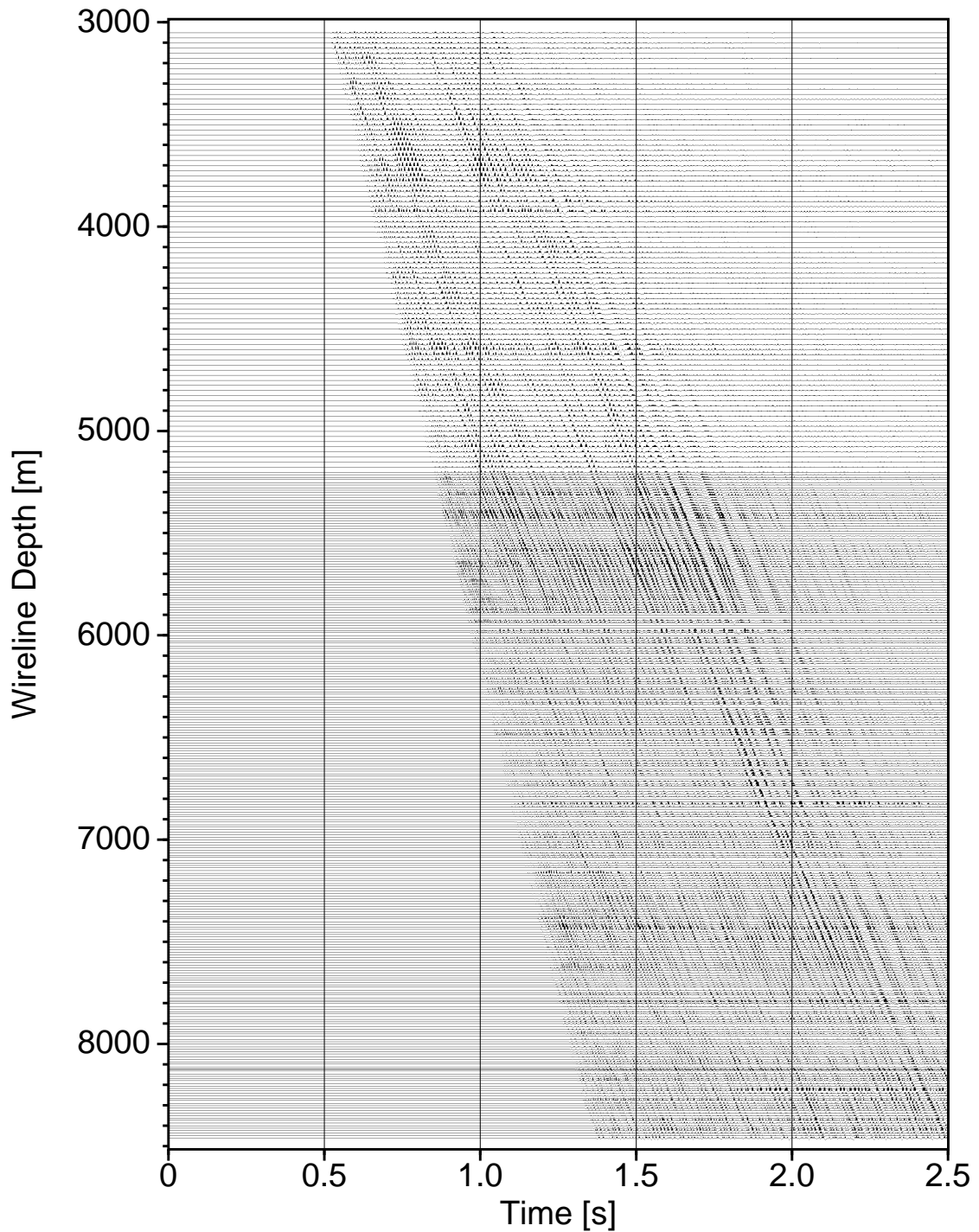


Fig. 5.3: The horizontal component S_2 (Figure 4.7) after the application of the shot statics for P -waves, rotated into the system of anisotropy, normalized according to the P -wave first break amplitude at each depth position, and f - k filtered to suppress velocities different from shear wave velocities.

Surprisingly, this did not work out for the converted waves (Figures 5.4 and 5.5). Tests showed that it made no difference whether the P-wave or the S-wave shot static correction was applied. Also, any combination of the two had different advantages and disadvantages. Finite-difference modeling supplied an explanation for this observation. This is also predicted by analytical calculations (Zoeppritz, 1919). Depending on the incident angle of the P-wave with respect to an impedance contrast surface converted waves usually head into different directions than the direct shear waves and hence appear with a different apparent velocity in the seismograms (consult Chapter 8 for details).

An additional complication is multi-pathing of a wavefront converted at different conversion points in a scattering environment. For complicated media this implies the determination of a complicated velocity-depth function for the converted waves velocity reduction, different from a velocity reduction of the direct shear waves. P-to-S converted waves therefore cannot be used for the determination of S-wave velocities as, e.g., Hackert & Parra (2002), propose. Thus, it was decided to integrate a residual statics step into the processing sequence, instead of trying to find a perfect correction for converted waves.

5.2.3 Residual Statics

The residual statics computation was carried out in a special iterative way for quality reasons. The statics were calculated starting in the low frequency range of the data (10 Hz). After every second residual statics computation the frequency was raised by doubling the upper frequency limit, and the residual statics were recalculated two times. This was repeated up to the upper frequency limit of 240 Hz. That way, the spectrum of the signal became wider in the progress of this processing step. The idea was to prevent the residual statics algorithm from sticking to local optima, but to try to detect the global optimum instead. The residual statics analysis window was of course restricted to the P-to-S converted wavefield and not extrapolated into the direct S-wavefield. Tests had shown that two residual static computation runs within one frequency band was sufficient. The result is a clear improvement of the discrimination potential of different converted phases (Figures 5.6 and 5.7) compared with the unprocessed images (Figures 5.4 and 5.5).

A better performance of the residual static calculation might have been possible if the residual static correlation window had been defined depth dependent, to minimize the variation of the number of traces included in the calculation. This would have refined the coherent line-up of onsets right after the first break, instead of picking dominating onsets in the later wavefield of the converted waves. Possibly, this could have also been achieved by the implementation of a certain muting window. However, this is left for future processing improvement, after all.

The last three processing steps mentioned (5.2.1-5.2.3), automatically produce a certain error. Since the velocity depth function of the converted waves does not follow the shear wave velocity function, certain converted wave velocities could already be

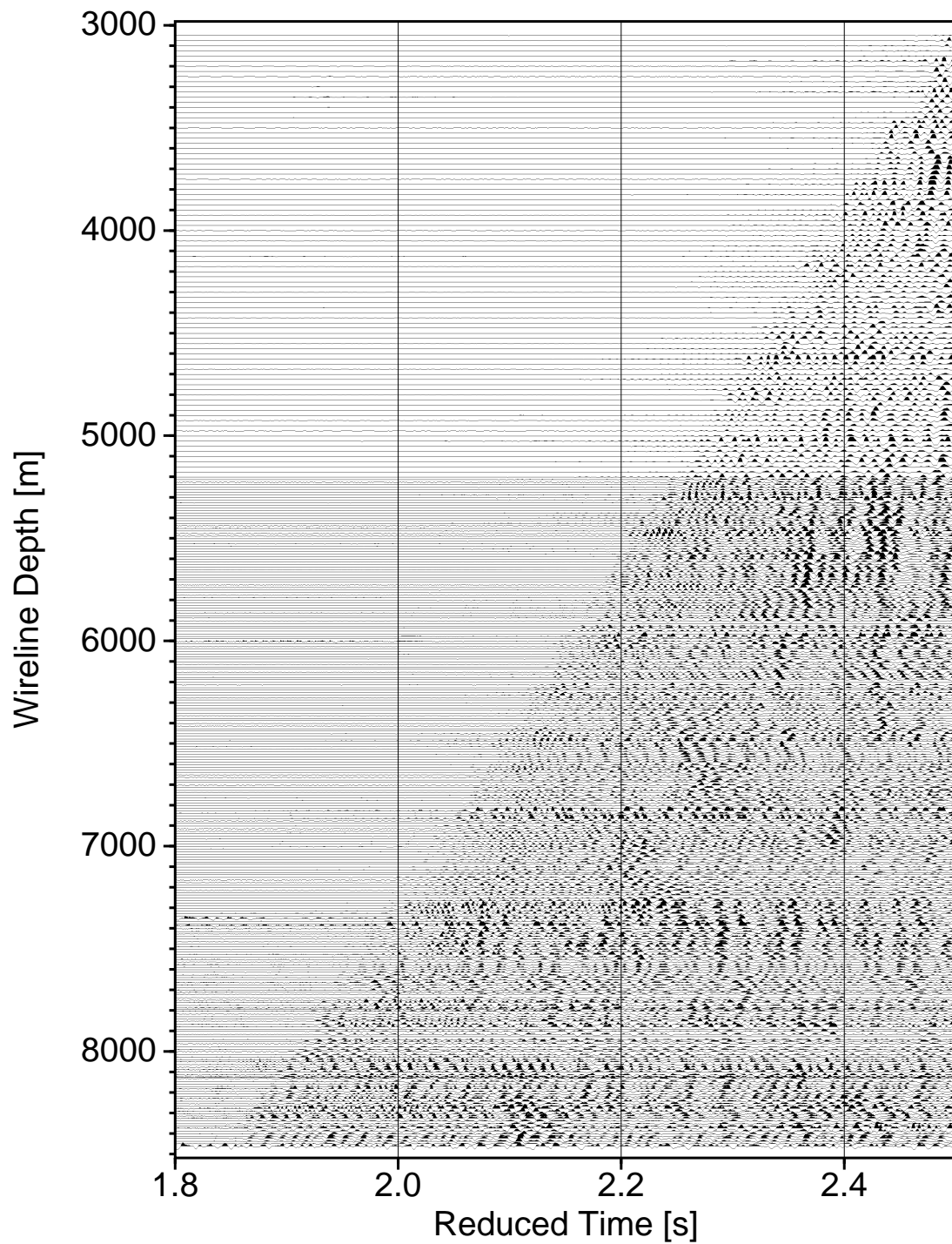


Fig. 5.4: The horizontal component $S1$ (Figure 4.6) after the application of the shot statics for P -waves, rotated into the system of anisotropy, normalized according to the P -wave first break amplitude at each depth position, f - k filtered to suppress velocities different from shear wave velocities, and velocity-reduced with the known S -wave velocity ($S1$ -wave first break times).

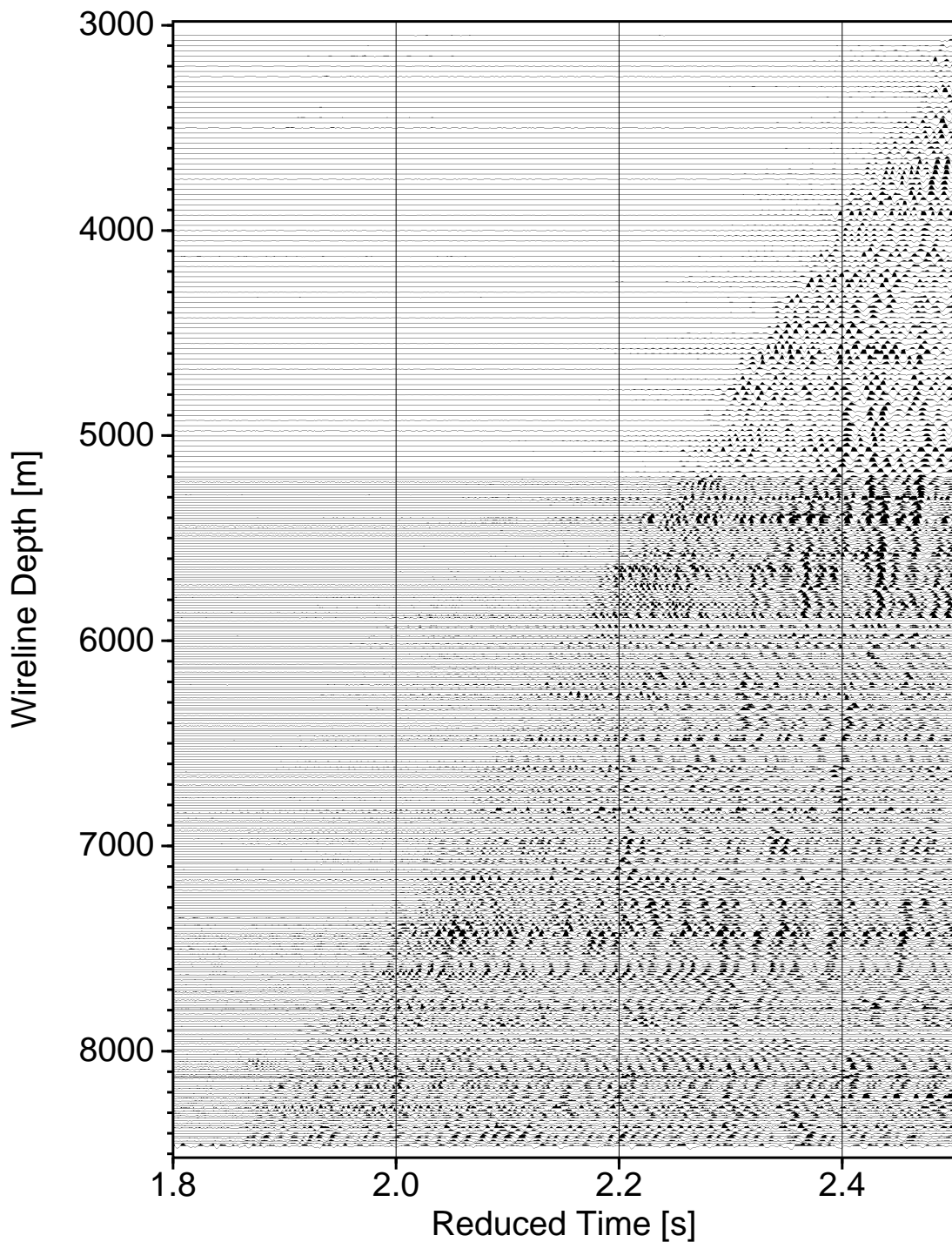


Fig. 5.5: The horizontal component S_2 (Figure 4.7) after the application of the shot statics for P-waves, rotated into the system of anisotropy, normalized according to the P-wave first break amplitude at each depth position, f - k filtered to suppress velocities different from shear wave velocities, and velocity-reduced with the known S-wave velocity (S_2 -wave first break times).

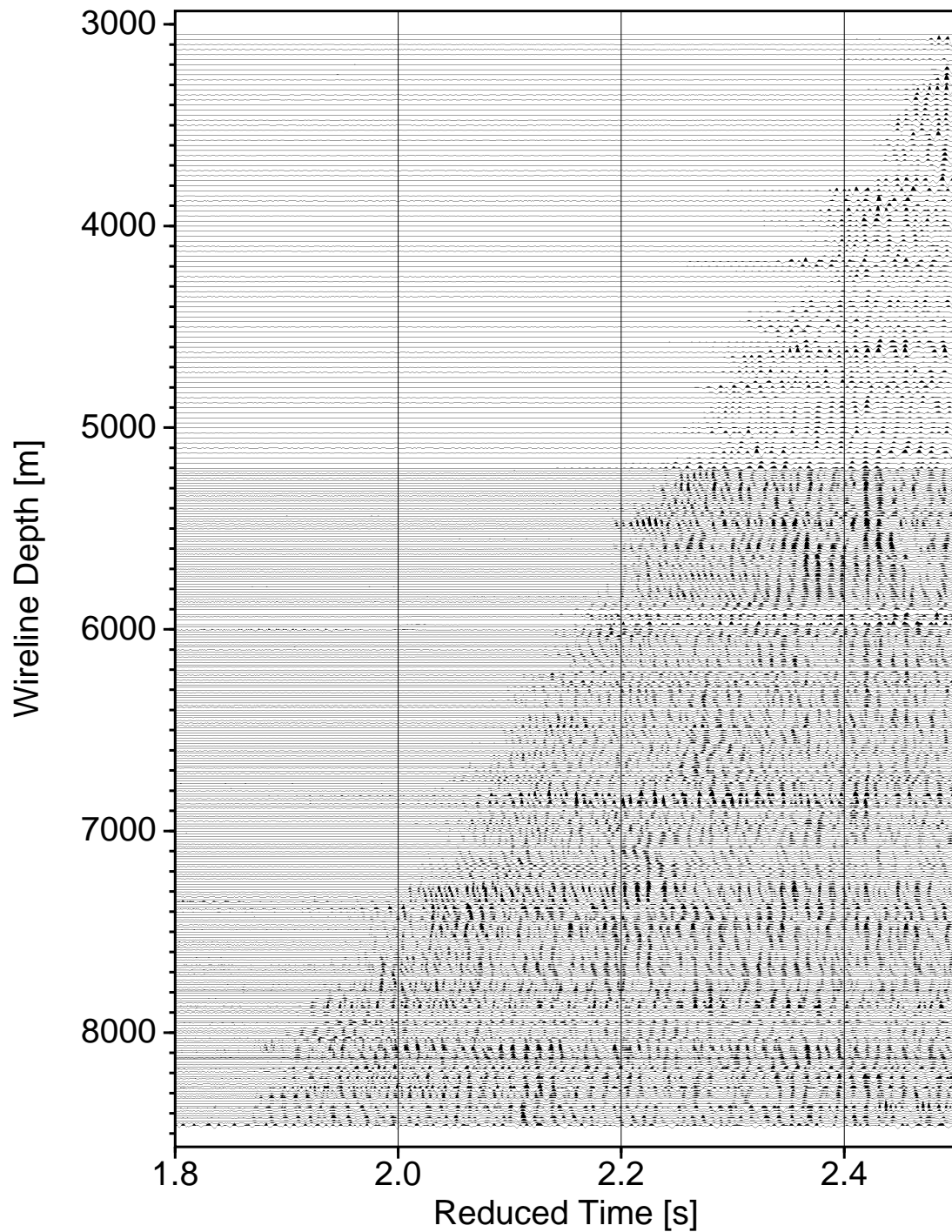


Fig. 5.6: The horizontal component $S1$ (Figure 4.6) after the application of the shot statics for P -waves, rotated into the system of anisotropy, normalized according to the P -wave first break amplitude at each depth position, f - k filtered to suppress velocities different from shear wave velocities, velocity-reduced with the known S -wave velocity ($S1$ -wave first break times), and applied residual statics trace shifts.

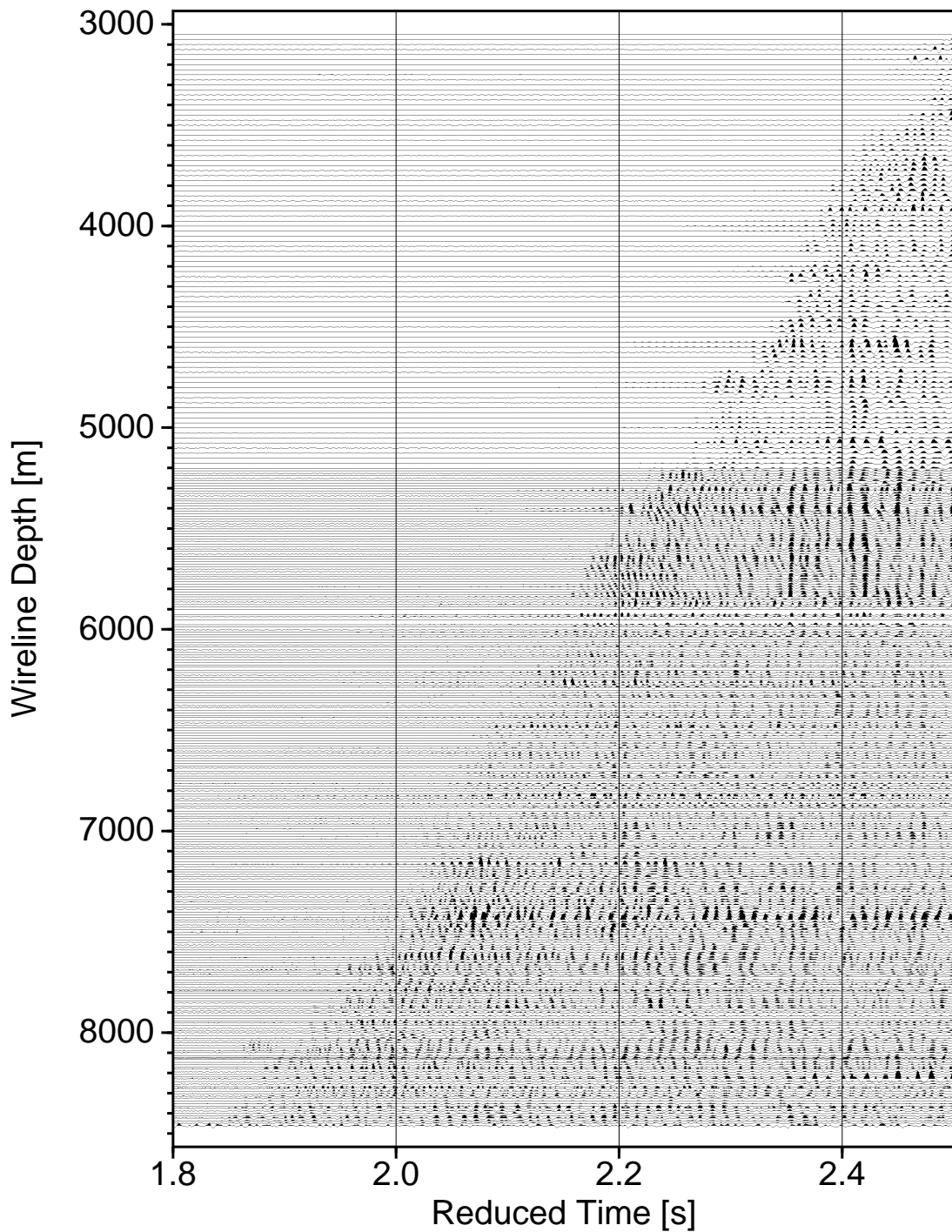


Fig. 5.7: The horizontal component S_2 (Figure 4.7) after the application of the shot statics for P-waves, rotated into the system of anisotropy, normalized according to the P-wave first break amplitude at each depth position, f - k filtered to suppress velocities different from shear wave velocities, velocity-reduced with the known S-wave velocity (S_2 -wave first break times), and applied residual statics trace shifts.

suppressed in the f-k filter process. Therefore, it is important to not choose the velocity window too narrow. On the other hand, by choosing a wider window, unwanted velocities remain in the data. This is a trade off. The velocity reduction and the residual statics cannot reduce this error.

An optional processing sequence could be the calculation of the residual statics before f-k filtering. In this case, the residual static calculation runs into the problem of which phases to pick. Hence, either sequence is not a perfect solution. Finding the perfect sequence would need more testing and perhaps the solution depends on each data set individually.

5.2.4 Stack

Phase Preserving Stack

The final but also delicate processing step was the stacking of traces. The stacking was carried out within a window to integrate a certain number of traces into the stacking process. A general rule reads: the more traces in the summation process, the smaller the statistical error. This is not true here. Despite the application of the f-k filter, there are still different phase velocities present in the converted waves data set (Figures 5.6 and 5.7). Velocity remnants of reflected, refracted, diffracted or other converted waves are therefore interfering the wavefield, increasingly with time. Hence, the later the analysis with respect to time or the higher the number of stacked traces within the wavefield, respectively, the more errors are present. It needs testing, to determine how many traces to sum in the stack. One possible solution to this problem is the comparison of results different window lengths yield.

Another question is where to place the stacking window. It seems reasonable to let it start at the P-wave first break time in the velocity reduced seismograms. This presumption is wrong. There are possible errors in the determination of the P-wave first break and the shot statics, but there are also additional time variations between traces due to the residual statics process. It is therefore safer to place the window a few samples later than estimated. Figures 5.8 and 5.9 show the windows within which traces are stacked, in this case 75.

An effect that needs discussion is the multiple first break in the vertical component seismogram (Figure 4.5 on page 33), because it can possibly lead to a blurred conversion to depth function. This could be the reason for the S1 component conversion log to display a kind of spatial frequency beat (see e.g., page 70 in Chapter 6). On the one hand, the multiple first break can be caused by the seismic source itself. On the other hand, it can be caused by multi-pathing of the signal on its way into the ground, an effect controlled by oriented velocity perturbations. This effect is even more obvious in seismogram sections with source signals of a high bandwidth. F-d modeling (Chapter 8) and a frequency analysis of the first break by J. Pujol (personal communication, 2001) exhibiting missing frequency bands in the spectrum, support the idea that most of the multiple first break is not source signal induced, but caused by the complicated

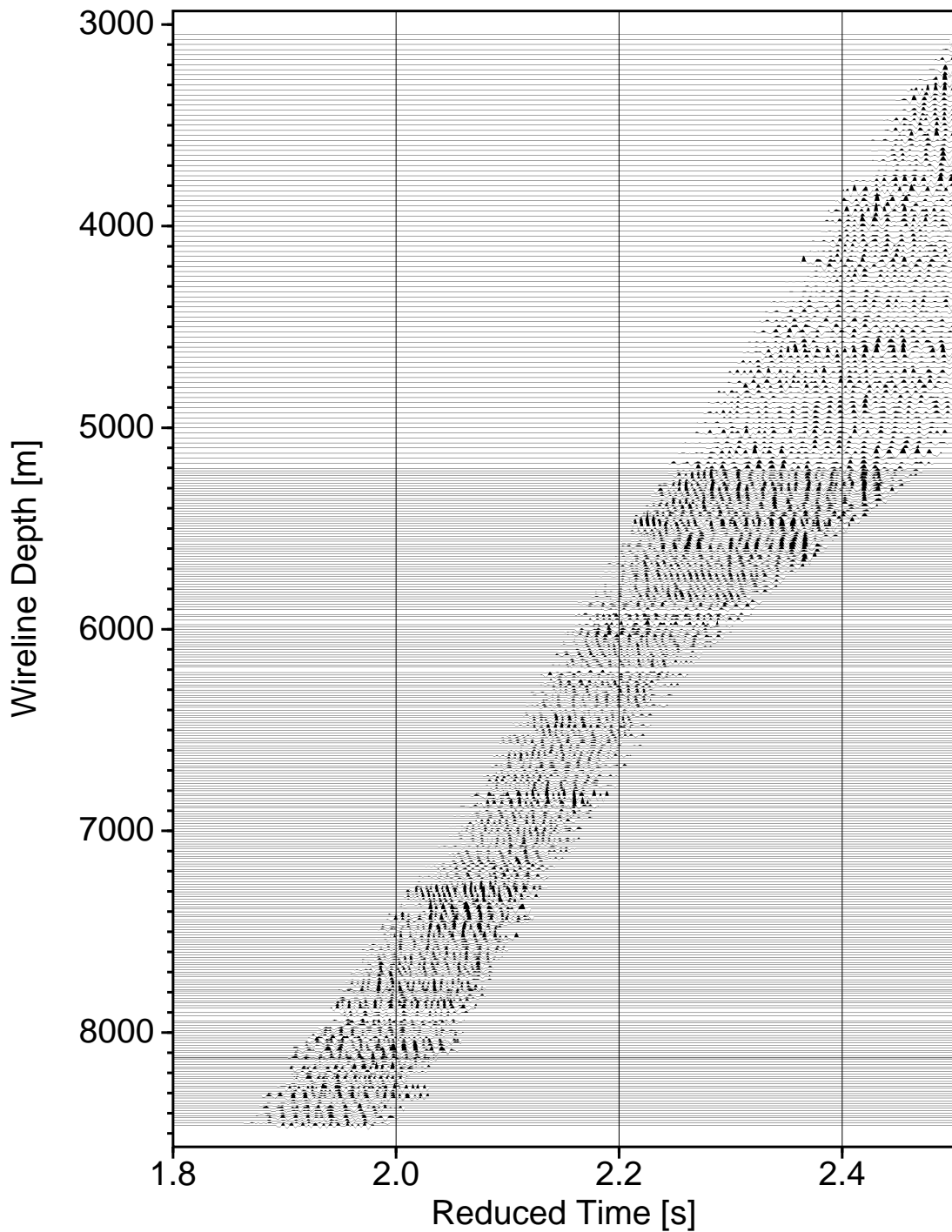


Fig. 5.8: The horizontal component $S1$ data from Figure 5.6 muted. The definition of the mute defines the number of traces in the stack. The mute window is adapted to the different trace spacing in the upper and lower part of the VSP. Note the deep end of the window. Here, less than the planned number of traces are being stacked due to the depth limit of the seismic data.

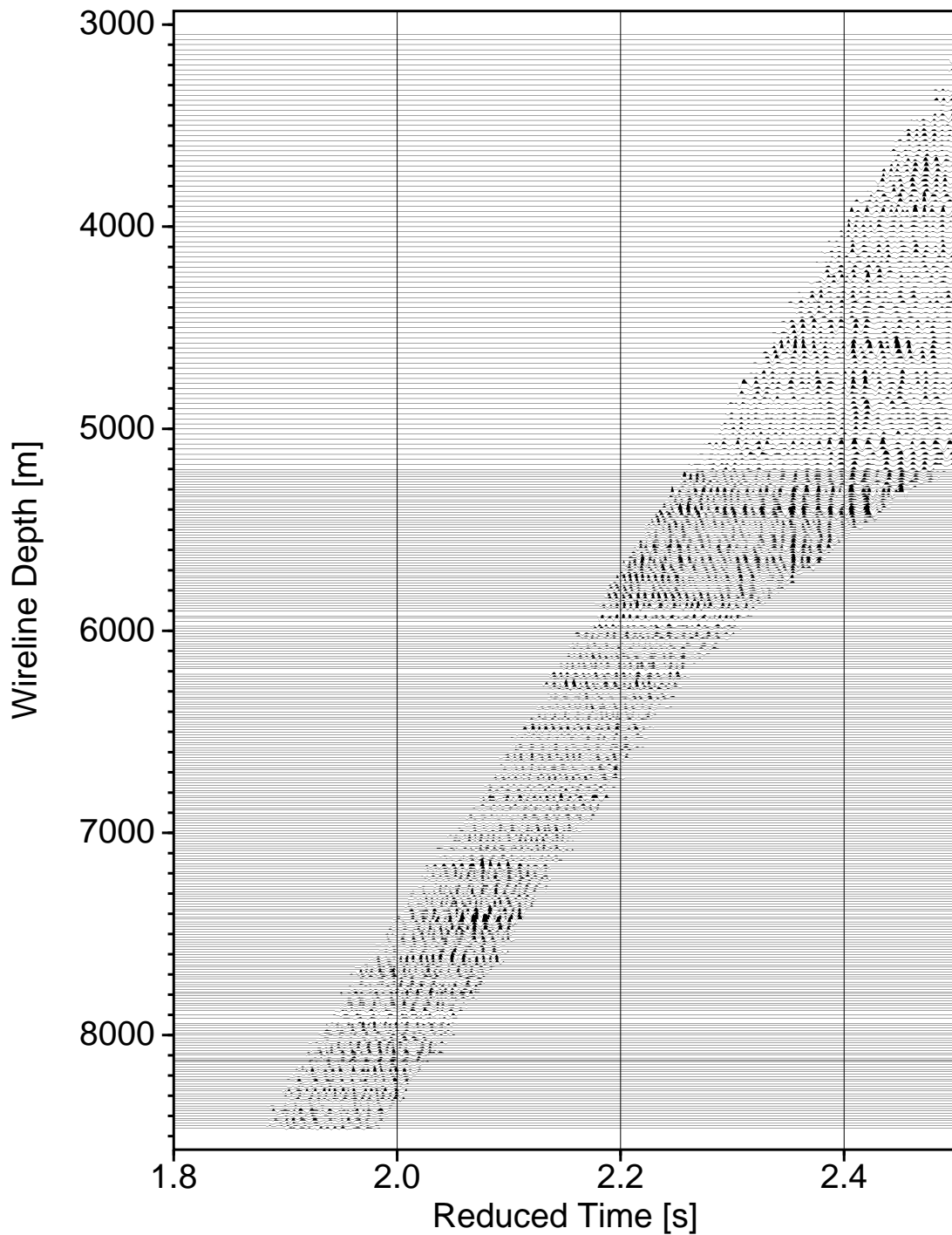


Fig. 5.9: The horizontal component S2 data from Figure 5.7 muted. The definition of the mute defines the number of traces in the stack. The mute window is adapted to the different trace spacing in the upper and lower part of the VSP. Note the deep end of the window. Here, less than the planned number of traces are being stacked due to the depth limit of the seismic data.

structure of the crust. Hence, it is multi-pathing. However, some reflections in the later wavefield do not show such multiple appearance. It seems the multi-pathing effect is especially strong for the P-wave traveling downward along the borehole.

A possible processing technique to correct for such a complicated signal is deconvolution. In this case, it does not help, though, because the shape of the first break varies with depth, due to varying multiple travel paths. Besides, it would probably be a difficult task to find a deconvolution technique that works on both, the P- and the S-waves in the same way, also leaving the amplitudes untouched. Because the onsets immediately following the first break might represent waves intercepting the borehole in such angles that they convert in values different from the direct wave, the resulting error in the conversion log is hard to estimate. The polarization of the oscillation of the single onsets within the first break would be needed to possibly separate these onsets. However, traditional polarization analysis techniques need at least more than one wave cycle, to determine the oscillation ellipsoid. Therefore, this techniques could not be implemented successfully here and the problem of how to unravel a possible multiple conversion at each depth position remains unsolved, so far.

As in the analysis of the amplitude decay with depth and the quality factor Q , the P-to-S conversion in transmission was analyzed for the whole spectrum covering 4 octaves (15-240 Hz), but also each of the octaves individually (15-30, 30-60, 60-120, 120-240) Hz. The parameters varied in the phase preserving stack are therefore (1) the number of traces and (2) the frequency content of the data. The whole processing sequence was carried out separately for the two shear wave components. The probable differences might point to the cause of the conversion.

The amplitude of the resulting stacks was finally divided by the number of stacked traces for normalization. The numbers of traces stacked were 15 and 75, respectively, to be able to compare a more detailed image on the one hand with a smoothed one on the other.

Envelope Stack

An optional approach for the final processing step is the stacking of envelopes. This was also used to prevent destructive interference from spoiling the results. Destructive interference is a problem for which especially migration and stacking processes in crystalline crust are known, due to the phase inconsistency of seismic onsets (Bittner & Rabbel, 1991). The envelope process cannot reverse destructive signal interference already recorded within a trace. Rather, it can prevent destructive interference from taking place in future stacking processes. The envelope stack was carried out for the same frequency octaves and number of traces as in the phase preserving stack.

The results of the different stacks are depicted and discussed in detail in the following chapter. They are compared with corresponding model data and analytical calculations in Chapter 9.

5.2.5 Time to Depth Conversion

The stacking of the traces is carried out while keeping the samples in the time domain. Because the depth information for each sample is not per se defined, the resulting P-to-S conversion to one-way traveltimes function must afterwards be converted into a P-to-S conversion to depth function. An exact one-way traveltimes to depth conversion function is a prerequisite for this. The P-wave first break time along the borehole is this function, since at the P-wave first break the conversion from P to S takes place. A more simple approach of a linear time to depth translation would in this case result in a depth error of up to 150 m (Figure 5.10).

5.2.6 Geophone Inclination

One parameter not taken into account is the geophone inclination. For the depth range from 3000 to about 7500 m the main hole can be regarded as more or less vertical and hence the inclination of the horizontal geophones within the 3-component geophone tool is basically zero. However, the wavefront of neither the compressional wave nor the ones of the converted waves are perfectly projected separately onto the 3 components because they travel according to the velocity and density field in the crust which can locally vary considerably. Especially the converted waves naturally refract in a distinct angle according to the dips and velocity and density contrasts present at geological unit interfaces. After the converted waves have been emanated they are constantly influenced by the velocity and density perturbations showing varying polarizations with respect to depth.

Even if the inclination of the converted wave would be accounted for at the conversion point by polarization analysis, the rotation of a specific trace would only be valid for that specific conversion. Conversions that had occurred above this point and that are present in the later wavefield of this trace would generally need a different polarization correction (Figure 5.11). A correct processing would therefore need to use different polarization correction angles within a single trace. Yet, even if this was attempted the practical determination of correct angles for the later wavefield would probably be difficult because of interference hampering the correct calculation of the oscillation ellipsoid. The determination would have to be carried out within a low pass filtered version comparable to the one used in the azimuthal optimization of the split shear waves (Section 5.1.2 on page 48) with the disadvantage of less resolution.

In a layered medium of equally inclined strata like in the model with 60° foliation dip starting on page 111 a correction for the inclination might basically be feasible; in a more complicated environment it is not.

The error resulting from the ray inclination on the geophones is not very large though, because the amplitude is reduced by the *cosine* of the emanation angle. A refraction of the converted wave by 20° would result in a relative amplitude error of only 6 %.

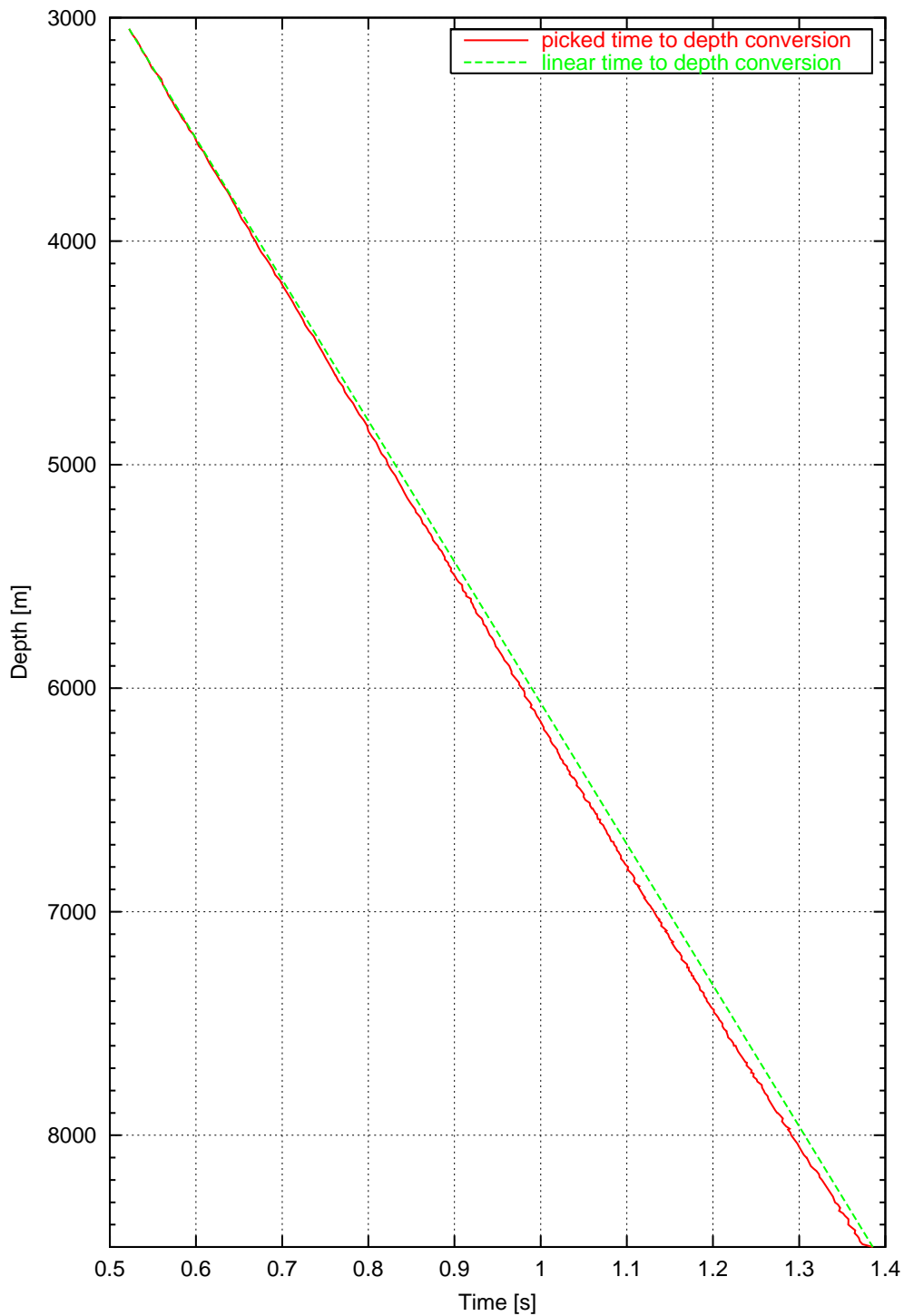


Fig. 5.10: Linear time to depth conversion (green) versus measured P-wave first break (red). The time to depth conversion is needed to convert the time axis of the stack into a depth axis. By using the P-wave first break the depth accuracy is in this case improved up to 150 m at about 7000 m depth.

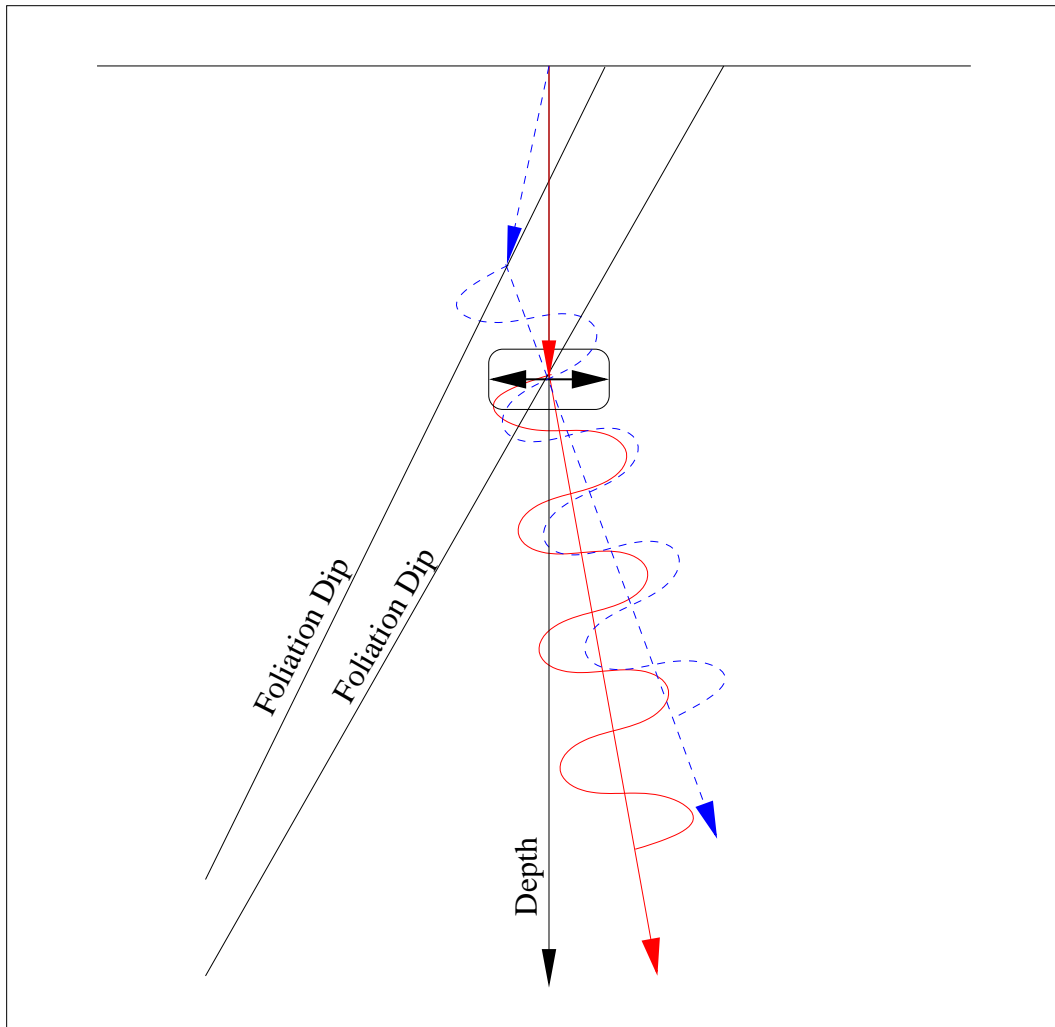


Fig. 5.11: Travel paths of incident compressional waves and the shear waves after conversion from P to S (red - waves close to first break, blue - waves represented in the later wavefield). The wavefronts are inclined according to the foliation dip at the velocity and density contrasts they emanate from. The horizontal geophones (black arrows in the box) are basically level in most of the KTB main hole.

5.3 Other Conversions

Other conversion types were not taken into account in this thesis because (1) the P-to-S conversion in transmission dominates the wavefield apart from the downward traveling direct waves and (2) reflections or other conversion types of the direct waves are hardly detectable. The search for those would require a higher order of effort. This is probably due to the complicated crustal structure encountered at the KTB drilling site. The strong reflection originating from the SE1 reflector in the later wavefield of this data set has been analyzed in a different thesis (Frank, 2002).

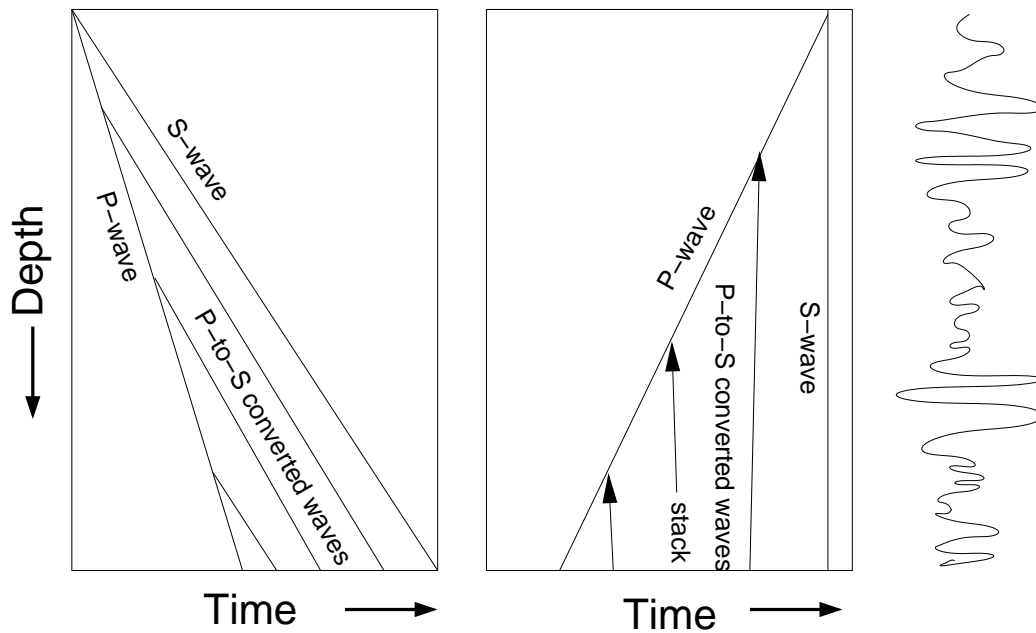


Fig. 5.12: Schematic drawing of the basic processing steps to derive the P-to-S conversion in transmission log. After a static shift and residual static correction, the converted onsets can be stacked (center). The result is the conversion vs. depth function (right).

5.4 Summary

In this chapter the seismic data processing for the downward traveling P-wave and for the determination of the P-to-S conversion in transmission was described in detail. The processing sequence used for the P-to-S conversion waves in transmission basically is a slant stack. It comprises (1) the application of the known shot statics picked in the pilot hole reference geophone data, (2) correction for the shot amplitude, (3) anisotropic trace rotation picked in the low pass filtered data of the VSP, (4) amplitude normalization with the P-wave first break, (5) careful velocity filtering including velocity reduction, (6) residual statics, (7a) phase preserving stack, (7b) envelope stack, and (8) time-to-depth conversion. Step (7) was carried out with different numbers of traces included in the stacks within different spectra. A schematic drawing of the basic procedure is depicted in Figure 5.12.

Within this sequence the main possible error sources are the velocity filtering process and the residual static step. The sequence of the two modules could create amplitude errors but a reverse succession of the two processing steps might as well. Without either module the result would be worse. The application of a certain muting window before the residual static calculation should be considered in the future for a better performance of the residual static step. The multiple P-wave first break might be another source of error. This effect cannot be estimated easily however. The geophone inclination with respect to the wavefronts possibly could be corrected for but would result

in a higher order of processing effort because the estimation of the polarization angles could be hampered by wave interference making the determination of the orientation of the oscillation ellipsoid uncertain. This needs more testing. Such a polarization correction would introduce varying polarization correction angles for each sample along each trace.

The result of this stack is the P-to-S conversion versus depth function with respect to the two different S-waves. This function can therefore be called a conversion log and can be used or compared with any other borehole log. The wave conversion represents an important part of *scattering Q* and the values of the conversion log can be used to correct the estimation of *in situ Q*-values.

Chapter 6

Conversion Log Analysis

The PS-conversion to depth function resulting from the processing described in Chapter 5 can be called “P-to-S-conversion log”. It relates the amplitude of emerging S-waves to the amplitude of the nursing downward traveling P-wave at every sampled depth position. Conversion logs were calculated for each of the two shear wave components present in the KTB Deep VSP 1999 data. Basically, the following analyzing options are discussed:

- *phase preserving stacks vs. envelope stacks*
- *full spectrum analysis and separate analysis of its 4 octaves*
- *stack of a small number of traces vs. a larger number of traces*

This adds up to 40 different plots that can possibly be taken into account for an analysis of the P-to-S conversion potential of the crustal structures at the KTB site. The interpretation in this chapter is focused on the comparison of the different options. A final interpretation and comparisons of the field data with model results and other information from the borehole can be found in Chapter 9.

6.1 Phase Preserving Stack

6.1.1 Full Spectrum Analysis

The resulting logs of the phase preserving stack of 15 traces are shown in Figures 6.1 (S1 component) and 6.2 (S2 component) with the spectrum 15-240 Hz. Stacks of 75 traces are shown in Figures 6.3 (S1 component) and 6.4 (S2 component). The depth is plotted along the y-axis, the amplitude of the converted wave in relation to the P-wave amplitude is displayed on the x-axis. The investigated depth covers 3 to 8.5 km, because the Deep VSP 1999 data set was used for this analysis. It is the only one available from the KTB site with a detailed amplitude and seismic signature calibration as described in Chapter 4.

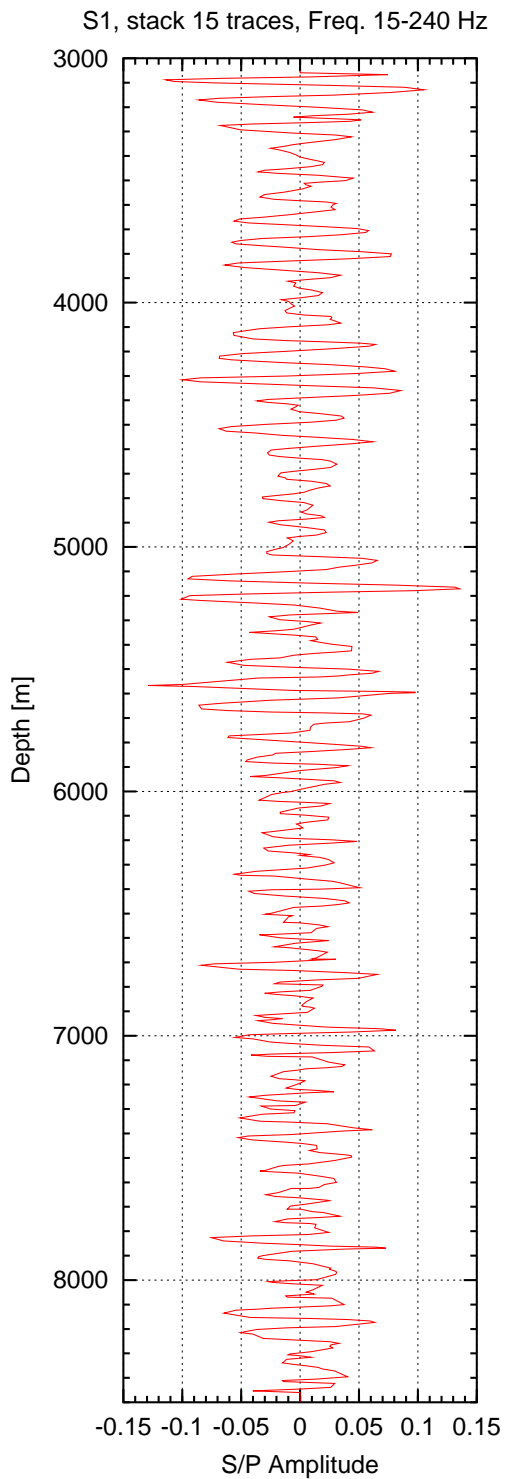


Fig. 6.1: *P-to-S conversion in transmission of the S1 component, stack of 15 traces of the full bandwidth.*

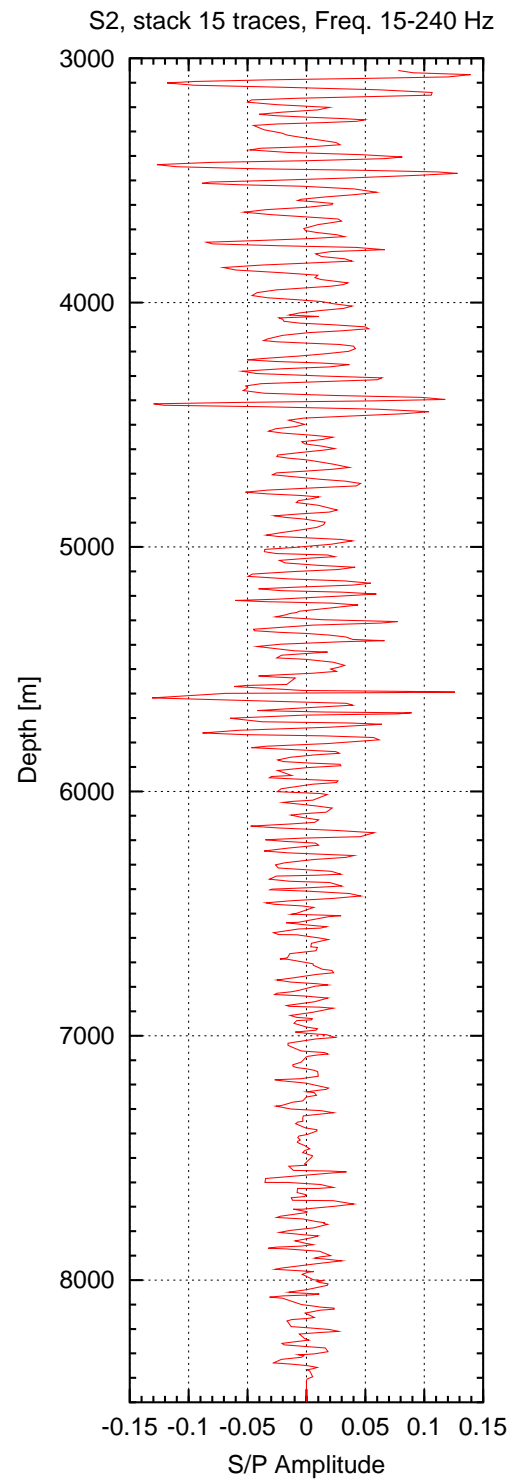


Fig. 6.2: *P-to-S conversion in transmission of the S2 component, stack of 15 traces of the full bandwidth.*

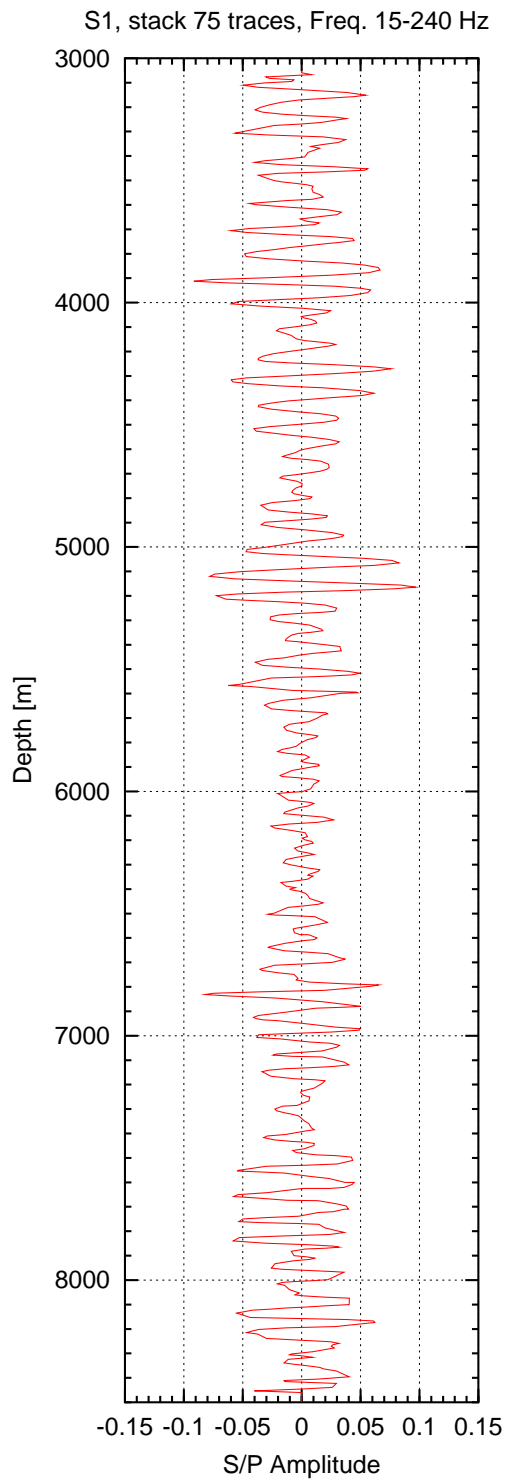


Fig. 6.3: *P-to-S conversion in transmission of the S1 component, stack of 75 traces of the full bandwidth.*

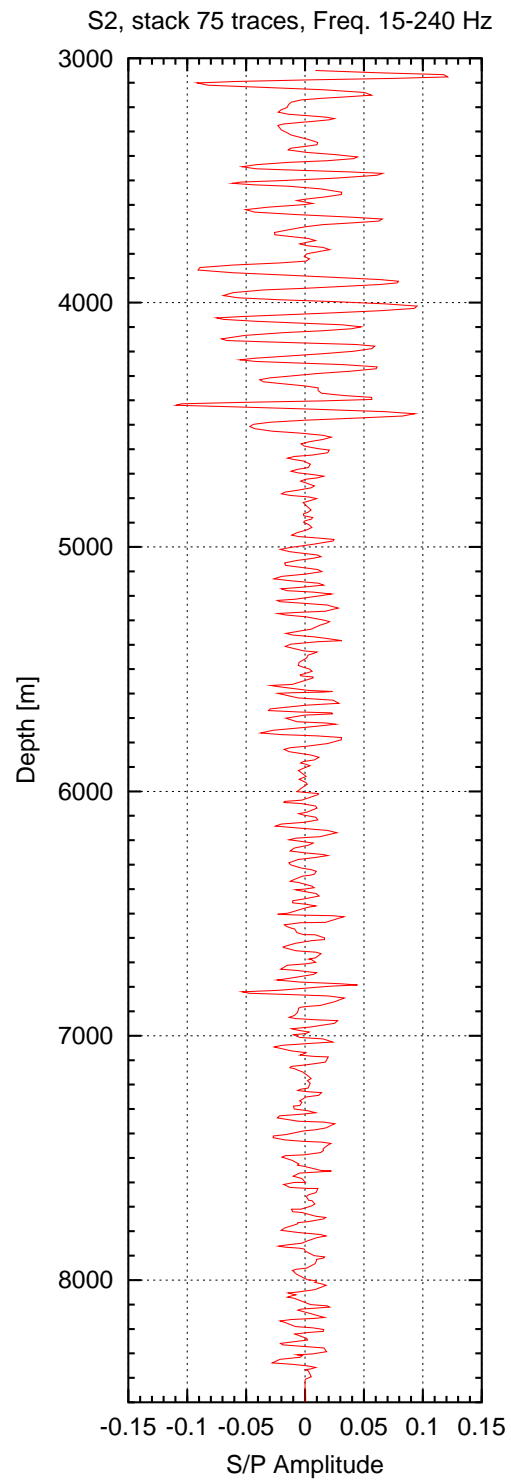


Fig. 6.4: *P-to-S conversion in transmission of the S2 component, stack of 75 traces of the full bandwidth.*

The stacks of 15 traces show a maximum conversion of about 15% of the P-wave amplitude in some distinct depths. Generally, the conversion amplitude is well above 2%. Whereas the S1 log shows this amplitude range over the whole depth, the S2 log shows small amplitudes below ~ 5.9 km and exceptionally small amplitudes from ~ 7.3 to ~ 7.5 km depth within a metabasic rock unit (Figure 6.5). The most prominent peaks are present in the S2 log at ~ 3.1 , ~ 3.45 , ~ 4.4 , and ~ 5.6 km depth. At each of these 4 positions a change from metabasic rocks to gneisses or vice versa, was found within the borehole.

The S1 component log seems to show a smaller spatial frequency, in fact, it shows similarities with a beat frequency in places. Its peaks are not as distinct although they show similar amplitudes. Perhaps the residual static process did only work well for sections of this component but not for the whole depth range. The influence of the multiple P-wave first break could also be responsible for this shape, as discussed in Chapter 5. In this case, a similar influence would however be detectable in the S2 component plot, too.

Generally, the main peaks can be found in the same depth positions in both components; however, the S1 component shows additional peaks at ~ 5.15 , ~ 6.7 , and ~ 7.8 km depth. Close to these depth positions are either lithologic contrasts or, in the case of 7.8 km, a combination of a fault zone with a lithological contrast between alternating layers and gneiss. On the other hand this component lacks the peak at ~ 3.45 km depth.

The 75 traces stacks have a similar appearance; the overall amplitude though, is decreased by about 2 percent points. The generally lower amplitudes in these stacks are no surprise, since destructive interference or an averaging effect can be expected. Basically, the peaks are detectable in the same depth positions as in the 15 traces stacks, except that the S1 component lacks the peaks at ~ 3.1 and ~ 7.85 km. The ~ 6.75 km peak seems to have moved to ~ 6.85 km and is now also visible on the S2 component. Here, the upper limit of the Franconian Line fault zone was proposed by [de Wall *et al.* \(1994\)](#). The S2 component additionally shows a dramatic reduction of amplitude for the ~ 5.6 km depth peak.

A surprise are the peaks at the top of the SE1 zone because they are not detectable in the stacks of 15 traces. This difference, resulting from the presence of high P-to-S converted wave amplitudes in the later wave-field, probably originates from conversion points not in the immediate vicinity of the borehole. In a scattering environment rays from offset conversion points can also be focused into the borehole at a deeper position at a later time. [Frank \(2002\)](#) compared the position of scatter points for reflected P-waves and P-to-S converted waves in reflection. The same model is valid for converted waves in transmission (Figure 6.6). The conversion logs produced with a stack of a larger number of traces would hence represent an average conversion image of a larger crustal section; the conversion logs produced with a smaller number of traces would rather represent the immediate vicinity of the borehole. This is well in agreement with the PP- and PS-migration of these VSP data carried out by [Frank \(2002\)](#) showing larger reflections on the SE1 reflector only in some distance from the borehole. However, the

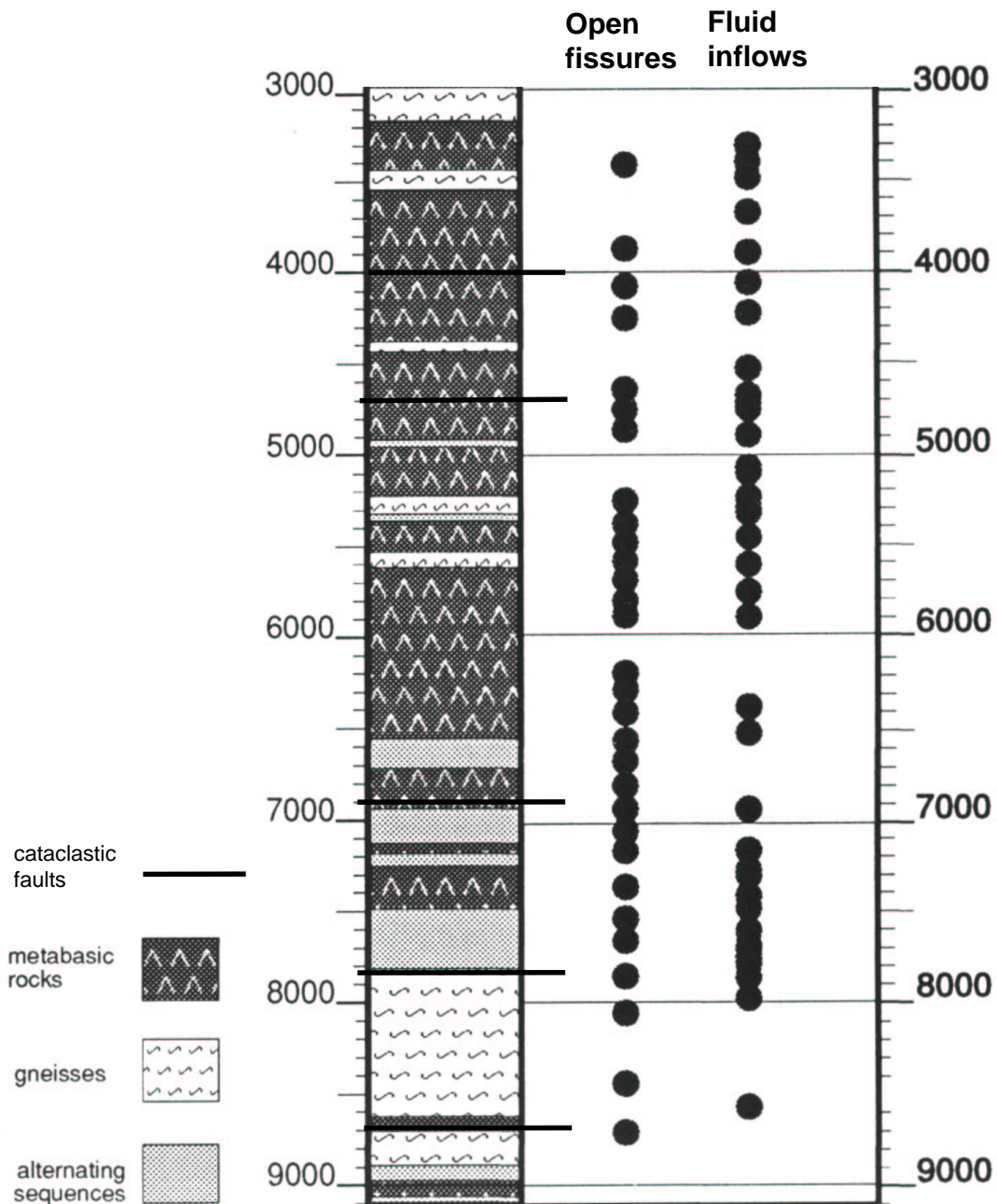


Fig. 6.5: Existence of open fissures and cataclastic fault zones in the simplified lithological profile of the KTB main hole and its correlation with fluid inflows (after Machon, 1995; Duyster et al., 1995b).

strongest reflections from the Franconian Line fault zone or SE1 respectively, were located in a distance of 1.0-1.6 km from the borehole in a depth range from 5.2-6.2 km. But already in a distance of about 200 m from the borehole the amplitudes of those reflections increase.

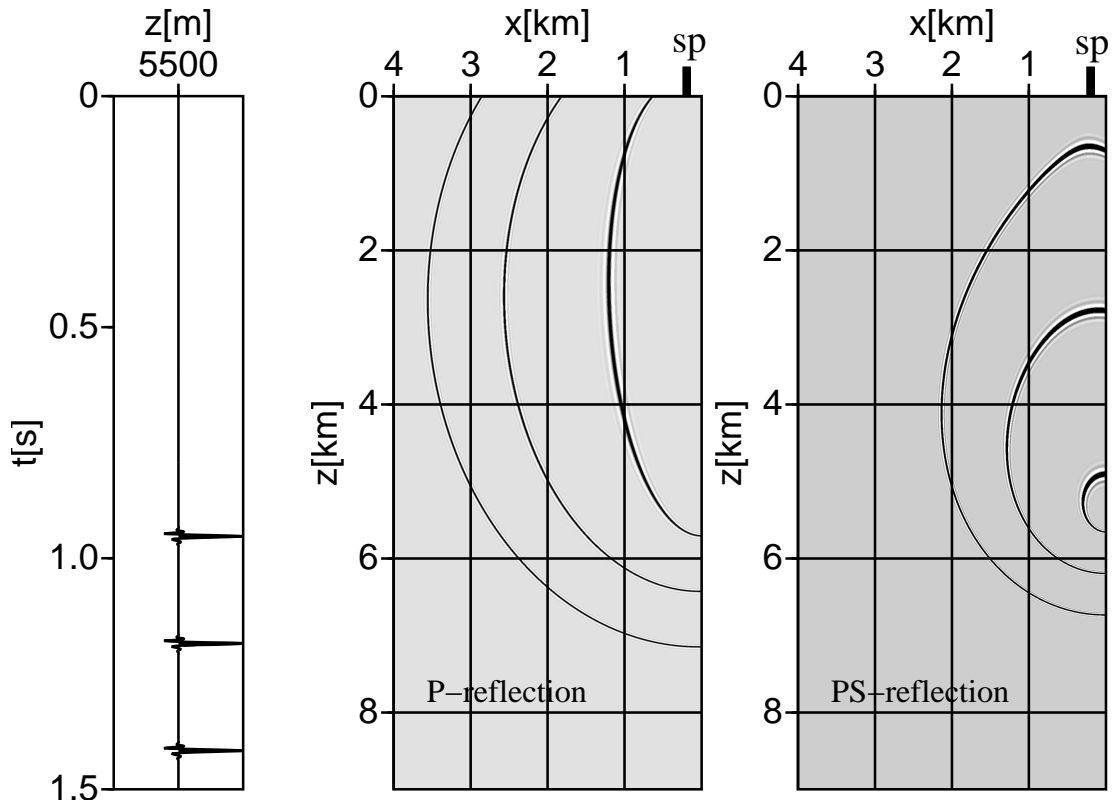


Fig. 6.6: Comparison of certain traveltimes in a seismogram (left) resulting in virtual reflection points in a homogeneous medium for reflected P-waves (center) and P-to-S converted waves (right) recorded at 5500 m depth. The shot point (sp) is located at an offset of 200 m from the borehole. In a scattering environment, rays from offset conversion points can be focused into the borehole at a deeper position, at a later time (after Frank, 2002).

6.1.2 Octave Analysis

The above analysis was also carried out in 4 octaves which cover the whole frequency range from 15-240 Hz (Figure 4.11), discussed here only for the 15 traces stacks. The following figures are shown for the S1 component: 6.7 (15-30 Hz), 6.8 (30-60 Hz), 6.9 (60-120 Hz), and 6.10 (120-240 Hz). Figures 6.11- 6.14 are the corresponding figures of the S2 component. Before stacking, each trace in the horizontal component seismograms, within each octave is normalized with the corresponding amplitude of the incident P-wave filtered in the same octave. This way the conversion amplitude is a measure for the amount of conversion as a function of octave for the whole depth range. The amplitude share of the downward traveling P-wave within each octave, at every sampled depth position, is plotted in Figure 4.12.

The most striking observation is that there is no linear trend in conversion amplitude with frequency range. Whereas the higher two octaves show similar conversion

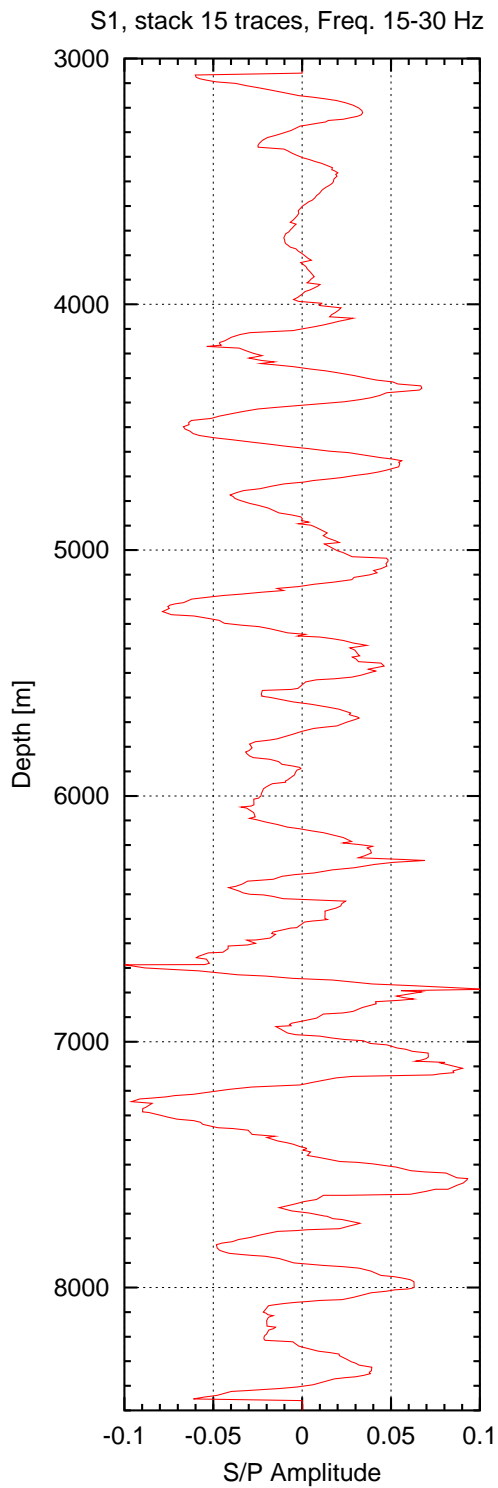


Fig. 6.7: *P-to-S conversion in transmission of the S1 component, stack of 15 traces with a bandwidth of 15-30 Hz.*

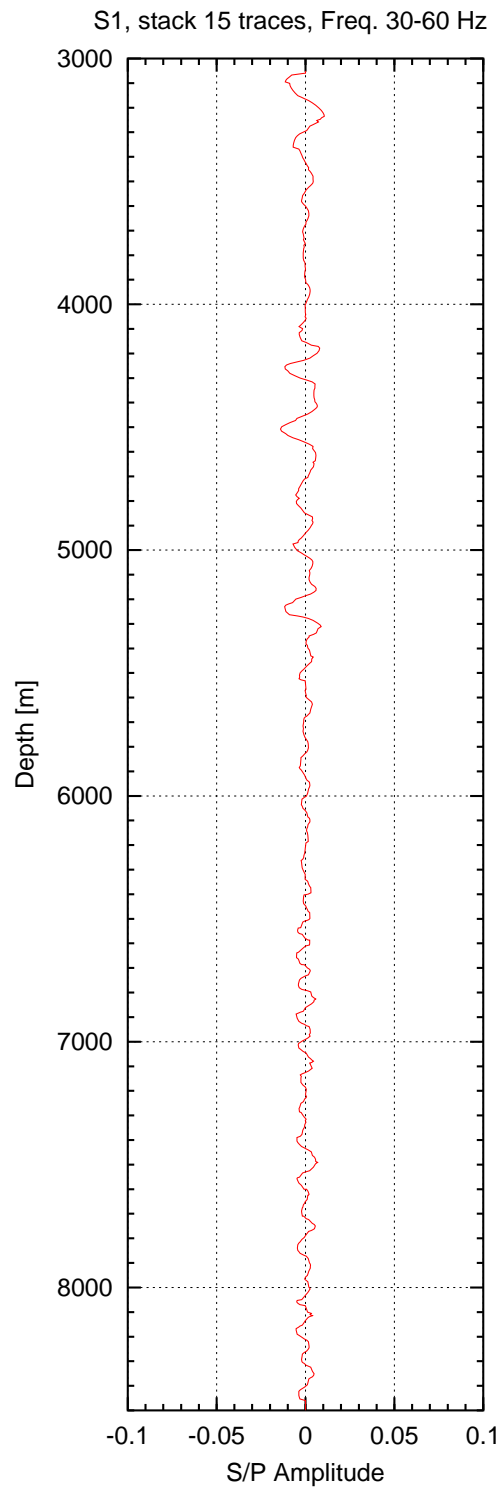


Fig. 6.8: *P-to-S conversion in transmission of the S1 component, stack of 15 traces with a bandwidth of 30-60 Hz.*

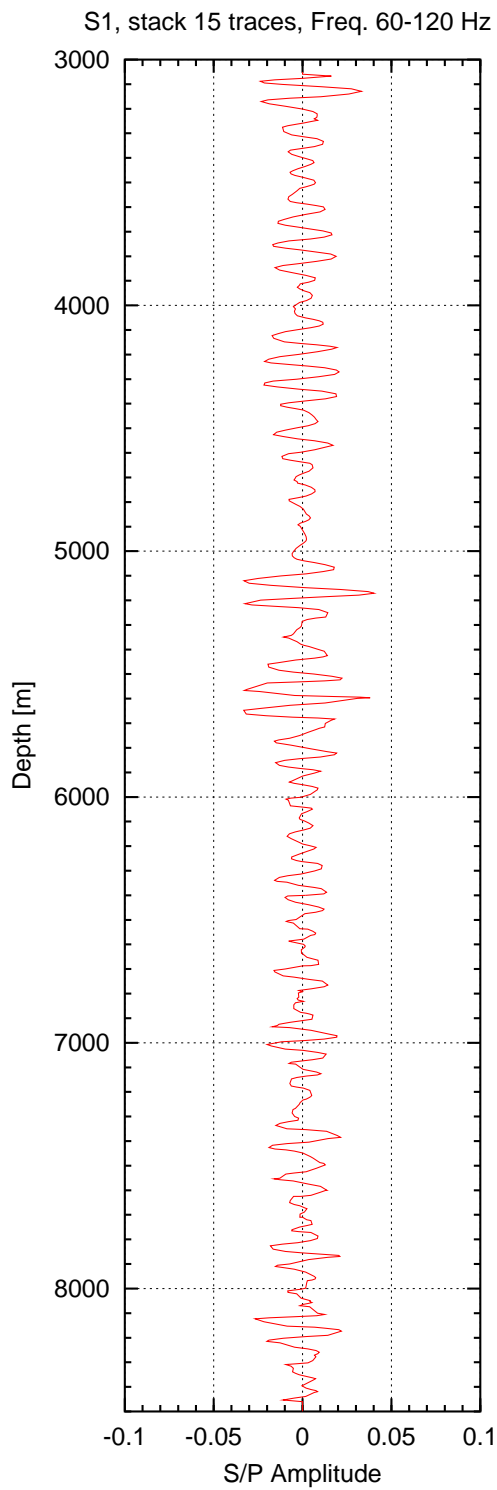


Fig. 6.9: P-to-S conversion in transmission of the S1 component, stack of 15 traces with a bandwidth of 60-120 Hz.

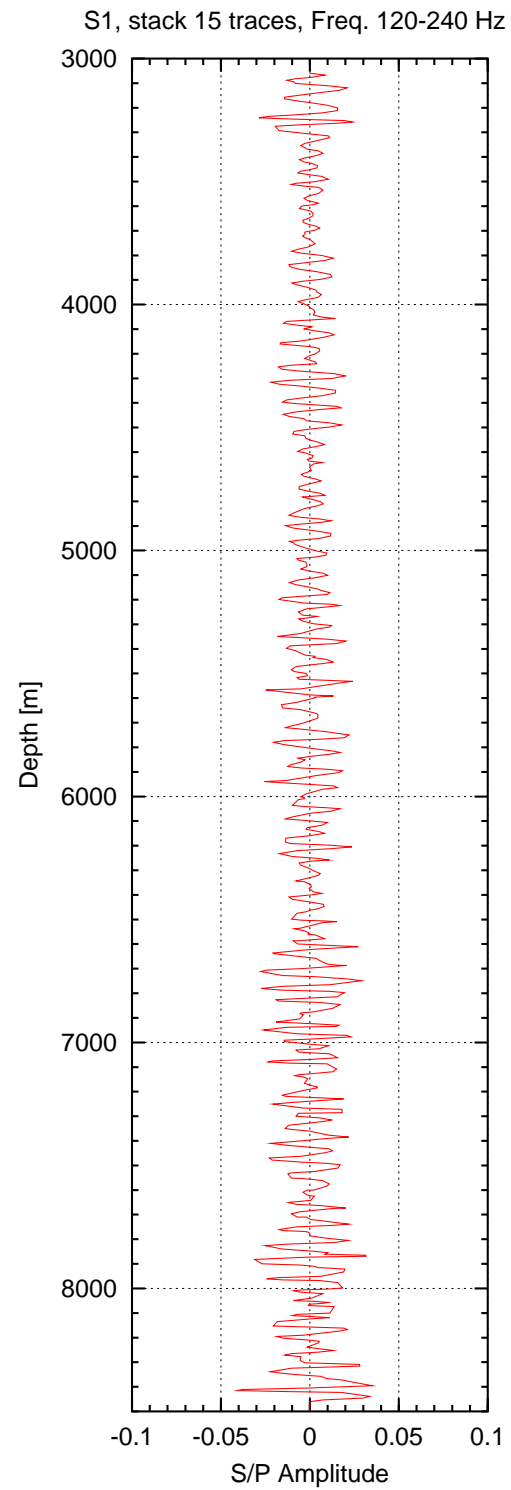


Fig. 6.10: P-to-S conversion in transmission of the S1 component, stack of 15 traces with a bandwidth of 120-240 Hz.

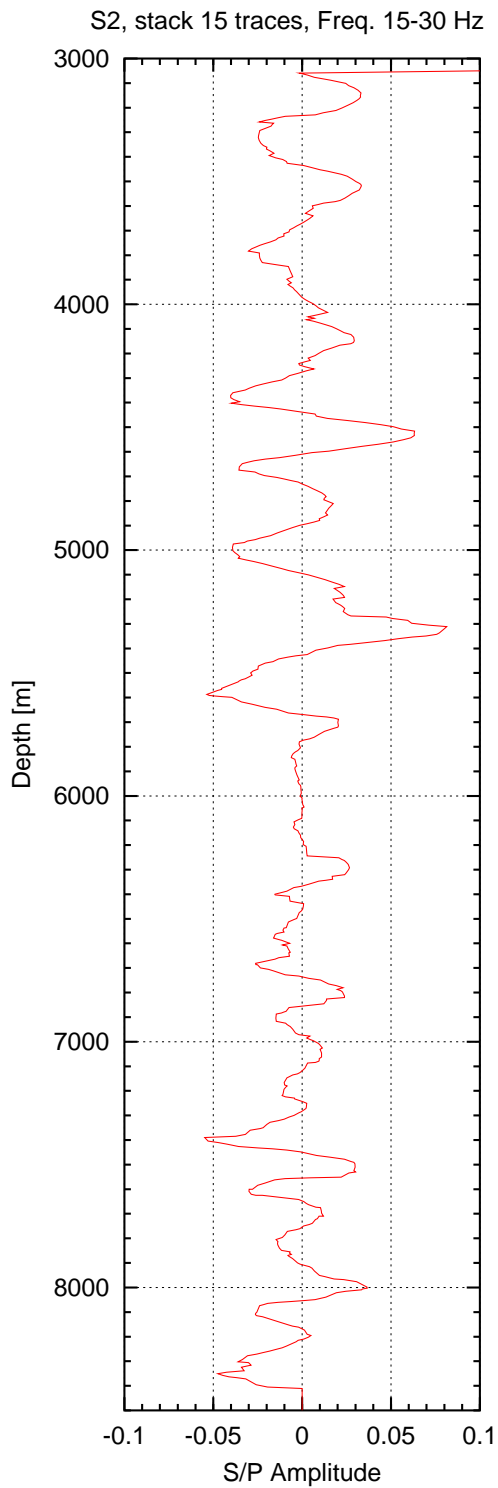


Fig. 6.11: *P-to-S conversion in transmission of the S2 component, stack of 15 traces with a bandwidth of 15-30 Hz.*

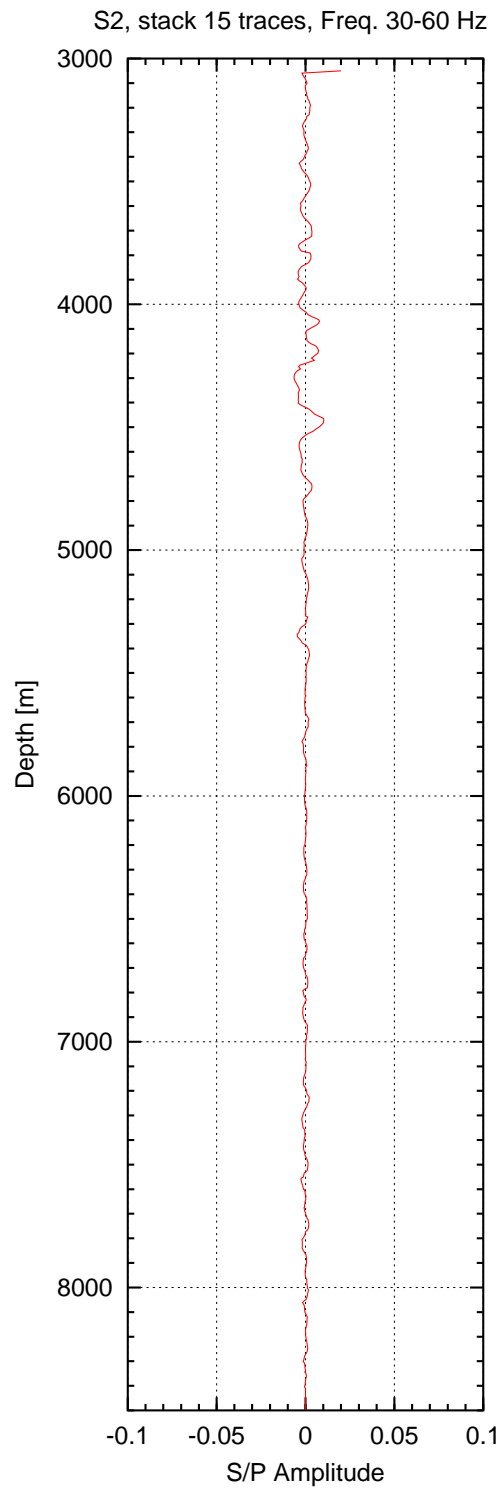


Fig. 6.12: *P-to-S conversion in transmission of the S2 component, stack of 15 traces with a bandwidth of 30-60 Hz.*

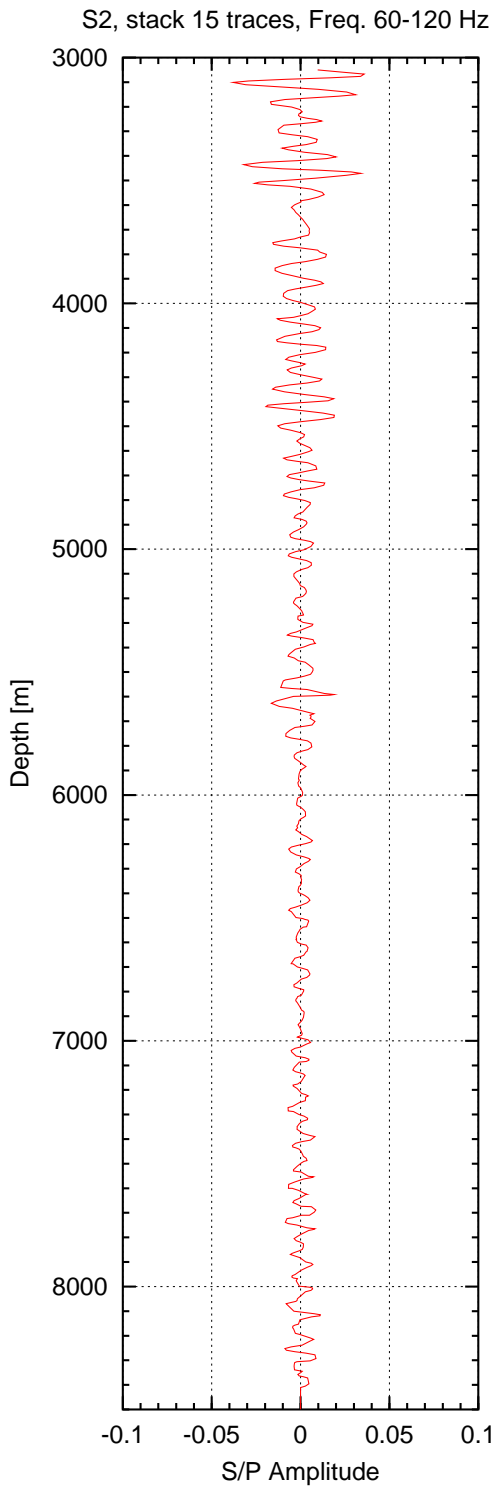


Fig. 6.13: *P-to-S conversion in transmission of the S2 component, stack of 15 traces with a bandwidth of 60-120 Hz.*

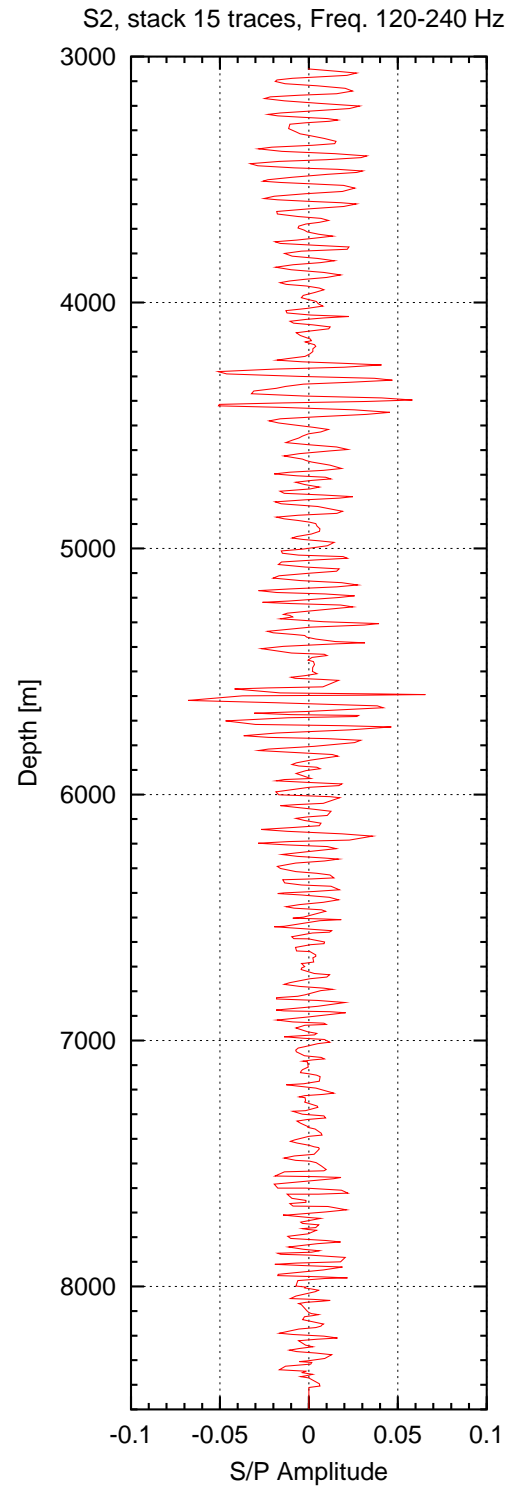


Fig. 6.14: *P-to-S conversion in transmission of the S2 component, stack of 15 traces with a bandwidth of 120-240 Hz.*

amplitudes of up to 7%, the lowest part of the spectrum (15-30 Hz) shows stronger conversions of up to 10%. Surprisingly, for the intermediate octave (30-60 Hz) the crust seems almost transparent, with respect to conversion. Here, the conversion amplitudes do not reach beyond 1.5%. This is basically in agreement with the observation that the share of this octave in the downward traveling P-wave increases with depth (Figure 4.12) and might explain why most of the crustal reflection seismic studies use a similar frequency range.

The 50 Hz notch filter that had to be applied on the seismic data in this analysis was first thought to be responsible for the amplitude drop in the intermediate frequency range. But because this filter had been applied on both, the nursing signal data and the converted wave data, there should be no amplitude influence. Also, synthetic models (see Chapter 8) show a similar behavior. Therefore, the frequency dependency of the conversion amplitude determined here, can be regarded as reliable.

A surprise to some extent is the strong sensitivity of the 15-30 Hz octave to the Franconian Lineament fault zone in the S1 component with 15 traces stacked. Here the strongest amplitudes are present in this conversion log, although this zone is not detectable in the full spectrum analysis. This is not only true for the upper limit of this lineament, conversions rather extend down to the lower limit of this zone at ~ 7.3 km (de Wall *et al.*, 1994).

The reason could be the larger Fresnel zone of lower frequency waves of about 900 m radius at that depth and supports the observation of stronger conversions at a certain distance from the borehole, as stated before. Although the wavelength is rather large, the amplitudes at 6.7, 6.8 km, and 7.25 km are very sharp and the negative amplitude at 7.25 km depth even pinpoints at the fault zone there (Figure 6.5). The S2 component in the same octave does not show any large onsets within this fault zone. This is consistent with the smaller conversion amplitude in the full spectrum of the 75 traces stack of the S2 component. However, it is a surprise since the S2 component oscillation direction should be rather sensitive for the detection of the SE1 reflector, or converter, in this case. Even if the frequency sensitivity of the S1 component was that strong compared to the S2 component, at least in the higher octaves there should be some indications of this zone in the S2 component. There is none, though. Even in the highest octave the S1 component shows slightly higher values than the S2 component.

One explanation could be a different fault zone geometry at some offset. But this would also have an impact on the azimuthal orientation of the PP-reflection of this structure. Basically, the latter can only be observed on the S2 component, which is in correlation with basically all the other observations collected during the years of research at this site. Therefore, a major geometry change of the SE1 zone at some distance from the borehole is out of question.

On the other hand, a complex fault zone with different minor branches might be a possibility to explain this amplitude behavior. In this case, reflected waves would not emerge from the structure but converted waves could. This structure would probably need to be very complicated. However, in this tectonic environment this is not unusual.

Another possible explanation would be a different orientation of the S1 oscillation

direction with respect to the strike of the SE1 zone. For this, no indications exist either. So, whatever reason for the strange behavior of the plots, the most important observation is the relatively strong conversion within the low frequency range compared with the small conversion in the adjacent frequency octave.

6.2 Envelope Stack

The question remains whether destructive interference partly veils the conversion amplitudes during the stacking process. To analyze this, the envelopes of the data were processed the same way as the true phase data.

6.2.1 Full Spectrum Analysis

The resulting logs of the 15 traces stacks are shown in Figures 6.15 (S1 component) and 6.16 (S2 component) with the spectrum 15-240 Hz. Stacks with 75 traces are shown in Figures 6.17 (S1 component) and 6.18 (S2 component).

The main difference compared with the corresponding true phase stacks is the amplitude level. This is especially true for the comparison of the 75 traces stacks. Although the difference in the number of stacked traces does not change the resulting amplitude level in the envelope stacks, this level drops with the higher number of stacked traces in the true phase stacks. The low level amplitudes are about twice as high in the envelope stacks for the stack of 15 traces and about 2.5 times as high for 75 traces. The high amplitudes do not differ much except for some peaks. So, basically destructive interference influences the true phase stacks.

One surprise is the disappearance of the high conversion amplitude at 3.1 km depth in the 15 traces envelope stack of the S1 component compared with the phase preserving stack. This observation remains unexplained, because in the case of envelope stacks destructive interference cannot be the reason. Another surprise is the existence of a peak at 4.85 km depth in both envelope components. In this case destructive interference can be the reason for its nonexistence in the phase preserving stacks. About 70 m below this depth an about 50 m thick alternating sequence is present in the lithological profile (Figure 6.5). The lower limit of this sequence can only be observed on the second component. Therefore, it is not clear whether this sequence is the reason for the existence of the 'new' peaks or possibly two fluid entry regions at about 4.8 km depth (Figure 6.5).

A generally interesting observation is a possible correlation of many peaks with open fissures or fluid inflows, because in some cases lithological contrasts are not present (at least in the simplified profile). An example might be the depth position ~ 5.05 km, because here the inflow is very exposed within a metabasic rock unit and without open fissures nearby. The S1 component 15 traces envelope stack shows a small peak here. So, even if no open fissures exist, the existence of water or a certain fluid inflow indicate a weakening of the rock matrix, with subsequent parameter

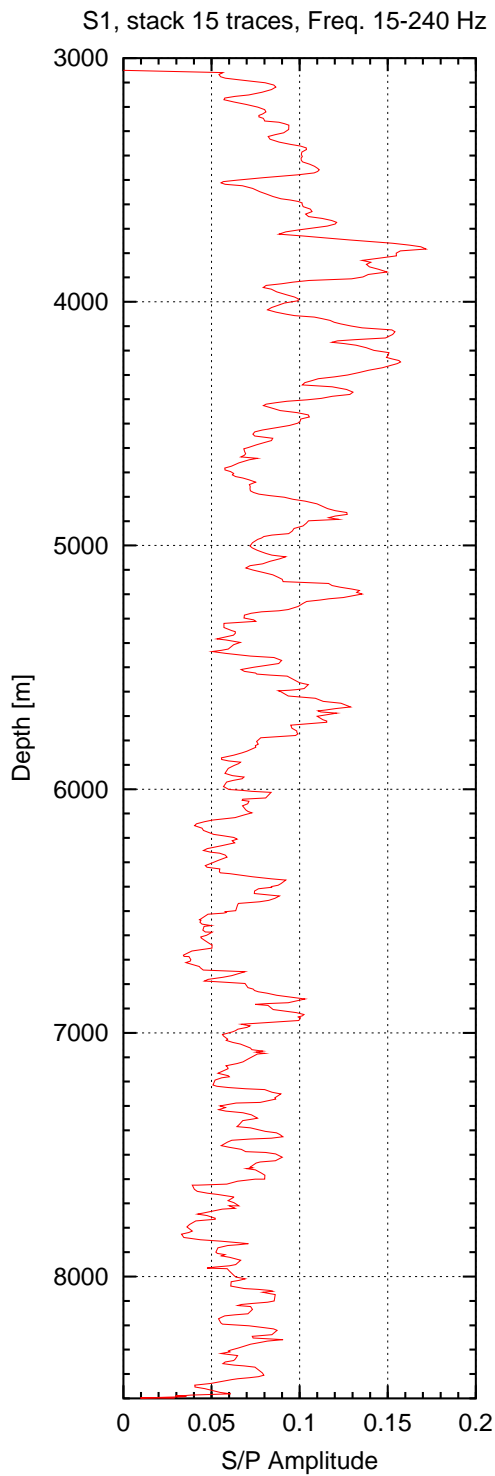


Fig. 6.15: *P-to-S conversion in transmission of the S1 component, stack of the envelopes of 15 traces with a bandwidth of 15-240 Hz.*

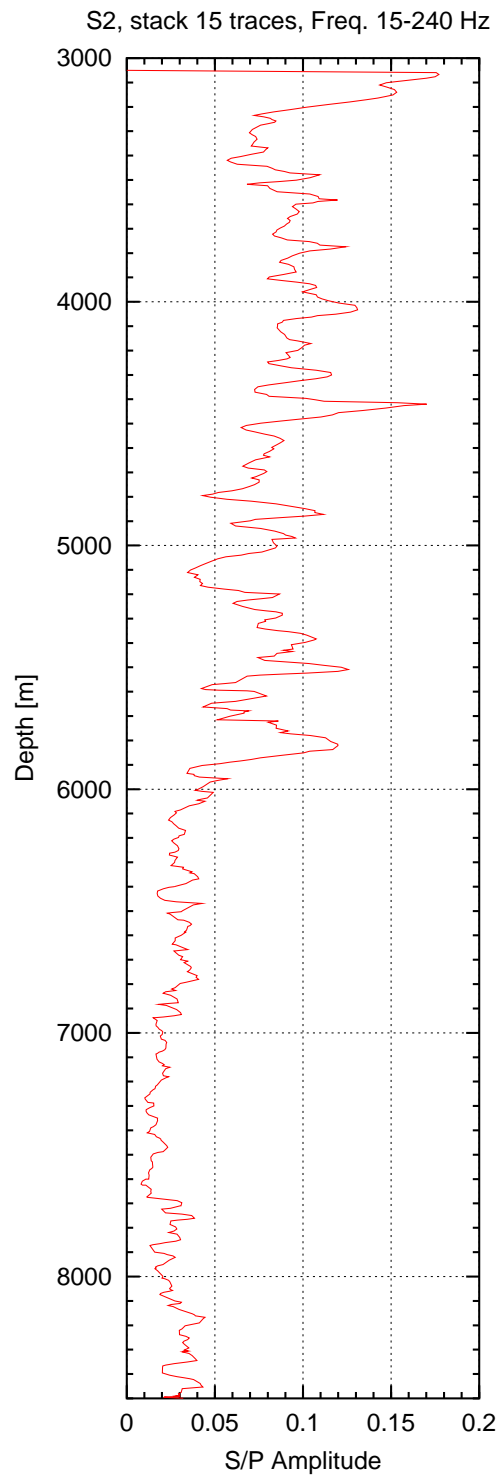


Fig. 6.16: *P-to-S conversion in transmission of the S2 component, stack of the envelopes of 15 traces with a bandwidth of 15-240 Hz.*

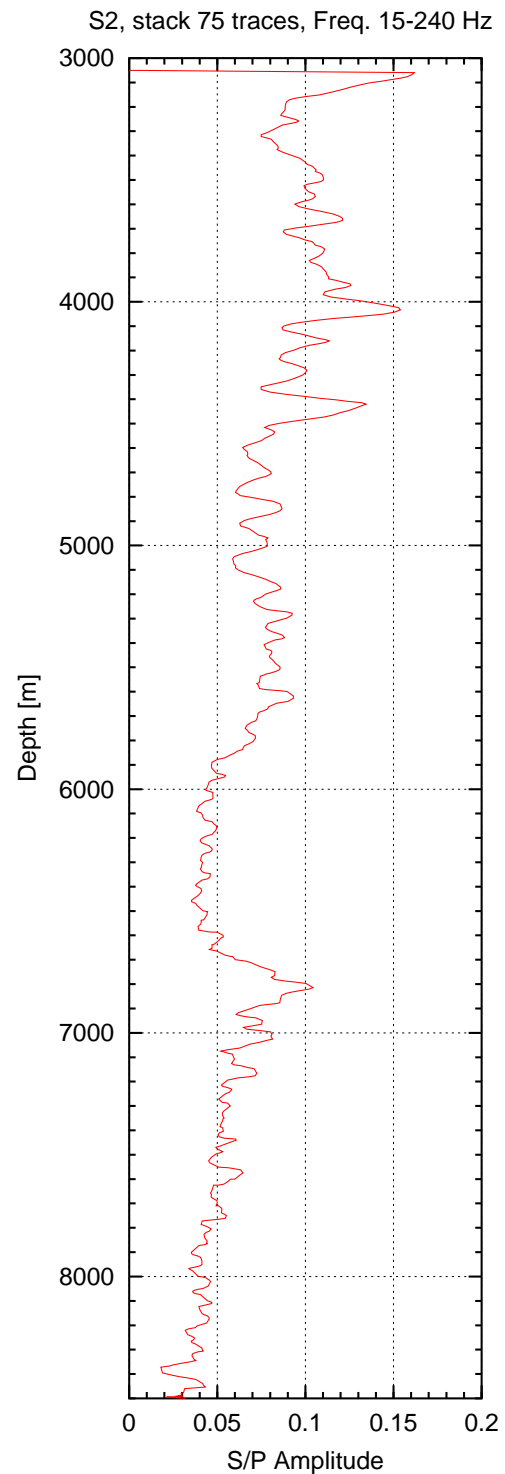
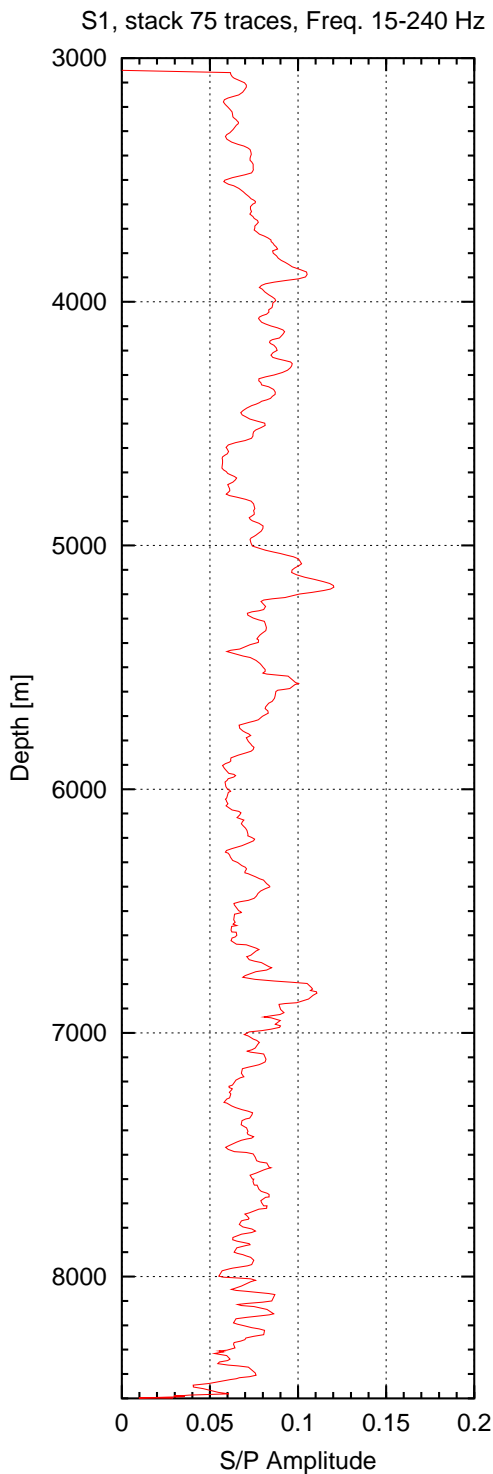


Fig. 6.17: *P-to-S conversion in transmission of the S1 component, stack of the envelopes of 75 traces with a bandwidth of 15-240 Hz.*

Fig. 6.18: *P-to-S conversion in transmission of the S2 component, stack of the envelopes of 75 traces with a bandwidth of 15-240 Hz.*

changes, probably detectable in the conversion log. In a most complicated environment like at the KTB site, it is however, difficult to discriminate all the different influences on the conversion of seismic waves. So, this small peak is just an indication and should not be taken as the final proof.

6.2.2 Octave Analysis

The octave analysis of the envelope stacks of the S1 component are shown in Figs. 6.19-6.22. The basic observation is that the envelope stacks show the same frequency behavior as the true phase stacks.

Unusual high amplitude peaks are apparent in the low frequency octave. At about 6.3 and 6.8 km depth these peaks are very prominent. It seems, the amplitude relation to the nursing P-wave signal might be incorrect, for whatever reason. If this is the case the unusual amplitudes of the true phase functions could result from amplitude normalizations and would be artificial.

In the high frequency octave the lower most part of the borehole shows relatively strong conversions compared with the upper part. This correlates with the corresponding true phase image (Figure 6.10) and is mainly responsible for the higher apparent spatial frequency in the full spectrum functions of the S1 component. Small scale variations in the elastic parameters should be responsible for this behavior. Especially in the lowest part of the borehole the crack orientation is normal to the foliation orientation probably resulting in complex wave behavior.

6.3 Summary

The analysis of the P-to-S conversion in transmission log was carried out comparing phase preserving stacks with envelope stacks for the full spectrum and its 4 octaves and with a different number of traces in the stacks.

The basic observations and interpretations are: (1) The less number of traces stacked the more distinct and higher the peak amplitudes. This is valid no matter whether the phase information is still preserved in the traces or not. The reason for this is the averaging effect of a high number of traces due to the normalization of the stack amplitude with the number of traces. (2) The more number of traces stacked the more influence from distant conversion points. (3) The envelope stacks show slightly higher peak amplitudes because without the phase information destructive interference cannot become effective. The small difference in amplitude between envelope stacks and true phase stacks are surprising, though, indicating that the true phase information is reliable. (4) Maximum amplitudes for the full spectrum stacks are as high as 17% and for large parts of the borehole they are well above 5 %. (5) Octave separated analysis shows surprising differences in amplitude behavior for the relation between the nursing P-wave and the converted S-wave amplitude, both of the same octave. This is true for the phase preserving analysis as well as for the envelope analysis. The low frequency

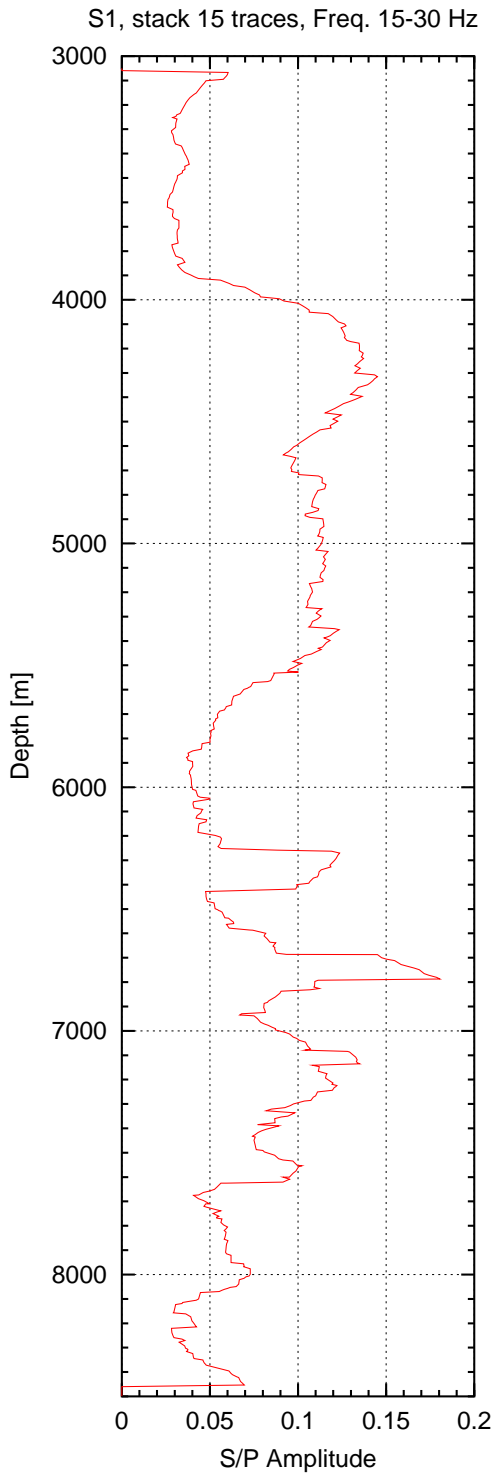


Fig. 6.19: *P-to-S conversion in transmission of the S1 component, stack of the envelopes of 15 traces with a bandwidth of 15-30 Hz.*

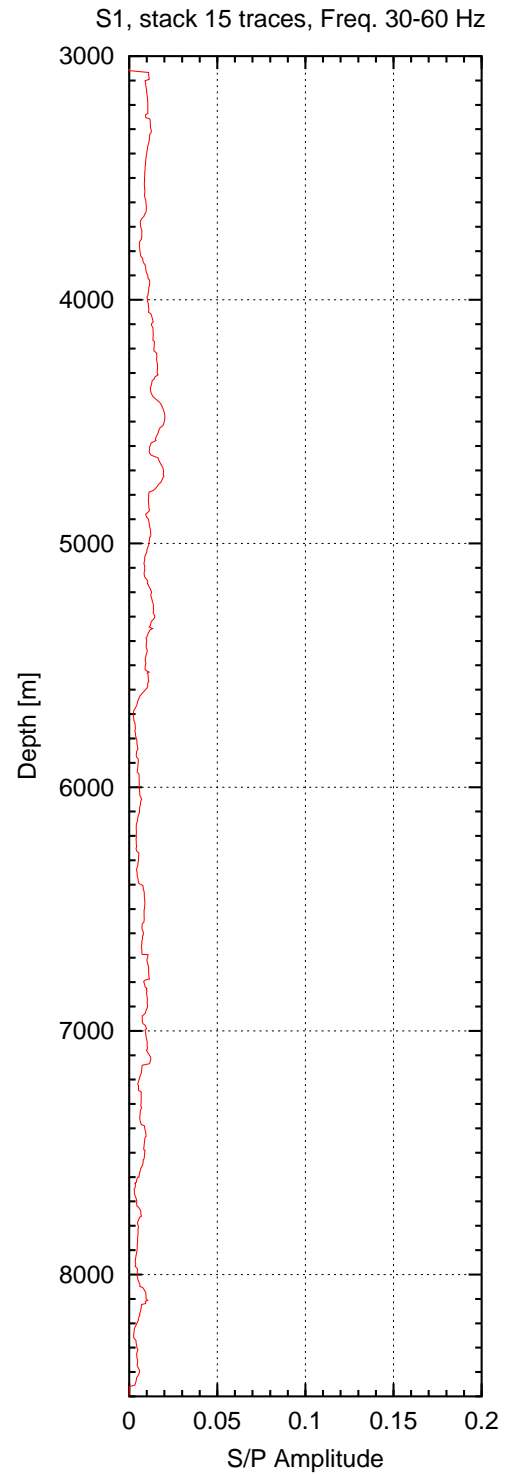


Fig. 6.20: *P-to-S conversion in transmission of the S1 component, stack of the envelopes of 15 traces with a bandwidth of 30-60 Hz.*

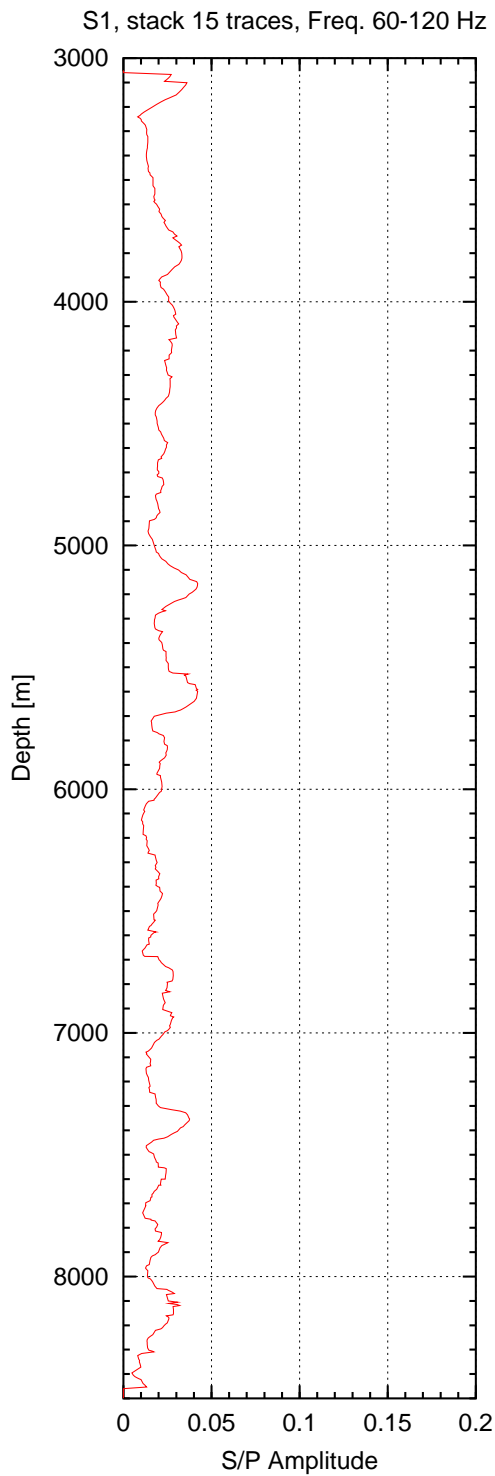


Fig. 6.21: *P-to-S conversion in transmission of the S1 component, stack of the envelopes of 15 traces with a bandwidth of 60-120 Hz.*

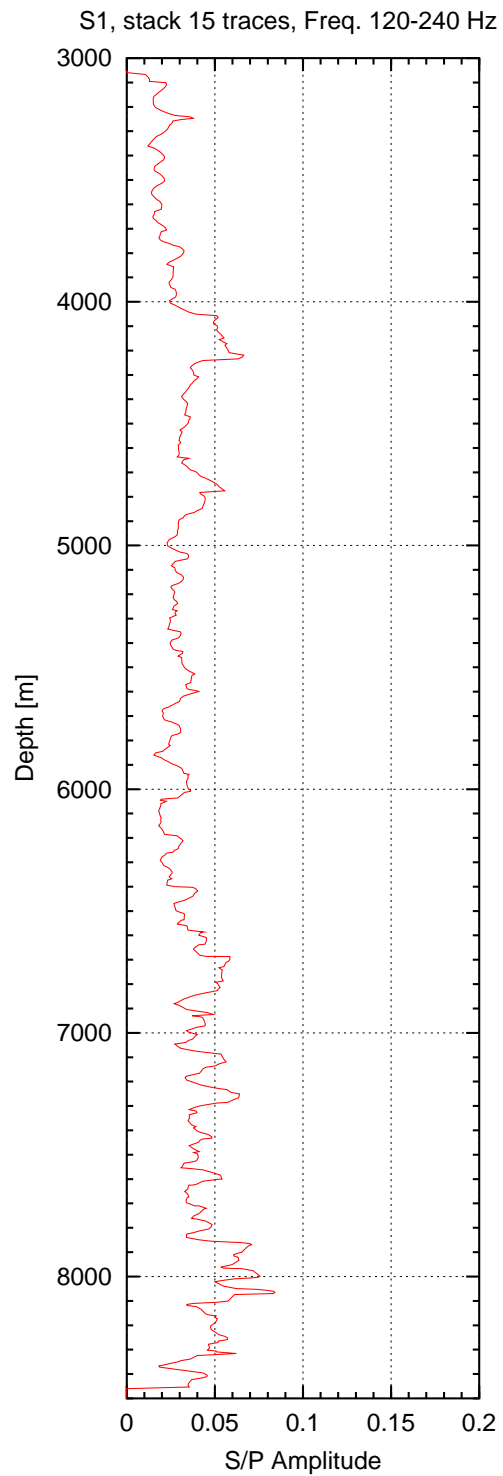


Fig. 6.22: *P-to-S conversion in transmission of the S1 component, stack of the envelopes of 15 traces with a bandwidth of 120-240 Hz.*

octave (15-30 Hz) amplitudes show about 10 times the amplitudes of the neighbouring octave, about 3-4 times the amplitude of the octave from 60-120 Hz and about 3 times that of the highest analyzed octave from 120-240 Hz. This is consistent for the whole depth range, considered in this thesis.

Basically, the destructive interference in the true phase stacks compared with the envelope stacks is evident. But since the polarity information is of high importance the true phase processing should always be carried along for the interpretation.

Chapter 7

Analytical Calculations

In the previous chapter, P-to-S converted waves in transmission amplitudes versus depth observed in the measured VSP data were discussed. Converted amplitudes as high as about 17% of the incident P-wave were found in certain locations. The amplitudes in the field data are the result of the convolution of the input shot signal with the crustal parameters velocities and density. These parameters are influenced by cracks and fissures present in the drillhole. In order to quantify their influence, the field data amplitudes were compared with analytical calculations of the Zoeppritz equations, for (1) simulated and (2) the measured VSP velocities in combination with an additional density profile. This could be carried out in detail because the KTB database offers independent information on petrophysical parameters found in the drillholes. The results of the different calculations and their validity in comparison to the field data will be discussed in this chapter. The basic idea is that the difference between model and field data is the result of the influence of cracks and fissures.

The first comparison was carried out between the in situ conversion amplitudes and conversion coefficients calculated for a simulated crack-free isotropic rock matrix. This rock matrix was inverted from cuttings analysis as well as x-ray diffraction and laboratory velocity and density measurements on cores, for each of the main mineral rock components, with respect to in situ temperature and pressure (Rabbel *et al.*, 2001). The resulting simulated P- and S-wave velocities are depicted as red lines in Figure 7.1, together with the weight percentage of each of the considered minerals along the borehole. Because of the isotropy of the model, the two simulated S-wave velocities do not differ as opposed to the ones from the Deep VSP 1999, indicated in blue for the probed depth section 3.0-8.5 km. These measured VSP velocities were the other basis for conversion coefficient calculations along the KTB main hole, in combination with the density log from the KTB database. The question is, whether the use of the measured velocities results in similar conversion amplitude values, as determined in the field data, discussed in the previous chapter, or rather results in values of the order determined for the simulated velocities.

For plotting, a median filter was applied to the measured velocities in Figure 7.1. The median filter parameters used in the conversion coefficient calculations, were 300

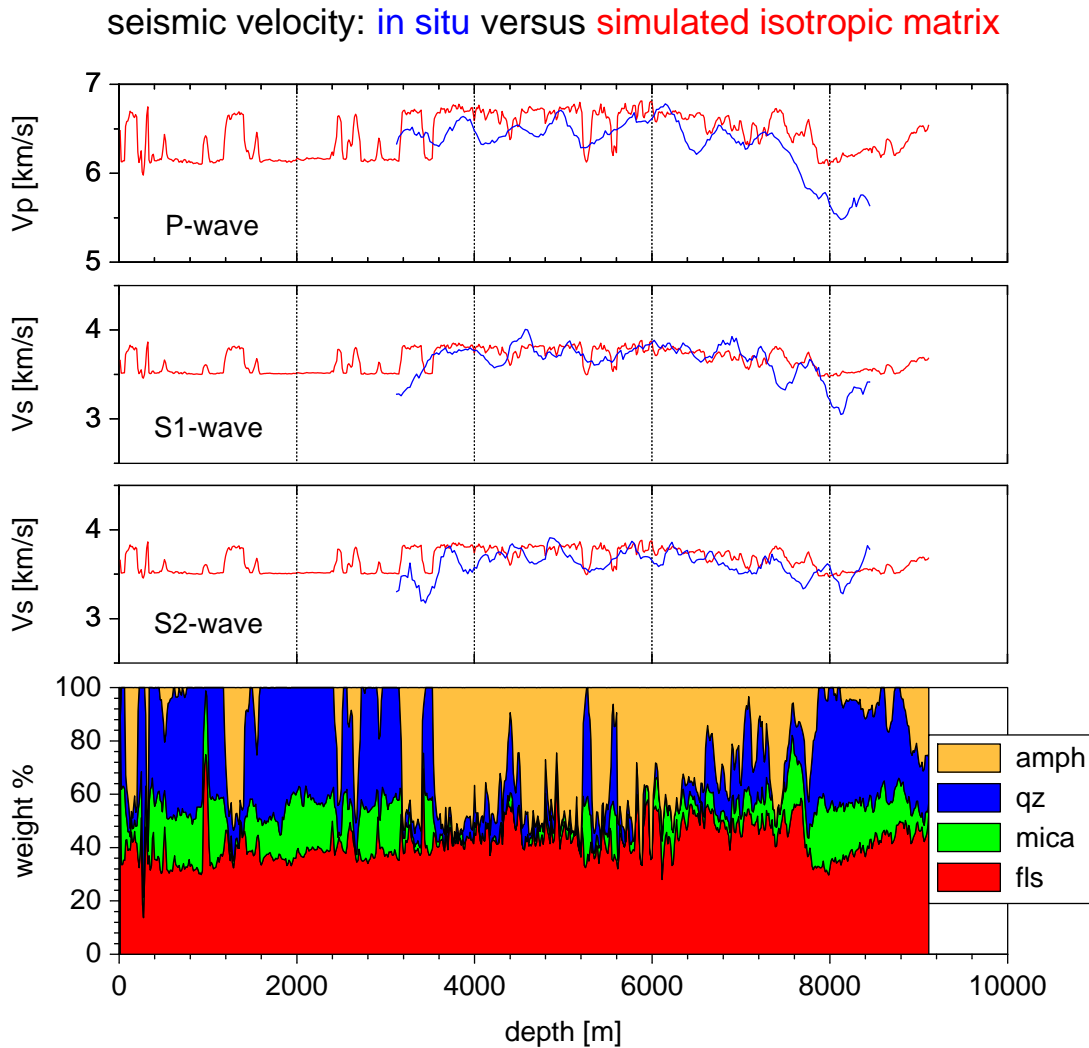


Fig. 7.1: Velocity model along the KTB main hole inverted from cuttings and core analysis for the four main mineral rock components (amph - amphibolite, qz - quartz, mica - mica, and fs - feldspar). The simulated velocities are inverted for a crack-free and isotropic rock matrix (red). The measured P- and S-wave velocities are indicated in blue for the depth range 3.0-8.5 km, smoothed with a median filter of 400 m window length and a window increment of 25 m (after [Rabbel et al., 2001](#)).

m window length and 25 m increment. Smoothing of the in situ velocity values was necessary to account for probable velocity errors in the raw data. Velocity errors can either result from an unknown error in the depth values of the geophone sonde during the experiment or from S-wave first break picking errors resulting from signal identification problems in the recorded VSP data. Picking had only been possible after the application of a low pass filter ([Fischer, 2000](#)). Therefore, the smoothed velocity contrasts are less distinct as the simulated ones, especially in places with high parameter contrasts like at the gneiss section in ~ 5250 m depth or the alternating sequence at ~ 5600 m (Figure 7.1). However, the measured values show larger variations.

7.1 Wave Conversion

A means to calculate conversion coefficients for large scale structures are the Zoeppritz equations (see Chapter 3). The equations are only valid for an incident *plane* P-wave and emitted waves, generated at a first order interface of large extent. For incidence angles not equal to zero, the coefficients can be calculated for P-waves in transmission and reflection and for P-to-S conversion in transmission and reflection. In situ the condition of a plane wave is basically fulfilled, because the Deep VSP 1999 profile starts at 3000 m depth. The second condition - interfaces of large extent - is of course not realistic in situ. Therefore, these calculations can only serve as a first order approach.

7.1.1 Simulated Isotropic Rock Matrix Velocities

For the simulated velocity-depth profiles shown in Figure 7.1 and corresponding density data, reflection-, transmission- and conversion coefficients were computed. This was carried out for two models, differing only in the foliation dip of the simulated layers, to determine the influence of the dip on the coefficients.

The simple model consists of layers with a foliation dip angle of 60° , being about the average within the KTB boreholes. The calculated results are depicted in Figure 7.2. Apparently, the dominant waves - apart from the P-wave in transmission not shown here - are the reflected P-wave (green) and the PS converted wave in transmission (red). They show about the same coefficient values of up to more than 5% but with opposite sign. This is only about 1/3 of the in situ conversion amplitudes. The PS converted wave in reflection (blue) is very small with values mostly less than 1%.

In the field data, Frank (2002) found average P-to-S reflection coefficients of about 20% for some parts of the SE1 reflector. These are exceptions, though. Basically, there are not many onsets in the field data that can be related to P-to-S conversion in reflection, basically confirming the small values found in the calculated model.

In a second, more realistic model, the in situ dip information from the KTB database is considered (Figure 7.3). Basically, the P-wave reflection coefficients are still about as strong as the P-to-S conversion in transmission coefficients in many places, but there are some differences especially in the lower part of the borehole. This is the region of the Franconian Lineament fault zone.

A more direct comparison of this dip angle influence is possible if the results of each of the two stronger wave modes, i.e., the P-to-S converted wave in transmission and the reflected P-wave, are plotted in separate figures: Figure 7.4 shows the absolute conversion coefficients of the PS converted wave resulting from the 60° model on top of the result from the in situ dipping foliation model. Figure 7.5 shows the same for the reflected P-wave. It is evident that the difference between a model with a foliation dip of 60° and a model with the in situ foliation dip is small for the PS converted waves in transmission. They do not seem to be influenced much by the foliation dip, as opposed to the reflected P-wave coefficients.

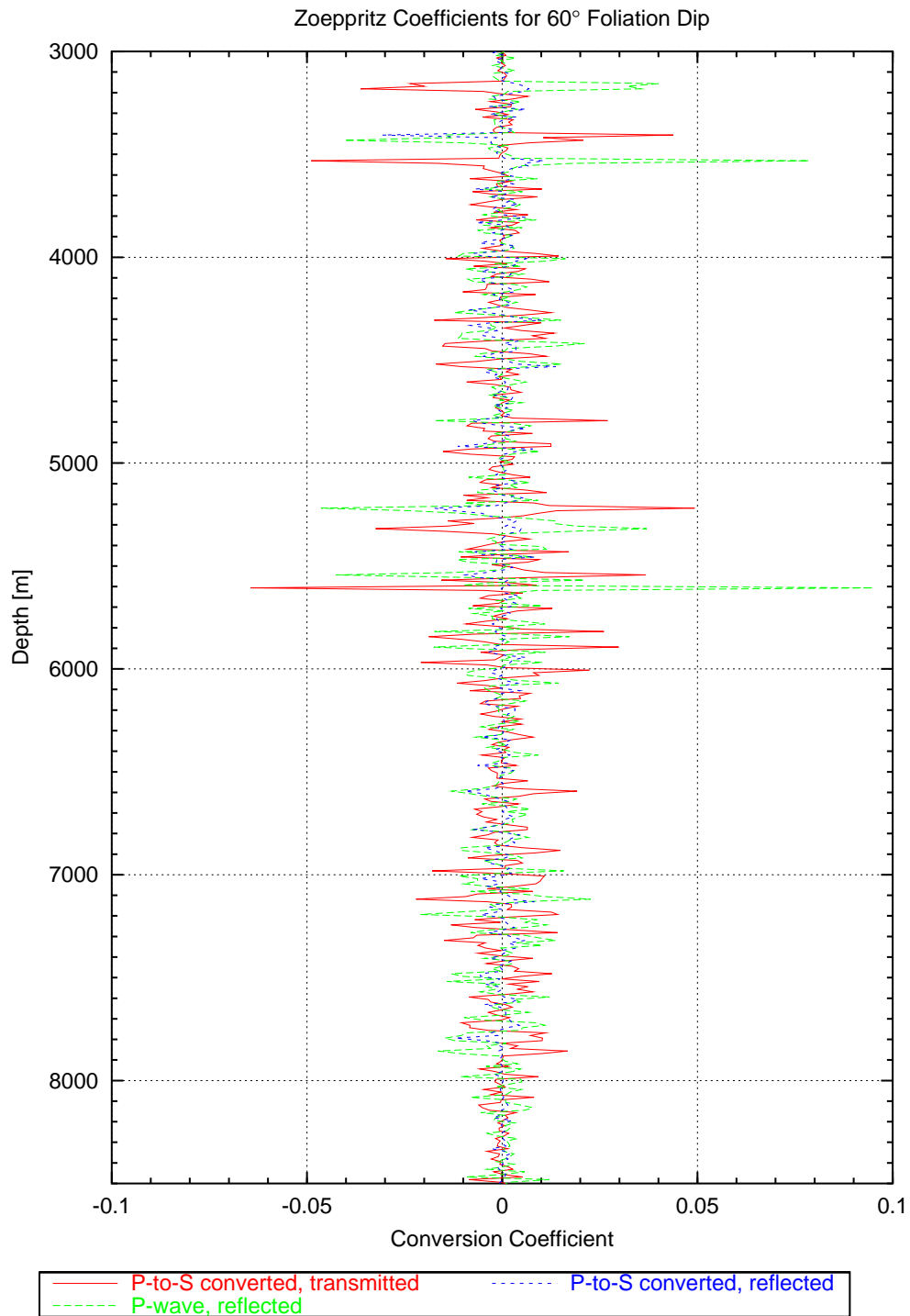


Fig. 7.2: Conversion coefficients for P-to-S conversion in transmission (red), P-to-S conversion in reflection (blue), and compressional wave in reflection (green), for the simulated velocity and density profile along the KTB main hole (Figure 7.1) and a virtual foliation dip of 60°.

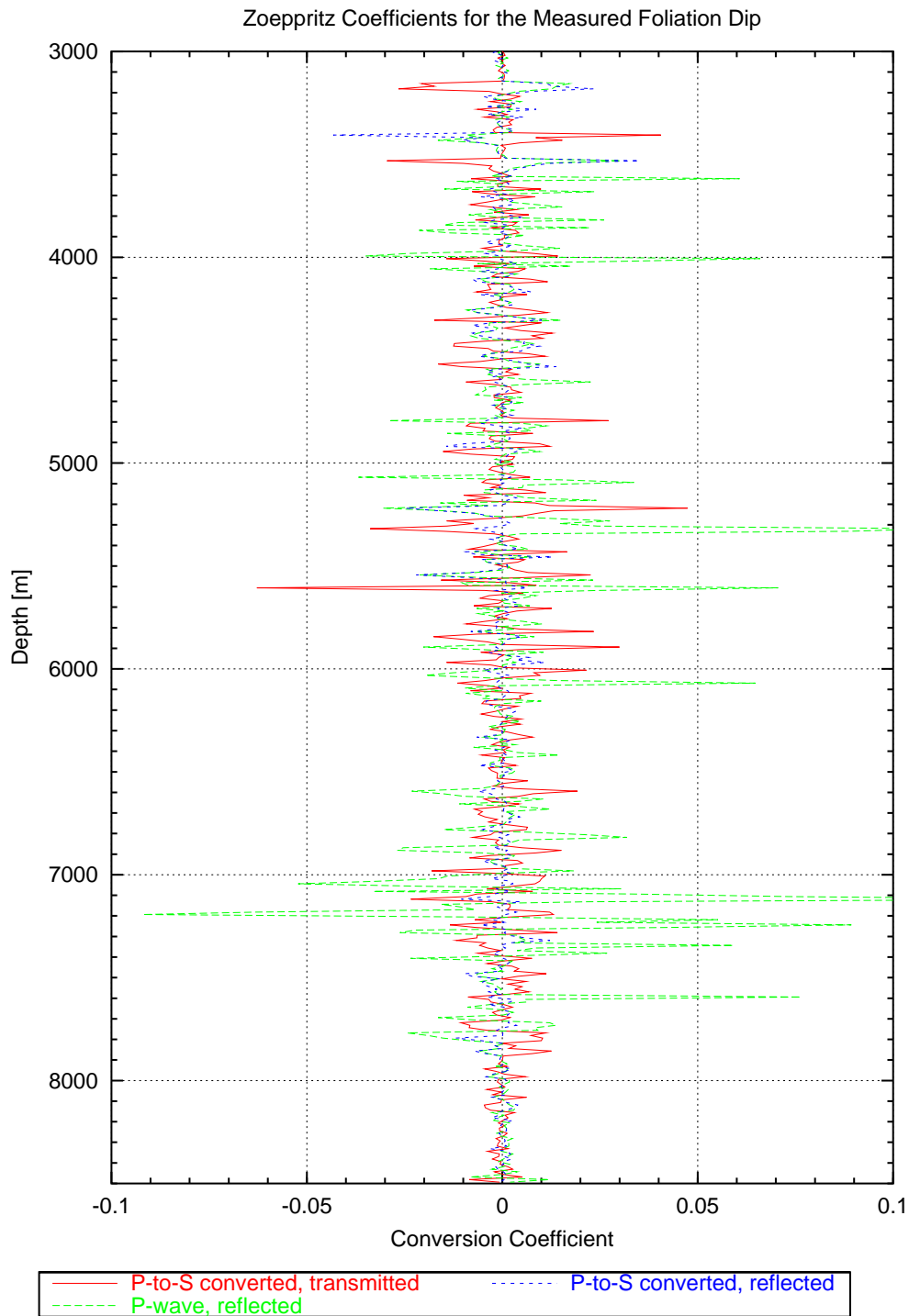


Fig. 7.3: Conversion coefficients for P-to-S conversion in transmission (red), P-to-S conversion in reflection (blue), and compressional wave in reflection (green), for the simulated velocity and density profile along the KTB main hole (Figure 7.1) and the in situ foliation dip.

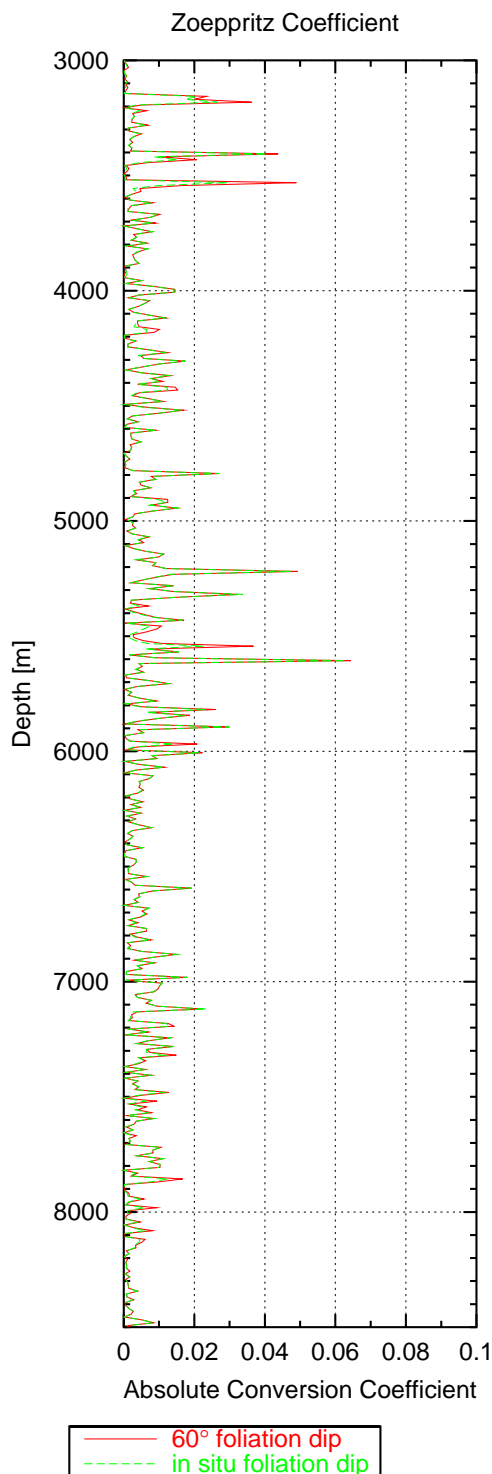


Fig. 7.4: Absolute conversion coefficients for P-to-S conversion in transmission for a virtual foliation dip of 60° (red) vs. the in situ foliation dip.

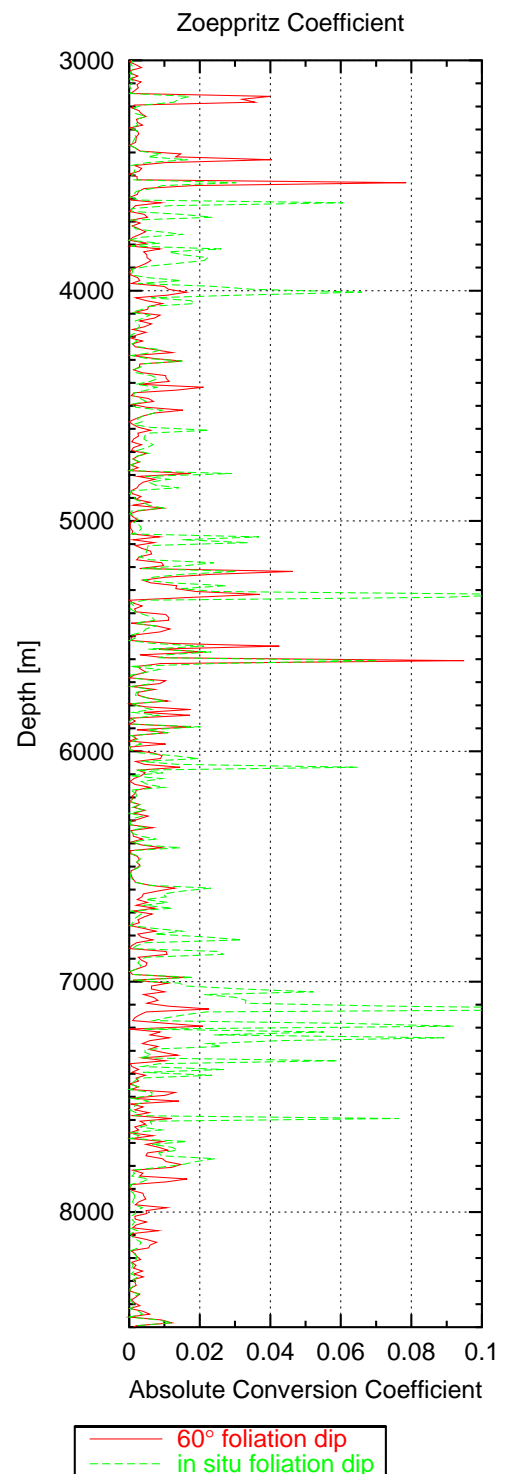


Fig. 7.5: Absolute reflection coefficient for the reflected P-wave for a virtual foliation dip of 60° (red) vs. the in situ foliation dip.

upper : lower parameter	Contrast 1	Contrast 2	Contrast 3	Contrast 4
$V_{p1} : V_{p2}$ [m/s]	6713 : 6513	6168 : 6507	6337 : 6215	6212 : 6220
$V_{s1} : V_{s2}$ [m/s]	3825 : 3658	3513 : 3695	3598 : 3547	3525 : 3529
$\rho_1 : \rho_2$ [kg/m ³]	2917 : 2756	2707 : 2795	2932 : 2857	2785 : 2785

Tab. 7.1: Velocity- and density contrasts chosen from Figure 7.1, used for the determination of P-to-S conversion coefficients and P-wave reflection coefficients with respect to the incident wave angle in Figures 7.6 and 7.7.

To analyze the dip angle dependency in more detail coefficients were calculated for the four chosen velocity and density contrasts shown in Table 7.1, which are derived from the simulated isotropic rock matrix. In this case the P-to-S conversion coefficients in transmission were calculated as a function of the *incident ray angle* (Figure 7.6). In a crack free medium the maximum conversion coefficient of about 6% is reached at an incident ray angle of $\sim 70^\circ - 80^\circ$ from the normal of the interface. This represents one of the stronger conversions. The small variability of the converted wave conversion coefficient between $\sim 45^\circ - 80^\circ$ is evident. In fact, in this range this relation can almost be called a plateau. Thus, any angle larger than $\sim 45^\circ$ and smaller than $\sim 80^\circ$ - which

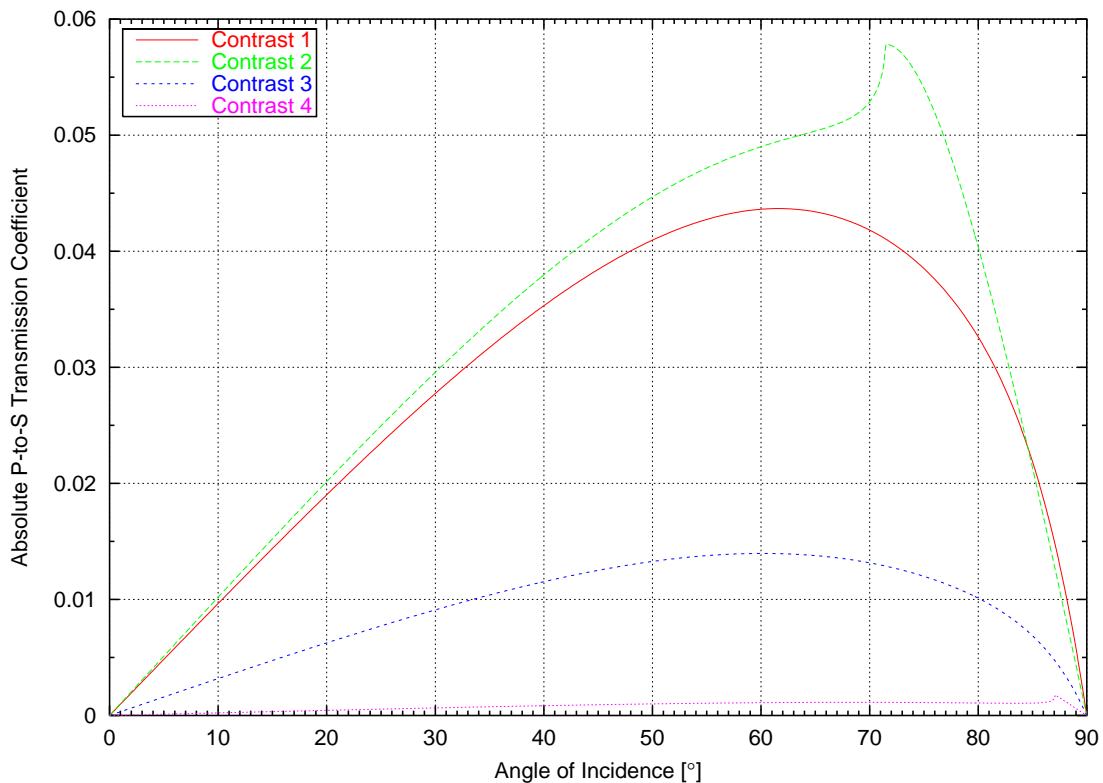


Fig. 7.6: Absolute conversion coefficients as function of the incident ray angle for a P-to-S converted wave in transmission. Four velocity and density contrasts (Table 7.1) are calculated as examples. For rock-rock contrasts the highest values are about 6%. The values do not vary much between $\sim 45^\circ - 80^\circ$ incident ray angle.

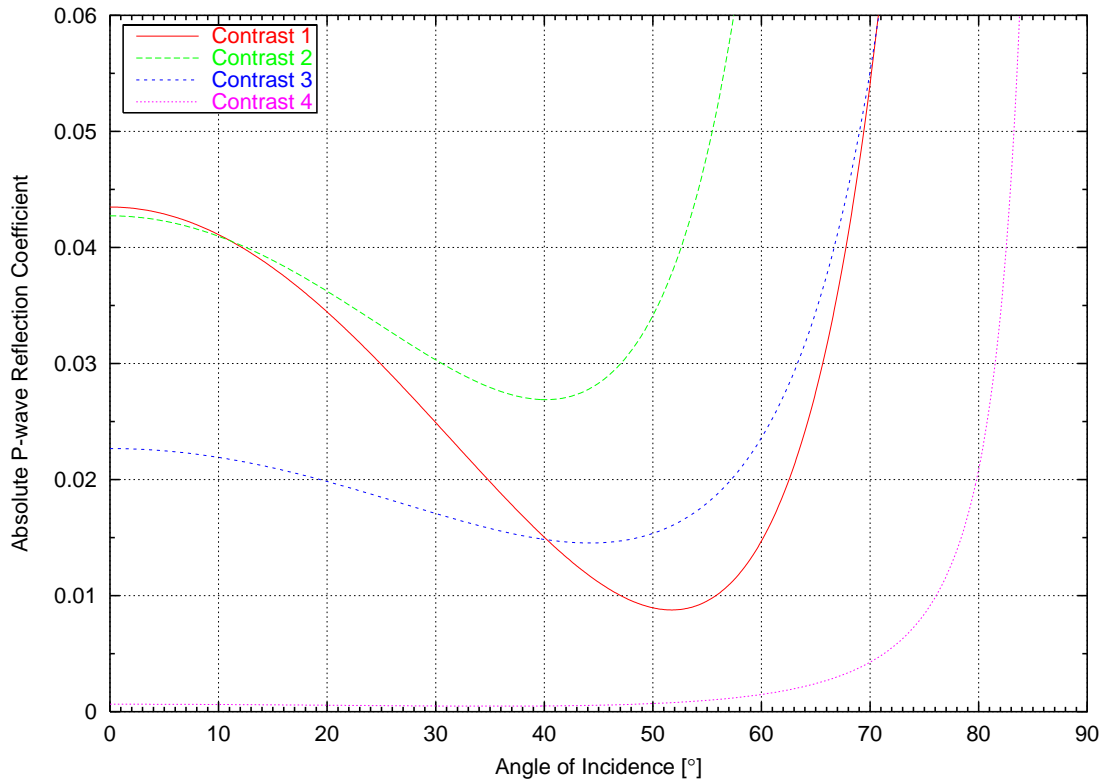


Fig. 7.7: Absolute reflection coefficient as a function of the incident ray angle for P-waves. The values are calculated for velocity and density contrasts shown in Table 7.1 and were also used in Figure 7.6. The strong incident ray angle dependency is obvious. Above about 60° the values rise by orders of magnitude towards the critical angle.

is about the range of the in situ dips found in the KTB drillholes - produces about the same transmission conversion coefficient. This can explain the small differences between the P-to-S converted waves in transmission in Figures 7.2-7.4.

Since the in situ foliation angles are $\sim 45^\circ - 80^\circ$ the reflected wave is basically reflected sideways with about infinite apparent velocity in a seismogram or in forward direction, resulting in positive apparent velocities. The reflection angle is very sensitive to changing foliation dips which makes the detection of these reflected onsets in a seismogram very difficult. The angle dependency of the P-wave reflection coefficient is depicted in Figure 7.7, for the same velocity and density contrasts as in Table 7.1 and Figure 7.6. With incident ray angles higher than about 60° the reflection coefficients strongly increase, as they approach the critical angle. Between $\sim 40^\circ - 70^\circ$ the red and the blue line even change their positions. Therefore, it is obvious that the reflected P-wave cannot serve as good an impedance contrasts indicator as the converted wave in transmission. In fact, because of the complicated travel paths of the reflected P-wave the PS converted wave can be trapped more easily.

Because of the basic dip-independence of the P-to-S conversion in the KTB in situ dip range the determination of a quantitative relation between the acoustic impedance

and the P-to-S conversion in transmission was attempted. The acoustic impedance was calculated for the simulated P-wave velocity and density (Figure 7.8). For comparison, the normalized values were then plotted into Figure 7.9 together with the normalized P-to-S conversion coefficient values determined for the in situ dip model. Apart from the polarity both functions seem to show the same pattern. This is a very important observation because this indicates that in steeply dipping environments the P-to-S-conversion in transmission function can be taken as acoustic impedance function without measuring the density in an extra (radioactive source) logging run, provided the signal frequency is high enough to not run into tuning problems. This method does not have the same spatial resolution as a logging tool, though. For this model, the relation between the P-to-S conversion in transmission coefficient and the acoustic impedance is about -50.

If this relation or another simple one is consistent for many models and also for field data, the major value of this method would be the deduction of the density from the later wavefield of the converted waves because - as shown in Chapter 6 - in a scattering environment the later wavefield is a representation of a greater volume around the borehole. Logging information is more or less, restricted to the direct vicinity of the borehole. It should be interesting to analyze this method for sedimentary environments where steep dips close to salt domes are not uncommon. However, less scattering can be expected in these environments.

7.1.2 Measured Velocities

As indicated at the beginning of this chapter, conversion coefficients were also calculated for in situ velocities and densities. The median filter window length for the VSP derived velocities (Fischer, 2000) and the density data was 300 m with 25 m increment. From the KTB database sonic log velocities are available too, but not considered here.

The basic problem using these velocities is the question of which foliation dip to use for the calculations. Basically, the split shear waves are rotated azimuthally in such a way that the faster one is maximized on one horizontal geophone record, and the slower one on the other. From these, two conversion to depth functions can be calculated, one for each component. Since the fast S-wave oscillates more or less parallel to the strike of the foliation (Figure 4.8), this implies that - in a strict sense - this wave does not encounter any foliation dip. This is of course not realistic. The dip orientation in the borehole is defined according to the majority of the dips for a given depth interval. Large minorities of other directions have a certain impact too. On the other hand, the S-waves need a certain distance to adapt to any new anisotropy orientation (W. Rabbel, personal communication, 2002). For most of the borehole the foliation direction and the crack orientation is more or less the same, resulting in a well defined anisotropy system. In the lowermost part of the borehole the orientations are different, though. Here, the anisotropic behavior is probably not simply hexagonal any more. Simulating this situation with the in situ dip for both components might therefore be an adequate solution for the calculations. Also, any foliation dip variation close to

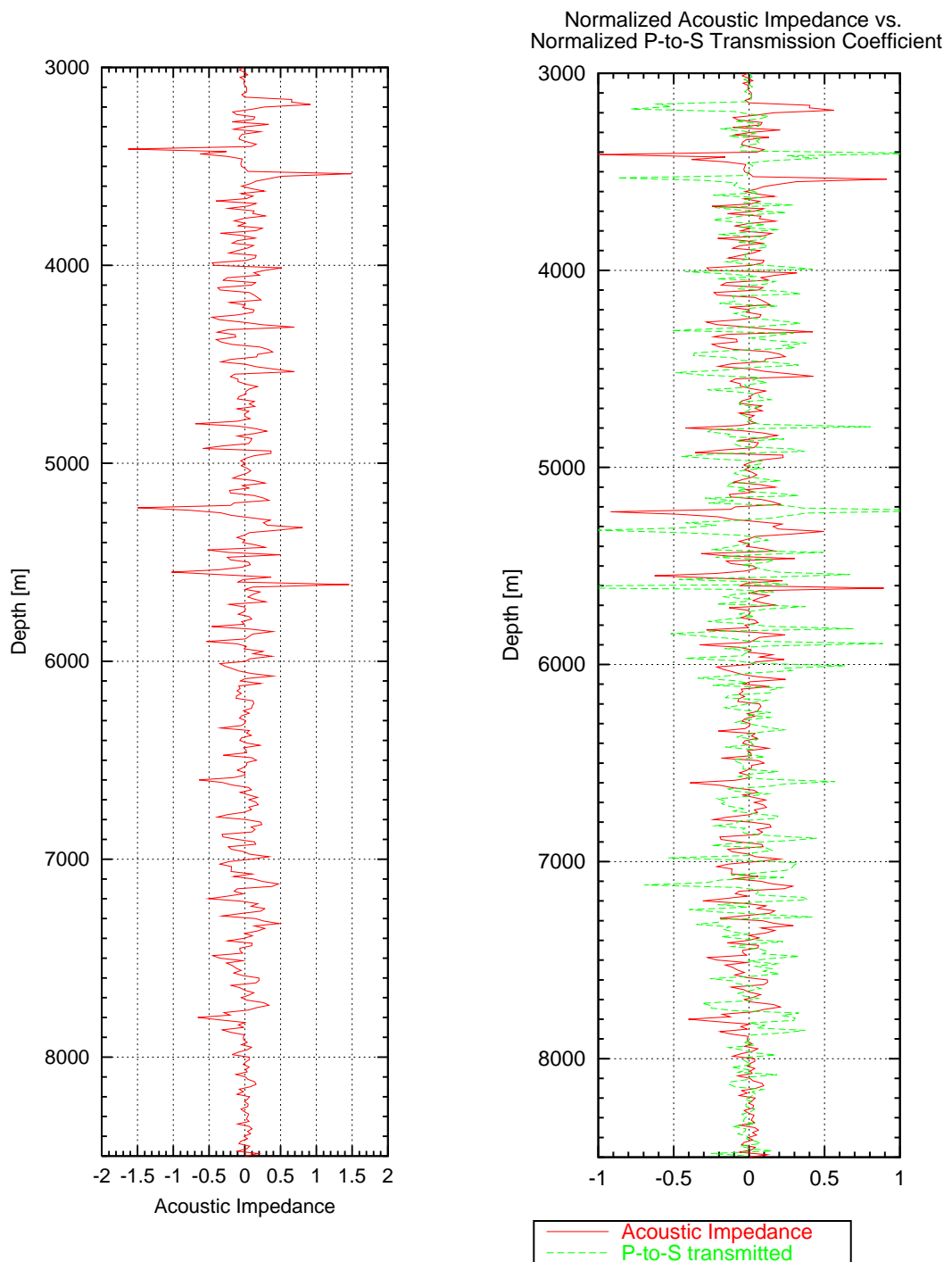


Fig. 7.8: Acoustic impedance of the model P-wave velocities and densities.

Fig. 7.9: Normalized acoustic impedance of the model P-wave velocities and densities vs. the normalized P-to-S converted wave in transmission for the in situ foliation dip.

zero would strongly influence the conversion coefficient, because here it cannot be regarded as basically dip independent.

In order not to run into unsolved speculation and to not vary more than one parameter at a time, it was decided to use the in situ foliation dip for both components. Figures 7.10 and 7.11 show the coefficients for the P-to-S1 and P-to-S2 converted waves in transmission, respectively. Figures 7.12 and 7.13 show the corresponding absolute values. Basically, these figures should be compared with Figures 6.1, 6.2, 6.15, and 6.16 because these are the corresponding results derived directly from the PS converted waves in the field data. For an exact comparison of the values, a convolution of the derived coefficients with an input signal would have been necessary. This was not attempted here, but can be regarded as being carried out in Chapter 8, in which finite-difference calculations of a few models will be discussed.

Instead, the basic appearance of the conversion coefficients derived from the VSP velocities with respect to depth are compared here with their seismically derived counterparts presented in Chapter 6. At a first glance the correlation seems weak. But taking a closer look at the corresponding true phase plots a surprising similarity appears. The best correlation exists in the upper part of the S2 component of either figure (Figures 7.11 and 6.2). Although not every single spike in the two figures correlate, some are very close, except for the wave-like behavior of the seismically derived P-to-S conversion log. Even the amplitude values are comparable to the values of the conversion coefficients. In the lower part of these two plots, the correlation is poor. However, in the lower parts of the S1 component plots surprising similarities can be detected, although the signals in Figure 6.1 are noisy. Amplitude values and conversion coefficients are comparable. The reason for this could be the crack orientation hampering a good anisotropic orientation of the shear waves but perhaps initiating strong conversion from P- to S-waves. The problem of the stronger conversion in the S1 component compared with the S2 component, discussed in Chapter 6, is related in this respect. For the central parts of the borehole (about 4.5 to 6.5 km depth) the correlations are not as obvious because the values differ strongly. The location of some of the features especially in the S1 component readings seem to match though.

After all, it seems at least some correlation exists between the seismically derived P-to-S conversion in transmission and the Zoeppritz coefficients for the same conversion, calculated for the measured seismic velocities. Assuming that smaller dip angles than about 45° are encountered by one or the other shear wave after the rotation into the system of anisotropy, resulting conversion amplitudes would decrease. In this case, the first order assumption that the P-to-S conversion in transmission is more or less independent from the dip is not true any more. However, a more important obstacle for the interpretation could be the necessity of interfaces of large extent for the calculation of reliable coefficients with the Zoeppritz equations. Therefore, the results should not be analyzed too detailed.

In a sedimentary environment with larger layer interfaces the situation might be different though. Should it be possible to determine reliable values for the elastic parameter dip angles either shear wave encounters while propagating in the crust, it might

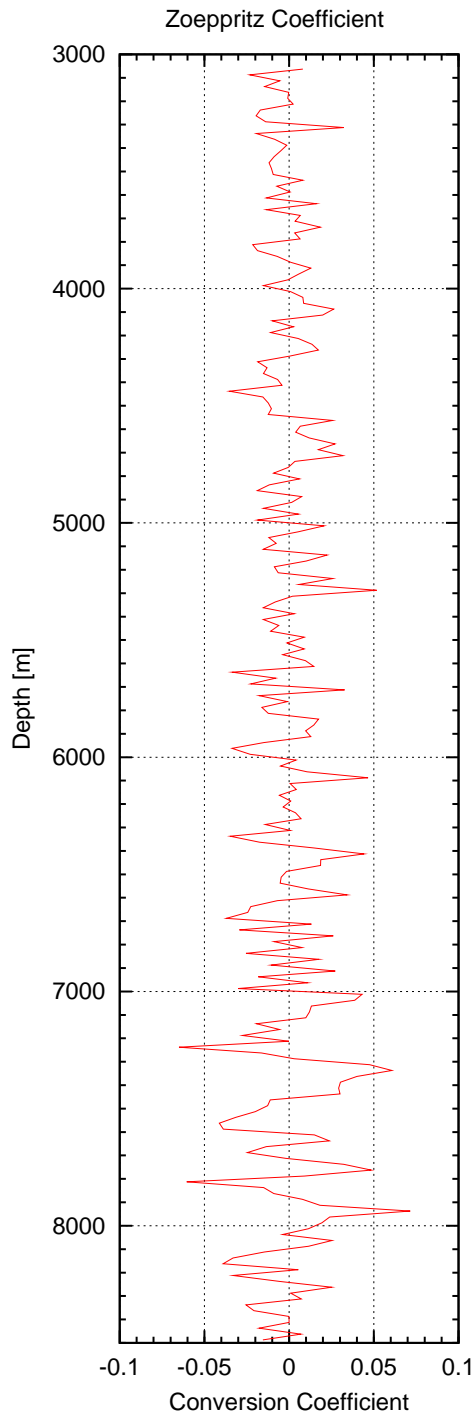


Fig. 7.10: Conversion coefficients for P-to-S1 conversion in transmission for the measured VSP velocities and density along the KTB main hole with applied in situ foliation dip, smoothed with a window length of 300 m and an increment of 25 m.

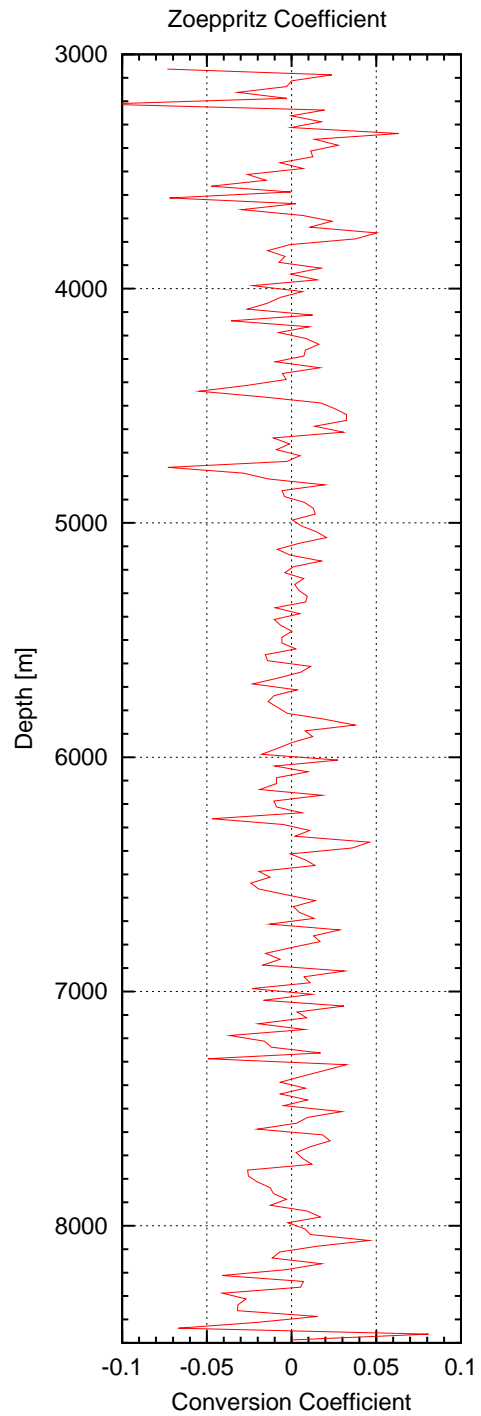


Fig. 7.11: Conversion coefficients for P-to-S2 conversion in transmission for the measured VSP velocities and density along the KTB main hole with applied in situ foliation dip, smoothed with a window length of 300 m and an increment of 25 m.

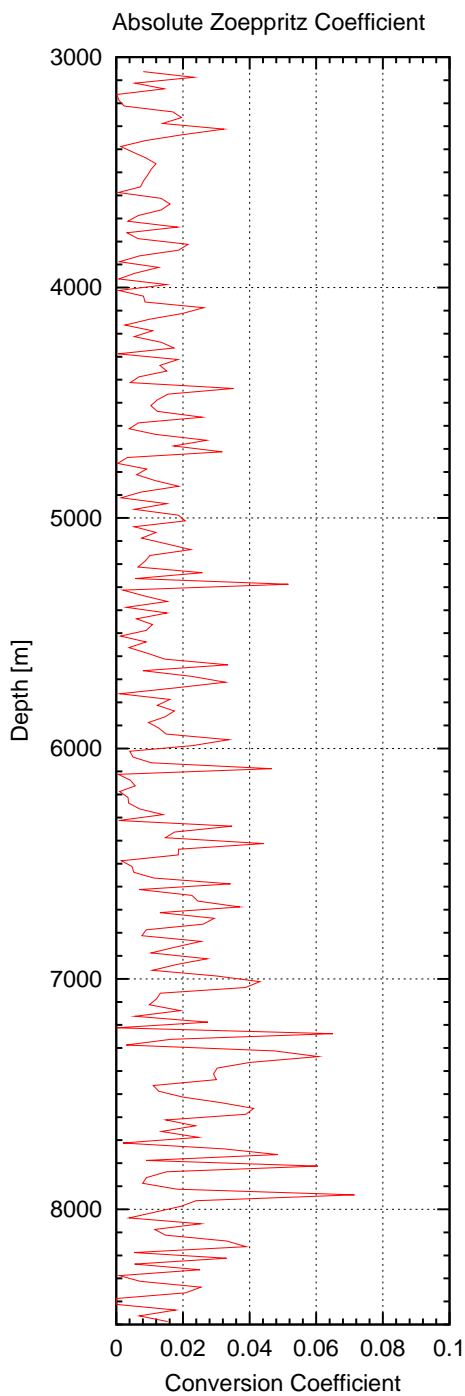


Fig. 7.12: Absolute conversion coefficients for P-to-S1 conversion in transmission for the measured VSP velocities and density along the KTB main hole with applied in situ foliation dip, smoothed with a window length of 300 m and an increment of 25 m.

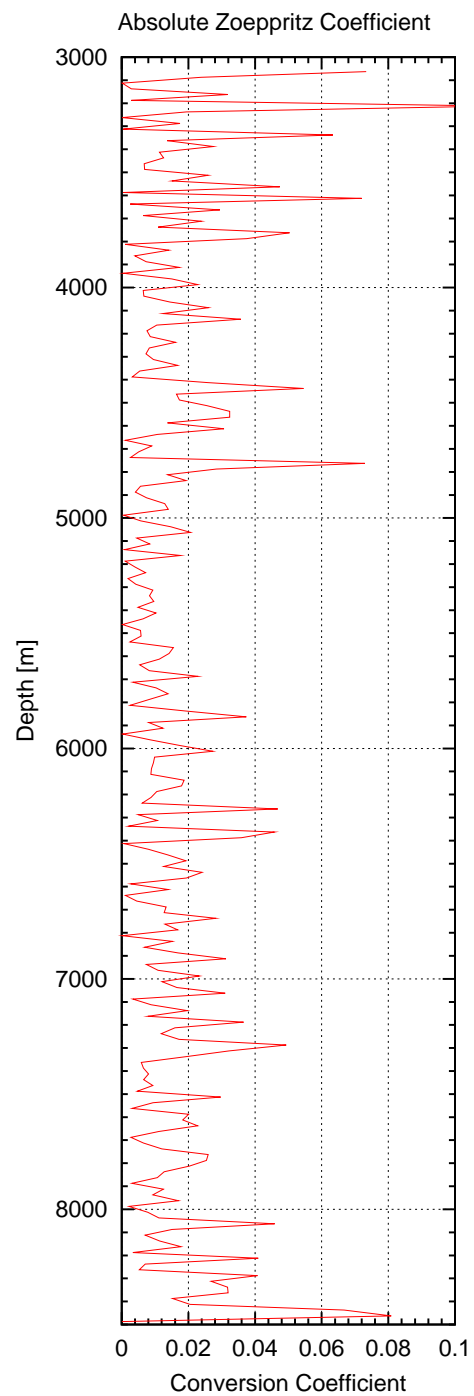


Fig. 7.13: Absolute conversion coefficients for P-to-S2 conversion in transmission for the measured VSP velocities and density along the KTB main hole with applied in situ foliation dip, smoothed with a window length of 300 m and an increment of 25 m.

be possible to define an optimum smoothing window for the raw VSP velocity picks to make the resulting P-to-S conversion values correlate with the corresponding seismically derived conversion logs. This could be a suitable tool for the quantification of VSP velocity picking errors.

7.2 Summary

One attempt to determine the influence of cracks and fissures on the conversion of waves is to compare the field data results with corresponding results from models, with simulated crack-free velocities calculated from the known mineral composition, with respect to depth. Conversion coefficients for a crack free model were calculated in a first order approach with the Zoeppritz equations, assuming layer surfaces of large extent and plane waves. Another important parameter effecting the result is the layer (foliation) dip at each depth position. It is known from borehole wall scans.

The strongest conversions belong to the reflected P-waves and conversions of P to S in transmission. The latter values only show about 1/3 of the conversion amplitudes found in the field data conversion logs in Chapter 6. The P-to-S conversion in reflection is generally weak. Whereas the reflection coefficient of the P-wave is very dependent on the incident ray angle, this is not as important for P-to-S conversion in transmission in the medium to steep dip angle range, encountered in the KTB drillholes. The reflection coefficients of the P-waves show about the same order of magnitude as the P-to-S conversions in transmission below a dip angle of 60° . Above that they grow fast towards the critical angle.

Since the P-to-S transmitting coefficients are basically independent from the incident ray angle existing in the KTB main hole, this conversion type is a very good independent impedance contrast indicator and can be used to quantify the influence of cracks and fissures on the elastic parameters in comparison with crack free models.

The accuracy of the seismically derived P-to-S conversion in transmission amplitudes in Chapter 6 can be studied by comparison of the isotropic crack-free rock matrix model results determined in this chapter with finite-difference calculations and subsequent seismically derived conversion amplitudes of the same models. Such comparative calculations will be explained and discussed in the following chapter.

Chapter 8

Finite-Difference Modeling

Finite-difference modeling can be a helpful tool for the interpretation of field data. Especially in the presence of complicated crustal structures or a complicated borehole geometry, no other tool can almost cope with the field data original. A recent example can be found in [Hackert & Parra \(2002\)](#).

The results of the many experiments at the KTB site led to a basic crustal model of the upper crust at KTB compiled by [Hirschmann \(1996\)](#). One of his models is a 3-dimensional block diagram (Figure 2.2 on page 7), the other a 2-dimensional more detailed cross-section (Figure 2.3 on page 8). In these images it was tried to integrate all of the information then available, including data from borehole and surface measurements. One of the major problems with the 2D cross-section is the projection of the 3D information to two dimensions without producing a false image. The 2D crustal model only discriminates 8 different rock units. Although it is detailed compared to other models, it is not representative down to the meter scale.

This 2D cross-section however, was the basis for a first VSP finite-difference modeling run by D. Okaya (personal communication, 2001), not shown here. One of the most interesting side-effects of FD-modeling is the possibility to visualize the evolution of the wavefield within the calculated model to be able to interpret the onsets in the resulting seismograms. Of special interest was the complicated first break of the P-wave in the field data. Although not very complex with respect to the number of rock units, the relatively complicated crustal structure in his model seemed to be responsible for an apparently complicated first break signal. It turned out to be the result of multi-pathing of the source signal because of the existence of steeply dipping rock units with different elastic properties (see Section 5.1.3 on page 49).

In this model based on the cross-section of Figure 2.3 - as opposed to reality - fault zones are just boundaries between two adjacent areas; they do not incorporate any fault zone specific properties. This way, fault zone related onsets in the model seismic data only result from impedance contrasts induced by simple lithological boundaries. Because of the large size of the model rock units however, the lithology on either side of the model fault zones does not always differ. In some places the same geological unit reaches across the fault zone, e.g., the fault zone in 4 km depth in the direct vicinity of

the borehole in Figure 2.3; therefore no impedance contrast exists across the fault zone. This partial nonexistence of model fault interfaces cannot produce any reflections or conversions and underlines the simplicity and limited validity of this basic model.

Since lithological contrasts and the complicated crustal structure at the KTB site had basically already been combined in this first model, it was not possible to discriminate the effects of each on the resulting seismic data. This was the reason to carry out an additional stepwise modeling process. Also, the large rock units of the basic model were to be replaced by smaller structures. The aim was set on the attenuation of the seismic signals with special focus on wave conversion, quality controlled by the grade of relationship between the field data seismograms and the model data seismograms.

These FD calculations had to be carried out in 2D, though. The calculation of a 3D model of this size with this high resolution (2 m grid point spacing) would have allocated more computer memory than available super-computers presently offer. Besides, no detailed model of this crustal block in 3 dimensions has been derived so far.

The calculations comprised a resolution test of the conversion log method described in Chapter 5, applied onto a simple model and a series of four crustal models:

1. a simple model (Figure 8.14) with equally spaced layers of 12.5 m vertical thickness with the average foliation dip of 60° found within the KTB main hole. This model represents the rock units found along the depth profile of the borehole but does not model the true dip of units. It is the same model that was used in the analytical calculations in Chapter 7. It therefore, represents a link between the analytical calculations and finite-difference modeling
2. a model within which the true dip of the foliation was tried to be simulated. Because of the restriction to 2D it is not possible to keep the in situ rock unit sequence as in the simple model
3. a model that incorporates the foliation dip of the above model plus the projection of its azimuth into 2D. Still the true rock unit sequence does not model the in situ situation
4. the end member model (Figure 8.30) incorporates the foliation dip, the projection of its azimuth into 2D and fault zones, the latter as simple as in the cross-section (Figure 2.3). However, because of the dense rock unit sequence, impedance contrasts are almost present anywhere across the fault zones. One side-effect of the simulated fault zones is a high velocity zone in the central part of the model borehole which is in close correlation to the in situ situation

In order to keep the analysis focused on the important results, only the resolution test, the simple 60° foliation dip model, and the last, complex model are discussed in the following sections.

The crustal models were calculated with a free surface and an absorbing frame around the subsurface part of the model to suppress reflections from the model boundaries. The grid point distance was set to 2 m because of slow shear wave velocities in

the lower part of the models. Although intrinsic damping can be calculated with FD code of [Bohlen \(2002\)](#), damping was reduced to a minimum, in order to determine the structural effects on Q .

Generally, the choice of a realistic wavelet is not easy. No wavelet information from the measured VSP data is available; the reference geophones in either position were only able to pick the convoluted signal mixed with reflections or refractions from inner-crustal interfaces and the surface. Since the source in the field experiment 1999 was dynamite and because of the results of the basic model calculated by D. Okaya (personal communication, 2001), discussed above, the simple Fuchs-Müller wavelet ([Fuchs & Müller, 1971](#)) was chosen as the source signal. Any complicated wave pattern observable in the model seismograms is therefore not caused by the source but by the crustal structure.

8.1 Spatial Resolution

To start the modeling sequence the spatial resolution potential of a simple seismic signal with respect to conversion was analyzed. Single layers of velocity and density contrast within a background medium were FD-modeled, differing only in layer thickness. The superposition of the reflection at the top and the bottom of a layer can affect the resolution and is widely known as tuning (e.g., [Widess, 1973](#)). This phenomenon does affect converted waves as well.

The layer thickness of the models was varied from 200 to 6 m superposed in [Figure 8.1](#). The velocities and densities were $V_p=(6254, 6748, 6254) \text{ m/s}$, $V_s=(3552, 3864, 3552) \text{ m/s}$, and $\rho=(2698, 2955, 2698) \text{ kg/m}^3$ above, within, and below the layer, respectively. The layer dip was set to 60° , which is about the average foliation dip within the crustal section drilled at the KTB site. For a downward traveling wave, this defines a positive impedance contrast at the top of the layer and a negative contrast at the bottom. The source location was inserted at 14 m depth at $x = 300 \text{ m}$, with a main signal frequency of 80 Hz, which results in a main wavelength of the P-wave of about 80 m. The simulated signals were collected in a vertical profile, indicated at $x = 300 \text{ m}$ in [Figure 8.1](#).

The S-wavefield snapshots for a traveltime of 0.2 s are depicted in [Figure 8.2](#) for a vertical layer thickness of 200 m to [Figure 8.7](#) for a layer thickness of 6 m. The amplitudes are clipped to enhance the converted and reflected waves. The strongest wave is the direct shear wave, with a distinct polarity change beneath the shotpoint, which results from the different initial shear to the left and right of the shotpoint. The shear waves reflected on the single layer are the reflections of only the left part of the direct shear wave; thus, they do not show any polarity change along their wavefront. The different polarity of the first and second reflected waves is the result of the different impedance contrasts at the top and the bottom of the single layer. The P-to-S converted waves in reflection travel off to the right, interfering the direct shear wave at about $x = 350\text{-}500 \text{ m}$ and $z = 300 \text{ m}$.

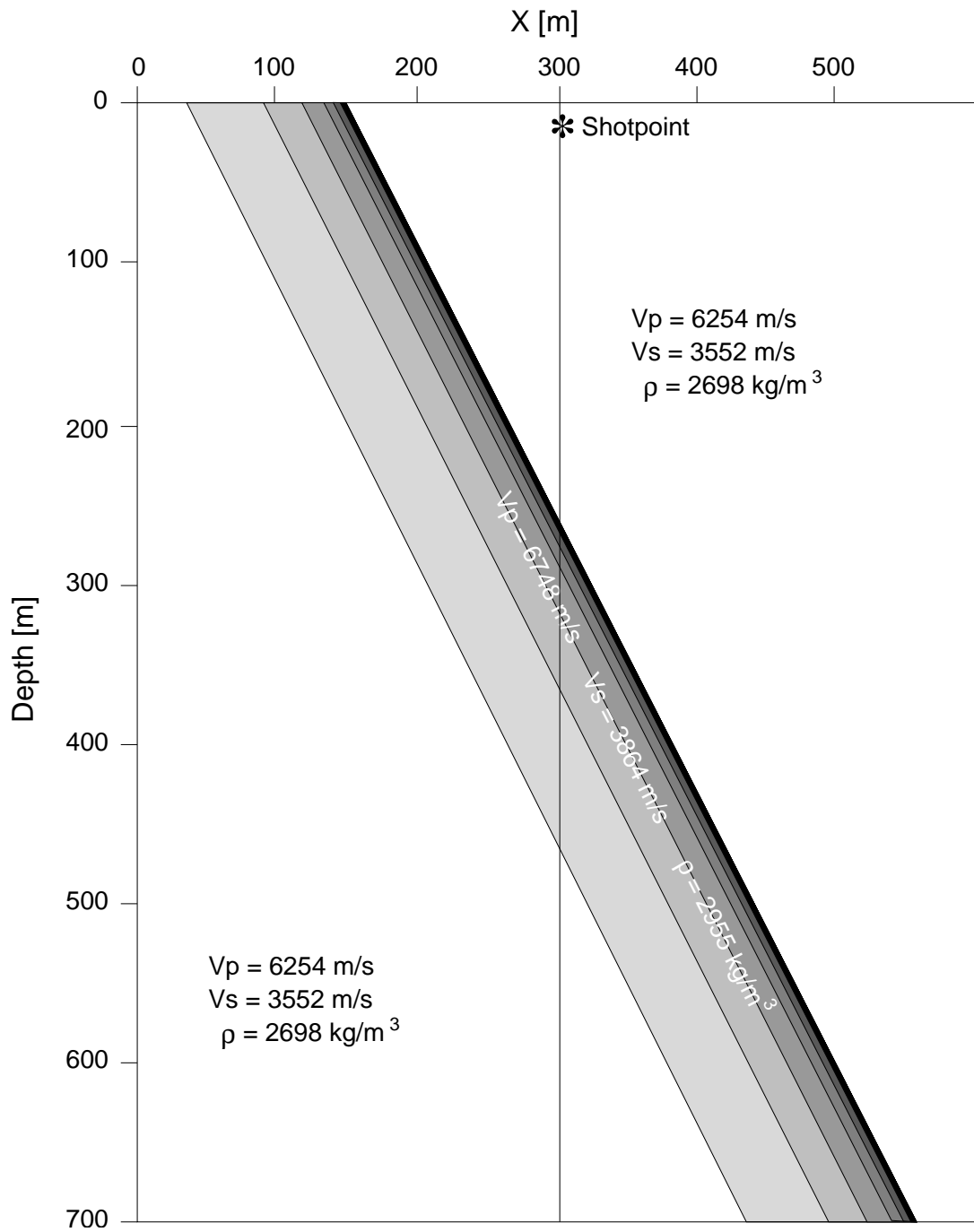


Fig. 8.1: Crustal models with vertical layer thicknesses of 6, 12, 25, 50, 100, and 200 m, indicated in different grey levels. Velocities and densities of the medium above, within and below the simulated layer are $V_p = (6254, 6748, 6254)$ m/s, $V_s = (3552, 3864, 3552)$ m/s, and $\rho = (2698, 2955, 2698)$ kg/m³, respectively, with a dip of 60°. The borehole is indicated at $x=300$ m. The shot point is located in 14 m depth.

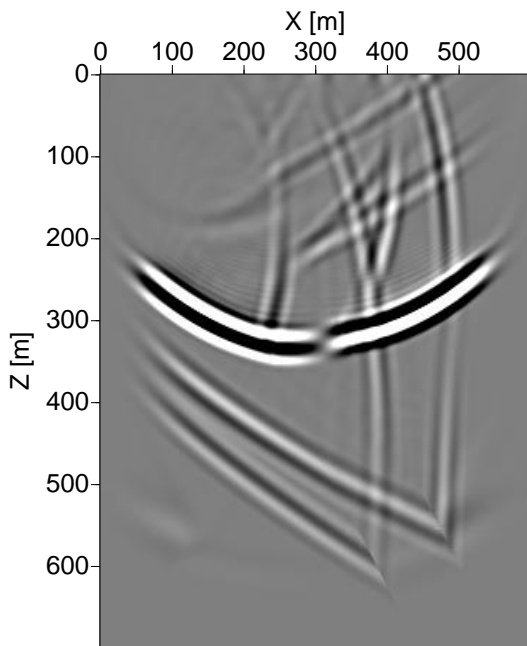


Fig. 8.2: Shear wavefield of a single layer with a thickness of 200 m dipping with 60° within a background medium at travelttime = 0.2 s.

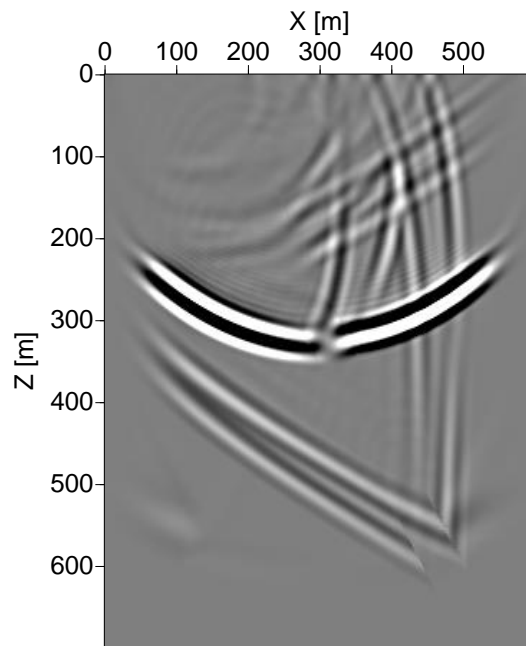


Fig. 8.3: Shear wavefield of a single layer with a thickness of 100 m dipping with 60° within a background medium at travelttime = 0.2 s.

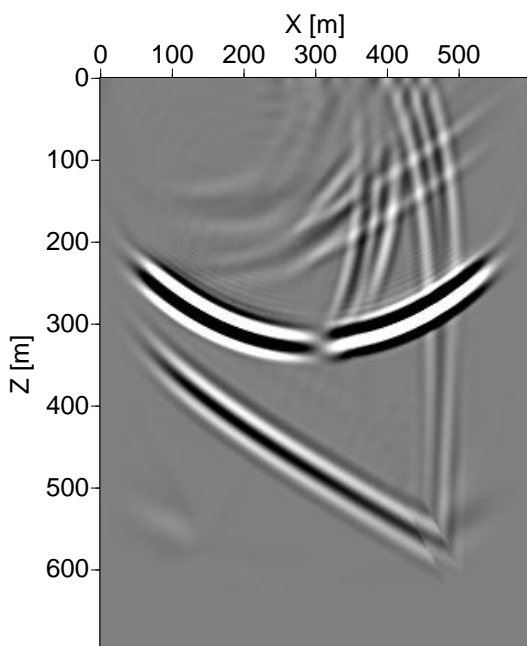


Fig. 8.4: Shear wavefield of a single layer with a thickness of 50 m dipping with 60° within a background medium at travelttime = 0.2 s.

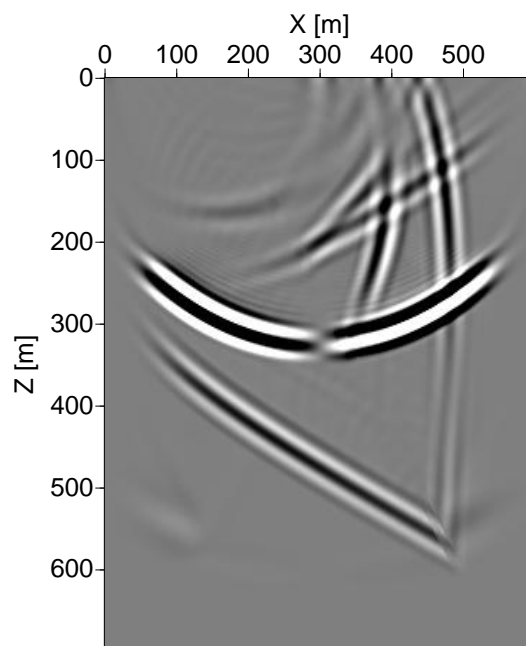


Fig. 8.5: Shear wavefield of a single layer with a thickness of 25 m dipping with 60° within a background medium at travelttime = 0.2 s.

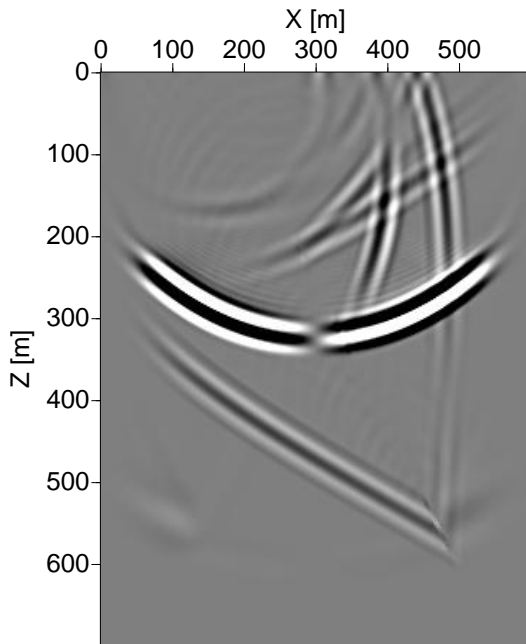


Fig. 8.6: Shear wavefield of a single layer with a thickness of 12 m dipping with 60° within a background medium at traveltimes = 0.2 s.

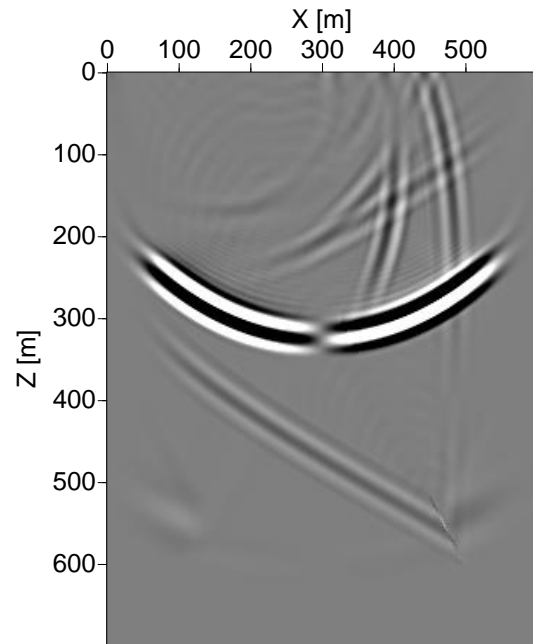


Fig. 8.7: Shear wavefield of a single layer with a thickness of 6 m dipping with 60° within a background medium at traveltimes = 0.2 s.

The model with the largest layer thickness (200 m) clearly shows two separate P-to-S converted waves in transmission as the lowest wavefronts (or first, in terms of time) also with reverse polarity due to the opposite impedance contrasts on both sides of the layer. The second model (Figure 8.3) still shows two wavefronts emerging from the layer boundaries, although it is obvious that the two waves are not perfectly separate in this case. It seems therefore reasonable to expect that the vertical resolution limit of a seismic wave with a main signal frequency of 80 Hz is somewhat close to 100 m. In the next two wavefield snapshots (Figures 8.4 and 8.5) the underlying model layers have a vertical thickness of 50 and 25 m, respectively. The waves converted at the upper and lower layer limit are not separate anymore. On the other hand the negative and positive amplitudes seem to be larger than in the first two examples. This is probably due to the constructive superposition of the two waves. In the last two examples (Figures 8.6 and 8.7) the vertical layer thickness of 12 and 6 m, respectively is far smaller than the wavelength of the incident P-wave but the amplitudes still seem basically comparable to the ones in the snapshots of the models with a larger layer thickness. This proves that even thin layers are recognized by the conversion log. The question remains whether the conversion log is able to resolve the layer limits and the impedance contrasts.

The resulting conversion logs are shown from Figure 8.8 for a thickness of 200 m to Figure 8.13 for a thickness of 6 m. They are indicated in red. The corresponding analytical values, calculated with Zoeppritz coefficients, are plotted in green as the reference information for quality control. These coefficients indicate the position of the impedance contrasts and the amplitudes that should be reached by a perfect conversion

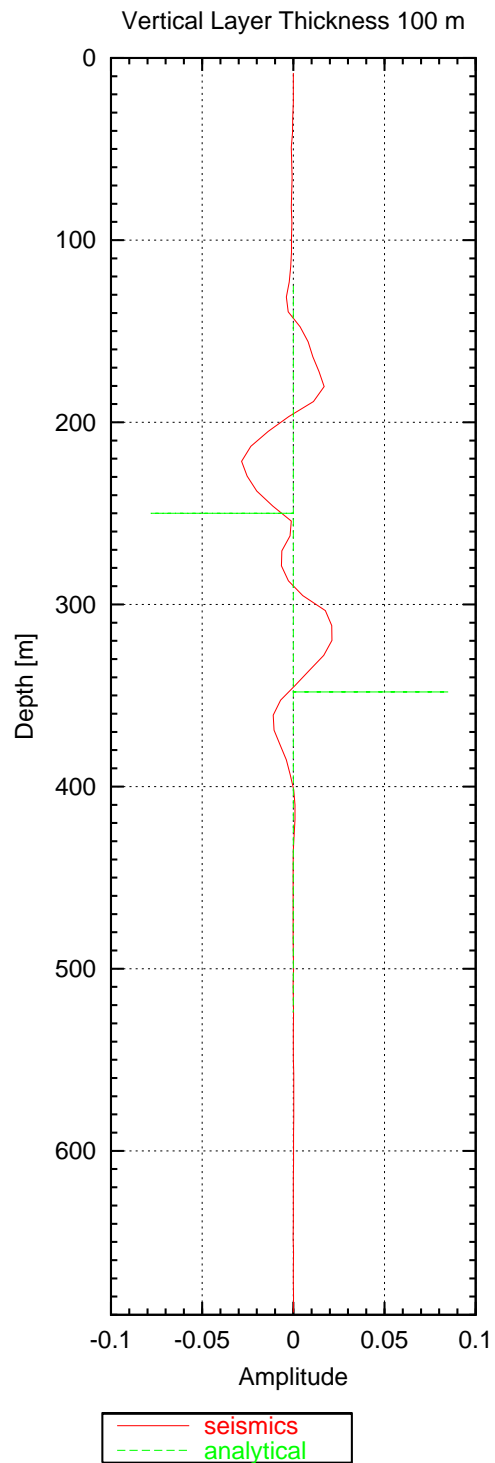
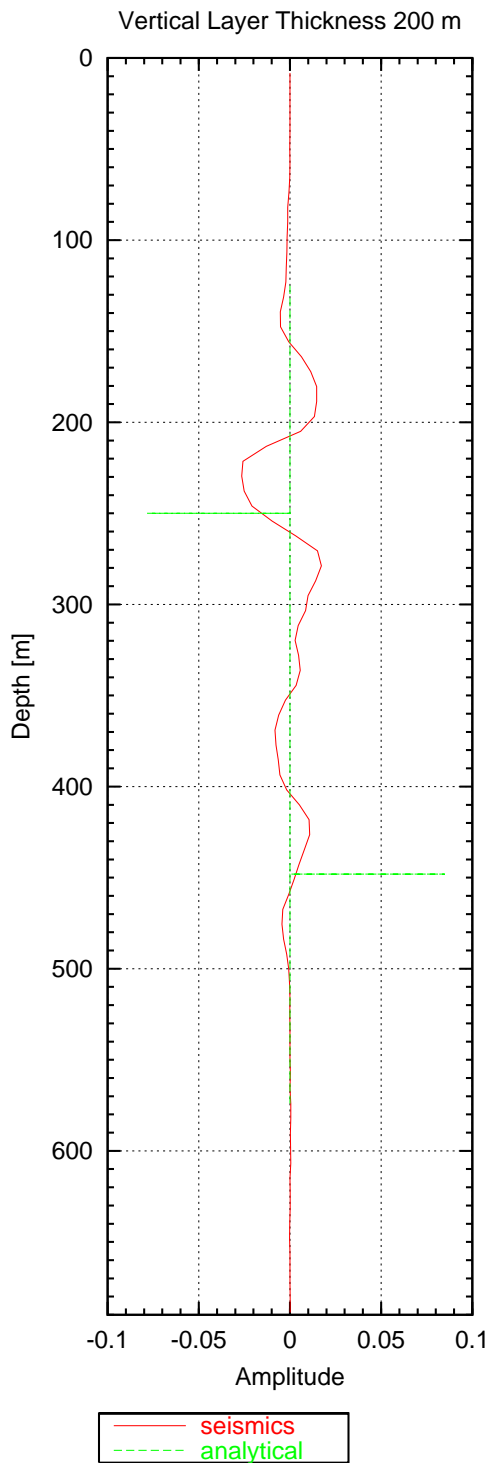


Fig. 8.8: Conversion-log of a single layer with a thickness of 200 m dipping with 60° within a background medium.

Fig. 8.9: Conversion-log of a single layer with a thickness of 100 m dipping with 60° within a background medium.

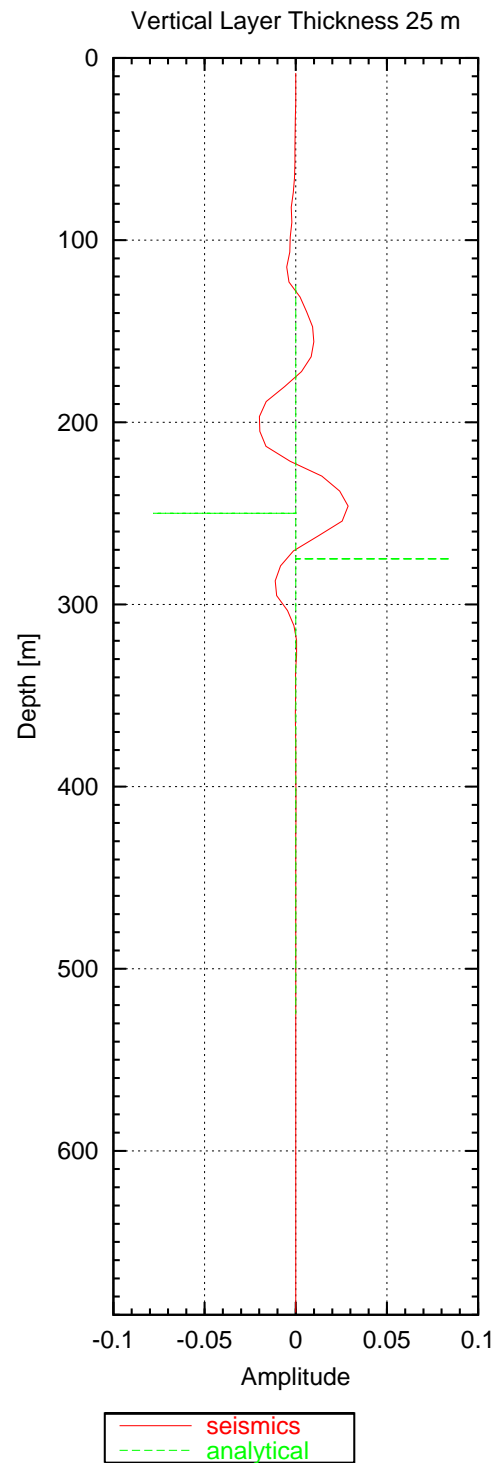
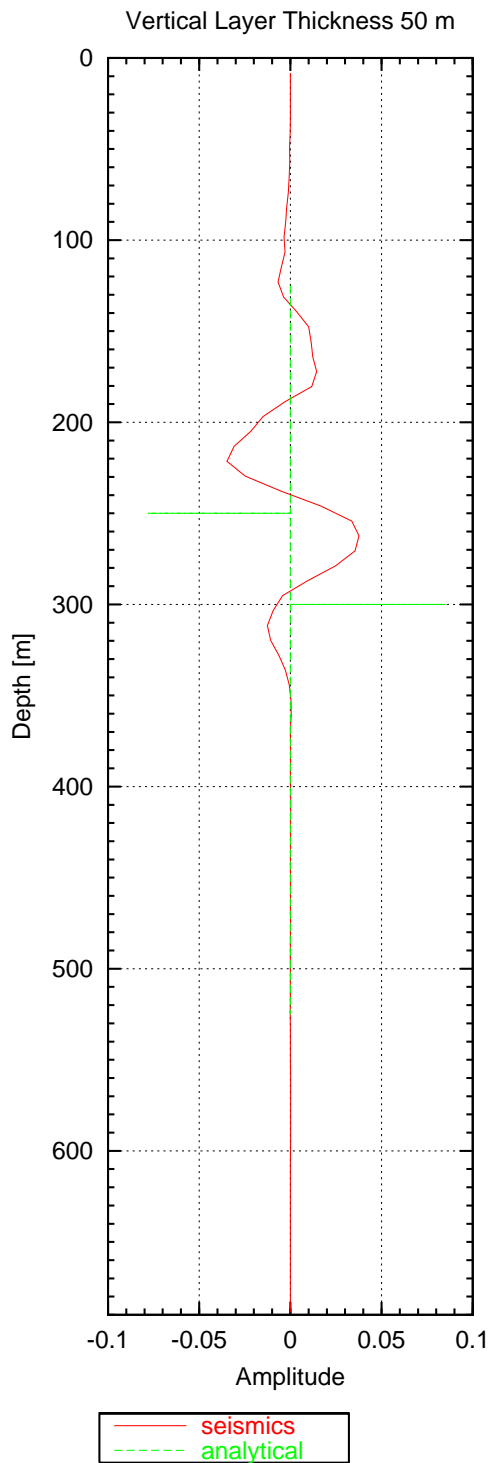


Fig. 8.10: Conversion-log of a single layer with a thickness of 50 m dipping with 60° within a background medium.

Fig. 8.11: Conversion-log of a single layer with a thickness of 25 m dipping with 60° within a background medium.

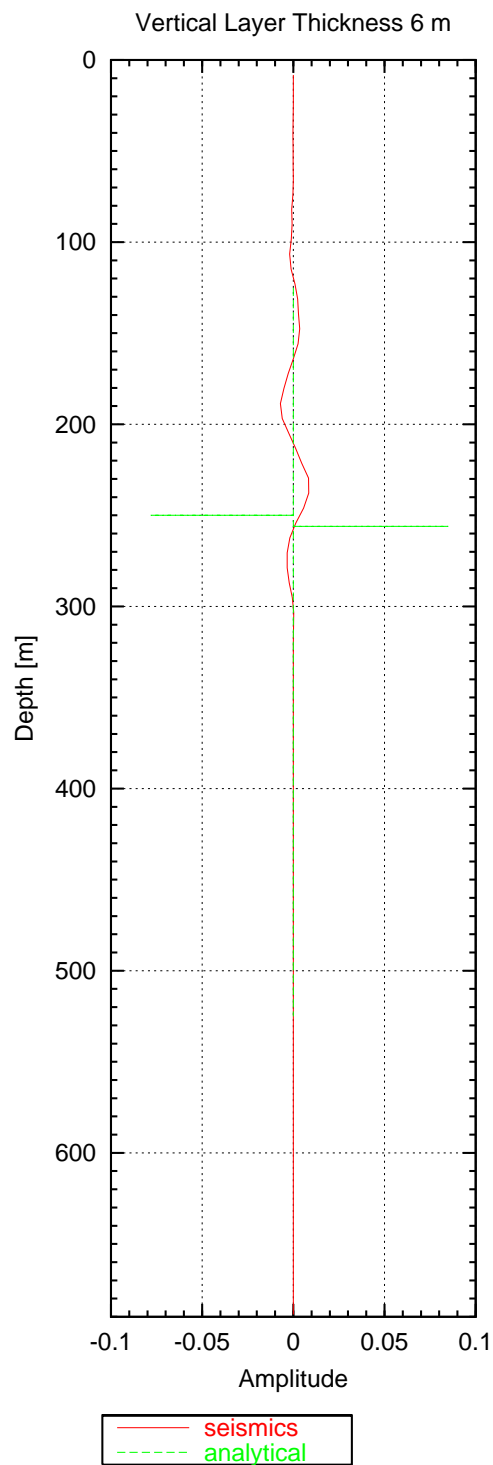
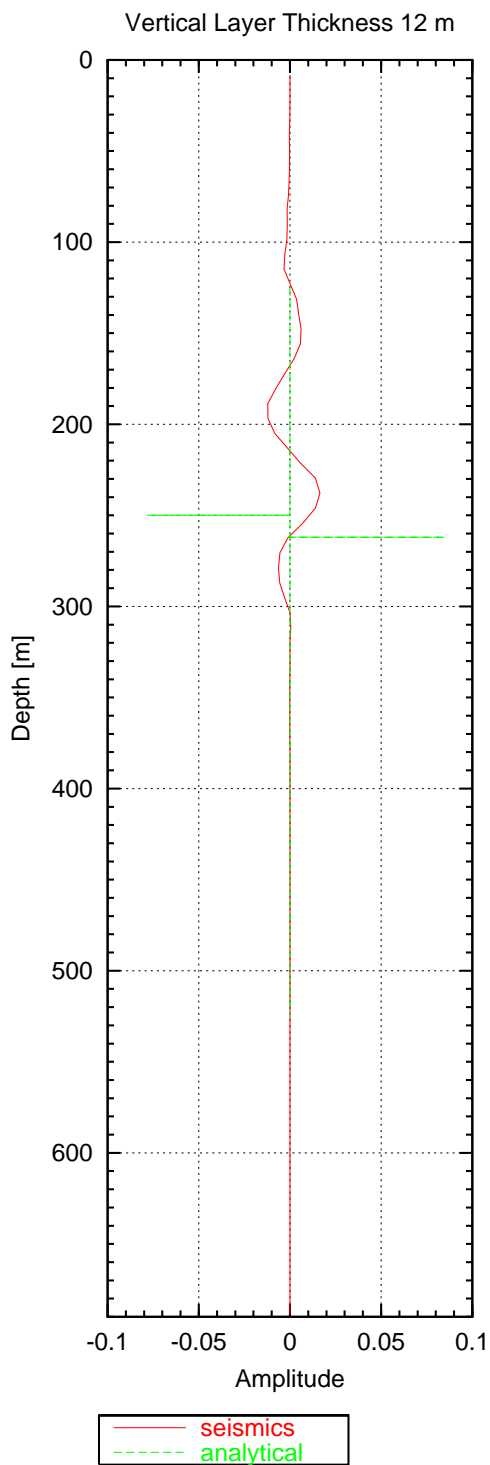


Fig. 8.12: Conversion-log of a single layer with a thickness of 12 m dipping with 60° within a background medium.

Fig. 8.13: Conversion-log of a single layer with a thickness of 6 m dipping with 60° within a background medium.

log. However, the in situ situation is a convolution of the impedance contrasts with the incident seismic signal. A certain prolongation of the contrast coefficient spike and a lowering of the resulting log amplitude can therefore be expected.

The amplitudes of the conversion logs of the first four figures (Figures 8.8-8.11) are similar. As already seen in the wavefield images, the explanation for parts of the amplitude behavior is probably the superposition of the upper impedance contrast wavelet with the lower one. The last two (Figures 8.12 and 8.13) show smaller amplitudes. It is a surprise to a certain extent that even the thin layer of only 6 m is able to produce a remarkable amplitude.

The Zoeppritz coefficients in the plots indicate a *negative* amplitude of the P-to-S converted wave in transmission at a *positive* impedance contrast and a *positive* amplitude at a *negative* impedance contrast. The corresponding conversion log graphs seem to represent this phase behavior. The maximum negative and positive amplitudes in Figure 8.8 are 200 m apart as are the Zoeppritz coefficient indications, which is in accordance with the model. Their highest values seem to be shifted upwards by about 30 m compared to the Zoeppritz spikes, though. The same seems to be true for the conversion log graph in Figure 8.9 with a vertical model layer thickness of 100 m and in Figure 8.10 with a vertical layer thickness of 50 m. Part of this phenomenon can be explained by the shot depth of 14 m, resulting in a smaller traveltime of the signal from the source to the corresponding layer boundary. But an error of 16 m still needs an explanation.

The three models with the thinnest layers do not seem to be represented by the conversion log function. In all of the latter plots the distance between the negative and positive maximum is 50 m, whereas the Zoeppritz coefficient spikes reflect a smaller distance between the upper and lower layer boundary. Here, the model and the resulting conversion log calculations differ with respect to the spacial resolution. The observations seem to indicate that impedance contrasts with a corresponding vertical layer thickness down to 50 m can be resolved by a (Fuchs-Müller) signal with a main frequency of about 80 Hz in this crustal environment.

The amplitudes of the impedance contrasts should almost be the same for the upper and lower layer boundary. In the conversion logs this is differently depending on the layer thickness. The origin of this difference is not quite clear. In spite of these uncertainties, though, it seems reasonable to approve this method as a possibility to get a basic idea of probable conversion coefficients in the subsurface.

8.2 Simulated Isotropic Rock Matrix

One of the main objectives of this experiment is the quantitative determination of the influence of (water filled) cracks or fissures on the reflection or conversion of seismic waves. This is to better understand the crustal structure at the KTB site but also to get a more general picture of what reflects in the earth's crust. The idea is to compare the measured seismic data representing the in situ situation with calculated seismic data of

models comprising simulated velocity- and density-contrasts but no cracks or fissures. The resulting difference should mainly be the representation of the latter influence.

The VSP study at the KTB site not only yielded seismic data, it also offers the unique possibility to combine the results with additional in situ measured physical properties of the same crustal section. For a quantitative comparison simulated isotropic rock velocities and densities had been inverted from cuttings-analysis and laboratory measurements of minerals and rock samples (Rabbel *et al.*, 2001), as already mentioned in Chapter 7. The specialty about these simulated parameters is the lack of the influence of cracks or fissures in models using these inverted elastic parameters. Such models were the basis for a number of FD-calculations to be discussed in the following sections. The sequence starts with a simple model (Figure 8.14) and continues with two intermediate models not shown here. The end-member is a complex model (Figure 8.30) that also comprises fault zones; however, only as boundaries between adjacent volumes. The important difference compared with the model calculated by D. Okaya, mentioned at the beginning of this chapter, is the thin layering of contrasts within the end-member model. This automatically produces impedance contrasts across these boundaries at almost any point along these zones. The advantage of this stepwise approach is the possibility to study the wavefield with increasing complexity of the model, to be able to differentiate the effects of the structural features on the evolution of the wavefields and subsequently on the collected seismic data.

8.2.1 60° Foliation Dip Model

Two of the properties collected at KTB were the dip and azimuth of the foliation. The dip of the rocks in this crustal section is steep. It was decided to take the average dip of 60° as a starting point for the seismic modeling of a simulated rock model, in correspondence with the analytic calculations in Chapter 7. This results in a very basic model with a simple layer sequence. The first model consists of simulated velocities with a layer thickness of 12.5 m (Figure 8.14 showing the P-wave velocities).

The wavefield of this model is shown as snapshots in Figure 8.15 (P-waves at traveltime $t = 1$ s), Figure 8.16 (S-wavefield at traveltime $t = 1$ s), and Figure 8.17 (S-wavefield at traveltime $t = 0.6$ s). Although the model is simple, the wavefield appears complicated. The P-wave first break (Figure 8.15) shows undulations because of the velocity variation along the borehole. Even focusing effects, channel waves, and multi-pathing are observable where the wavefront propagates more or less parallel to the layer boundaries. In the P-wave snapshot image the main waves are the downward traveling P-wave and the reflected P-waves which are reflected forward close to the first break or sideways because of the steep foliation dip (PP^b in Figure 8.15). The latter can therefore be observed in the horizontal component seismogram (Figure 8.19) as reflection hyperbolas. The P-wave snapshot also exhibits S-to-P converted waves in transmission and reflection (SP^f and SP^b). This is obvious if the corresponding S-wave snapshot is also taken into account (Figure 8.16). The main S-wave (S) is situated exactly where the S-to-P converted waves separate into the transmitted and reflected

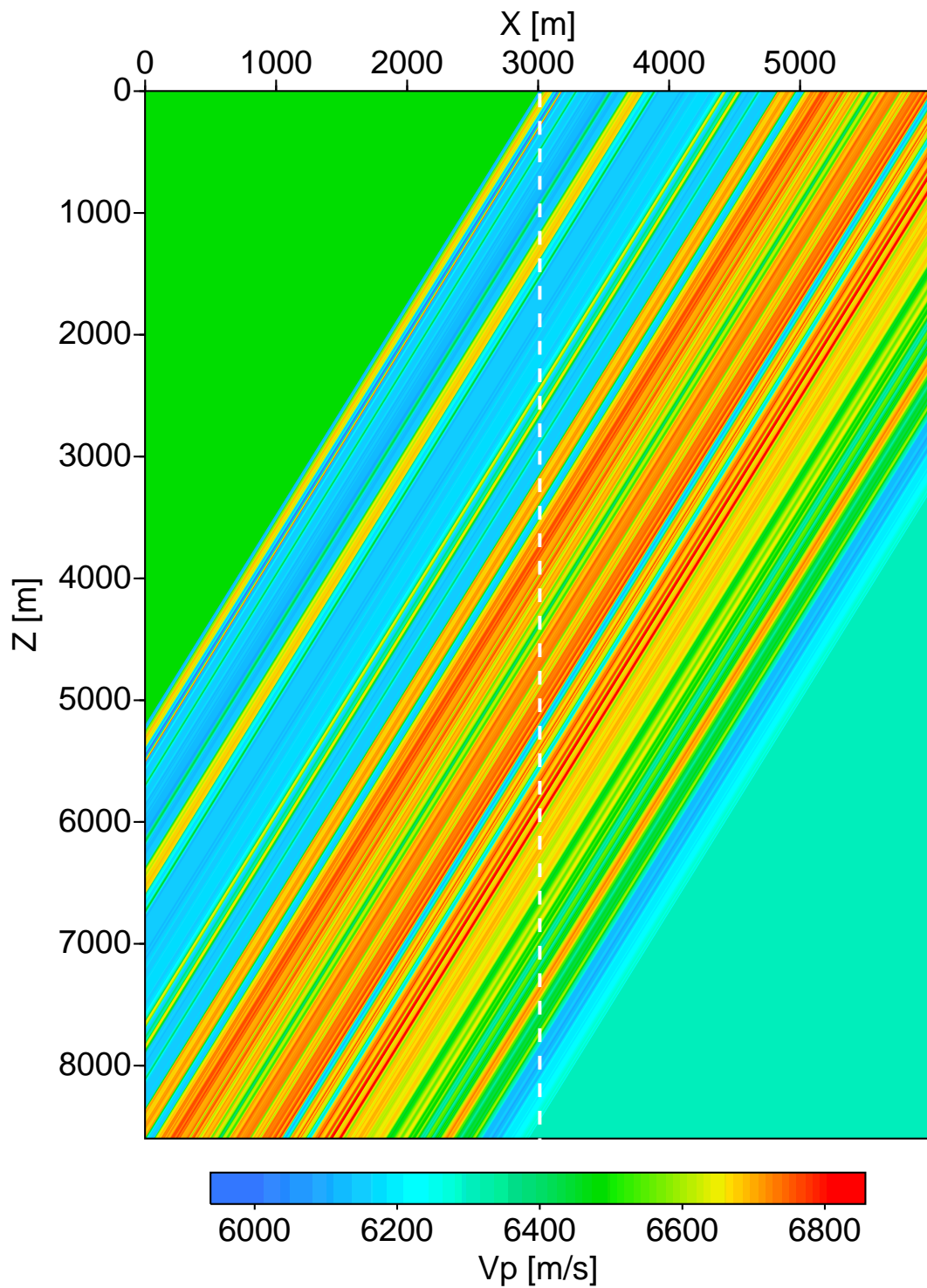


Fig. 8.14: The P-wave velocities of the simulated crack free, isotropic crustal velocity model with a foliation dip angle of 60° . The location of the simulated borehole is indicated at $x = 3000$ m.

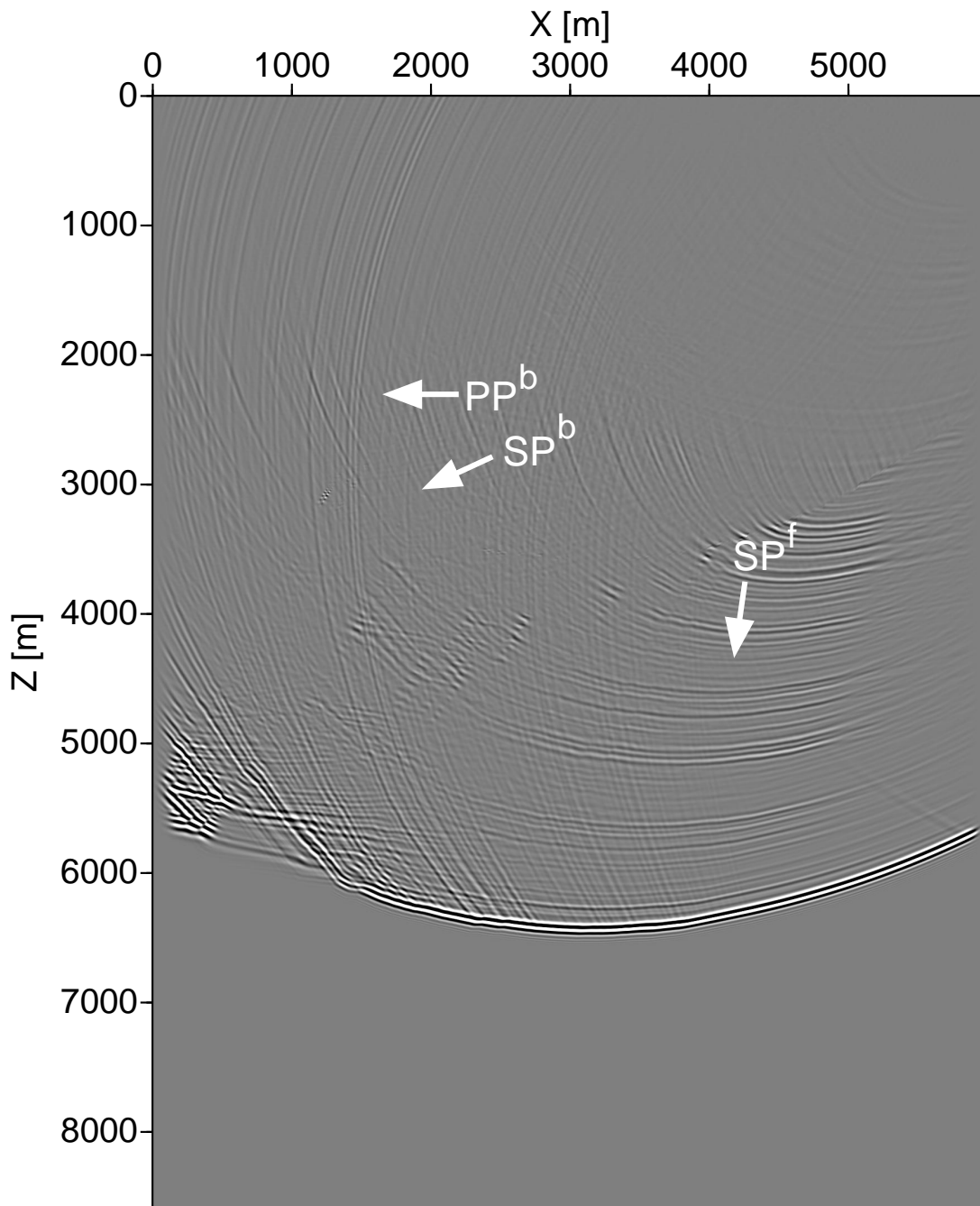


Fig. 8.15: The P-wavefield of the crustal velocity model shown in Figure 8.14 with a dip angle of 60° at travelttime $t = 1$ s, amplitude clipped. PP^b - reflected P-wave, SP^f - S-to-P converted wave in tranmission, SP^b - S-to-P converted wave in reflection.

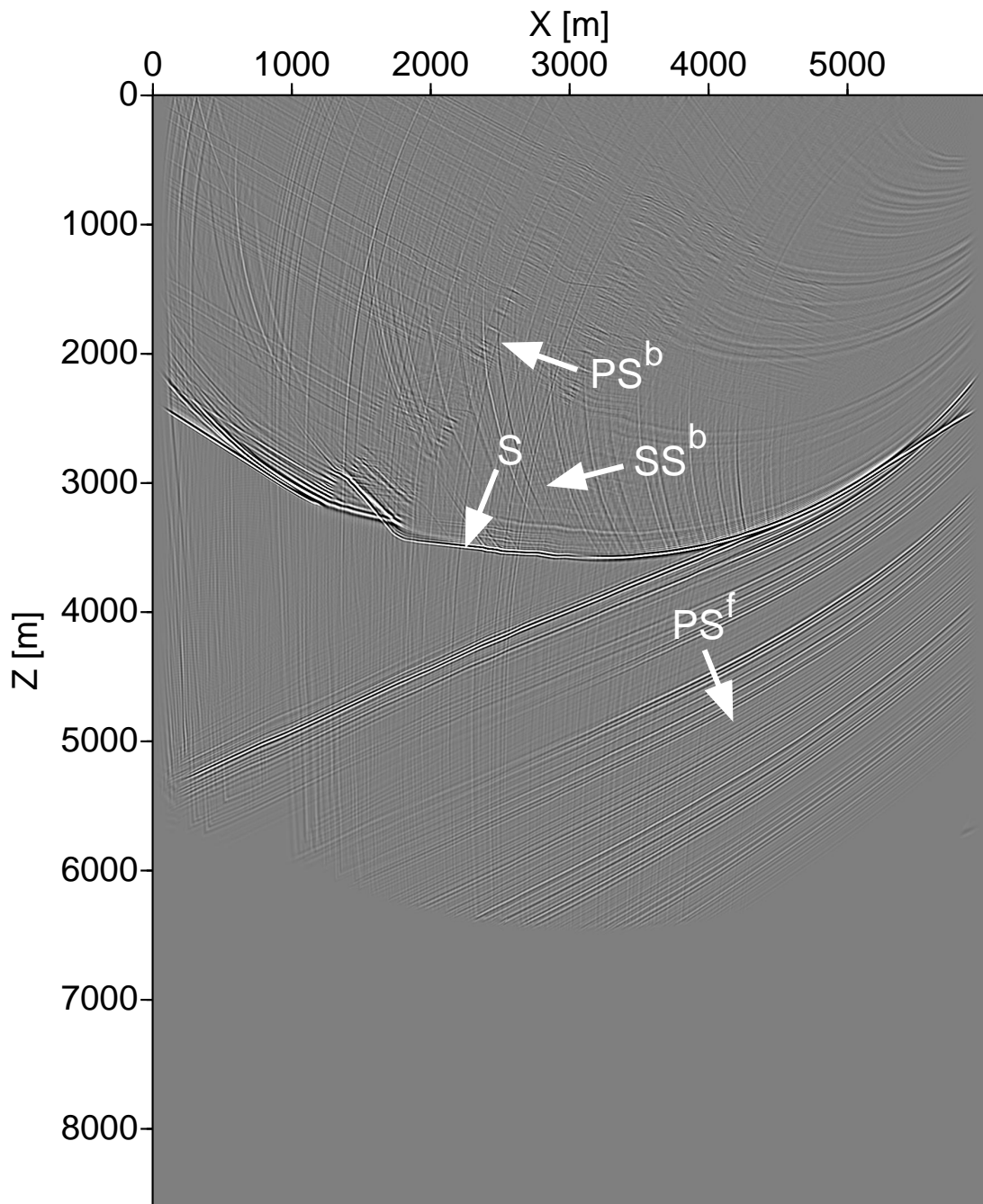


Fig. 8.16: The S-wavefield of the crustal velocity model shown in Figure 8.14 with a dip angle of 60° at travelttime $t = 1$ s, amplitude clipped. S - direct S-wave, SS^b - reflected S-wave, PS^f - P-to-S converted wave in transmission, PS^b - P-to-S converted wave in reflection.

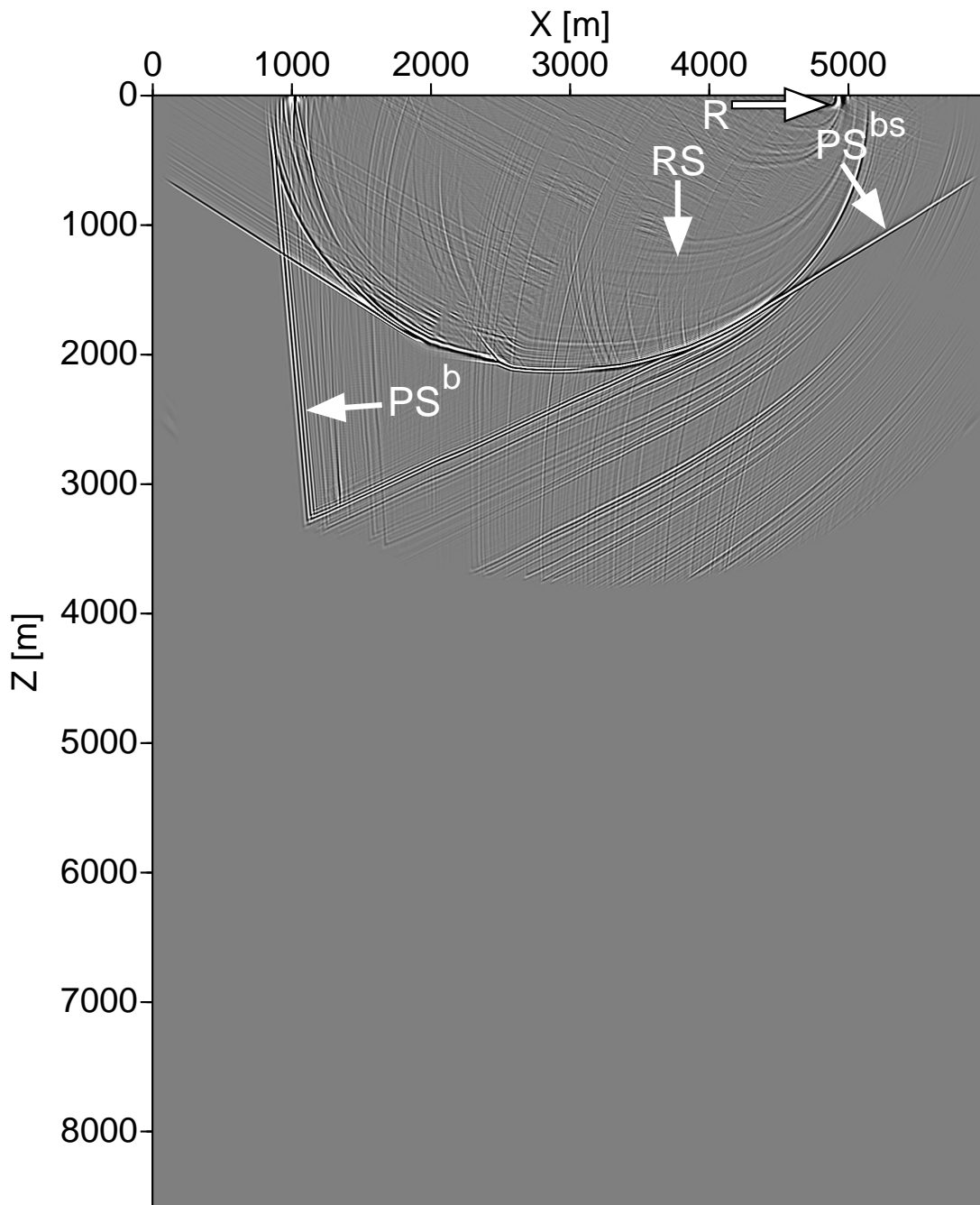


Fig. 8.17: The S-wavefield of the crustal velocity model shown in Figure 8.14 with a dip angle of 60° at traveltime $t = 0.6$ s, amplitude clipped. R - Rayleigh (surface) wave, RS - surface waves converted to S-waves, PS^{bs} - P-to-S converted wave, reflected at the surface, PS^b - P-to-S converted wave in reflection.

wavefield in the P-wave snapshot. Furthermore, all kinds of reflected and converted waves are detectable in the S-wave image. In front of the main S-wave the P-to-S converted waves in transmission are visible heading downward with a ray dip direction of about 50° (PS^f). This explains why the main S-wave and the P-to-S converted waves do not show the same apparent velocities in the horizontal component seismogram (Figure 8.19). The P-to-S converted waves in transmission are relatively strong compared with the other reflected or converted waves and originate from the same points where the reflected P-waves cross-cut the first break of the horizontal component seismogram. This is the position of the impedance contrast initiating these waves. In Figures 8.16 and 8.17 the corresponding P-to-S converted waves in reflection travel off to the left, barely visible. Because of their vertical oscillation they would show up as infinite apparent velocity in the vertical component seismogram (Figure 8.18). Here they do not because the amplitude of the first break is too large compared to their amplitudes. In the field data however, this wave is easily detectable in the vertical component seismogram (Figure 4.5 on page 33). There, this event is related to the SE1, the reflection of the Franconian Lineament fault zone, dipping with about the same dip as the layers in this model.

Stepping back in time (S-wavefield in Figure 8.17) additional waves are more easily detectable. Reflected S-waves, which are reflected at the layer boundaries and reflected a second time at the surface confuse the wavefield increasingly with time. Surface waves can be detected (R); at layer interfaces they convert into shear waves (RS). The strong surface induced P-to-S converted wave travels in front of the main S-wave at greater offsets (PS^{bs}). Barely visible, the interface induced P-to-S converted waves in reflection is also reflected at the surface. Many of these waves are only visible in the plot because the amplitudes were clipped. Although the model is very simple it already hints at the problems that can be encountered in the interpretation of seismic data. Apparent velocities in seismograms can lead to misinterpretations in the presence of steeply dipping layers.

The resulting seismic sections are shown in Figure 8.18 and Figure 8.19, both trace-normalized. The vertical component seismogram only shows the P-wave first break. It is simple as opposed to the corresponding field data (Figure 4.5). No multiple first break is detectable. It is basically just the representation of the model source signal. Reflected or converted waves are not apparent here because they are too weak compared with the first break signal amplitude.

The horizontal component seismogram (Figure 8.19) on the other hand shows a very complex behavior. The latest wave in the seismogram is the S-wave originating from the surface. It shows a slightly slower apparent velocity than the earlier P-to-S converted waves in transmission dominating the wavefield. The apparent velocity difference can be explained by the different travel paths of both wave types within the crust (compare Figures 8.16 and 8.17). These converted waves in transmission are stronger than the hyperbola shaped reflected P-wave onsets, a fact already observed in the analytical analysis in Chapter 7.

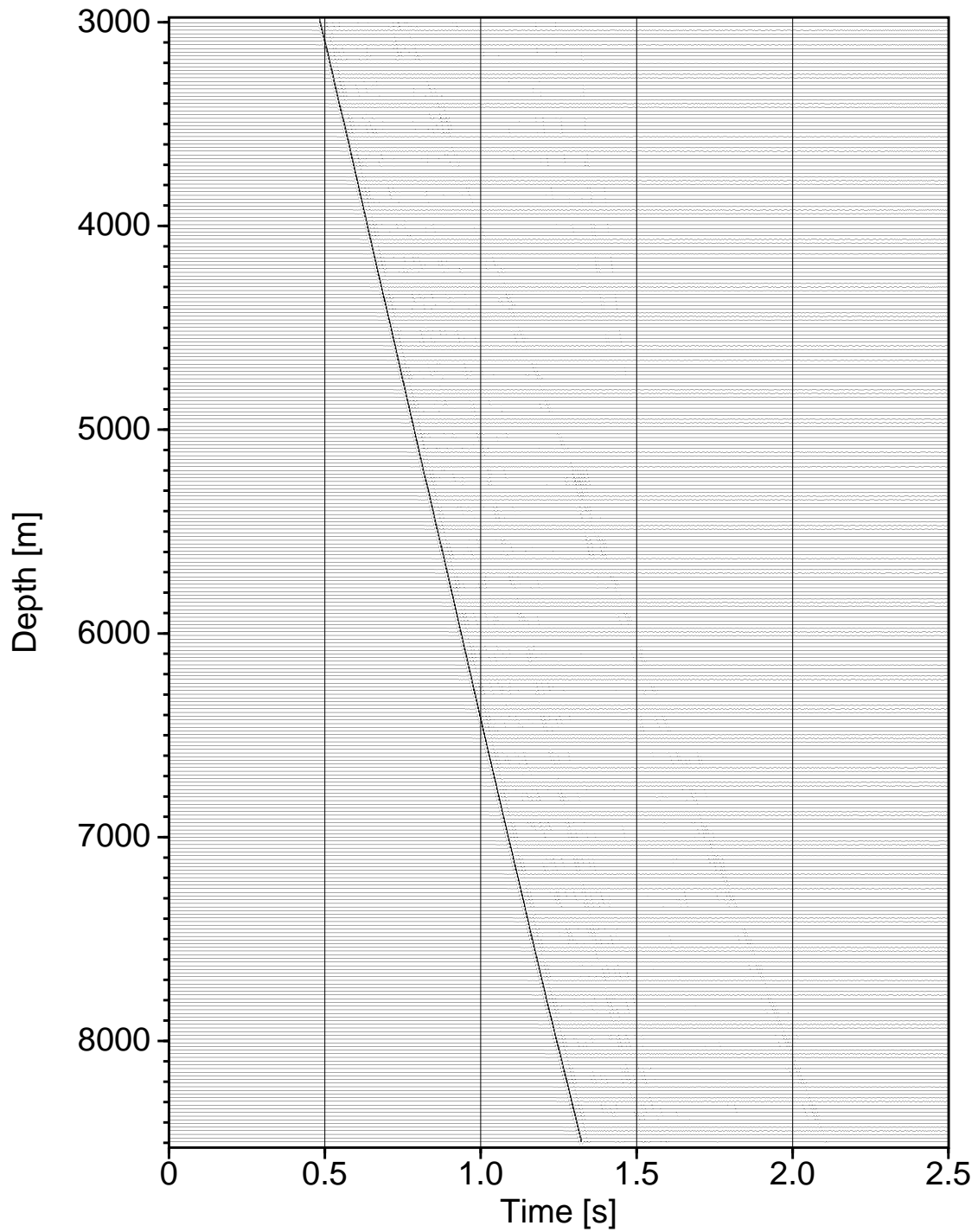


Fig. 8.18: The seismic section of the vertical component geophone of the crustal velocity model of Figure 8.14, trace-normalized. Because of its strong amplitude only the direct P-wave can be detected, with an average velocity of about 6.7 km/s for this depth section.

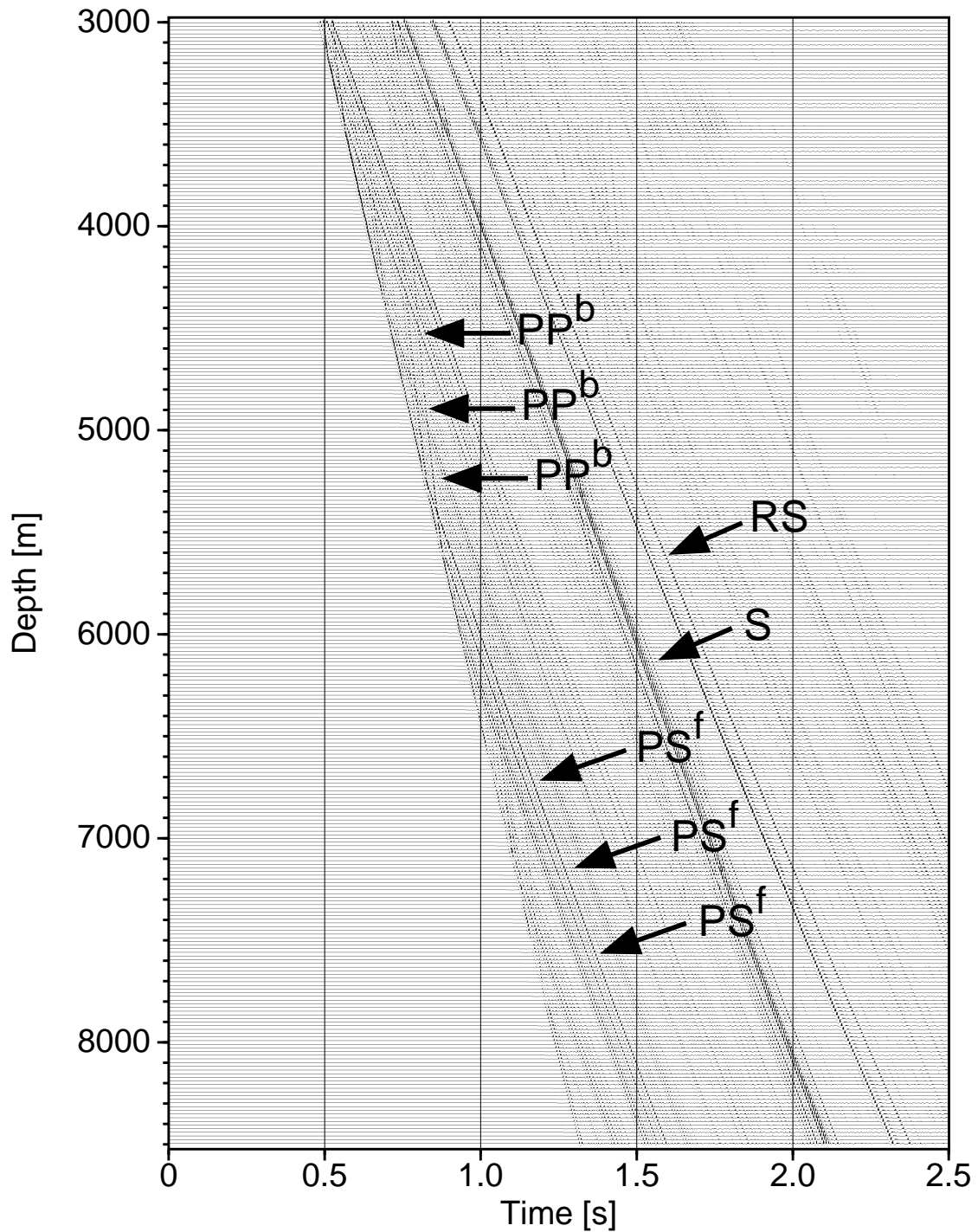


Fig. 8.19: The seismic section of the horizontal component geophone of the crustal velocity model of Figure 8.14, trace-normalized. PP^b - reflected P-wave, PS^f - P-to-S converted wave in transmission, S - direct S-wave, RS - surface waves converted to S-waves.

Amplitude Decay with Depth, Q

The amplitude decay of the P-wave with depth (Figure 8.20) was analyzed in the same manner as in Chapter 4. For comparison reasons the depth range is only shown from 3000 m downward. Because the FD calculation had been carried out with a 2D code the resulting geometrical amplitude decay is only $1/\sqrt{z}$. The intrinsic Q within the model was set to 10000, i.e., basically no intrinsic attenuation, in order to study the influence of the crustal structure on the quality factor Q. The amplitude drop at the bottom of the plot is a result of the absorbing frame around the model, necessary to prevent reflections from the model boundaries. Despite the high Q-value the amplitude values generally show short scale oscillations and some larger undulations. The latter can be related to (simulated) gneiss layers at about 3.0, 3.5, 5.3, and 5.5 km depth. Sudden decreases and increases of the amplitudes indicate interference phenomena because of the long signal wavelength compared to the layer thickness. However, the long scale amplitude decay is much smoother compared to the field data (Figure 4.9 on page 39).

To not interpret small scale interference phenomena the amplitude values were median filtered before the determination of Q, with a moving window length of 1000 m and an increment of 25 m, as in the field data analysis in Chapter 4. Again for comparison reasons, the resulting Q-values are depicted as $1/Q$ in Figure 8.21. Although Q was defined as 10000 in the model, Q-values as low as 200 were derived from the calculated seismic data, with values around 1000 being common. Negative Q-values are also present. Long scale oscillations of Q can be found, as in the field data on page 41, except that values are mainly positive. It seems, even though some smoothing had been carried out before the derivation of Q the intrinsic Q-values cannot be reproduced with this method. This is not surprising however, since part of the energy converts into S-waves not being considered in the amplitude decay of the P-wave. But even the consideration of converted waves cannot not explain negative Q-values. Thus, any method not taking the phase of the signal into account is not able to explain the whole phenomenon of signal decay with depth, or correct Q-values, respectively.

Octave Analysis of Amplitude Decay and Q

As in the field data analysis, the P-wave amplitude behavior with depth and Q of the FD modeled data were also analyzed within the four octaves from 15-240 Hz. The amplitude share of each octave was determined by normalization of the amplitude of the whole bandwidth at every depth position to account for any signal decay, with subsequent octave bandpass filtering and amplitude picking. The result is plotted in a figure presenting the share of each octave of the P-wave signal at every depth position (Figure 8.22). Whereas the corresponding field data plot (Figure 4.12 on page 43) shows strong, large scale variations of the shares along the borehole, only small scale variations can be found in the values of this (rotated 1D) model. But even these small-scale oscillations often show opposing amplitude extrema of the 60-120 Hz octave

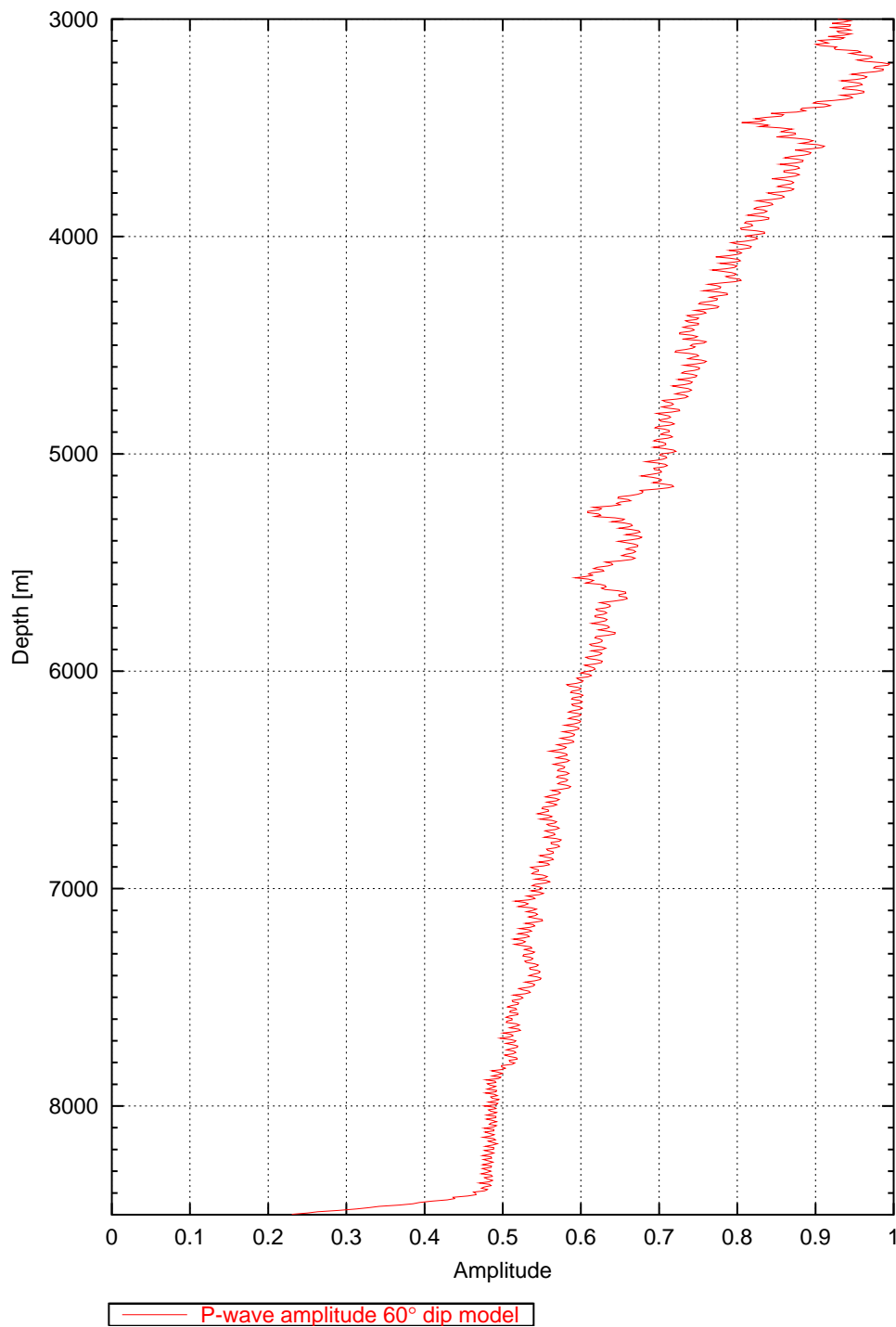


Fig. 8.20: Amplitude decay of the P-wave first break with depth in the 60° layer dip model. Note that the data were calculated in 2D resulting in a geometrical spreading of $1/\sqrt{z}$. The amplitude drop in the lower end results from the damping frame around the model.

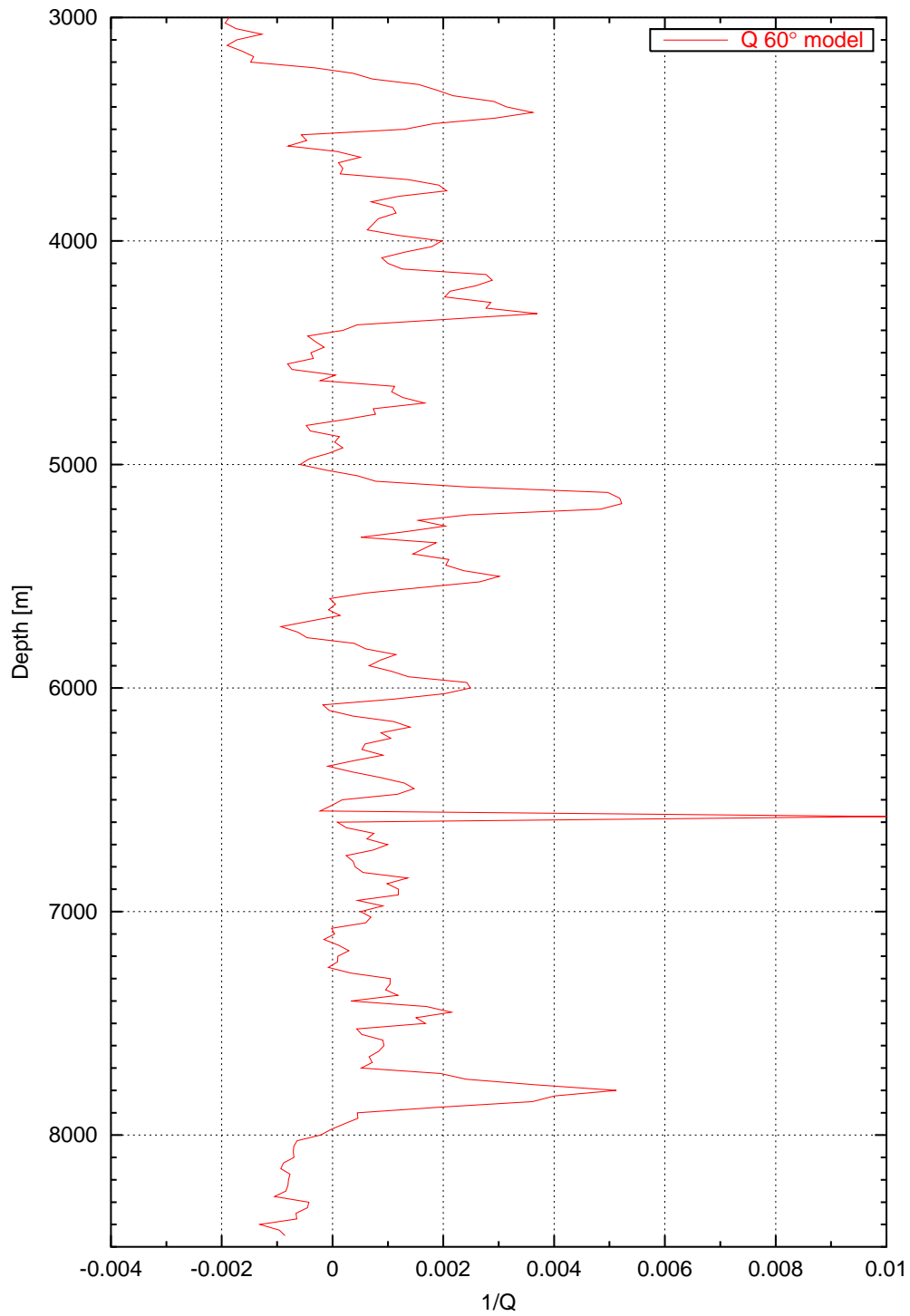


Fig. 8.21: Quality factor Q derived from median filtered amplitude values with a moving filter window length of 1000 m and increment of 25 m.

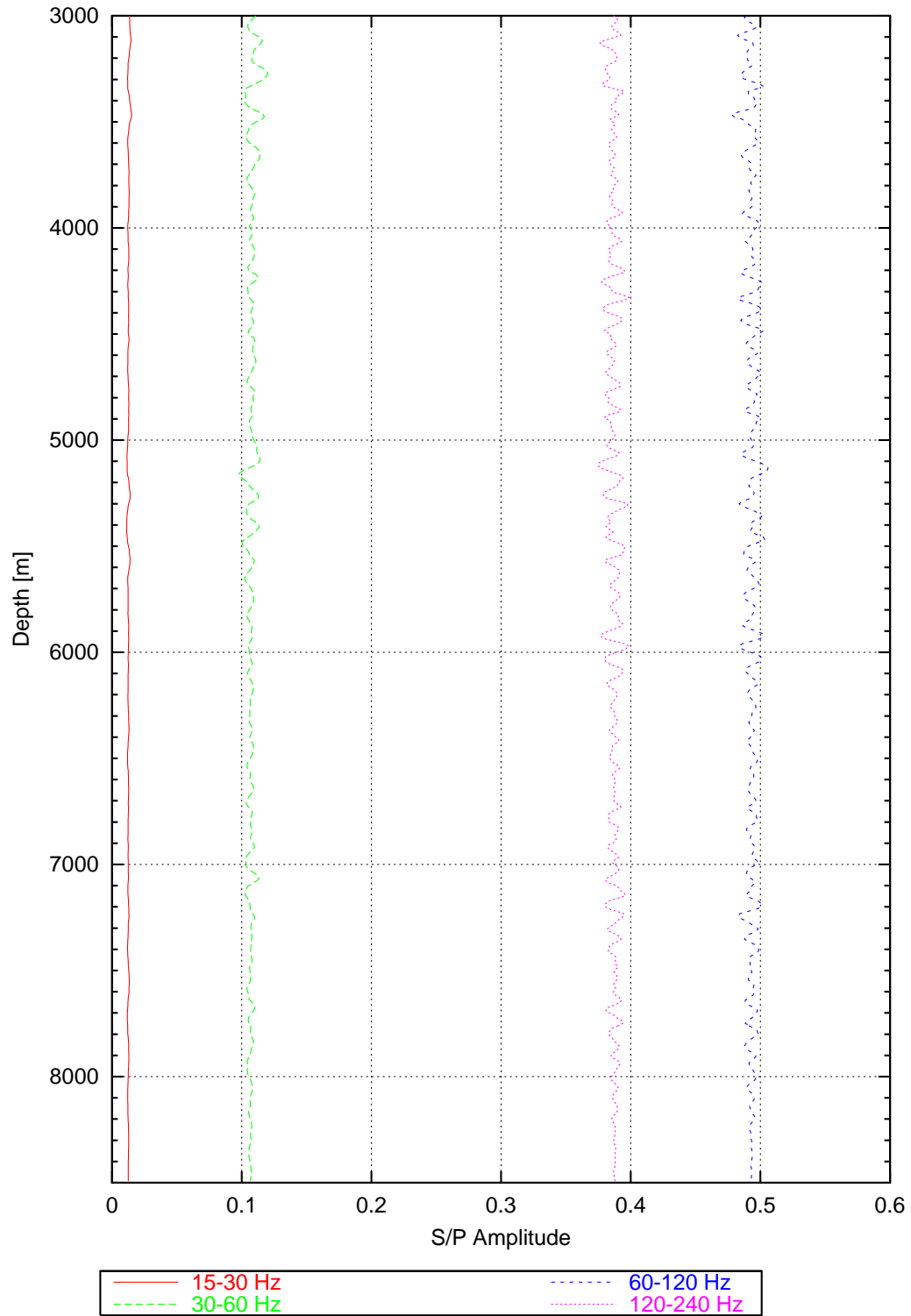


Fig. 8.22: Amplitude share of each of the four main octaves making up the signal of the downward traveling P-wave first break with respect to depth.

values compared to the ones from other octaves, an observation similar to the field data observations, but at smaller scale.

The corresponding Q-values along the borehole are depicted in Figure 8.23 with respect to octave. Again, the values do not oscillate as strong as the corresponding field data values (Figure 4.13 on page 45). The small scale oscillations are suppressed by the median filter of the amplitude values. Therefore, a possible opposing behavior of the 60-120 Hz octave Q-values cannot be observed. Because the low frequency octave accounts for only a minor percentage of the whole signal, its influence on the full spectrum Q is almost neglectable, although it seems dominant in Figure 8.23.

P-to-S Conversion Logs

In Chapter 5 the definition and processing of P-to-S conversion in transmission logs was described in detail, the subsequent interpretation of these logs in Chapter 6. A resolution test of this method was carried out at the beginning of this chapter.

The conversion logs resulting from this 60° model for the whole frequency range are shown in Figure 8.24 (true phase) and Figure 8.25 (envelope stack). The corresponding octave analysis is shown in Figures 8.26 (15-30 Hz), 8.27 (30-60 Hz), 8.28 (60-120 Hz), and 8.29 (120-240 Hz). Since analytical calculations for this model also exist in Chapter 7 and this model basically represents the simulated crack free mineral composition sequence of the rocks found in the borehole, the results of this analysis mark a pivot of this work. Important restrictions compared with the in situ situation are the simplification of the crustal structure to a 2D finite difference model and the simple rotated 1D layer sequence not representing the true dip and true azimuth of the foliation.

The basic features of the full spectrum true phase and envelope conversion log plots (Figures 8.24 and 8.25) correlate. However, in more detail some differences are obvious. The amplitudes differ by about one percent point. This can very likely be related to destructive interference in the stacking process of the true phase data, because even in this simple model the f-k filter and the residual static calculations cannot align the different onsets perfectly.

The impedance contrasts related to gneiss layers at 3.0, 3.5, 5.3, 5.5 and 5.8 km or an amphibolite intercalation at about 7.2 km depth can be traced in the logs. A structure around 6 km depth produces strong conversions, although no strong impedance contrasts seem to be present. Here, resonance effects might be responsible.

One of the important parameters under observation is the order of the conversion from P to S compared with the field data conversion because the main difference between the two media is the influence of cracks. The maximum conversion in the envelope plot is close to 6%, with the low level around 1%. This is about one third of the corresponding values found in the field data conversion logs. The true phase analytical calculations of this model, discussed in Chapter 7, match surprisingly well, except that the analytical values are only valid for a high frequency approach and the main signal frequency in the FD calculations is 80 Hz. Furthermore, it seems the differences

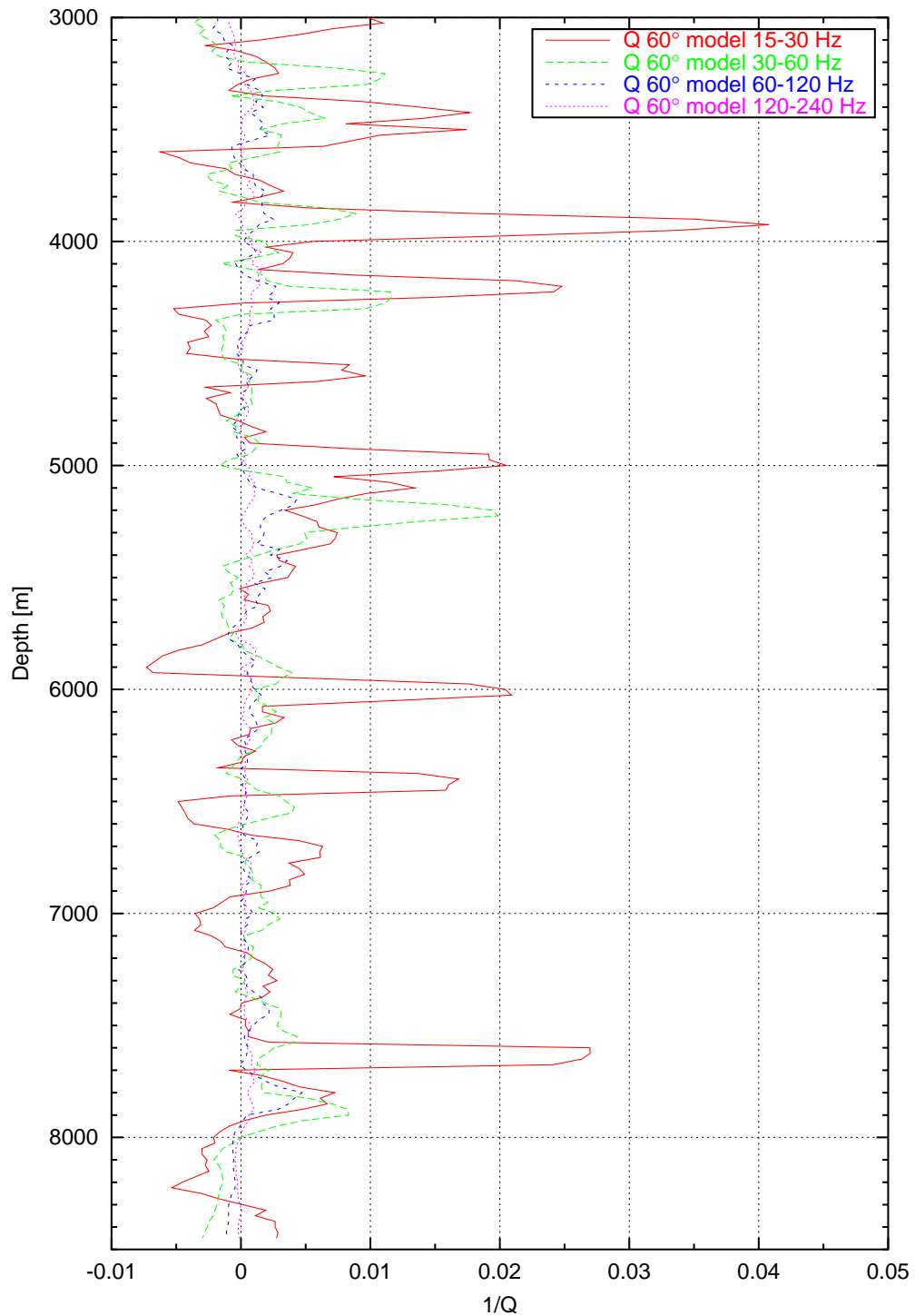


Fig. 8.23: Octave separated inverse quality factor Q , determined with median filtered amplitudes with a moving window length of 1000 m and an increment of 25 m.

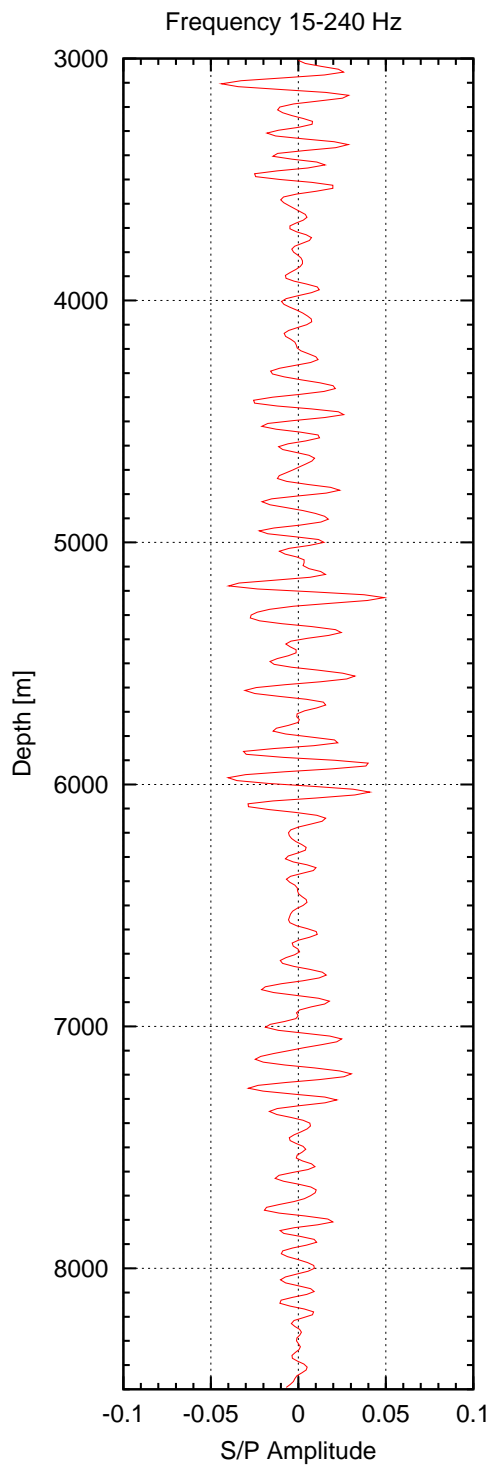


Fig. 8.24: Conversion log of the simple 60° dip model, stack of a small number of traces, true phase, full spectrum.

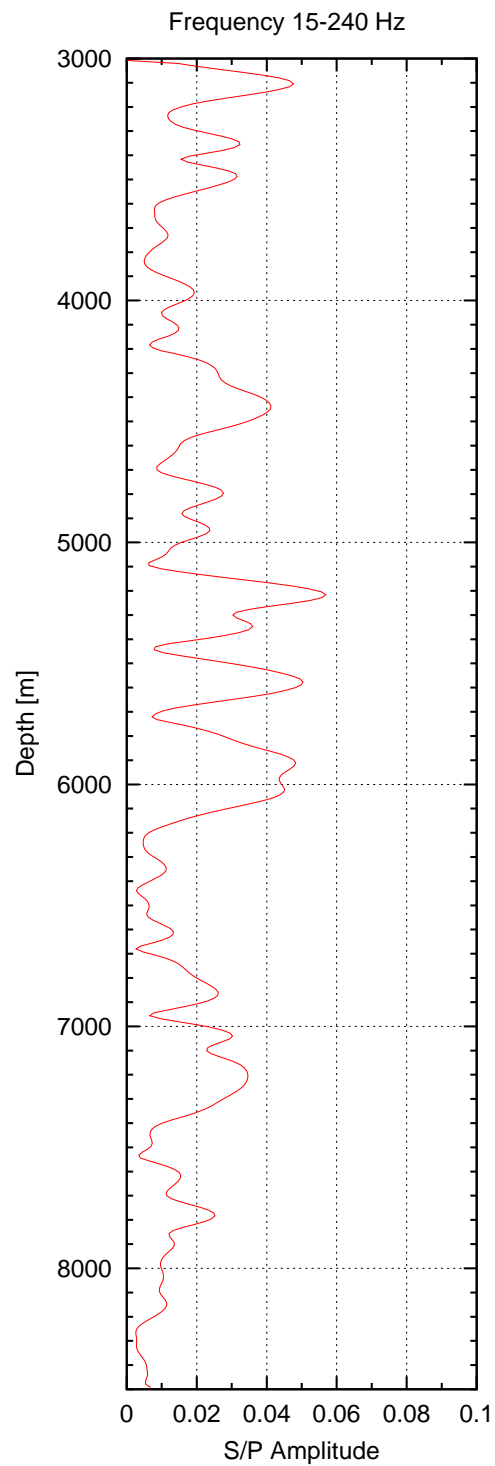


Fig. 8.25: Conversion log of the simple 60° dip model, envelope stack of a small number of traces, full spectrum.

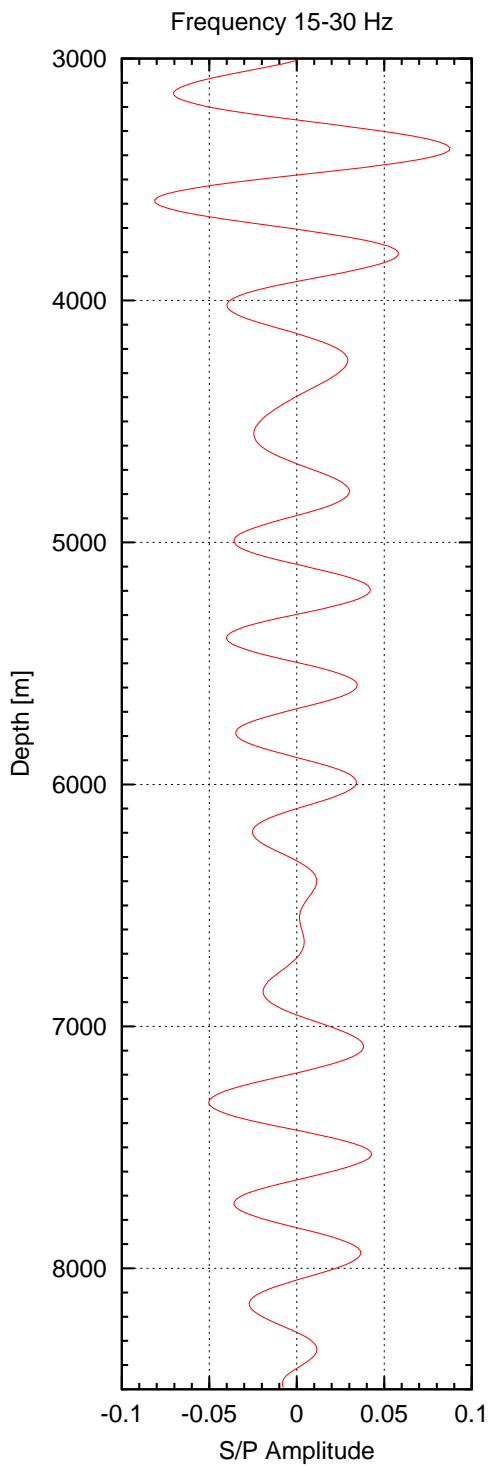


Fig. 8.26: Conversion log of the simple 60° dip model, stack of a small number of traces, true phase, frequency range 15-30 Hz.

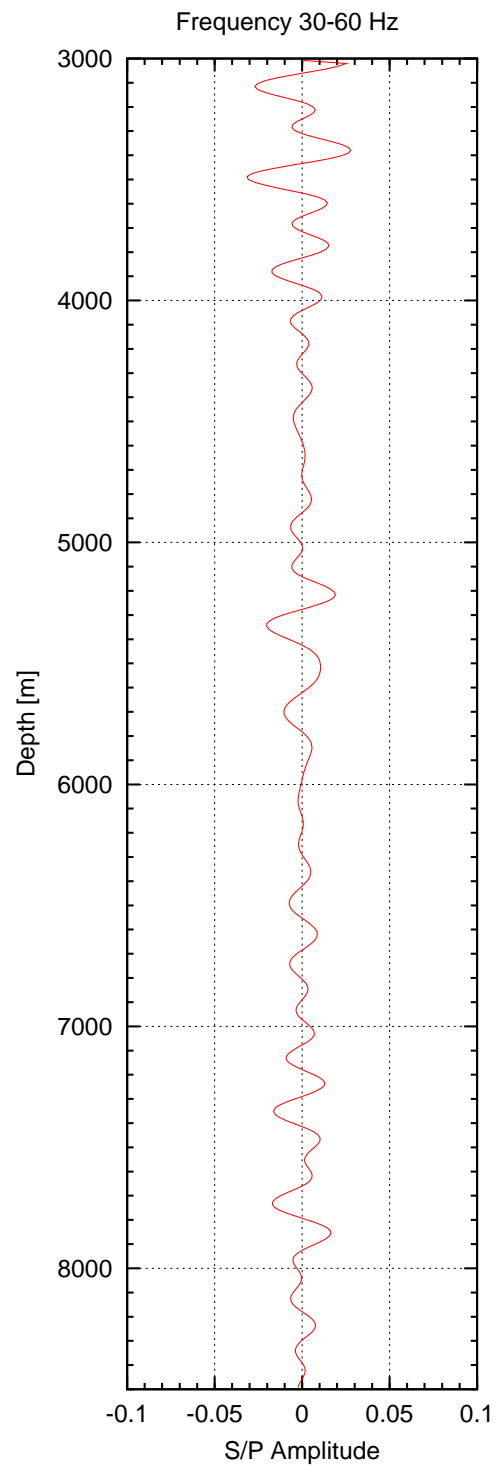


Fig. 8.27: Conversion log of the simple 60° dip model, stack of a small number of traces, true phase, frequency range 30-60 Hz.

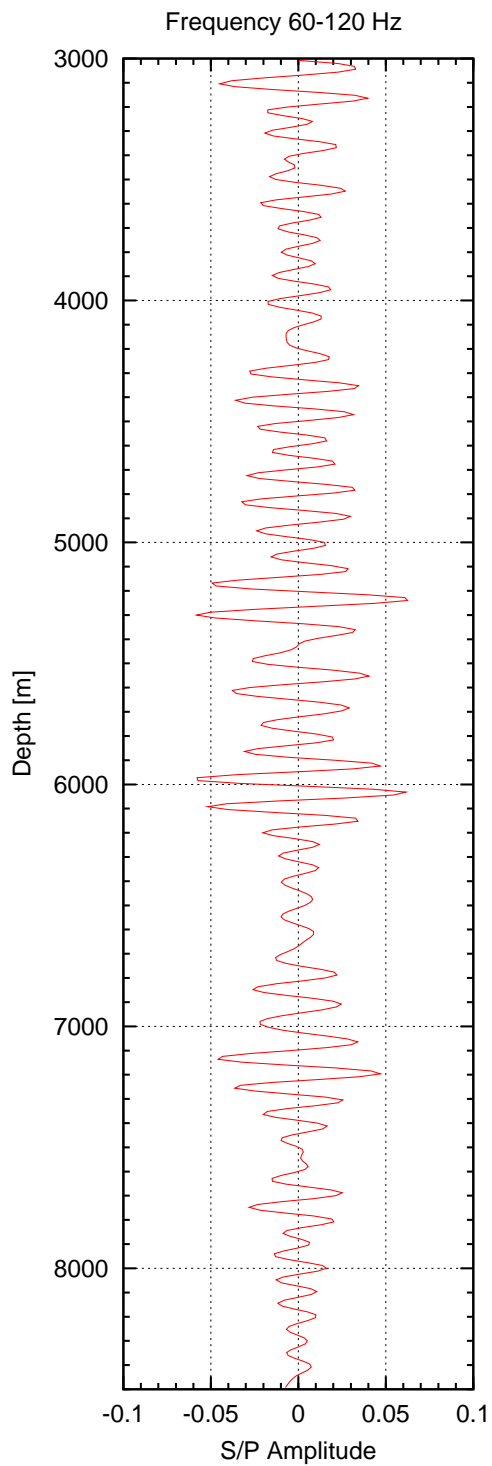


Fig. 8.28: Conversion log of the simple 60° dip model, stack of a small number of traces, true phase, frequency range 60-120 Hz.

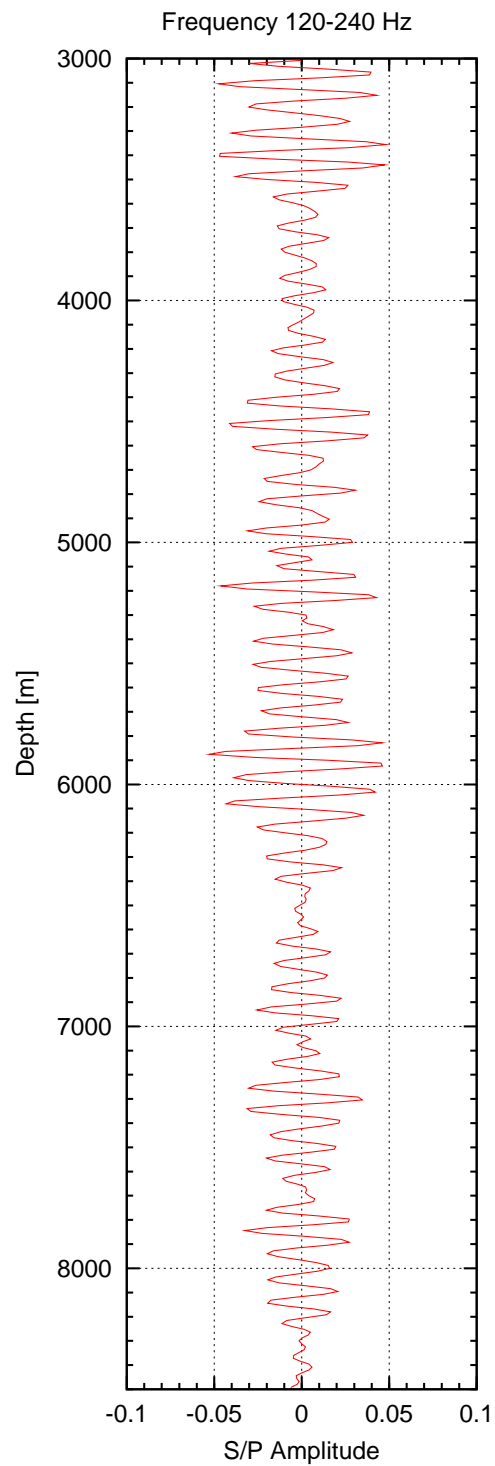


Fig. 8.29: Conversion log of the simple 60° dip model, stack of a small number of traces, true phase, frequency range 120-240 Hz.

are less pronounced as expected from the resolution test in Section 8.1. Perhaps the geometrical spreading close to the source has some influence on that resolution test as compared to the analytical calculations.

A basic similarity between the conversion logs of this model and the field data, especially with the S1 component, can be identified, which is a confirmation of the success of the inversion process for the determination of crack-free elastic parameters of the crust at the KTB site. Since the influence of the complicated crustal structure apart from the petrophysical parameters is not included in this model, this correlation is a surprise to some degree.

A usual frequency dependency is observable. Different parts of the spectrum seem to be differently sensitive to the impedance contrasts, depending on the similarity of layers within a depth range (blocking). The smaller the intercalation (block) the stronger the resulting conversion in the high frequency range and vice versa.

A surprising observation in the field data was the existence of an unusual frequency dependency of the conversion with the second octave showing unusual small conversion values. The latter was first thought to be influenced by the 50 Hz notch filter, necessary to suppress contaminating mains. A similar frequency dependency can be found in the model data, however (Figures 8.26-8.29). Therefore, this effect seems to be universal. The effect in the model data is obvious but not as prominent, i.e., the conversion in the octave 30-60 Hz is not as weak as in the field data. To study this dependency in more detail and because of the restrictions concerning the dip and azimuth of the foliation, more complicated models were also FD calculated, one of which is discussed in Section 8.2.2.

Comparison of Attenuation and Conversion

In a first order comparison of the full spectrum Q plot (Figure 8.23) with the full spectrum conversion plot (Figure 8.25) there seems to be some correlation. However, since the determination of Q included some smoothing of amplitude values the two plots cannot correlate perfectly. For a simple model like the one presented in this section there seems to be room for more detailed analysis work with better techniques for the determination of Q, though. Perhaps then a correction of the apparent Q-values with corresponding conversion values is possible.

8.2.2 Complex Model

The end-member in the sequence of calculated FD-models is the model shown in Figure 8.30 (P-wave velocities). It was created to incorporate features like dip and azimuth of the foliation but also a simple simulation of fault zones. Again, the main difference compared to the field data is the lack of in situ anisotropy and cracks or fissures. Because of the limitation to 2D, the azimuth of the in situ dip of the foliation comprising 360° had to be simplified by rotation onto a 2D plain at every depth position in a special way, to prevent crossing layers. This method does not perfectly project the in situ

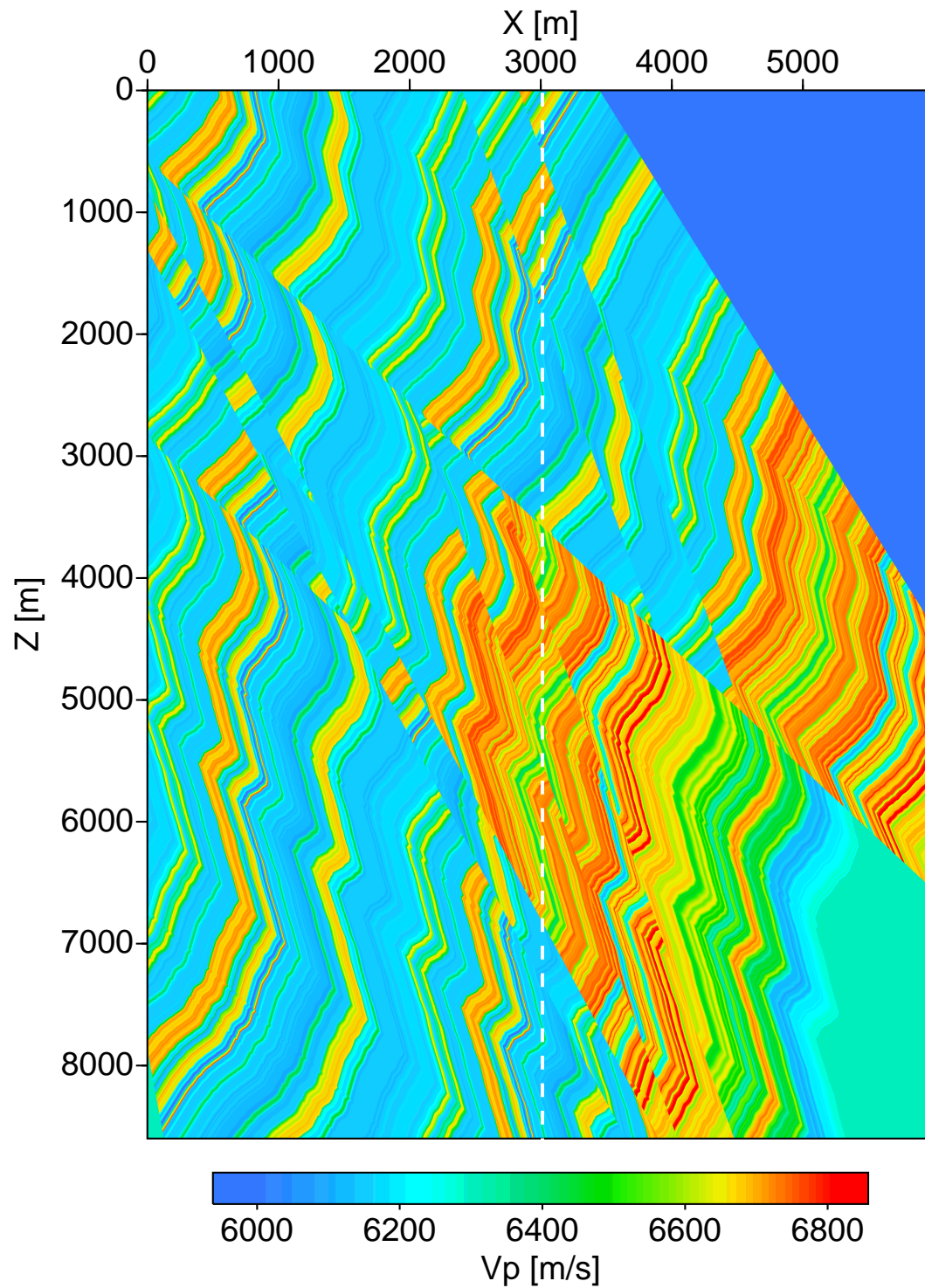


Fig. 8.30: A crustal velocity model with applied in situ rock unit dip angle and in situ azimuth of the dip, projected onto a 2D plain. 5 simulated fault zones are added. The location of the simulated borehole is indicated at $x = 3000$ m.

situation into 2D but results in a more realistic appearance of the crustal model. Random layer sequences on the left and right were added to simulate in situ existing crustal structures without knowing their explicit parameters. This does not alter the resulting calculations much, however, since the analysis is focused on the downward traveling wavefield. The fault zones were introduced in a simple manner. No fault zone specific properties are taken into account here; fault zones are just local impedance contrasts coming into existence through displacement of parts of the model along these faults, similar to normal or reverse faulting in nature. These fault zones make it possible though, to simulate the high velocity zone in the central part of the borehole. A simplification of the Falkenberg granite on the right, between $x = 3500\text{--}6000$ m, was also added. The resulting model can be described as the complex counterpart of the basic model introduced by Hirschmann (Figure 2.3 on page 8) and calculated by D. Okaya (personal, communication, 2001). The main difference between the two is the thin layering in this end-member model.

Wavefield snapshots of this model are shown in Figure 8.31 (P-wavefield at travelttime $t = 1$ s), Figure 8.32 (S-wavefield at travelttime $t = 1$ s), and Figure 8.33 (S-wavefield at travelttime $t = 0.6$ s). The resulting seismic sections are shown in Figure 8.34 (vertical component) and Figure 8.35 (horizontal component). The most striking feature in the P-wave snapshot at $t = 1$ s is the far more complicated first break, than the one resulting from the 60° model. A lot of diffractions make the detection of a single first break almost impossible. In fact, the differentiation of reflected and transmitted P-waves does not seem possible at all. The first break shows up in the vertical component seismogram (Figure 8.34) as a multiple, reverberating signal very similar to the one seen in the field data (Figure 4.5), discussed in Section 4.4.1 on page 32. Also the increase in the number of multiples in the later wavefield of the lower part of the borehole is similar to the field data. The result: a simple source signal produced by the explosive source in the field experiment can show up as a complicated first break in the vertical component seismogram of the field data, due to the impedance structure of the crust at the KTB site. The first break hence only represents the complicated local velocity and density structure. This explains why deconvolution on the field data failed to work. The choice of a simple wavelet for the FD-modeling seems to be adequate.

An alternative concept to the deconvolution of the first break signal for the extraction of the source signal could perhaps be the use of the signal polarization. The orientation of each wavefront within the first break coda due to multi-pathing varies. As can be seen in Figure 8.31, the bigger the time lag between the first break and following onsets the bigger the difference in the dip of the wavefronts, or of the polarization ellipsoids, respectively. A polarization filter could possibly be a good tool for suppressing the sideswipe energy to focus a wave analysis into a certain direction. This might work better than an f-k or τ -p filter. But perhaps a combination of one of these techniques with a polarization filter could serve as a more sophisticated tool.

As in the 60° dip model, the S-wavefield (Figures 8.32 and 8.33) is generally far more complicated than the P-wavefield. The focusing and defocusing is not as prominent in the main S-wave in comparison to the main P-wave though. Partly the ampli-

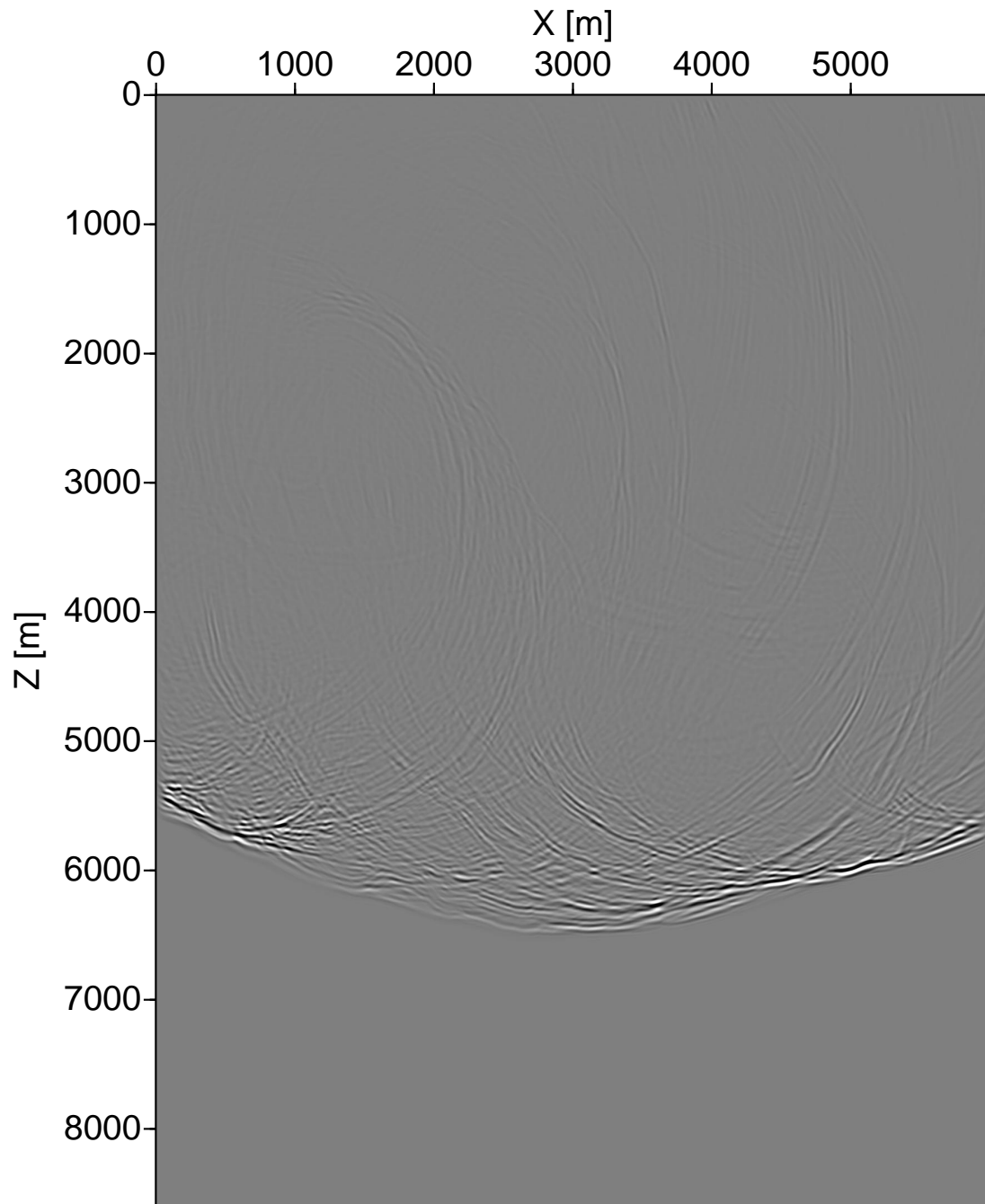


Fig. 8.31: The P-wavefield of the crustal velocity model shown in Figure 8.30, at traveltime $t = 1$ s, amplitude clipped.

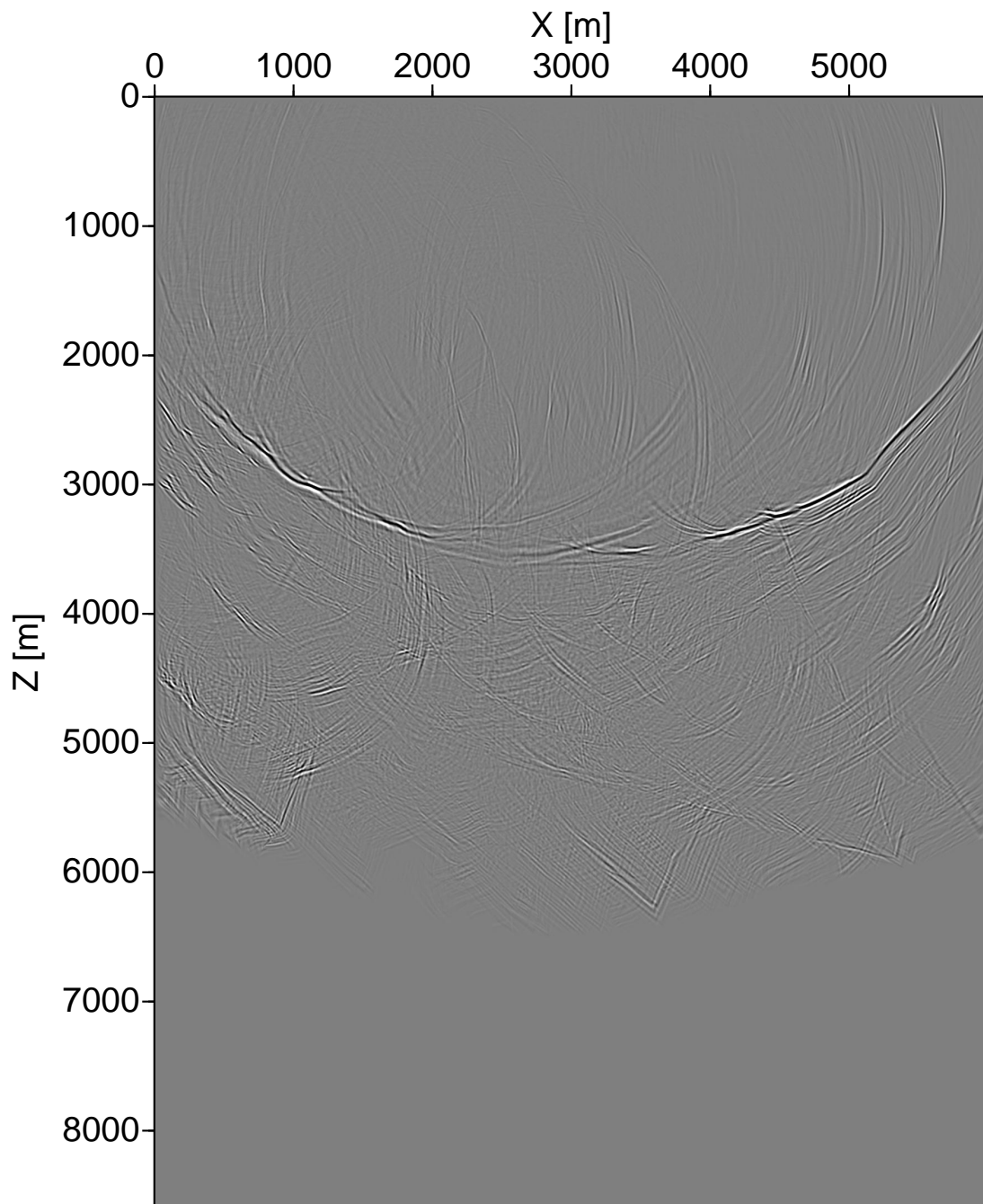


Fig. 8.32: The S-wavefield of the crustal velocity model shown in Figure 8.30, traveltime $t = 1$ s, amplitude clipped.

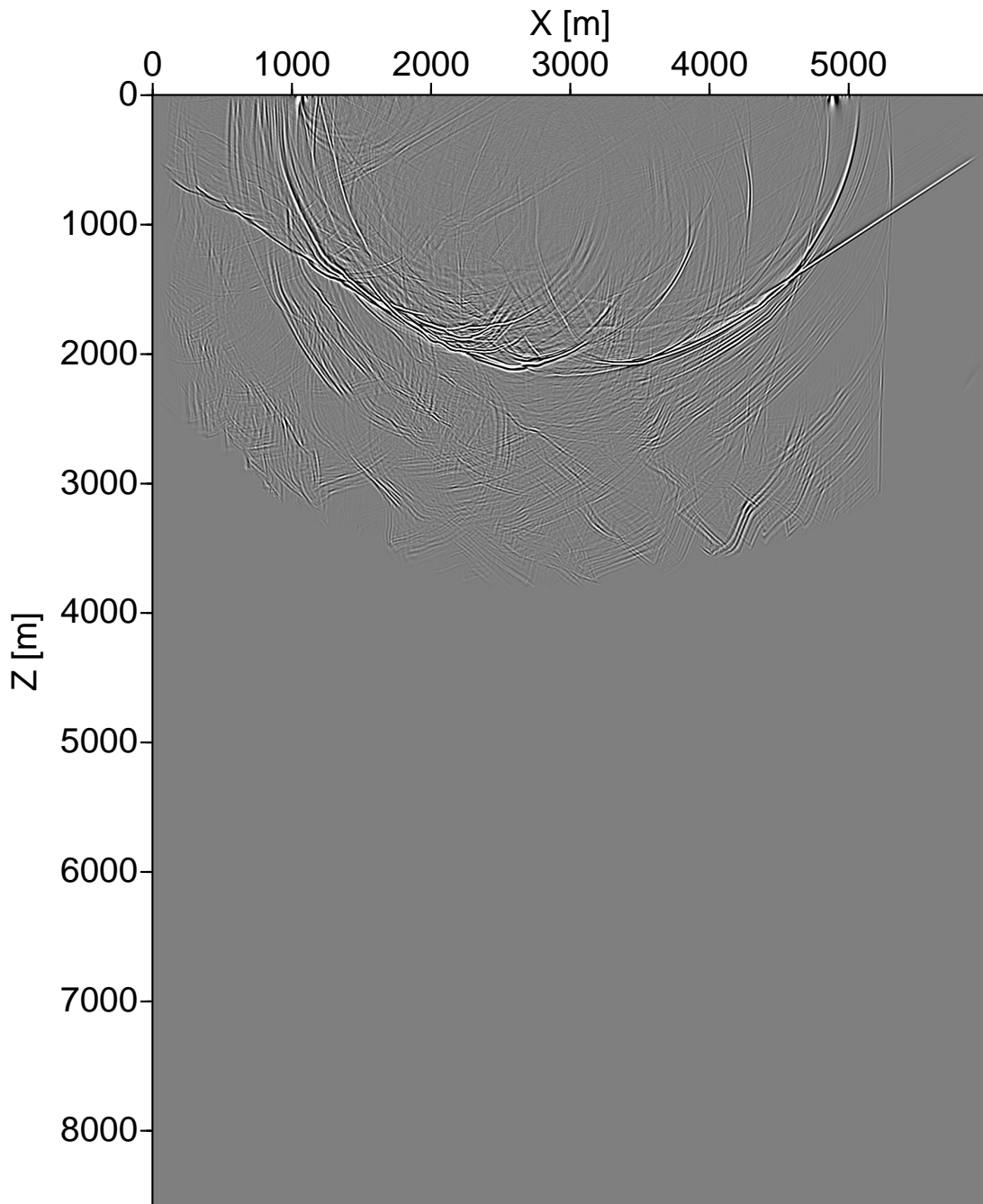


Fig. 8.33: The S-wavefield of the crustal velocity model shown in Figure 8.30, at traveltime $t = 0.6$ s, amplitude clipped.

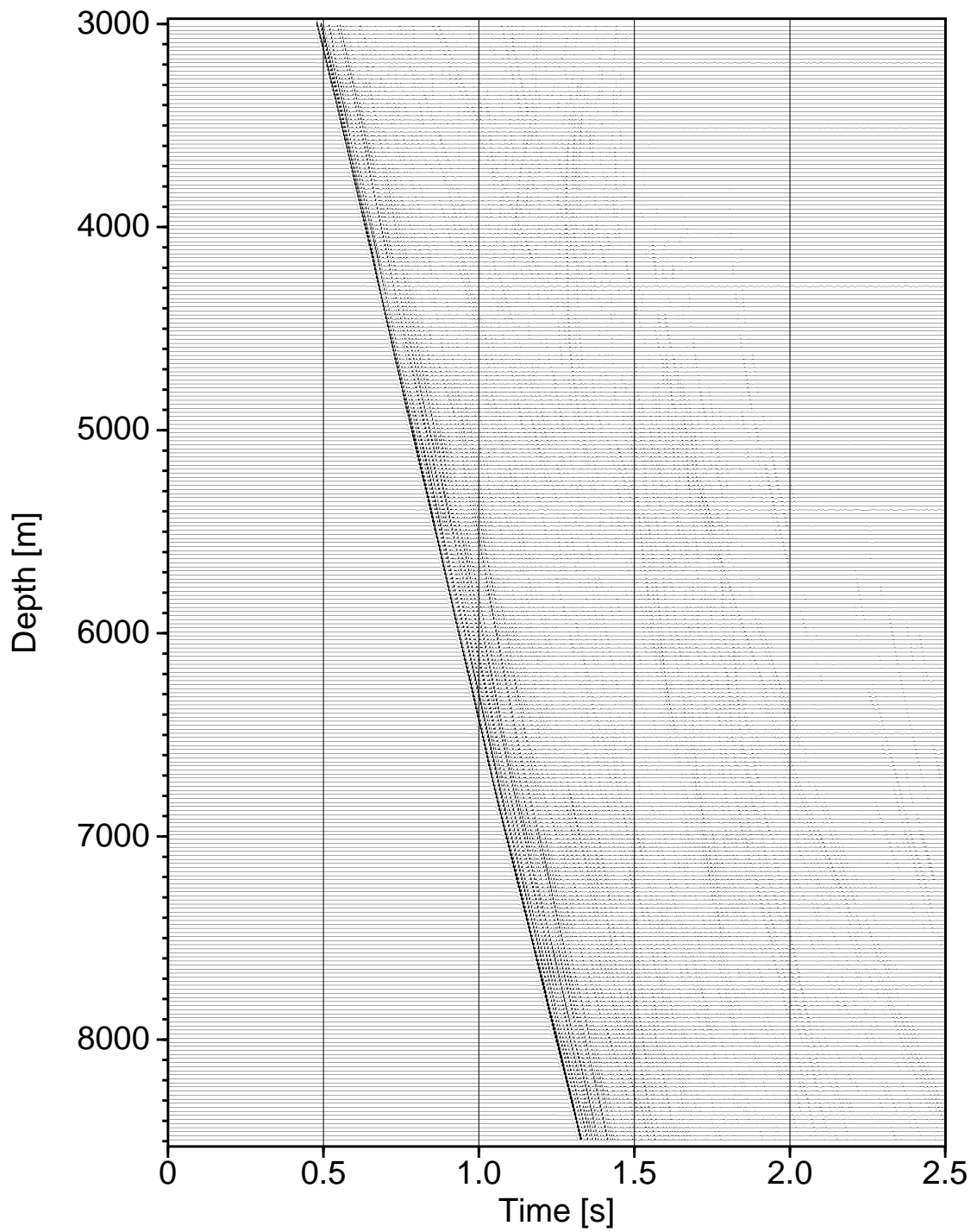


Fig. 8.34: Seismic section of the vertical component of the crustal velocity model of Figure 8.30, trace-normalized.

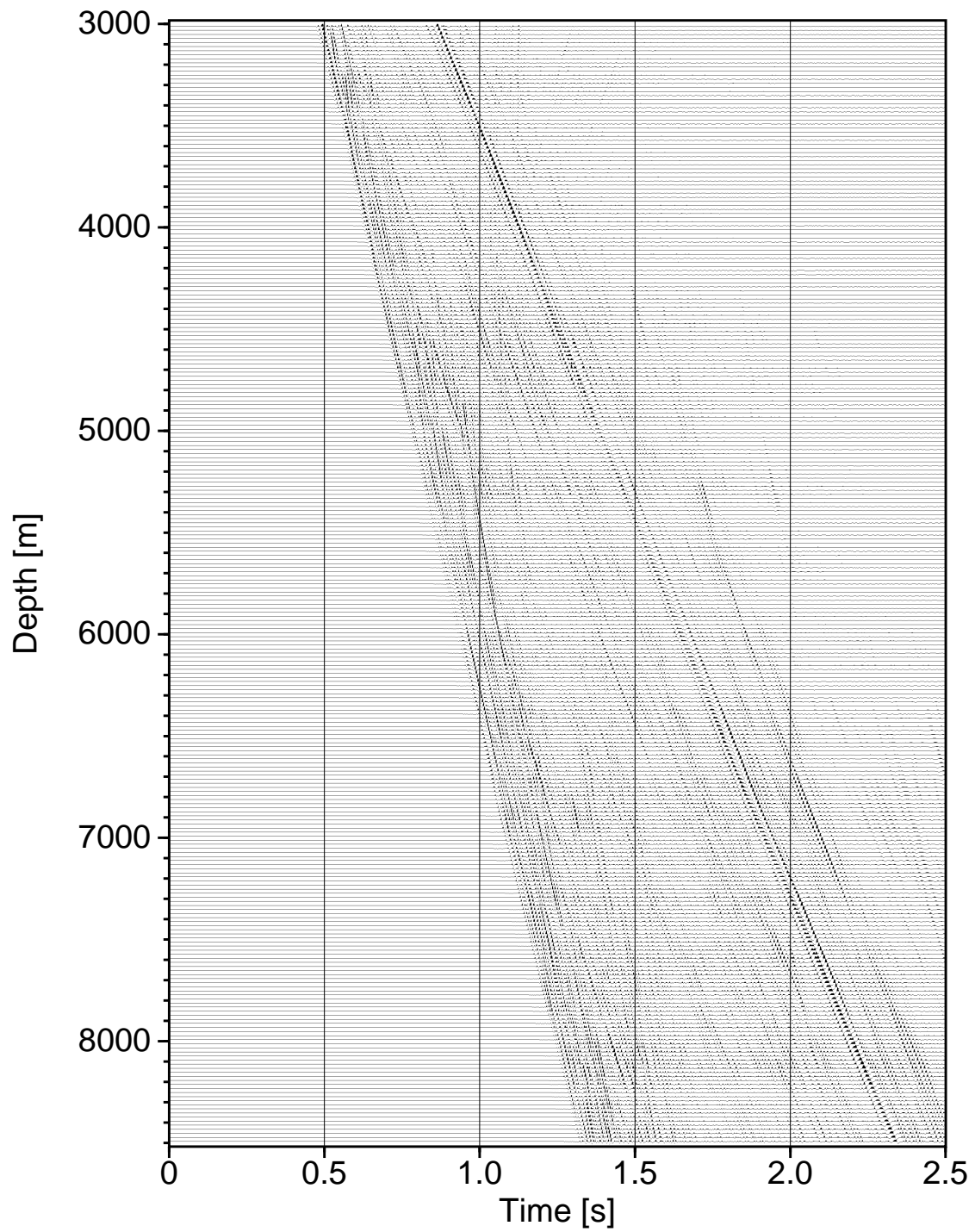


Fig. 8.35: Seismic section of the horizontal component of the crustal velocity model of Figure 8.30, trace-normalized.

tude seems weak compared with coda S-wave branches, explaining the problems of picking the first break time of the S-waves in the field data (Fischer, 2000).

In front of the main S-wave all kinds of P-to-S converted waves in transmission and reflection are present. Multiple conversion is also possible for each wave type but unlikely to be detectable here, because of the weak resulting amplitudes. P-to-S conversions in reflection off the Franconian Lineament fault zone are observable in the vertical component seismogram (Figure 8.34) but they are far from being as prominent as in the field data (Figure 4.5).

There seems to be no basic travel direction of P-to-S converted waves in transmission, rather they seem to travel into many directions or enter the borehole from many directions, respectively. This can explain the small scale differences in the velocities of the P-to-S converted waves observed in the field data seismograms. This can also explain, why it seems important to stack only a few traces for the deduction of the conversion-log and not scan too far into the later wavefield for the analysis of the close vicinity of the borehole. Too much noise from offset converters would disturb the image. The vicinity of the borehole is rather represented by the immediate time window starting at the P-wave first break.

The wavefield images can also explain how a classical VSP basically already acts as a polarization filter looking into the crust. Amplitudes of waves crossing the borehole from the sides are naturally suppressed by the geophone geometry. The horizontal geophones catch up the smaller amplitudes the more horizontal the S-waves' ray direction. Without optimizing the amplitude of the incoming S-wave by means of rotation of the oscillation ellipsoid the less disturbed the evidence of the downward traveling wave information close to the borehole. In this case this is an advantage. However, there seems to be much room for a sophisticated adaptive polarization filter and analysis tool in the processing and interpretation of VSP data especially in focusing on special target areas within the crust.

Amplitude Decay with Depth, Q

The analysis of the amplitude decay (Figure 8.36) and Q (Figure 8.37) was carried out as in the field data analysis and the 60° model analysis. Again, note that the geometrical spreading is not $1/z$ but $1/\sqrt{z}$ because of the 2D nature of the model. The trace spacing was not 2 m as in the 60° model but only 6 m. This could be the reason why a small scale amplitude oscillation as observed in the 60° model amplitude decay is not resolvable. The large scale oscillation seems to be exaggerated compared with the *field data* (Figure 4.9). At a closer look however, these apparent differences are not as prominent, because the small scale oscillations in the field data camouflage the large scale ones. That the exact extrema do not always correlate is not surprising, since the exact impedance contrasts and the crustal structures could not be modeled or are not known exactly, respectively. Besides, the lack of the third dimension in the model should have an additional impact.

The analysis of the Q-value plots of the different data sets shows far more correla-

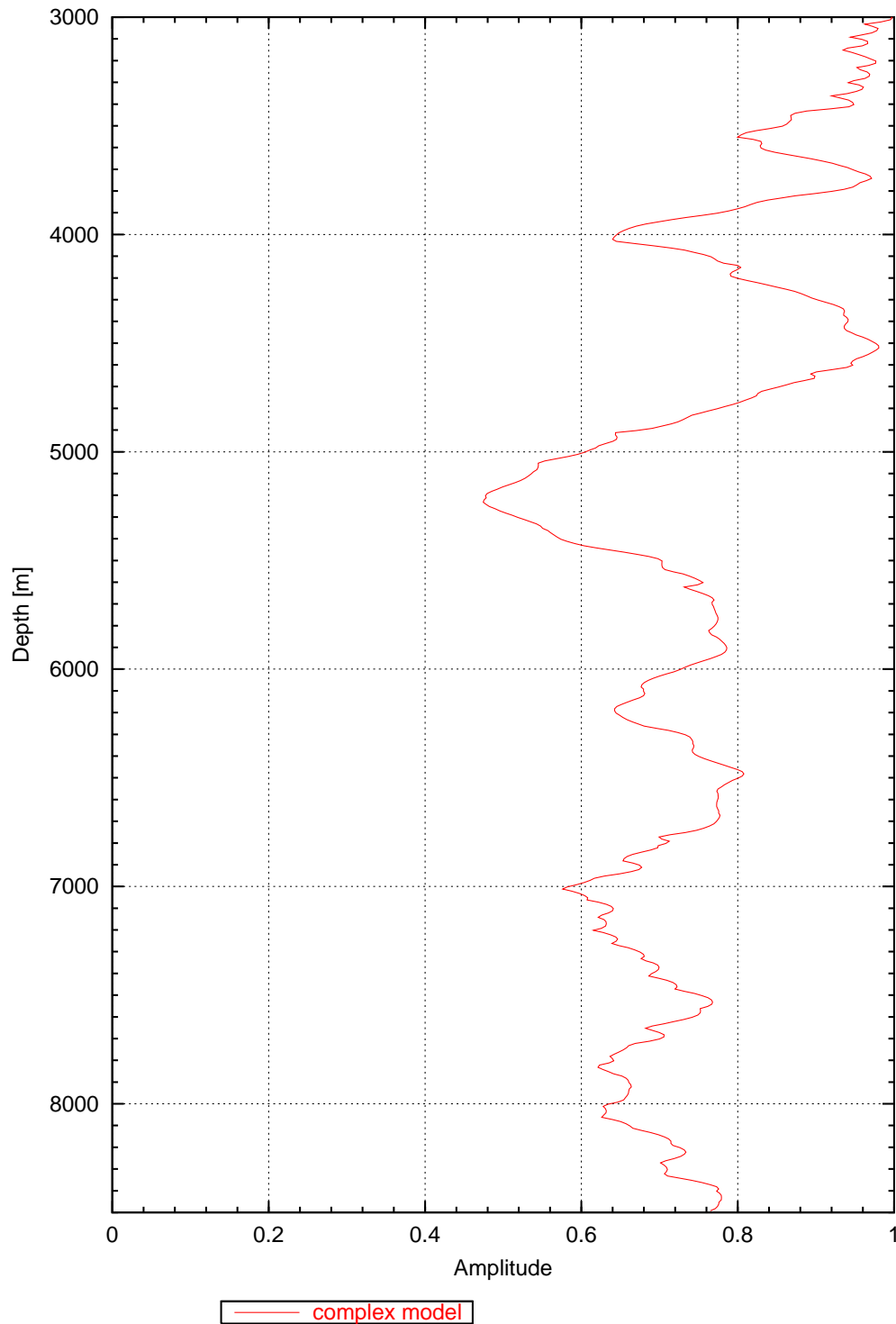


Fig. 8.36: Amplitude decay with depth in the complex isotropic, crack-free model.

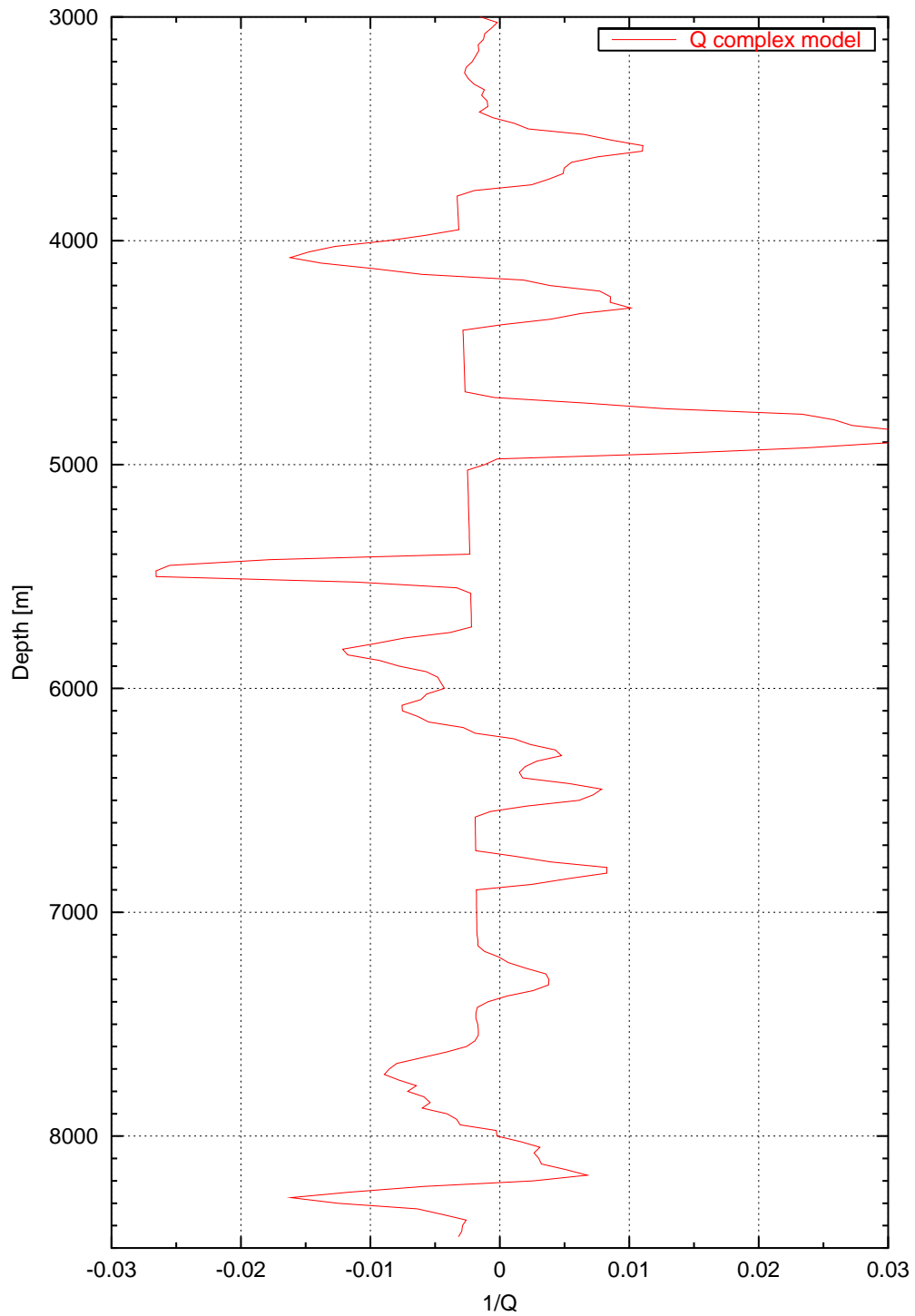


Fig. 8.37: Quality factor Q with a determined with previous median filtering, with a window length of 1000 m and an increment of 25 m.

tions between the field data and the complex model (Figures 4.10 on page 41 and 8.37) than with 60° model. Again, the exact extrema are not met but the basic nature of the curves is similar. The 1/Q-values of the field data show about two to three times the model values which is about half to one third the Q-values. Hence, it can be deduced that the structure of the model has an additional impact on the quality factor Q.

Octave Analysis of Amplitude Decay and Q

The amplitude shares of the downward traveling P-wave with respect to octave along the borehole are depicted in Figure 8.38. They show a strong correlation with the field data (Figure 4.12) but basically no correlation with the corresponding plot of the 60° model (Figure 8.22). This is an impressive manifestation of the structural influence on the first break of the downward traveling P-wave. However, the reverse or opposing behavior of the 60-120 Hz octave in relation to the remaining octaves is not as prominent as in the field data or even the 60° model. In this model the high frequency octave, if any, shows the most different behavior. Remarkable is the slightly growing share of the low frequency octave with depth. This is different in the corresponding field data plot. Also remarkable is the relatively large share in the 15-30 Hz frequency range (almost 0.1). This is in close correlation to the field data but not to the results of the 60° model, although the same source signal was used in both FD models.

The corresponding Q-values are depicted in Figure 8.39. The overall impression is more closely related to the field data than to the corresponding 60° model result. This is no surprise, since the Q-values determined for the whole spectrum and the amplitude behavior of the octave shares already suggested this.

P-to-S Conversion Logs

The amount of P to S conversion in transmission of the complex model was also analyzed for the whole spectrum (Figure 8.40, true phase and Figure 8.41, envelope stack) as well as for its octaves (Figures 8.42- 8.45). The first impression of the full spectrum plots is a surprisingly uniform conversion level for most of the depth range compared with the corresponding 60° model plots. The difference between the true phase and envelope values are as large as 3 percent points especially in the depth range 6.0-6.8 km. This is three times as large as in the corresponding 60° model comparison and could be an indication of an imperfect performance of the residual static and stacking process. Such an imperfect process could also be the reason for an apparently high average conversion level without pronounced maximum values or minimum values close to zero contrary to some locations of the 60° model envelope conversion plot. One conclusion of the above observations could be that the difference between the true phase stack and the envelope stack could possibly be used as a quality control for the conversion log processing.

The only exceptional high amplitudes in both full spectrum plots can be found in the range from from 7.3-7.7 km depth. In that region of the crustal model seems to be

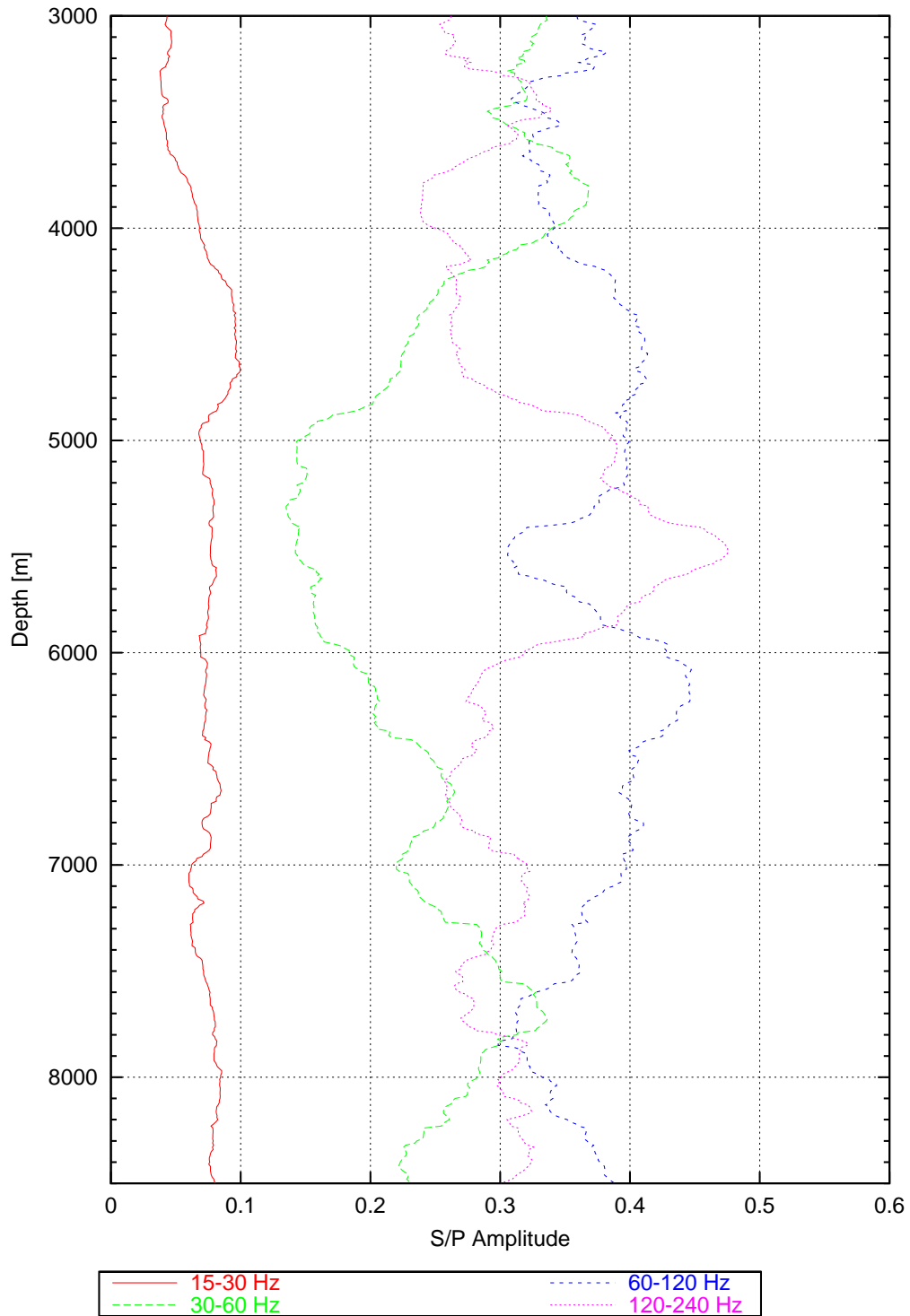


Fig. 8.38: Amplitude share of each of the four main octaves making up the signal of the downward traveling P-wave first break with respect to depth, smoothed with median filter with the length of 350 m and an increment of 12.5 m.

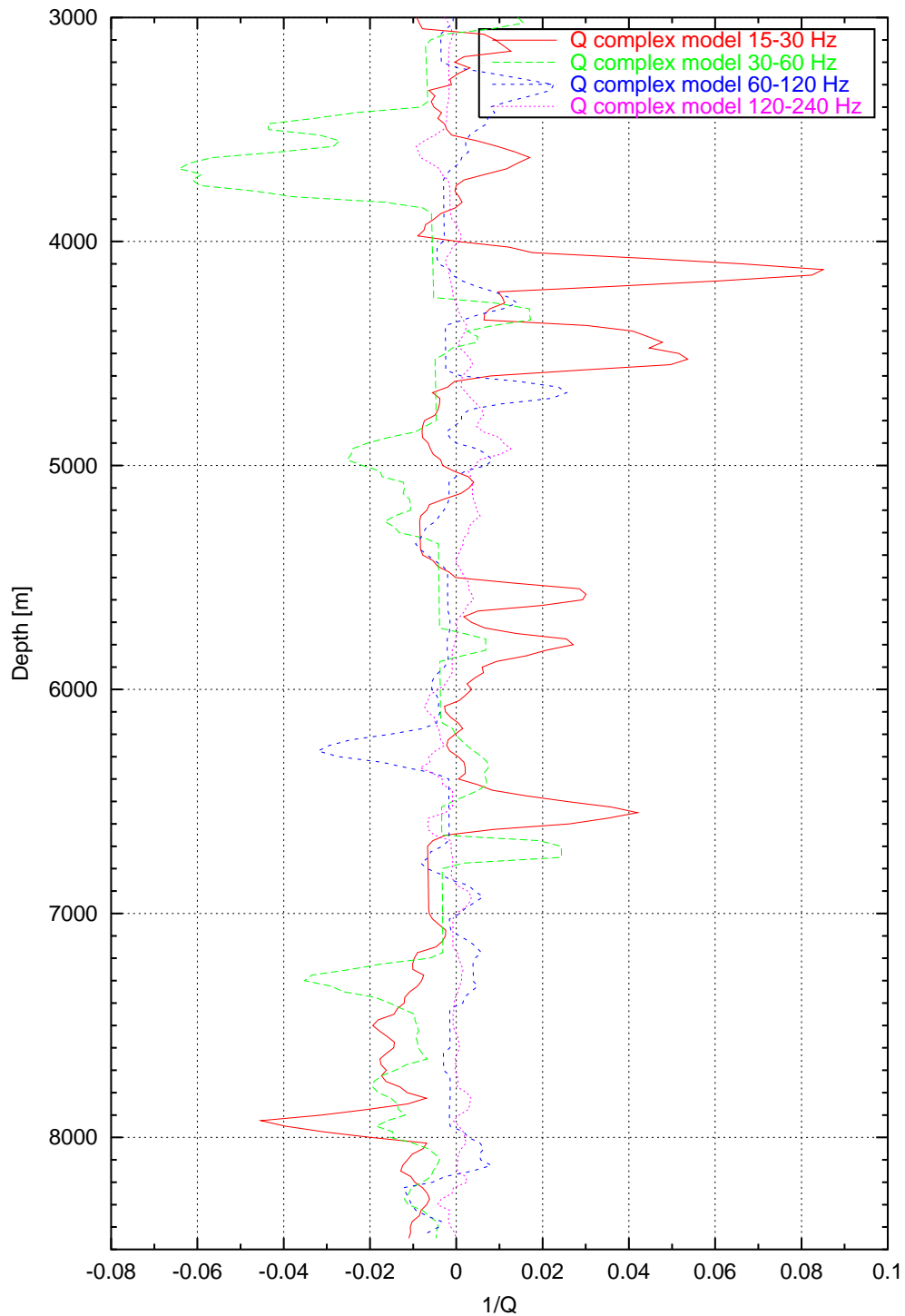


Fig. 8.39: Median filtered quality factor Q with the signal frequency content split into its four octaves. The moving filter window length was 1000 m with 25 m increment.

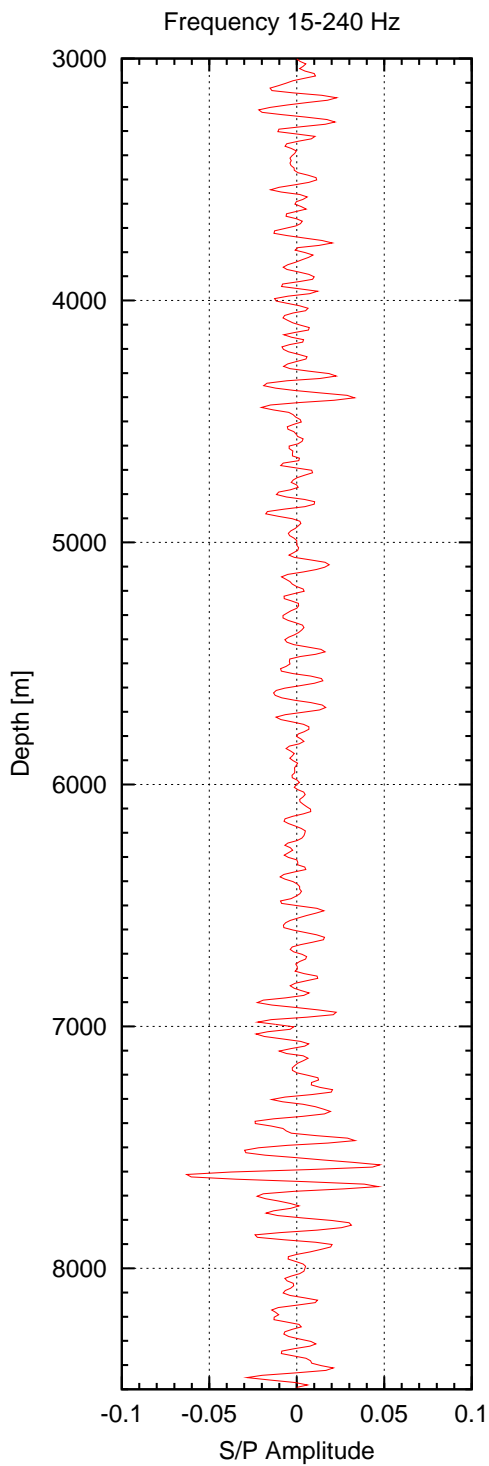


Fig. 8.40: Conversion log of the complex model, stack of a small number of traces, true phase, full spectrum.

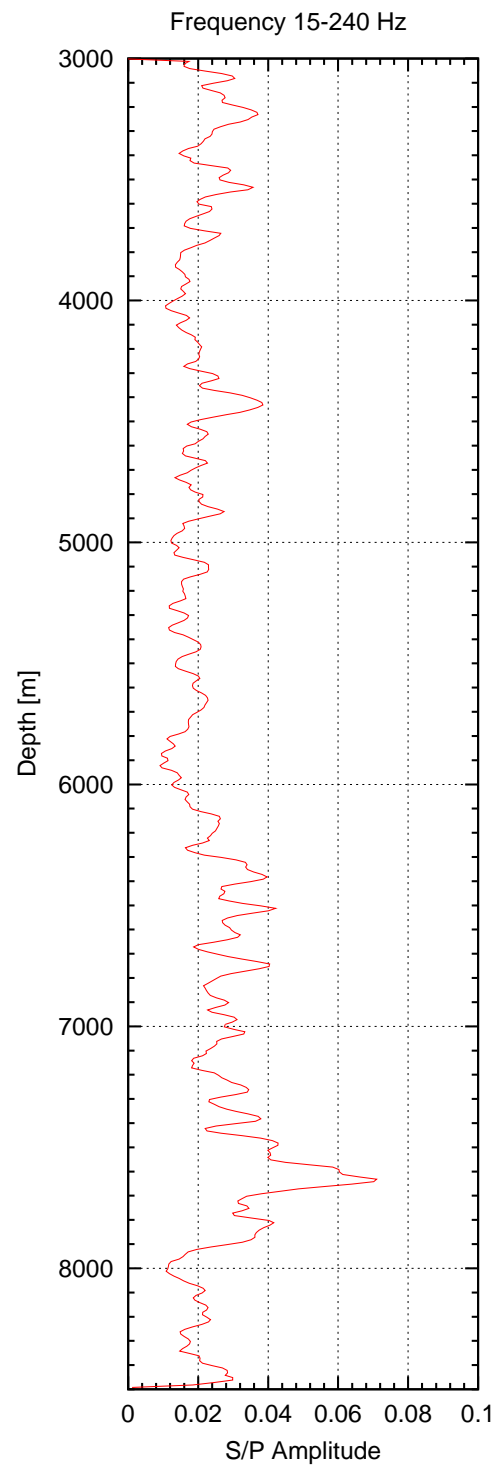


Fig. 8.41: Conversion log of the complex model, envelope stack of a small number of traces, full spectrum.

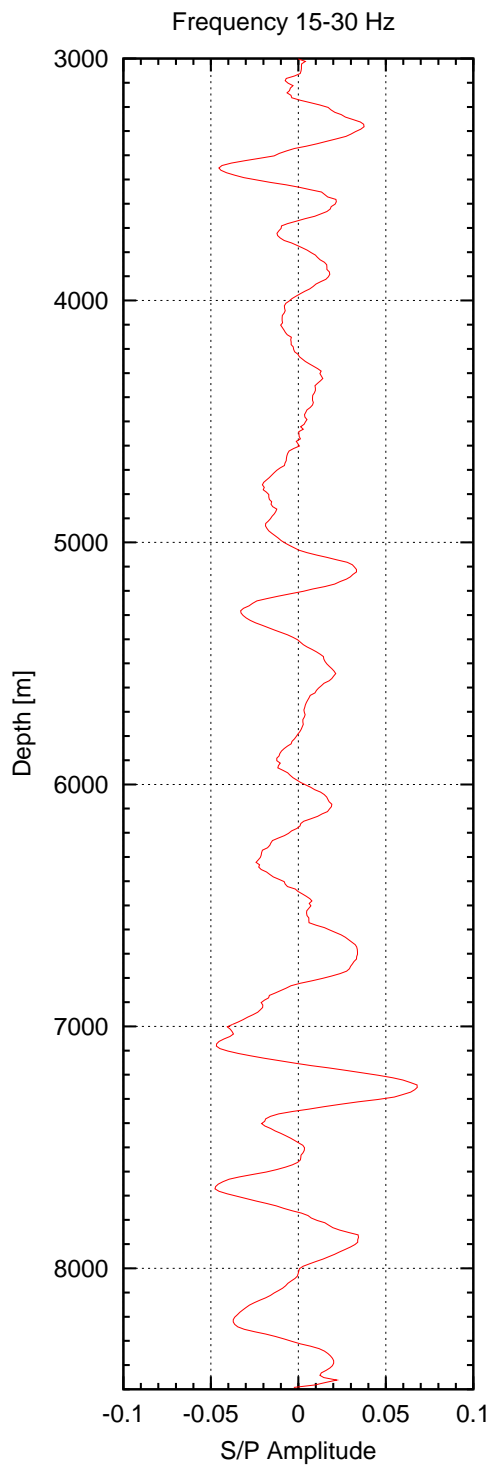


Fig. 8.42: Conversion log of the complex model, stack of a small number of traces, true phase, frequency range 15-30 Hz.

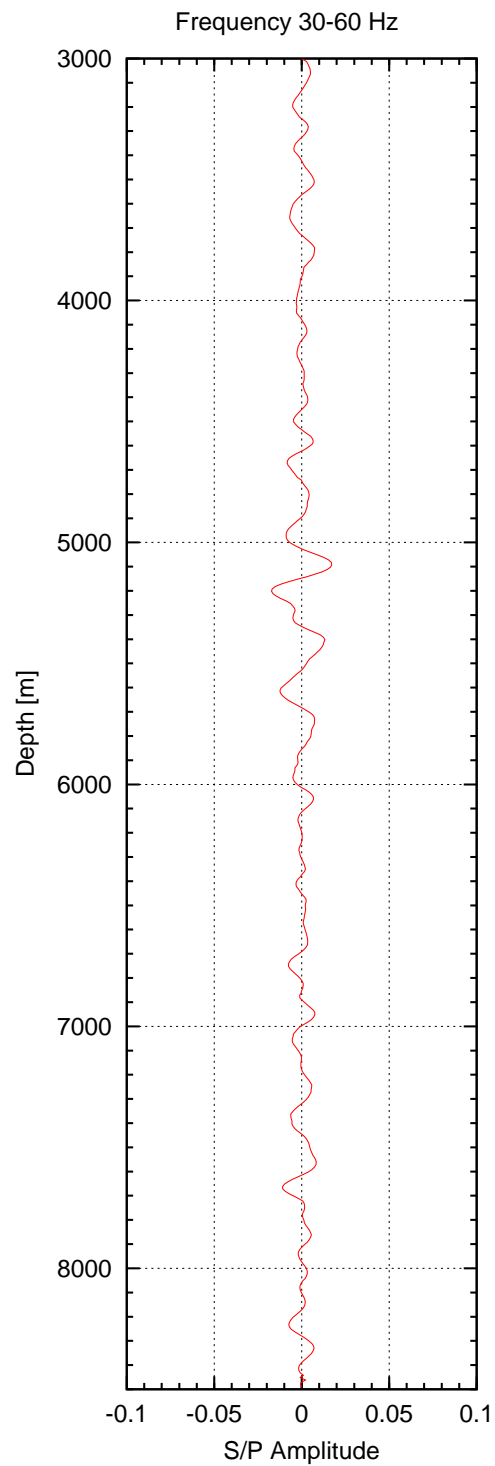


Fig. 8.43: Conversion log of the complex model, stack of a small number of traces, true phase, frequency range 30-60 Hz.

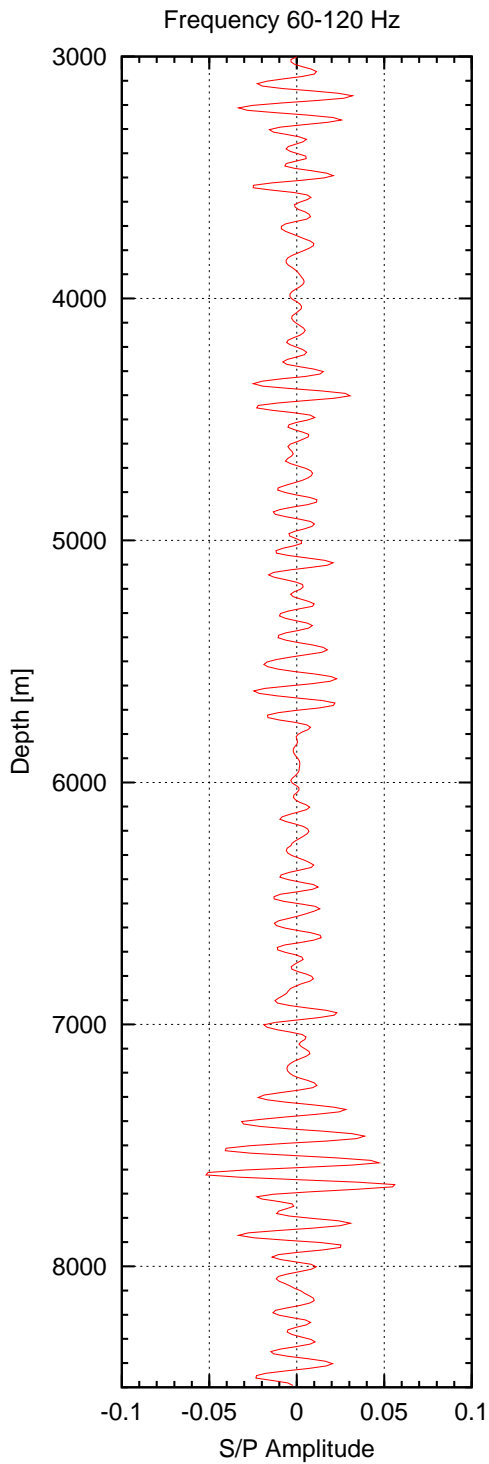


Fig. 8.44: Conversion log of the complex model, stack of a small number of traces, true phase, frequency range 60-120 Hz.

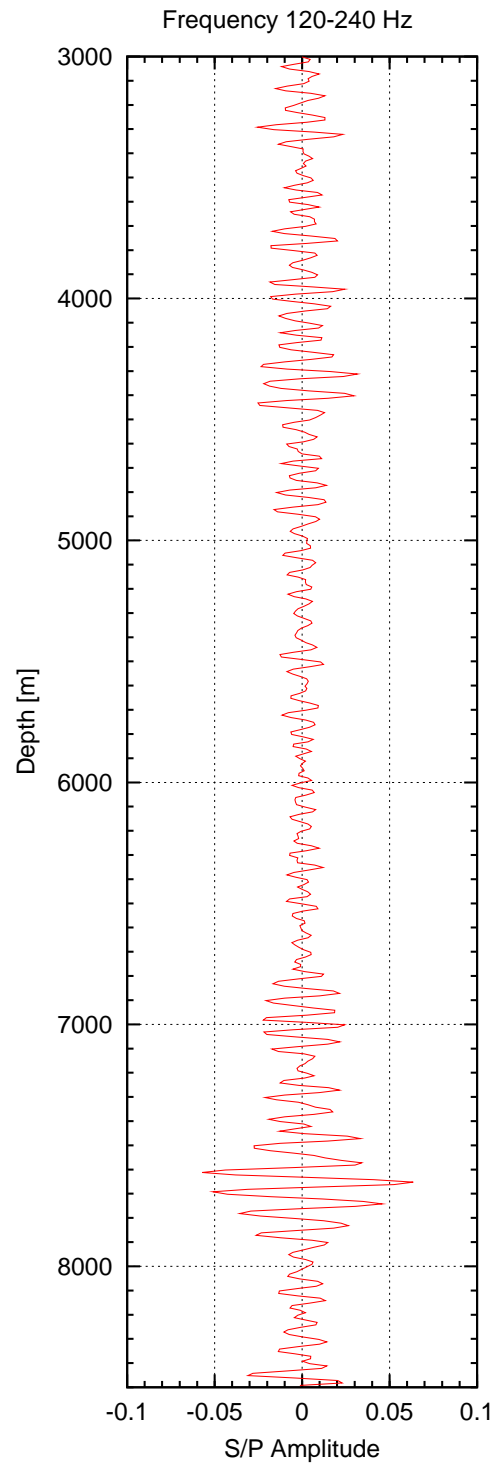


Fig. 8.45: Conversion log of the complex model, stack of a small number of traces, true phase, frequency range 120-240 Hz.

no indication of an exceptional structure or impedance contrast, however. Therefore the source of these amplitudes needs to remain unexplained.

The frequency dependency of the conversion is basically concordant with the field data and 60° model observations. Of course the different structures and impedance contrasts differently convert part of the nursing P-wave into S-waves depending on their size. However, the important observation in the field data as well as in the 60° model that the second octave (30-60 Hz) shows smaller values than the other octaves is also true for the complex model analyzed here. In fact, at a more detail look, its share seems slightly smaller than the corresponding share within the 60° model. The frequency dependent conversion shares of the complex model are therefore slightly more related to the field data than to the 60° model data. Thus, it seems the influence of the crustal structure plays an additional role in the frequency behavior of the wave conversion.

Comparison of Attenuation and Conversion

As could be expected by the complex behavior of Q with depth and a basically monotonous shape of the conversion log for this model, there seems to be no possibility to correct the apparent attenuation at least for conversion in transmission. It seems the influence of the whole crustal structure needs to be taken into account as well, in the determination of in situ Q-values.

8.3 Summary

In this chapter, finite-difference models with a certain variation of parameters were studied. Three basic goals were aimed at: The first was the deduction of simulated seismograms of which the underlying models are known, as an interpretation aid for the field data. The second goal was the study of the potential of the conversion log technique by comparing model data and analytical calculations. The third goal was the analysis of simulated isotropic, crack-free velocity and density models to permit the deduction of the influence of cracks and fractures on absorption and conversion through comparison of model data and field data.

One basis of the models were velocities and densities inverted from the mineral composition and laboratory information collected from the rocks in the KTB drill-holes over the years. Another basis is the dip and azimuth of the foliation derived from in situ formation-micro-scanner measurements. The last precondition is the large scale crustal pattern that had led to a 2D cross-section from all the information available until 1995. The models were designed in 2D basically because of the lack of computer memory. Therefore, there might exist restrictions to some of the results as to the validity in 3D. The basic effects should not be influenced by this, however.

The comparison of the field data seismograms with the ones from the simple 60° foliation dip model incorporating the corresponding crack-free isotropic parameters

show less correlation than the field data sections with the ones from the complex model. A simple source signal shows a complicated P-wave first break only in the presence of a complicated crustal structure. A simple rotated 1D model is not enough. Other features observable in the seismic data can also only be related to a more complicated crustal structure.

Q-values determined from the amplitude decay of the downward traveling P-wave need to be interpreted with care. It could be shown that intrinsic Q-values cannot be derived from the data with the simple amplitude decay method. This is partly due to the fact that wave conversion is not taken into account in this method. It could also be shown that the complicated crustal structure is responsible for an intense spatial oscillation of Q-values. This oscillation even results in negative Q-values indicating apparent amplification.

The resolution capacity of the conversion log technique for a single layer dipping with 60° seems to be around 50 m for a source signal with the central frequency of 80 Hz. The maximum and minimum values corresponding to negative and positive impedance contrasts seem to be shifted up by about 15 m though, compared with analytical calculations. Conversion amplitudes reach values of about 1/5-1/4 of the coefficients calculated with the Zoeppritz equations. The results from the large scale 60° layer dip model suggest however, that the conversion log values and the Zoeppritz coefficients correlate better than that.

The conversion log values derived from the 60° dip model basically show correlations with the corresponding field data results. This can be taken as a proof of the validity of the inversion process for the determination of the isotropic, crack-free seismic parameters. But this can also be taken as a proof of the usability of the conversion log method. The amount of conversion in the model is smaller than in the individual field data S-wave component readings. This is mainly the influence of fissures and cracks.

The conversion log values derived from the complex model show almost no correlation. This is not surprising, since the rock parameter sequence had been changed in the designing process of the complex model. However, the relatively large difference between the true phase and envelope stack conversion log values could be an indication of a less successful processing of these conversion logs, with the source of the problem being related to the f-k filter and/or residual static process, necessary in the conversion log processing sequence.

The correction of apparent Q-values with conversion values seems to be a vague possibility in a simple 1-dimensional environment. In a complex environment with varying dips and fault zones any correction seems to be impossible.

Chapter 9

Discussion

The main results of the individual chapters of this work will be discussed in the following sections and related to some other information from the KTB main hole.

The aim of this study was the quantification of the influence of cracks and fissures on the pattern of seismic waves in the upper and middle crust by means of a VSP experiment. The location of the Continental Deep Drilling Site (KTB) in southern Germany was chosen because its advantage is the large depth of main borehole, the existence of a second deep hole, and the detailed knowledge of a large variety of geoscientific parameters of the drilled crustal block including a large scale geological model. Besides, it is one of only a few borehole sites that were drilled to further our knowledge about the crystalline parts of the crust.

The experiment yielded seismic data with reliable frequencies, traveltimes, and amplitudes. Two different tools were used for the analysis:

- The amplitude decay of the downward-traveling compressional wave was used for the determination of full spectrum and octave dependent quality factor values.
- The newly developed P-to-S conversion log technique quantifies the conversion of compressional waves into shear waves at dipping impedance contrasts. It was analyzed for the full spectrum and with respect to its octaves.

In any data interpretation there is usually the hope to find a simple explanation for the measured values. Since seismic waves were analyzed in this work the parameter defining the measured values is the impedance contrast which is controlled by the elastic parameters density, compressional wave velocity and shear wave velocities. In a complex environment the velocities are usually anisotropic and frequency dependent. The reasons for these parameters to vary can be manifold though, and can result in possible correlations between the measured seismic data and borehole logs not carrying any elastic information. This is due to geological processes having an influence on more than just the elastic parameters.

9.1 Quality Factor Q

The study showed that the determination of reliable Q-values seems to be hampered in the presence of complicated crustal structures, where interference within the first break is strong. Apparent amplification in certain depth positions is common. This phenomenon is not limited to the field data shown in Chapter 4. It is similar in the complex FD model analysis shown in Chapter 8. In the simple rotated layer model, also shown in Chapter 8, the problem seems to be less prominent. The strong dependence of Q-values on the frequency octave seems to require the rewriting of equation 3.4 on page 18

$$1/Q_{eff} = 1/Q_i + 1/Q_{scatter} \quad (9.1)$$

with an additional structural term, which is frequency dependent

$$1/Q_{eff} = 1/Q_i + 1/Q_{scatter} - 1/Q(f)_{struct} \quad (9.2)$$

As a result the analysis of Q carried out in this study does not seem to be of any value concerning local elastic parameter variations. More research work needs to be carried out for the study or development of more sophisticated methods. The smoothing of amplitude values for the determination of Q should be analyzed in more detail with respect to conversion.

9.2 Wave Conversion in Transmission

9.2.1 Conversion Log Capability

Analytical calculations of P-to-S conversion coefficients within a rotated 1-layer model carried out Chapter 7 were compared with finite-difference calculations of the same model in a resolution test in Chapter 8. The result was a resolution capacity of about 50 m for a signal with a main frequency of 80 Hz. The amplitudes of the Zoeppritz coefficients reached about twice the amplitudes of the corresponding seismic conversion log values.

To derive a more universal impression of the conversion log capability the conversion log values of the whole 60° dip model are compared with the corresponding Zoeppritz coefficients in the depth range 3.0-8.5 km. One result is presented in Figure 9.1. Drawn in green is the seismically derived conversion log of the envelopes for the full spectrum. Indicated in red are the absolute values of the corresponding Zoeppritz coefficients. The seismic conversion values are usually slightly smaller in the presence of single strong converters, which is similar to the resolution test results. In some sections with a sequence of small converters however (e.g., 4.2-4.7 km depth), they seem to be too large by a factor of up to 2.

If the seismic true phase conversion log of only the high frequency octave (120-240 Hz) is compared with the signed Zoeppritz conversion coefficients (Figure 9.2)

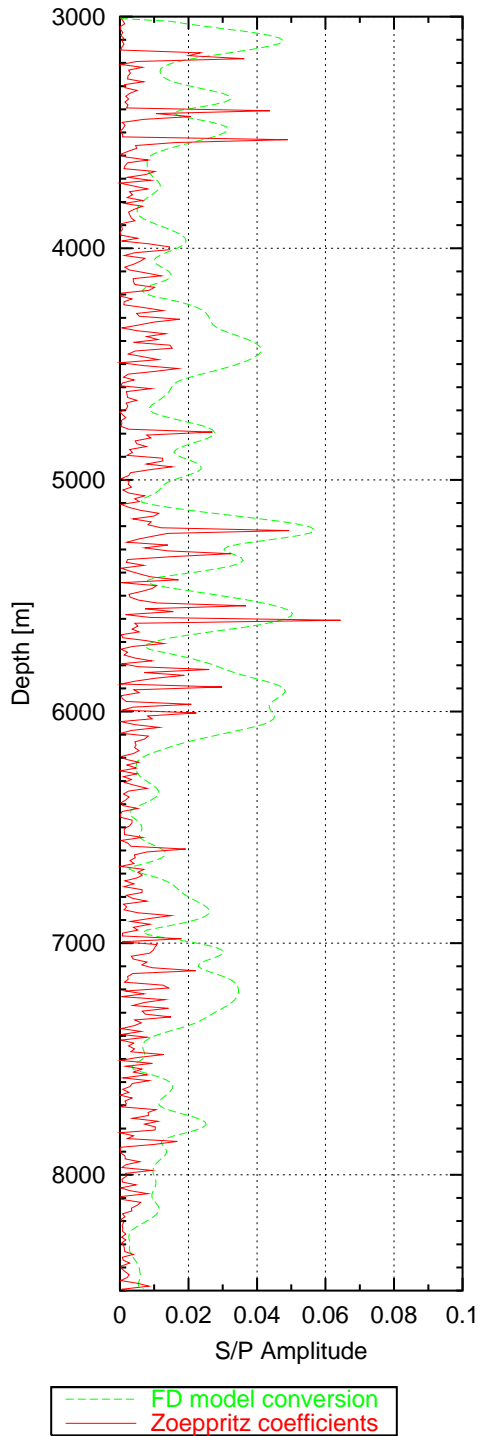


Fig. 9.1: Comparison of the envelope conversion in transmission log of the simple 60° dip model (green) with the absolute Zoepritz conversion coefficients (red).

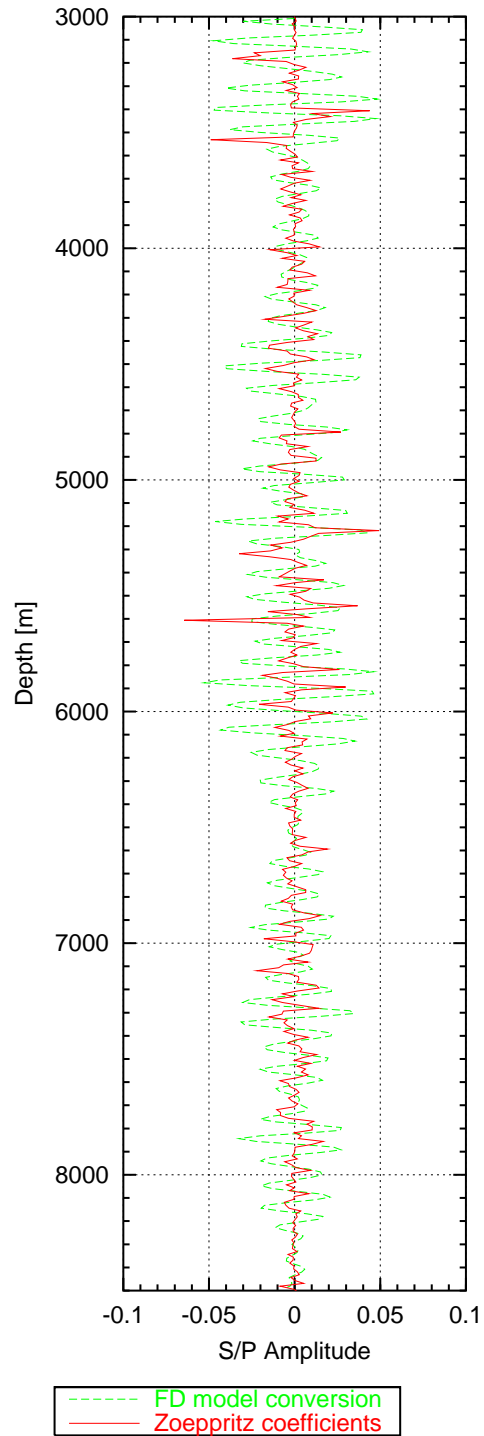


Fig. 9.2: Comparison of the high frequency octave, true phase conversion in transmission log of the simple 60° dip model (green) with the true phase Zoepritz conversion coefficients (red).

the result in terms of amplitude is similar. However, the resolution is much higher. The latter is simply the result of the high frequency data selected here. The amplitude behavior can only be explained with interference. The conversion potential of single converters is not fully represented, whereas a sequence of smaller converters can cause constructive interference with subsequent exaggerated conversion values. The same phenomenon can be expected to occur in the field data.

The influence of the size of the converters cannot be estimated from the data. The Zoeppritz equations are only valid for large interfaces. The models used for the above comparison meet this necessity. However, the field data does not, due to the complicated crustal structure.

9.2.2 Field Data Conversion

Field data P-to-S conversion in transmission for the full spectrum is as high as 17% and well above 5% for individual components (Figure 9.3). The total conversion is even as high as 20%, whereas its value for a crack-free, isotropic rock model rotated by 60° shows a maximum conversion of about 6% with the low level 'noise' around 1% (Figure 9.4). A similar amplitude vs. depth trend exists between the model and the field data. This indicates that the basic influence of the mineral composition on the conversion of waves along the borehole is not fully camouflaged by other factors. However, minor differences in the correlation of the corresponding single components with respect to the model conversion can be detected (Figure 9.3).

The shape of the corresponding complex model conversion plot does not show such a similarity because due to the model design process its rock parameter sequence differs from the field data and the simple model (Figure 8.41 on page 142). The conversion values however, show about the same level of values as the simple 60° dip model.

Thus, one fundamental result for the crust at the KTB site is that a maximum of 50% of the wave conversion is driven by the mineral composition contrasts but usually most of the conversion originates from other factors.

The blue line in Figure 9.4 represents the total conversion reduced by the model conversion. Hence, it represents the residual influence on P to S conversion without the composition part. As stated above, it can be expected that not only the foliation induced conversion values within the model are exaggerated in the presence of a sequence of small converters; the same should be true for the field data. So this simple subtraction seems to be adequate as a first order approach for the determination of the residual conversion values.

Conversion within the Anisotropy System

Another interesting observation is the opposite behavior of conversion into S1 and S2 in some sections (Figure 9.3). Larger conversion values of one component correlate with smaller values of the other, for example in the depth range 5.6-5.7 km, at about

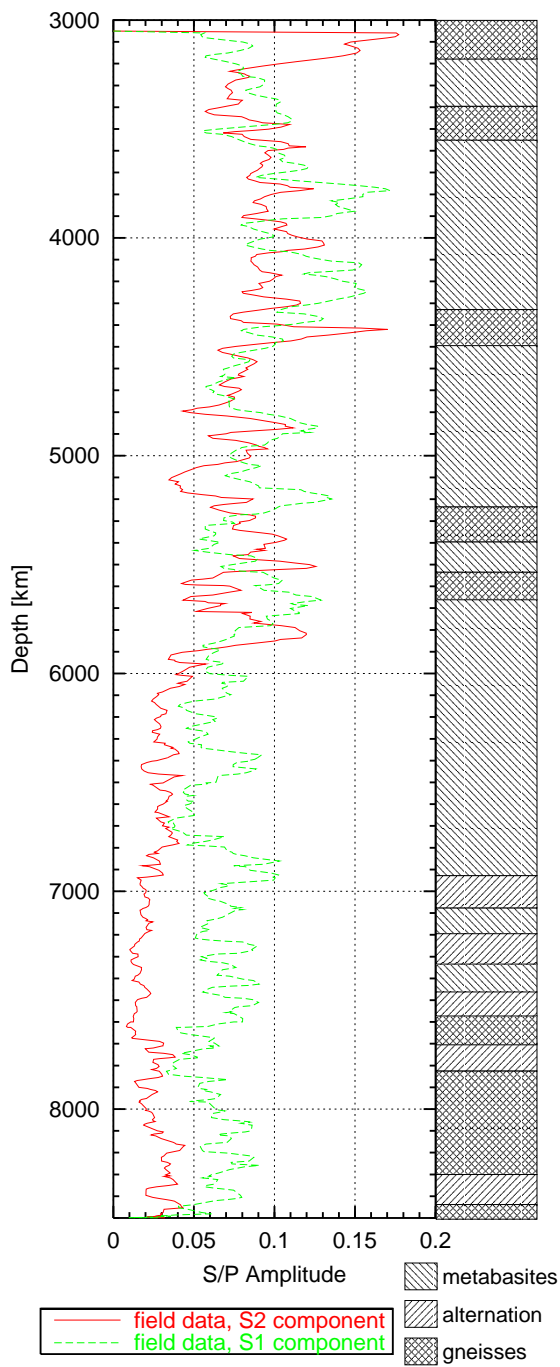


Fig. 9.3: Full spectrum P-to-S conversion in transmission of the S1 (red) and S2 (green) component, stack of 15 traces. The geological profile is depicted on the right with gneiss, metabasites, and alternating sequences of the two rock types.

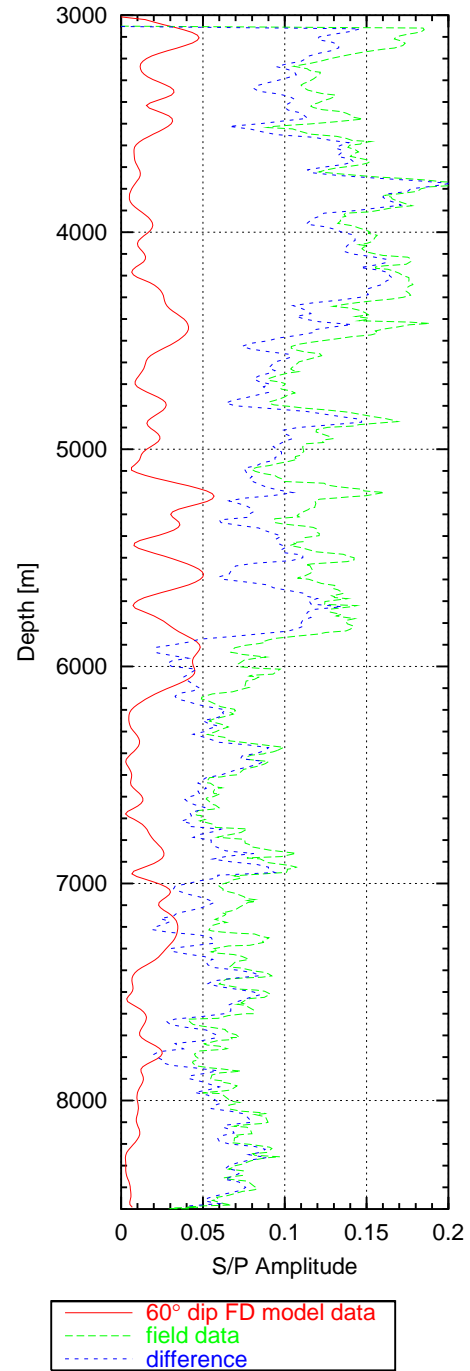


Fig. 9.4: Full spectrum P-to-S conversion in transmission of the 60° model data (red) and the total conversion of the field data depicted in Figure 9.3 (green). Blue - subtraction of the model foliation influence from the field data.

6.4 km, and 6.8 km to the final depth. The optimum shear wave separation by rotation of the oscillation ellipsoid (explained in Chapter 5) apparently also optimizes the separation of the two converted wave oscillation azimuths. It seems the cause for shear wave splitting (see Figure 4.8) is linked to the cause for conversion. Consequently, the two conversion logs could also be used as an independent quality control for the shear wave separation.

Velocity and Density

In the preliminary field data conversion log analysis in Chapter 6 some of the most prominent peaks within the conversion logs were found to be bound to rock unit interfaces, in some cases in combination with fault zones. The lithology column in Figure 9.3 can only be a very basic orientation though, because the local mineral composition does not always allow the exact distinction of one rock type from the other. This becomes clear by the comparison of the lithology column with Figure 6.5 on page 73 and the mineral composition plot in Figure 7.1 on page 88.

The measured density and measured sonic log and VSP velocity values could be expected to have a certain influence. These parameters are plotted in Figure 9.5. It seems however, no first order correlation with the conversion anomalies can be found. Only in case of large anomalies in the velocity logs a direct correlation is obvious. This is the case at the depth position 5.2 km, for example. All logs show a decrease, especially the Vp logs. The decrease of the S1 velocity is larger than the S2 velocity. Perhaps this is the reason for a stronger conversion into S1 than into S2. The conversion takes place at a lithologic contrast from an alternating sequence to gneiss. An influence of cracks or fissures cannot be derived from this.

The difference between the two S-wave component conversion logs is even more interesting if the different frequency octaves are also taken into account. The velocity and density anomalies at 5.2 but also at 5.55 km depth correlate the most with high conversion amplitudes in the S1, 60-120 Hz component (Figure 6.9 on page 76) but in the S2-component the most with octave 120-240 Hz (Figure 6.14 on page 78). This could imply that the anisotropy also causes the detection of different apparent structure sizes depending on oscillation azimuth.

The section between 7.0 and 7.6 km is characterized by two very large velocity drops in Vp. Because of borehole break-outs no reliable sonic shear wave velocities could be sampled here. The VSP S1-wave velocity indicates that this section is also unusual in terms of shear waves. However, the conversion plots show only minor anomalies here. So even if the velocity or density logs can explain single conversion peaks, this correlation cannot be generalized.

Chlorite and Fracture Indicators

A very prominent feature of the conversion pattern is the drop of conversion values in the field data below about 6 km depth. This is especially true for the P-to-S2 conver-

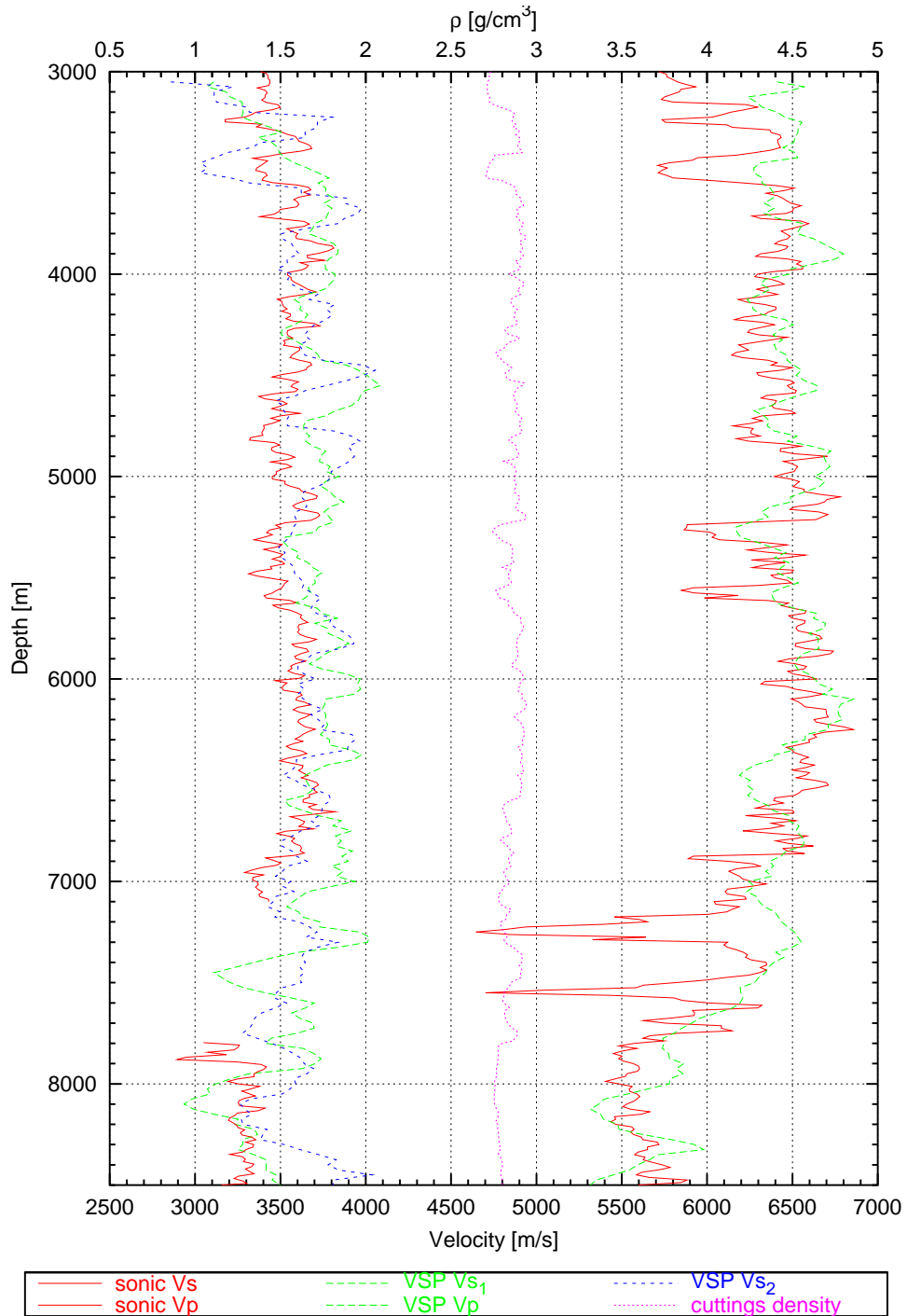


Fig. 9.5: Sonic log velocity values (red) of Vs (left) and Vp (right), median filtered with a window length of 25 m and 12 m increment vs. VSP field data (green, blue), median filtered with a window length of 300 m and an increment of 25 m. The sonic Vs velocities in the depth range from 7.1-7.8 km are not reliable because of borehole break-outs. The density of the cuttings (magenta) is median filtered with 25 m window and 12 m increment.

sion. The model conversion does not show an equivalent pattern. Perhaps the existence of chlorite hampers the conversion of waves. The relatively large level of chlorite below 6000 m depth (Figure 9.6) correlates well with a lower level of conversion. On the other hand, the larger conversions in certain sections below 6000 m seem to be bound to locations with a smaller chlorite content, e.g., in 6.5, 6.8, or 7.5 km depth. There exists a possible explanation for this correlation: In porous media with open holes or water filling mainly the P-wave velocity is lower, with possible variations of impedance contrasts. In case chlorite instead of water is the filling of the cracks, fissures, or pores the P-wave velocity anomaly is not as strong. Thus, chlorite does not seem to be the reason for waves to convert but the reason for them to convert less. This is a hint on part of the problem but does not explain the total conversion phenomenon.

In this context the stacks of 75 traces are interesting (Figures 6.17 and 6.18 on page 82). Here, the SE1 zone shows stronger conversions than in the 15 traces stacks. If chlorite was a cause to suppress or reduce conversion this would imply that at some offset from the borehole the chlorite content of this fault zone is considerably smaller. Whether this automatically implies that there are larger cracks or fissures responsible for that offset conversion is difficult to estimate. A special modeling of that zone including P-wave reflection, P-to-S conversion in reflection and P-to-S conversion in transmission might shed more light on that question.

Other fracture indicators like serpentine, zeolite, or epidote do not seem to correlate in any way with the conversion functions (Figure 9.6).

Porosity and Fracture Density

In a first interpretation the influence of fluids was analyzed in Chapter 6. Nevertheless, there are many places within the section from 3.0-8.5 km with fluid indications (Figure 73 on page 6.5). For a differentiation of the individual influence rather the amount of fluid and the thickness of this region are the important parameters and not just the presence of fluids. Also, as discussed in the last section, the influence of chlorite seems to show strong influence on conversion.

It could be expected that a quantitative indicator for conversion could be the porosity or fracture density vs. depth function (Figure 9.7). The core porosity was derived from electrical conductivity measurements. Porosity values above 4% are considered as fluid filled or mineralized fracture zones, whereas values below 4% are considered as matrix porosity (Pechinig *et al.*, 1997). Surprisingly though, there seems to be no direct correlation of conversion anomalies with porosity values. There are places with high porosity values and high conversion amplitudes but also sections with high porosity values and low conversion amplitudes.

This is different for the fracture density values, however. That function shows a far stronger correlation with the conversion logs, especially below 6 km depth where the crack density is smaller, which correlates with low level conversion amplitudes, but also with a high level in chlorite content. A combination of fracture density and chlorite content seems to provide a convincing reason for waves to convert in the crust.

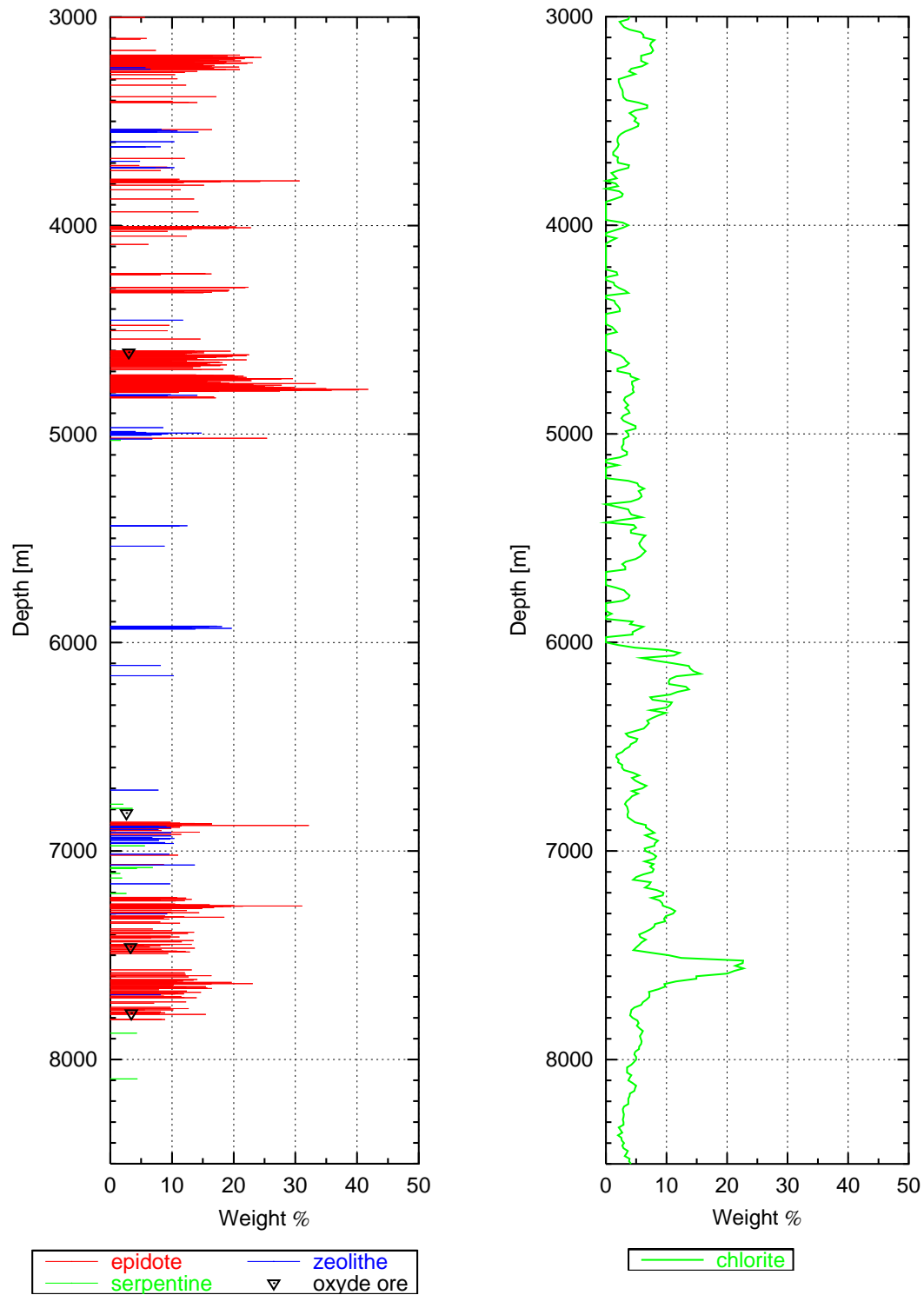


Fig. 9.6: Indicators of fractures and thermal water. The chlorite values are median filtered with a 25 m long moving window, with an increment of 12.5 m.

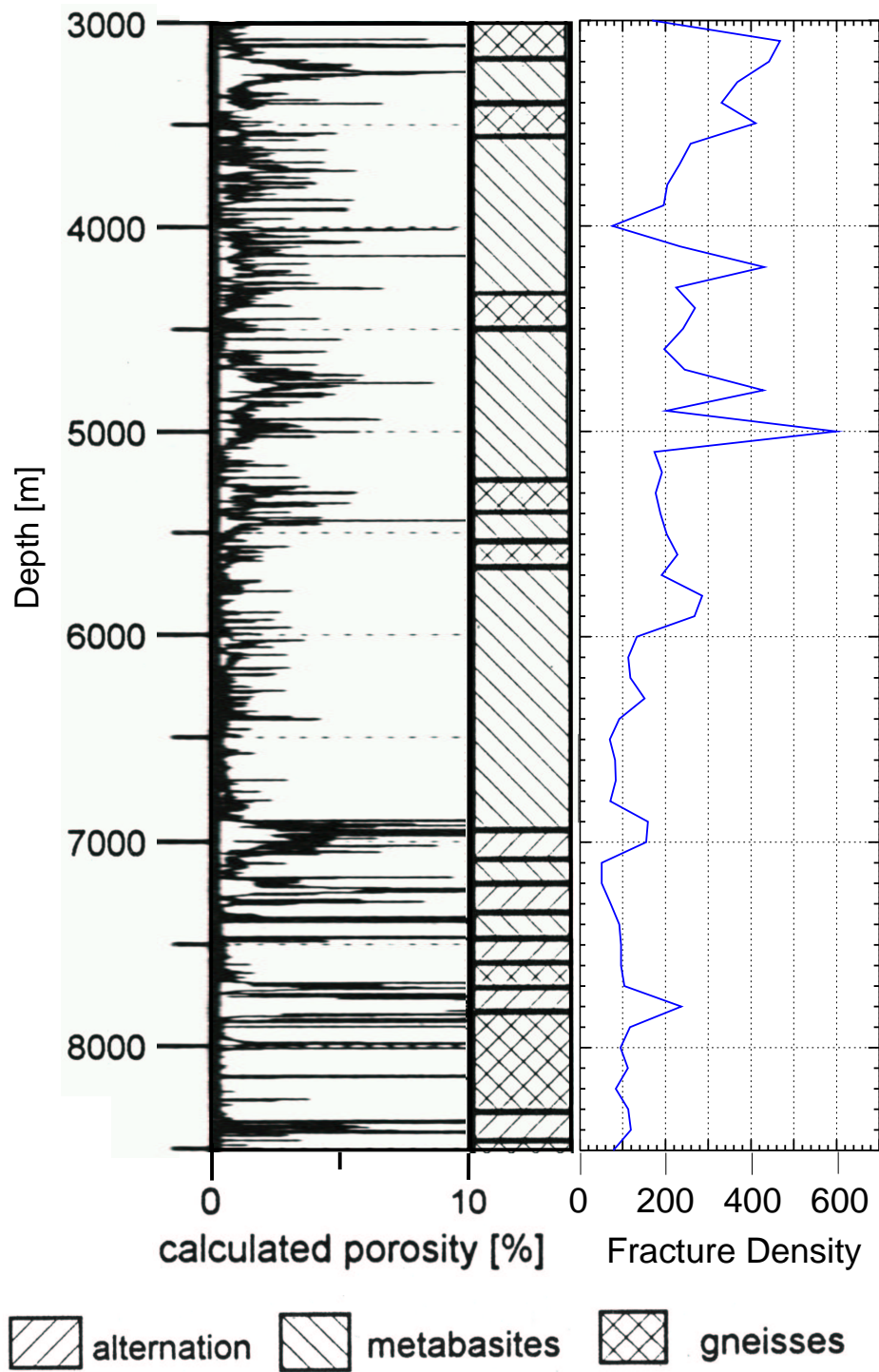


Fig. 9.7: Porosity estimation correlating core porosity and electrical conductivity (after [Pechnig et al., 1997](#)) and fracture density [no. of fractures / 100 m] vs. depth.

Azimuth and Dip of Foliation and Cracks

Other parameters that could explain at least some of the conversion are the azimuth and dip of foliation and cracks. The orientation of foliation and cracks was derived from measurements with a formation MicroScanner - FMS, HFMS for high temperatures, or formation MicroImager - FMI. Figures 9.8 and 9.9 show the corresponding values as histograms with a moving window length of 150 m and an increment of 25 m (Beilecke *et al.*, 2001). These parameters are likely to have an influence on the conversion because their variation changes the shape of the impedance contrast surfaces.

Basically, the foliation and crack orientations are similar, except in the depth range below 7.8 km. Thus, any correlation between conversion log and foliation orientation is also valid for the crack orientation above 7.8 km depth. Since the orientation parameters show a certain sectioning with respect to distribution pattern along the borehole the following comparison is carried out section-wise:

3000-3200m: The depth range sampled in the VSP experiment 1999 starts at 3000 m. The uppermost section from 3.0-3.2 km shows a strong total conversion (Figure 9.4) originating only from the S2-component (Figure 9.3). This is within a gneiss section with varying dip around 45° but well defined southwest azimuth. The lower limit of the strong conversion correlates with the lower limit of that gneiss section, which is very distinct in this case.

3200-5800m: A common variation of dip and azimuth of foliation and cracks is evident in the section from 3.2-5.8 km. The dip varies basically between 45°-80°, but its azimuth is mainly oriented twofold, northeast or southwest. The total conversion plot (Figure 9.4) shows relatively large values with a certain sub-sectioning. The ranges 3.2-3.7 km, 3.7-4.5 km, and 4.5-5.8 km can be correlated with subgroups of variations of the foliation and crack orientation. The conversion level for the whole section is relatively high.

5800-6600m: Below about 6 km the conversion values are smaller, which can be correlated with higher amounts of chlorite. In terms of azimuth and dip of foliation and cracks the range from 5.8-6.6 km is very uniform. The core porosity seems very small. This region seems like a solid block. In the subsection from 6.3-6.5 km however, the dip angle is smaller and the crack azimuth is more distinct than in almost any other section of the borehole. Here the conversion amplitudes are higher than in the rest of this section.

6600-7400m: In this section of the borehole the SE1 reflector is located. The dip of foliation and cracks is very distinct and steep. The azimuth is not. It points towards northeast in places and towards southeast in others, comparable to the range 3.7-5.8 km. The conversion amplitudes are relatively small, except at the upper limit of the SE1 zone at about 6.9 km. If the influence of the (model) foliation is subtracted from the total conversion (blue line in Figure 9.4) this amplitude anomaly is more remarkable.

7400-8500m: The foliation orientation is variable in this range with dip azimuths southeast and west. The dip is mostly moderate. Below 7.8 km the azimuth of cracks and foliation differ by about 90°. The growing conversion amplitudes here can be re-

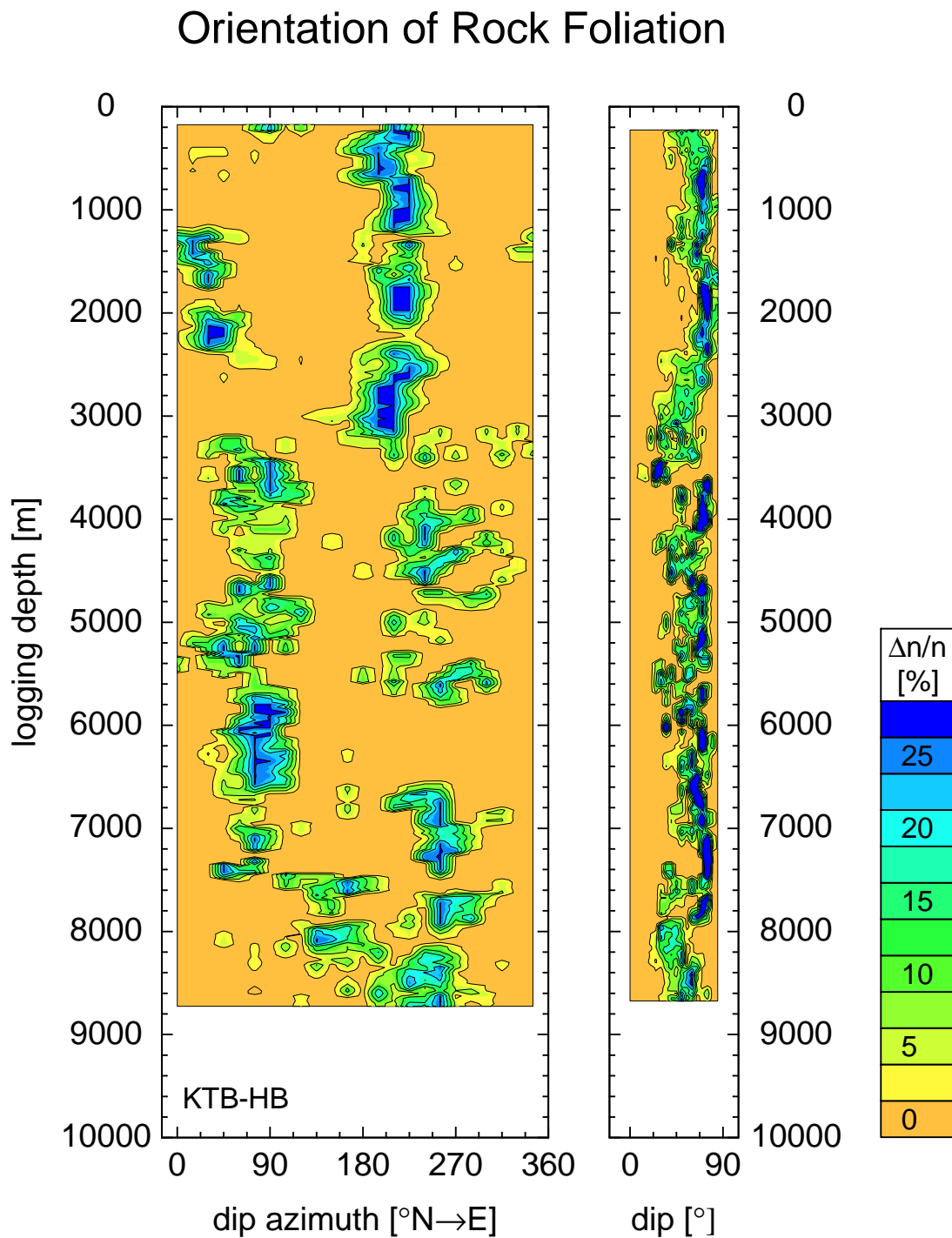


Fig. 9.8: Foliation azimuth and dip derived from measurements with formation MicroScanner - FMS, HFMS for high temperatures, or formation MicroImager - FMI. The values are depicted as histograms with a window length of 150 m and an increment of 25 m (Beilecke et al., 2001).

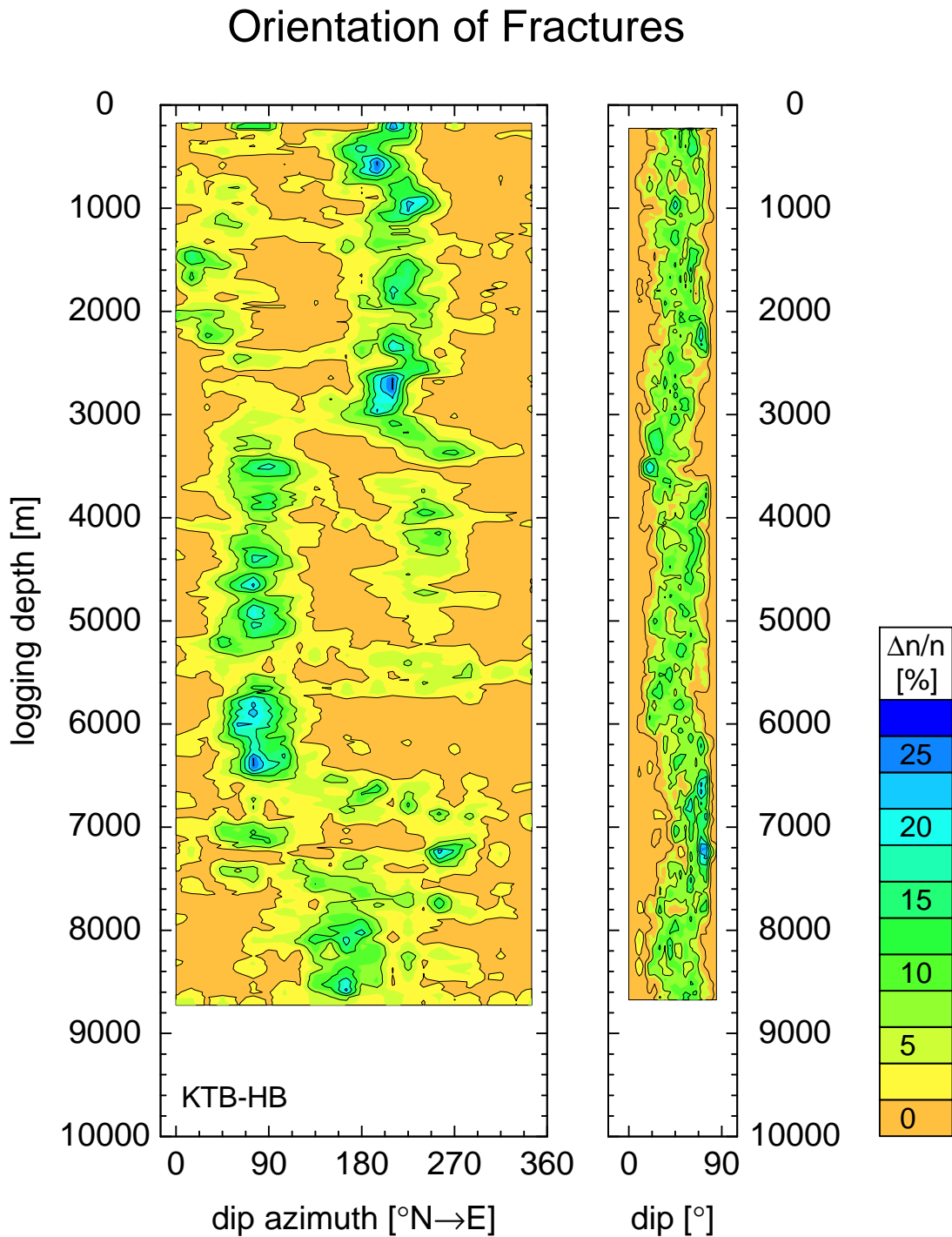


Fig. 9.9: Fracture azimuth and dip derived from measurements with formation MicroScanner - FMS, HFMS for high temperatures, or formation MicroImager - FMI. The values are depicted as histograms with a window length of 150 m and an increment of 25 m (Beilecke et al., 2001).

lated with a reduction in chlorite content though, and do not seem to be related to the crack or foliation orientation. Towards the lowermost end of the VSP data from 8.4-8.5 km depth the chlorite values grow again which correlates with smaller conversion amplitudes.

The main result is that there seems to be no first order correlation between the orientation of the foliation and cracks with the conversion from compressional to shear waves. In some cases more distinct orientations of foliation or cracks correlate better with the conversion logs, in other cases a higher variability of values is related to stronger conversions.

9.3 Frequency Considerations

One of the most interesting observations is the variation of Q and the P-to-S conversion in transmission with respect to frequency, in the field data and the calculated models. Whereas the values for Q are difficult to interpret, especially in the field data and the complex model, the P-to-S conversion shows very large values in the low frequency octave (15-30 Hz), large values in the two high frequency octaves (60-120 Hz), but low values in the low intermediate octave range (30-60 Hz).

In this context the Q analysis by Li & Richwalski (1996) and Pujol *et al.* (1998) of vibroseis VSP data collected between 3 and 6 km depth in the KTB main hole is of special interest (Figure 9.10). The values show a strong variability with respect to frequency and the standard deviation seems large if the two curves are compared. It is difficult to estimate, whether there exists a certain trend with respect to frequency. But statistical calculations by Shapiro & Hubral (1996) on the basis of a random medium approach with sections of thin layers of different dip (Figure 9.11) shed light on frequency dependent Q -values. The basis of the calculations are borehole logs. In this case

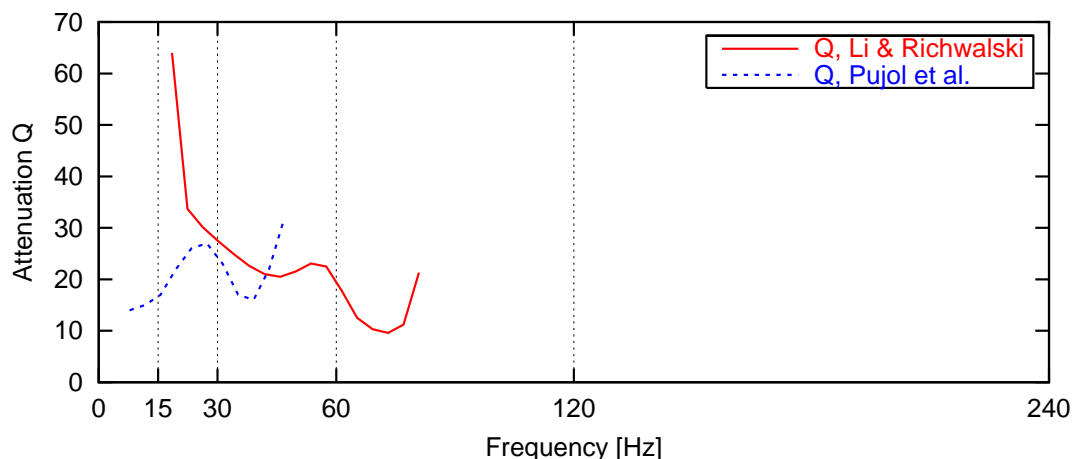


Fig. 9.10: Q -values derived from VSP measurements carried out in the KTB main hole by Li & Richwalski (1996) and Pujol *et al.* (1998) with respect to the frequency octaves analyzed in this thesis.

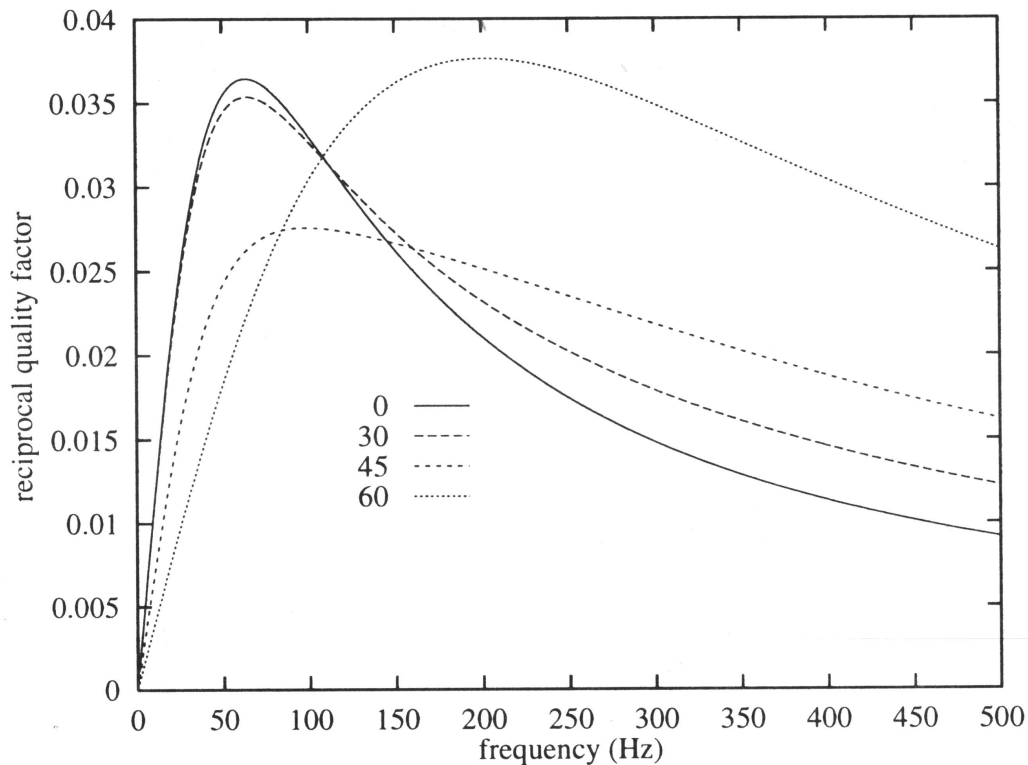


Fig. 9.11: *Q-values derived from borehole logs using statistical values. The Q-values were determined for thin layers dipping with 0° , 30° , 45° , and 60° (Shapiro & Hubral, 1996).*

the data used are not from the KTB site but from a different location. Therefore, the values are not directly comparable with the Q estimations shown in Figure 9.10. However, the deduction of relatively high Q-values in the low and high frequency range, with relatively low Q-values in the medium frequency range suggests a nonlinear trend of the frequency dependency of Q in the presence of thin layers.

The method used by Shapiro & Hubral (1996) involves a certain blocking of the input data which is described in Shapiro & Hubral (1999). One parameter needed for the calculations is the correlation length which was analyzed by Gritto et al., 1994 for the KTB site, without the deduction of attenuation values, though.

Since wave conversion is one part of P-wave attenuation, the observed octave dependency of conversion and the frequency dependency of Q should correspond to a certain degree. However, the estimations by Shapiro & Hubral (1996) and the observations in this work show the opposite behavior with respect to frequency, apart from the different data basis. High conversion amplitudes in the low frequency range should correspond to low Q-values, whereas low conversion amplitudes should correspond to high Q-values in a medium frequency range. Whereas the Q-values by Li & Richwalski (1996) show a better correlation with the estimations by Shapiro & Hubral (1996), the

frequency trend of the P-to-S conversion in transmission observed in this thesis suggests a frequency trend of Q-values more related to the results of Pujol *et al.* (1998). This is true for the layer model that would be required for the statistical approach by Shapiro & Hubral (1996), but this is the same for the complex model and the field data that do not have a pronounced layer structure.

After all, the compound analysis of Q and P-to-S conversion leads to diverging results. However, the sole analysis of P-to-S conversion in transmission is not enough to resolve the whole phenomenon of wave attenuation. The reflection of P-waves and the conversion in reflection additionally need to be taken into account to derive the whole balance. Perhaps this would reduce the discrepancies between the different observations and model results.

Chapter 10

Conclusions and Future Work

The deep VSP experiment carried out in 1999 at the site of the German Continental Deep Drilling Project (KTB) yielded high quality data with respect to amplitudes, bandwidth, and source signal repeatability. An additional offset shot point and the possibility to use the KTB pilot hole as a reference permitted the amplitude recovery and the reorientation of the 3-components recordings in the main hole.

The influence of cracks and fissures on the seismic wave pattern were to be studied. For this, field data, analytical calculations, and modelling results have been compared. The attenuation of seismic waves was one approach for the study, a newly developed wave conversion quantification method was the other.

The geology at the KTB site is a very complex metamorphic regime in a crystalline environment. This is a disadvantage. However, the very detailed knowledge of the local geoscientific parameters and a lot of research that has been carried out at that site is an advantage. Besides, the main hole is one of the deepest holes ever drilled giving the opportunity to study phenomena of deeper parts of the crust.

10.1 Conclusions

The main results were derived with seismic data in VSP geometry. Whether some of the following results are applicable in surface seismics remains to be studied:

10.1.1 Wave Pattern

(1) A simple source signal in an FD model imitating the crustal structure at the KTB site imitates the wave pattern encountered in the field data. Therefore, it can be presumed that the explosives source at the KTB Deep VSP 1999 zero offset shot point emitted a simple signal. (2) The variation of the frequency content of the P-wave first break is the result of the complicated crustal structure.

10.1.2 Q

(1) The simple amplitude decay method does not recover intrinsic Q-values. This is especially true for the field data and the complex model. (2) Large scale structural elements in the crust are responsible for stronger fluctuations of Q-values and need to be taken into account besides scattering attenuation in more sophisticated Q measurements. (3) There is hope that for (rotated) 1D structures, apparent Q can be corrected for conversion.

10.1.3 P-to-S Conversion

(1) P-to-S conversion in transmission is easily detectable in VSP geometry and can be quantified with relatively simple processing methods. (2) Analytical calculations and model results show that P-to-S conversion in transmission is much stronger than P-to-S conversion in reflection, for the structural dip angles encountered at the KTB site. (3) P-to-S converted waves are much less sensitive to incident angles than reflected P-waves in terms of amplitude. (4) The less number of traces are stacked the more distinct the extrema because less averaging can come into effect and the less influence from imperfect processing methods. (5) The more number of traces are stacked the more information is integrated from distant conversion points in a scattering environment. (6) True phase stacks can differentiate positive and negative impedance contrasts. (7) The difference in amplitude between stacked envelopes and stacked true phase stacks can be used as a quality control for the conversion log processing. (8) Amplitudes of converted waves in transmission are as high as 20% of the P-wave amplitudes in the field data and 6% in the crack-free isotropic rock models. A single reason for conversion to take place could not be found. The fact that chlorite can hamper the conversion and the fracture density shows a certain correlation suggest however that (water filled) cracks or fissure are responsible for most of the conversion phenomenon. Their influence makes up about 50%-90 % of the conversion amplitude, whereas the mineral composition only provides about 10%-50%. This observation is summarized in Figure 10.1 on the next page. (9) The conversion logs are sensitive to anisotropy. (10) The conversion amplitudes depend on frequency range with low and high frequency ranges (15-30 Hz and 60-240 Hz) showing stronger conversion and the low intermediate frequency range (30-60 Hz) showing less conversion. This is true for the field data as well as for the model data.

10.1.4 Crustal Properties

(1) The strong inverse relation between conversion amplitude and chlorite is remarkable and should also be responsible for varying reflection amplitudes at fault zones found in crustal surface seismic data. (2) Due to the chlorite content the conversion amplitudes for the SE1 fault zone at the KTB site are small in the direct vicinity of the borehole. They are larger at some distance from the borehole. Whether this im-

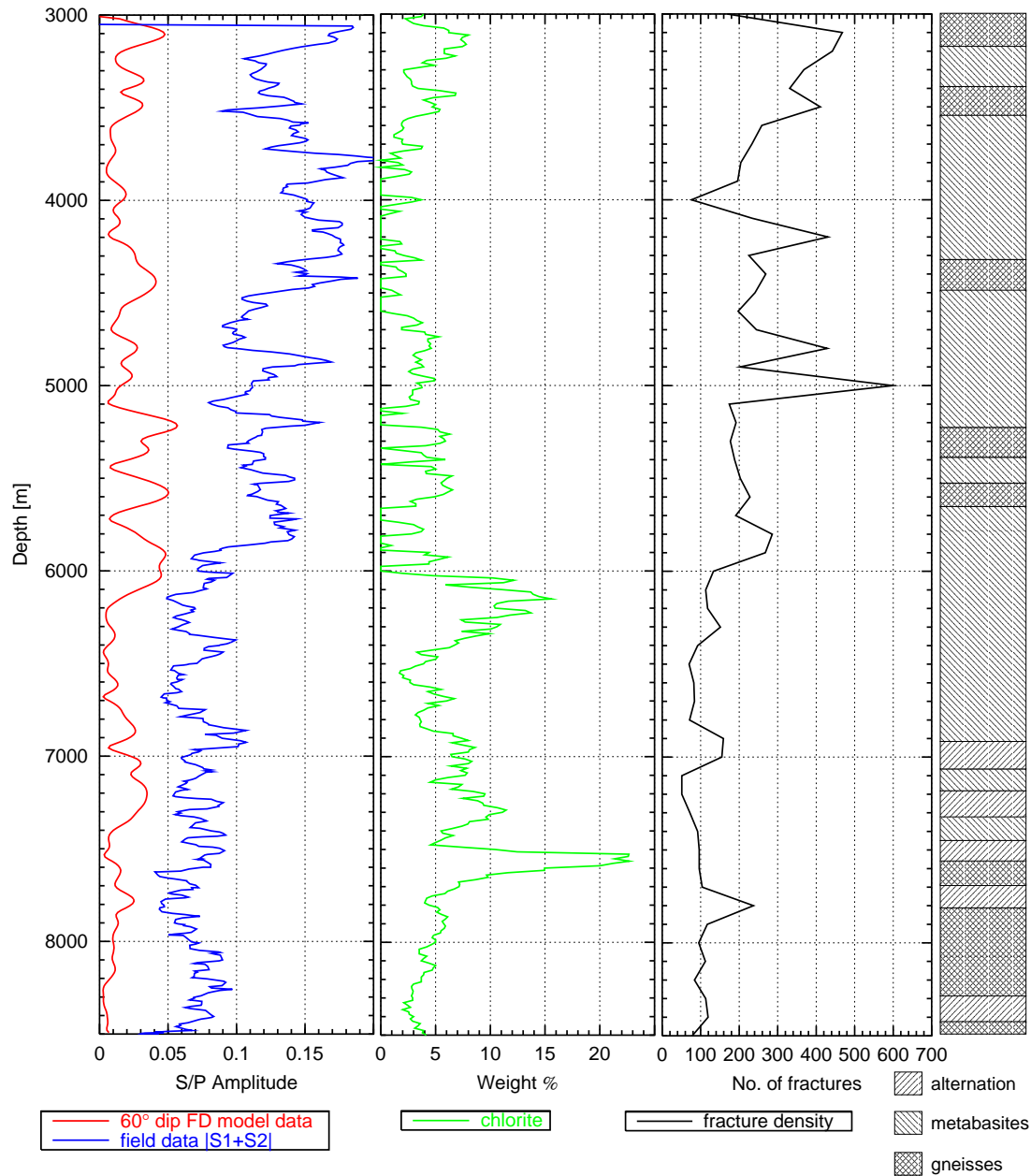


Fig. 10.1: *P*-to-*S* conversion amplitudes derived from the 60° model (red) and the field data (blue) and weight percentage of chlorite (green) and fracture density (black) vs. the geologic depth profile (right).

plies that open cracks or fissures are responsible for this or a complicated sequence of positively interfering impedance contrasts remains obscure. A compound modeling of that zone including *P*-wave reflection, *P*-to-*S* conversion in transmission as well as in reflection might permit a reliable interpretation. (3) The complicated first break is a result of multi-pathing in the crust within steeply dipping rock units of different wave velocity.

10.2 Future Work

The analysis of the deep vertical seismic profile experiment has yielded a wealth of results. Some had been more or less expected but some are surprising. The conversion log method has proved to be very valuable, although the simple question of what makes waves convert in the crust remains obscure, at least in a quantitative sense.

There seems to be a first order inverse correlation between the chlorite content and the conversion amplitudes. Chlorite grows within open holes. This points at the main source of the conversion - the crack density. It might be possible, to derive a quantitative relation between conversion and perhaps a multifold of factors by multi-variable analysis of the different logs and rock parameter-to-depth functions, to derive a multi-parameter conversion function.

There is one obvious possibility for optimization of the conversion log processing technique. The residual static correction in the seismogram should be carried out only in the region of interest, not for the whole seismogram. This could probably improve the resolution, especially in the direct vicinity of the borehole.

Another point that needs some adjustment is the choice of the window within which the traces are stacked to yield the conversion values. In this work a window with a constant number of traces was used. This makes sense from a statistical perspective. Because of the varying trace spacing along the borehole this trace window resulted in a time window, varying with depth. This is less appropriate from a physical perspective. In a scattering environment the time difference between the first break and an individual onset defines the subsurface volume that can possibly be illuminated. A constant time window thus more precisely defines the volume being included in the conversion analysis.

One draw-back seems to be the limitation of the conversion log to steep dips. However, this is only a limit in case varying dips are encountered within a borehole. In case the object is a simple layer structure with comparable dips along the borehole this method should also work with small dip angles. Basically, the results are a function of the geometry and special experiment layouts could be planned to make use of this method.

One of the surprising results of the method is the capability to derive information about locations at some distance away from the borehole. This effect is the result of the scattering environment though, and can probably not be generalized. In simple layered (sedimentary) environments additional offset shot points would be needed to derive an image of a larger vicinity around the borehole.

After all, the conversion log method seems an interesting tool for further testing. Its potential should be studied not only in some additional models but also in sedimentary environments with simple but perhaps also with more complicated structures.

Bibliography

- ADAM, E., & LANGLOIS, P. 1995. Elimination of Monofrequency Noise from Seismic Records. *LSPF Newsletter*, **8**(1), 59–65.
- AKI, K., & RICHARDS, P.G. (eds). 1980. *Quantitative Seismology*. W.H. Freeman and Company.
- ALFORD, R.M., KELLY, K.R., & BOORE, D.M. 1974. Accuracy of finite-difference modeling of the acoustic wave equation. *Geophysics*, **39**, 834–842.
- BATH, M. 1974. *Developments in solid Earth Geophysics 7, Spectral analysis in Geophysics*. Elsevier Scientific Publication Company.
- BEILECKE, T., BORM, G., BRAM, K., DRUIVENGA, G., FISCHER, D., FRANK, A., GEBRANDE, H., GIESE, R., KÜCK, J., LÜSCHEN, E., OKAYA, D., RABEL, W., & SMITHSON, S. 2001. Seismic velocity and anisotropy measured in situ until 8550 m Depth at the KTB deep drillhole (Oberpfalz, South Germany). *Page 269 of: Proceedings of the XXVIth EGS General Assembly*, vol. 3.
- BERCKHEMER, H., RAUEN, A., WINTER, H., KERN, H., KONTNY, A., LIENERT, M., NOVER, G., POHL, J., POPP, T., SCHULT, A., ZINKE, J., & SOFFEL, H.C. 1997. Petrophysical properties of the 9-km-deep crustal section at KTB. *Journal of Geophysical Research*, **102**(B8), 18,337–18,361.
- BITTNER, R., & RABEL, W. 1991. Energy and power sections in seismic interpretations. *Pages 409–415 of: MEISSNER, R. ET AL. (ed), Continental Lithosphere: Deep Seismic Reflections*. Geodyn. Ser., vol. 22. AGU, Washington, D.C.
- BOHLEN, T. 1998. *Viskoelastische FD-Modellierung seismischer Wellen zur Interpretation gemessener Seismogramme*. Dissertation, Universität Kiel.
- BOHLEN, T. 2002. Parallel 3-D Viscoelastic Finite-Difference Seismic Modelling. *Computers & Geosciences*, **28**(8), 887–899.
- BRAM, K., DRAXLER, H., KESSELS, W., KÜCK, J., & ZOTH, G. 2001. Detection of dominant faults by borehole logging in crystalline rocks drilled by KTB. *In: VIIIth International Symposium on Observations of Continental Crust Through Drilling*. U.S. Dep. of Energy, Santa Fe, N.M.

- BUSKE, S. 1999. 3-D Prestack Kirchhoff Migration of the ISO89-3D Data Set. *Pure and Applied Geophysics*, 157–171.
- BUTTLER, K.E., & RUSSELL, R.D. 1993. Subtraction of powerline harmonics from geophysical records. *Geophysics*, **58**, 898–903.
- COHEN, J. K., & STOCKWELL, JR. J. W. 2001. *CWP/SU: Seismic Unix Release 35: a free package for seismic research and processing*. Tech. rept. Center for Wave Phenomena, Colorado School of Mines, Golden, USA.
- DE WALL, H., DUYSER, J., HIRSCHMANN, G., KOTNY, A., & SPANGENBERG, E. 1994. Die Störungszone in 7 km Tiefe - Ursachen eines seismischen Reflektors. *Pages 83–96 of: KTB-Report*, vol. 94-3. Hannover, Germany: Niedersächsisches Landesamt für Bodenforschung.
- DÜRBAUM, H.-J., REICHERT, CH., SADOWIAK, P., & BRAM, K. (eds). 1992. *Integrated Seismics Oberpfalz 1989. Data evaluation and interpretation as of October 1992*. KTB-Report (DEKORP Report), vol. 92-5. Hannover, Germany: Niedersächsisches Landesamt für Bodenforschung.
- DUYSER, J., DE WALL, H., & ZULAUF, G. 1994. 9101 m Profile in the Superdeep Well KTB. Where are the Depth-dependent Gradients? *Pages A15–24 of: KTB-Report*, vol. 94-2. Hannover, Germany: Niedersächsisches Landesamt für Bodenforschung.
- DUYSER, J., KOTNY, A., DE WALL, H., & ZULAUF, G. 1995a. Postvariszische Krustenstapelung am Westrand der Böhmisches Masse. *Geowissenschaft.*, **13,4**, 135–141.
- DUYSER, J., GRAWINKEL, A., & KOTNY, A. 1995b. Petrographic and Structural Characterization. *Pages B1–B80 of: KTB-Report*, vol. 95-2. Hannover, Germany: Niedersächsisches Landesamt für Bodenforschung.
- EMMERMANN, R., & LAUTERJUNG, J. 1997. The German Continental Deep Drilling Program KTB: Overview and major results. *Journal of Geophysical Research*, **102**(B8), 18,179–18,201.
- EMMERMANN, R., ALTHAUS, E., GIESE, P., & STOECKERT, B. (eds). 1995. *KTB Hauptbohrung: Result of Geoscientific investigation in the KTB Field Laboratory; Final report:0-9101m*. KTB-Report, vol. 95-2. Hannover, Germany: Niedersächsisches Landesamt für Bodenforschung.
- FISCHER, D. 2000. *Intervallgeschwindigkeitsbestimmung an der KTB im Rahmen des Tiefen-VSP99*. Diploma Thesis, Universität Kiel.
- FRANK, A. 2002. *Migration und quantitative Interpretation primärer und konvertierter Reflexionen des tiefen VSP99 an der KTB*. Diploma Thesis, Universität Kiel.

- FRENJE, L., & JUHLIN, C. 2000. Scattering attenuation: 2-D and 3-D finite difference simulations vs. theory. *J. Appl. Geophys.*, **44**, 33–46.
- FUCHS, K., & MÜLLER, G. 1971. Computation of synthetic seismograms with the reflectivity method and comparison with observations. *Geophys. J. R. astr. Soc.*, **23**, 417–433.
- FUTTERMANN, W.I. 1962. Dispersive body waves. *J. Geophys. Res.*, **69**, 5279–5291.
- GEBRANDE, H., BOPP, M., NEURIEDER, P., & SCHMIDT, T. 1989. Crustal structure in the surroundings of the KTB drill site as derived from refraction and wide-angle seismic observations. *Pages 151–176 of: EMMERMANN, R., & WOHLBERG, J. (eds), The German Continental Deep Drilling Program (KTB)*. Springer-Verlag, New York.
- GOLD, N., SHAPIRO, S.A., & BURR, E. 1997. Modelling of high contrasts in elastic media using a modified finite difference scheme. *Page Page ST 14.6 of: 67th Annual Internat. Mtg. Expanded Abstracts*, vol. 97. Hannover, Germany: Soc. Expl. Geophys.
- HACKERT, C.L., & PARRA, J.O. 2002. Calibrating well logs to VSP attributes: interval velocity and amplitude. *The Leading Edge*, 52–57.
- HARDAGE, B.A. 1985. *Vertical seismic profiling, Part A: principles*. Handbook of Geophysical Exploration, vol. 14A. London: Geophysical Press.
- HARJES, H. P., & JANIK, M. 1994. Origin of reflections from the Altenparkstein Fault Zone (KTB). *Pages A97–A106 of: KTB-Report*, vol. 94-2. Hannover, Germany: Niedersächsisches Landesamt für Bodenforschung.
- HARJES, H. P., BRAM, K., DÜRBAUM, H.-J., GEBRANDE, H., HIRSCHMANN, G., JANIK, M., KLOECKNER, M., LUESCHEN, E., RABELL, W., SIMON, M., THOMAS, R., TORMANN, J., & WENZEL, F. 1997. Origin and nature of crustal reflections: Result from integrated seismic measurements at the KTB superdeep drilling site. *Journal of Geophysical Research*, **102**(B8), 18,267–18,288.
- HIRSCHMANN, G. 1996. Ergebnisse und Probleme des strukturellen Baues im Bereich der KTB-Lokation. *Geologica Bavarica*, **101**, 37–51.
- HIRSCHMANN, G., & LAPP, M. 1994. Evaluation of the Structural Geology of the KTB Hauptbohrung (KTB-Oberpfalz HB). *Pages 285–308 of: KTB-Report*, vol. 1. Hannover, Germany: Niedersächsisches Landesamt für Bodenforschung.
- JIA, Y., & HARJES, H.-P. 1997. Seismische Q-Werte als Ausdruck von intrinsischer Dämpfung und Streudämpfung der kristallinen Kruste um die KTB-Lokation. *In: Abstracts*. Contributions to the 10th ann. KTB colloquium.

- JONES, T.D. 1986. Pore fluids and frequency dependent wave propagation in rocks. *Geophysics*, **51**, 1939–1953.
- KERN, H., & POPP, T. 1995. Physical properties of KTB-rock samples measured at simulated in-situ conditions. *Pages 225–228 of: Abstracts*. Contributions to the 8th ann. KTB colloquium.
- KERN, H., SCHMIDT, R., & POPP, T. 1991. The velocity and density structure of the 4000 m crustal segment at the KTB drilling site and their relationship to lithological and microstructural characteristics of the rocks: An experimental study. *Sci. Drill.*, **2**, 130–145.
- KESSELS, W., & KÜCK, J. 1995. Hydraulic communication in the crystalline rocks between the boreholes of the Continental Deep Drilling Program in Germany. *Int. R. Rock Mech. Min. Sci. Geomech. Abstr.*, **32**, 37–47.
- KJARTANSSON, E. 1979. Constant Q-Wave Propagation. *Journal of Geophysical Research*, **84**(B9), 4737–4748.
- KNOPOFF, L., & MCDONALD, G.J.F. 1958. Attenuation of small amplitude stress waves in solids. *Reviews of Modern Physics*, **30**, 1178–1192.
- KOSSMAT, F. 1927. Gliederung des variszischen Gebirgsbaues. *Abh. Sächs. Geol. Landesamtes*, **1**, 39pp.
- KUSTER, G. T., & TOKSÖZ, M. N. 1974. Velocity and attenuation of seismic waves in two-phase media. *Geophysics*, **39**, 607–618.
- LI, X.-P. 1995. Estimation of apparent seismic attenuation of crystalline rocks in the KTB area using VSP data. *Scientific Drilling*, **5**, 199–216.
- LI, X.-P., & RICHWALSKI, S. 1996. Seismic attenuation and velocities of p- and s-waves in the German KTB area. *J. Appl. Geophys.*, **36**, 67–76.
- LÜSCHEN, E., SOELLNER, W., HOHRATH, A., & RABEL, W. 1991. Integrated P- and S-wave borehole experiments at the KTB-deep drilling site in the Oberpfalz area (SE-Germany). *Pages 121–133 of: MEISSNER, R. ET AL. (ed), Continental Lithosphere: Deep Seismic Reflections*. Geodyn. Ser., vol. 22. AGU, Washington, D.C.
- LÜSCHEN, E., BRAM, K., SOELLNER, W., & SOBOLEV, S. 1996. Nature of seismic reflections and velocities from VSP-experiments and borehole measurements at the KTB-deep drilling site in SE-Germany. *Tectonophysics*, **264**, 309–326.
- MACHON, L. 1995. Geochemistry/Fluid Analysis. *Pages C1–C28 of: KTB-Report*, vol. 95-2. Hannover, Germany: Niedersächsisches Landesamt für Bodenforschung.

- MEISSNER, R. 1986. *The Continental Crust*. International Geophysics Series, vol. 34. Academic Press, Inc.
- MEISSNER, R., & THE DEKORP RESEARCH GROUP. 1991. The DEKORP surveys: Major achievements for tectonical and reflective style. *Pages 69–76 of: MEISSNER, R. ET AL. (ed), Continental Lithosphere: Deep Seismic Reflections*. Geodyn. Ser., vol. 22. AGU, Washington, D.C.
- MÖLLER, P., WEISE, S.M., ALTHAUS, E., BACH, W., BEHR, H.J., BORCHARDT, R., BRÄUER, K., DRESCHER, J., ERZINGER, J., FABER, E., HANSEN, B.T., HORN, E.E., HUENGES, E., KÄMPF, H., KESSELS, W., KIRTSEN, T., LANDWEHR, D., LODEMANN, M., MACHON, L., PEKDEGER, A., PIELOW, H.-U., REUTEL, C., SIMON, K., WALTHER, J., WEINLICH, F.H., & ZIMMER, M. 1997. Paleofluids and Recent fluids in the upper continental crust: Results from the German Continental Deep Drilling Program (KTB). *Journal of Geophysical Research*, **102**(B8), 18,233–18,254.
- NEEP, J.P., SAMS, M.S., WORTHINGTON, M.H., & O'HARA-DHAND, K.A. 1996. Measurement of seismic attenuation from high-resolution crosshole data. *Geophysics*, **61**(4), 1175–1188.
- O'BRIEN, P. J., DUYSER, J., GRAUERT, B., SCHREYER, W., STOECKERT, B., & WEBER, K. 1997. Crustal evolution of the KTB drill site: From oldest relics to the late Hercynian granites. *Journal of Geophysical Research*, **102**(B8), 18,203–18,220.
- O'CONNELL, R. J., & BUDANSKY, B. 1974. Seismic velocities in dry and saturated cracked solids. *Journal of Geophysical Research*, **79**, 5412–5426.
- PECHNIG, R., HAVERKAMP, S., WOHLBERG, J., ZIMMERMANN, G., & BURKHARDT, H. 1997. Integrated log interpretation in the German Continental Deep Drilling Program: Lithology, porosity, and fracture zones. *Journal of Geophysical Research*, **102**(B8), 18,363–18,390.
- PRASAD, M., MANGHNANI, M., & SIEGESMUND, S. 1994. Compressional wave velocity and quality factor characteristics of selected KTB core samples. *Scientific Drilling*, **4**, 227–231.
- PUJOL, J., LUESCHEN, E., & YIGUANG, H. 1998. Seismic wave attenuation in metamorphic rocks from VSP data recorded in Germany's continental super-deep borehole. *Geophysics*, **2**(63), 354–365.
- RABEL, W. 1987. *Seismische Erkundung oberflächennaher Störzonen: Strahlentheoretische Grundlagen und Feldbeispiele*. Dissertation, Universität Kiel.
- RABEL, W. 1994. *Seismische Anisotropie der kristallinen Kruste im Feldexperiment*. Habilitation, Universität Kiel.

- RABEL, W., BEILECKE, T., BORM, G., BRAM, K., DRUIVENGA, G., GEBRANDE, H., GIESE, R., KÜCK, J., LÜSCHEN, E., & SMITHSON, S. 1999. Deep VSP at the Continental Deep Drilling Site - first results. *EOS Transact.*, **80**, F 677.
- RABEL, W., BEILECKE, T., FISCHER, D., FRANK, A., BORM, G., BRAM, K., DRUIVENGA, G., GEBRANDE, H., KÜCK, J., LÜSCHEN, E., & SMITHSON, S. 2001. New VSP to 8.5 km Depth at the KTB Super-deep Drillhole - Seismic In Situ Investigation of Deformed Crystalline Crust. *EOS Transact.*, **82**, F 862.
- RICHARDS, P.G., & MENKE, W. 1983. The apparent attenuation of a scattering medium. *Bull. Seis. Soc. Am.*, **73**, 1005–1021.
- ROBERTSSON, J.O.A., BLANCH, J.O., & SYMES, W.W. 1994. Viscoelastic finite-difference modeling. *Geophysics*, **59**(9), 1444–1456.
- SAENGER, E.H., GOLD, N., & SHAPIRO, S.A. 2000. Modeling the propagation of elastic waves using a modified finite-difference grid. *Wave Motion*, **31**(1), 77–92.
- SAMEC, P., & BLANGY, J.P. 1992. Viscoelastic attenuation, anisotropy and AVO. *Geophysics*, **57**, 441–450.
- SAMS, M.S., NEEP, J.P., WORTHINGTON, M.H., & KING, M.S. 1997. The measurement of velocity dispersion and frequency-dependent intrinsic attenuation in sedimentary rocks. *Geophysics*, **62**, 1456–1464.
- SCHMOLL, J., BITTNER, R., DÜRBAUM, H.-J., HEINRICHS, T., MEISSNER, R., REICHERT, C., RÜHL, T., & WIEDERHOLD, H. 1989. Oberpfalz deep seismic reflection survey and velocity studies, in The German Continental Deep Drilling Program (KTB). Springer-Verlag.
- SHAPIRO, S.A., & HUBRAL, P. 1996. Elastic waves in thinly layered sediments: The equivalent medium and generalized O'Doherty-Anstey formulas. *Geophysics*, **61**, 1282–1300.
- SHAPIRO, S.A., & HUBRAL, P. 1999. *Elastic waves in random media: fundamentals of seismic stratigraphic filtering*. Lecture notes in earth sciences; 80. Springer-Verlag.
- SHERIFF, R. E. 1991. *Encyclopedic Dictionary of Exploration Geophysics*. Tulsa: Society of Exploration Geophysicists.
- SHERIFF, R.E. 1975. Factors affecting seismic amplitudes. *Geophys. Prospecting*, **23**, 125–138.
- SHERIFF, R.E., & GELDART, L.P. 1995. *Exploration Seismology*. 2 edn. Vol. I. Cambridge: Cambridge University Press.

- SIEGESMUND, S., VOLLBRECHT, A., CHLUPAC, T., NOVER, G., DUERRAST, H., MUELLER, J., & WEBER, K. 1993. Fabric-controlled anisotropy of petrophysical properties observed in KTB core samples. *Scientific Drilling*, **4**, 31–54.
- SIMON, M. 1993. *Entwicklung eines 3D-Migrationsverfahrens mit Anwendungen auf seismische Daten aus dem Umfeld der Kontinentalen Tiefbohrung, Oberpfalz*. Dissertation, Universität München.
- SÖLLNER, W., LÜSCHEN, E., LI, X.-P., HUBRAL, P., GUT, T.W., & WIDMAIER, M. (eds). 1992. *VSP - A Link between Reflection Seismic Profiling and Lithology*. KTB-Report (DEKORP Report), vol. 92-5. Hannover, Germany: Niedersächsisches Landesamt für Bodenforschung.
- SPANGENBERG, E., & UMSONST, T. 1993. Lithology and seismic impedance at KTB - A first correlation. *Pages 153–157 of: KTB-Report*, vol. 93-2. Hannover, Germany: Niedersächsisches Landesamt für Bodenforschung.
- SPENCER, T.W., SONNAD, J.R., & BUTLER, T.M. 1982. Seismic Q-Stratigraphy or dissipation. *Geophysics*, **47**, 16–24.
- STROH, A., HANSMANN, J., HEINSCHILD, H. J., HOMANN, K. D. TAPFER, M., WITTENBECKER, M., & ZIMMER, M. 1990. Drillhole KTB Oberpfalz VB-Geoscientific investigations in the KTB field laboratory, depth interval 0-4000.1 m. *Pages C1–C37 of: KTB-Report*, vol. 90-8. Hannover, Germany: Niedersächsisches Landesamt für Bodenforschung.
- TOKSÖZ, M.N., & JOHNSTON, D.H. (eds). 1981. *Seismic wave attenuation*. Geophysics Reprints Series 2. Tulsa: Society of Exploration Geophysicists.
- TONN, R. 1988. *Die Bestimmung der seismischen Güte Q - Ein Vergleich unterschiedlicher Berechnungsmethoden*. Dissertation, Universität Kiel.
- TONN, R. 1991. The determination of the seismic quality factor Q from VSP data: A comparison of different computational methods. *Geophysical Prospecting*, **39**, 1–28.
- ČERVENÝ, V., MOLOTOV, I.A., & PŠENČÍK, I. 1977. *Ray method in seismology*. Tech. rept. Univerzita Karlova, Praha.
- VIRIEUX, J. 1986. P-SV wave propagation in heterogeneous media: velocity-stress finite-difference method. *Geophysics*, **51(4)**, 889–901.
- WAGNER, G. A., COYLE, D. A., DUYSER, J., HENJEST-KUNST, F., PETEREK, A., SCHROEDER, B., STOECKHERT, B., WEMMER, K., ZULAUF, G., AHRENDT, H., BISCHOFF, R., HEJL, E., JACOBS, J., MENZEL, D., NAND LAL, P., VAN DEN HAUTE, C., VERCOUTERE, C., & WELZEL, B. 1997. Post-Variscan thermal and

- tectonic evolution of the KTB site and its surroundings. *Journal of Geophysical Research*, **102**(B8), 18,221–18,232.
- WIDESS, M.B. 1973. How thin is a thin bed? *Geophysics*, **38**, 1176–1180.
- WORTHINGTON, M.H., KING, M.S., & MARSDEN, J.R. 2001. Determining the damping factor of sedimentary rocks required for seismically designed structures. *Int. J. of Rock Mech. and Mining Sci.*, **38**, 801–806.
- YILMAZ, Ö. 1987. *Seismic Data Processing*. Tulsa: Society of Exploration Geophysicists.
- YILMAZ, Ö. 2001. *Seismic Data Analysis; Volume I and II*. Tulsa: Society of Exploration Geophysicists.
- ZHANG, C., & ULRYCH, T.J. 2002. Estimation of quality factors from CMP records. *Geophysics*, **67**(5), 1542–1547.
- ZOEPPRITZ, K. 1919. Über Reflexion und Durchgang seismischer Wellen durch Unstetigkeitsflächen. Über Erdbebenwellen VII B. *Nachrichten der Königlichen Gesellschaft der Wissenschaften zu Göttingen, Mathematik-Physik*, **K1**, 57–84.

Erklärung

Ich erkläre hiermit an Eides Statt, daß ich die vorliegende Arbeit selbständig und ohne Benutzung anderer, als der angegebenen Hilfsmittel angefertigt habe. Die aus fremden Quellen direkt übernommenen Gedanken sind kenntlich gemacht.

Diese Arbeit wurde in gleicher oder ähnlicher Form keiner anderen Prüfungsbehörde vorgelegt oder veröffentlicht.

Kiel, April 2003

(Thies Beilecke)

Lebenslauf

Name: Thies Carl Helmut Beilecke
Geburtsdatum: 12. März 1965
Geburtsort: Kiel
Staatsangehörigkeit: deutsch

Schulbildung

1971-1975 Grund- und Hauptschule Flintbek
1975-1985 Gymnasium Max-Planck-Schule, Kiel
1981/82 Cashmere High School, Cashmere, Washington, USA
1982 amerikanisches High School Diploma
1985 Abitur

Wehrdienst

1985-1986 Monteur in der Panzerinstandsetzung

Studium

1986-1989 Ozeanographie an der Christian-Albrechts-Universität zu Kiel
1989-1996 Geophysik an der Christian-Albrechts-Universität zu Kiel
Abschluß: Dipl. Geophysiker

Berufliche Tätigkeit

Während des Hauptstudiums
1996 Geophysik Consulting GmbH Kiel: Altlasten, Baugrund- und Flachwasseruntersuchungen
GeoForschungsZentrum Potsdam (GFZ): Reflexionsseismik im Nordostdeutschen Becken
1997-1998 Institut für Geophysik, Universität Kiel: Reflexionsseismik im Nordostdeutschen und im Kanarischen Becken
1998-2001 Institut für Geowissenschaften, Universität Kiel: Bohrlochseismik an der *Kontinentalen TiefBohrung* (KTB)
2002-2003 Institut für Geowissenschaften, Universität Kiel: Bohrlochseismik an der *Kontinentalen TiefBohrung* (KTB) und Erforschung seismoelektrischer Verfahren

Kiel, den 29. April 2003

Danksagung

Die vorliegende Arbeit wäre ohne die vielfältige Mitarbeit und professionelle Erfahrung vieler Menschen nicht denkbar gewesen. Ich möchte mich für die Unterstützung bedanken. Die Danksagung ist vielleicht ein wenig lang geraten, aber ich meine, es gibt gute Gründe, sie so ausführlich zu halten. Im Nachhinein ist es fast unglaublich, wie viele Personen im Laufe der Zeit ihren Anteil an dem meiner Arbeit zugrundeliegenden Experiment hatten. Aber ein Experiment mit 8.5 km in situ Teufe ist ja auch nicht von Pappe. Es sind sogar noch nicht einmal jene Personen erwähnt, die an den MSP-Messungen bzw. Weitwinkelmessungen teilgenommen haben.

Viele haben leider auch unter Vernachlässigung leiden müssen - ich war einfach von der Bildfläche verschwunden. Ich hoffe, ich kann das wieder gerade biegen.

Zu allererst möchte ich mich für die Geduld meiner Familie bedanken, deren Mitglieder wahrscheinlich innerlich immer ungläubig mit dem Kopf geschüttelt haben. Aber es gibt irgendwann einfach kein Zurück mehr.

Mit Prof. Dr. Wolfgang Rabbel zusammenzuarbeiten bedeutet immer wieder überraschende Sichtweisen nicht nur aus der Geophysik kennenzulernen. Die vorliegende Arbeit hat davon in besonderem Maße profitiert. Dafür möchte ich mich bedanken. Ich möchte mich aber auch für die langjährige Zusammenarbeit in einem äußerst angenehmen Arbeitsklima bedanken.

Herrn Prof. Dr. Rolf Meißner danke ich für seine spontane Bereitschaft, engagierter Korreferent meiner Arbeit zu werden. Seine immerwährende Neugierde und Freude an der Geophysik aber auch an allem Schönen waren und sind inspirierend und werden mir immer in guter Erinnerung und Vorbild bleiben.

Ohne das große Engagement von Günther Druivenga von den Geowissenschaftlichen Gemeinschaftsaufgaben Hannover (GGA) und seine Freude am Projekt wären nicht nur die VSP Messungen weniger als halb so erfolgreich gewesen. Auf Günther konnte man sich immer verlassen - wahrscheinlich mehr, als ihm lieb war.

Prof. Dr. Günther Borm vom GeoForschungsZentrum Potsdam (GFZ), Prof. Dr. Helmut Gebrande und Dr. Ewald Lüschen von der Universität München, aber auch Dr. Kurt Bram von den GGA danke ich für die Unterstützung in Vorder- und Hintergrund und für die Begleitung der Auswertung.

Vielen Dank an Dr. Rüdiger Giese vom GFZ Potsdam. Aschermittwoch in der Oberpfalz war für uns beide der Tiefpunkt bei der Vorbereitung des Experiments.

Mit Tips zur Hand waren auch Prof. Dr. Scott Smithson von der University of Wyoming, Laramie, Prof. Dr. Jose Pujol von der University of Memphis und Prof. Dr. David Okaya von der University of Southern California, Los Angeles. Ihre aktive Begleitung hat mich sehr motiviert.

Insbesondere möchte ich mich auch bei Lothar Wohlgemuth, Jochem Kück und Karl Bohn vom GFZ Potsdam bedanken, die das Arbeiten an der Bohrung angenehm unterhaltsam gestalteten, aber auch bei Christian Carnein, Mike Hönig und Martin Töpfer ebenfalls vom GFZ Potsdam, die selbst in scheinbar aussichtslosen Situationen noch einen Ausweg fanden. Die Geophonsonden bemühten sich zwar, uns einen Strich durch die Rechnung zu machen, hatten aber gegen ihre Kreativität keine Chance.

Vielen Dank auch an Walther Rode, E. Großmann, Jürgen Lips, und Wolfgang Weitmüller von den GGA Hannover, die mit ihrer ruhigen Art jeglichen potentiell aufkommenden Stress bei der Aufnahme der Daten im Keim erstickten und für die es kein schlechtes Wetter sondern höchstens schlechte Kleidung gab.

Vielen Dank an Dr. Raimund Seitz von der Geophysik GGD Leipzig und an Raimund Hopfe, Peter Pohl und deren Mitarbeitern von der Thüringischen Sprenggesellschaft. Es ist immer schön, angenehme Zeitgenossen um sich zu haben.

Ohne die kräftige Unterstützung bei den Messungen und der Auswertung durch die Mitglieder der Abteilung Geophysik des Instituts für Geowissenschaften an der Universität Kiel Filiz Bilgili, Daniel (Fischi) Fischer, Axel Frank, Jörg Hasenclever, Christina (Tina) Klein, Sonja Krivanek, Nils Märklin, Mirko Sattler und Susanne Wölz wären die Messungen überhaupt nicht durchführbar gewesen. Ich konnte mich immer auf euer Mitdenken verlassen. Hoffe, es hat euch trotz Tätigkeiten wie Rasenmähen und Plastiksplitter sammeln Spaß gebracht. Mit Fischi und Mirko gab's immer viel zu lachen in unserem Büro. Nicht zu vergessen sind aber auch weitere Mitglieder der Kieler Geophysik. Sogar Dr. Harald Stümpel und Georg (Schorsch) Lohr wurden bei dieser tiefenseismischen Kampagne eingespannt. Das kann man getrost historisch nennen.

Bedanken möchte ich mich auch bei Dr. Thomas Bohlen, dessen Interesse an den Ergebnissen und Zuspruch bei der Modellierung eine wichtige Rolle in dieser Arbeit gespielt haben. Diese Arbeit hat aber auch profitiert von der parallelen Auswertung und den Modellierungen von Dr. Christiane Trela vom GFZ Potsdam.

Dr. Tobias (Tobi) Karp, den ich "fast" noch mit der Abgabe der Dissertation überholt hätte, half immer mit einem trockenen Spruch, Dr. Christof Müller und Dr. Christian Goltz erweiterten mittags des öfteren das Gesichtsfeld durch cineastische und andere Assoziationen.

Ich danke meinem Bruder Lars, meinem Vater Eckard und Dr. Christof Müller für die kritische Durchsicht des Manuscripts.

Ich danke der Deutschen Forschungsgemeinschaft (DFG), der Amerikanischen National Science Foundation (NSF), dem International Scientific Continental Drilling Program (ICDP), dem GFZ Potsdam und den GGA Hannover, daß diese Daten aufgenommen werden konnten aber auch für die Unterstützung bei der Auswertung.

ISBN: 3-00-012281-8